

DIVISION: MPLS

DOCTOR OF PHILOSOPHY IN MATERIALS



THE EFFECTS OF MICROSTRUCTURE ON STRENGTH AND FRACTURE RESISTANCE OF NUCLEAR GRAPHITE

THOMAS ZILLHARDT

Supervised by James Marrow

and co-supervised by Dong (Lilly) Liu

UNIVERSITY OF OXFORD

DEPARTMENT OF MATERIALS

Doctor of Philosophy

Academic Year 2020 - 2021

THOMAS ZILLHARDT
Wadham College
The Queen's College

The Effects of Microstructure on Strength and Fracture Resistance of Nuclear Graphite

Supervisor: Prof James Marrow
Co-supervisor: Dr Dong Liu
June 2021

This report is submitted in partial fulfilment of the requirements for the degree of Doctor of Philosophy

© University of Oxford 2021. All rights reserved. No part of this publication may be reproduced without the written permission of the copyright owner.

ABSTRACT

Cracking from stress concentrations of the graphite neutron moderator, or keyway root cracking, is a potential limit for the lifetime of the UK Advanced Gas-cooled Reactors (AGR), and there is a need to better understand how damage occurs prior to fracture. Gilsocarbon graphite is a heterogeneous and quasi-brittle material, a class that includes concretes and natural materials such as bone. This project has made use of, developed, or participated in the development of advanced neutron and X-ray synchrotron techniques to improve the understanding of the deformation of Gilsocarbon graphite. In-situ High-Resolution Tomography and X-ray Diffraction Mapping has confirmed the non-linearity of graphite deformation in compression of a flattened disc and has highlighted the heterogeneity of the microstructure's response to stress. To this extent, codes have been written to process and match the DVC and XRD strains and extract comparative strain quantities. A novel in-situ technique and associated post-processing routines have been developed with Neutron Bragg Imaging to investigate grain reorientation, and combined with In-situ Three-dimensional X-ray Diffraction (3DXRD) they reinforced indications that this mechanism is recoverable. In-situ High Speed Synchrotron Tomography provided unique time-resolved observations of crack initiation, propagation and coalescence away from a stress concentration, indicating the prevalence of lenticular cracks. With as much as 72 hours of beamtime, this project has developed reusable techniques and provided unique insight of the damage accommodation in nuclear-grade graphite.

ACKNOWLEDGEMENTS

Whereas most authors conclude their acknowledgements by mentioning their family, this should be my beginning. My parents, Alain Zillhardt and Claudine Jahan, have been extremely supportive of my long education, both mentally and financially, often at the expanse of their own dreams. From my electrical engineering studies in France, to my masters in the UK and finally PhD, they have always admired my progress whilst often laughing that 'I will end up starting my professional career at retirement'. Their support was certainly motivated by pride, of a first engineer and scientist in our middle-class family, but more particularly by love, with the conviction to give every opportunity possible to their sons. This is a privilege. My brother, Matthew Zillhardt, was my best mental support over the years, bridging the distance by playing online video games, escaping the day-to-day troubles. I dedicate this thesis to them.

This PhD is not my first research project, and I became convinced early on that a good symbiosis with my main supervisor was essential for me to be productive and complete any project in time. Rumours say that Prof Thomas James Marrow is the best supervisor in Oxford, and I surely concur. But more importantly, his supervision style was compatible with me. Not only does James give space to his students to flourish and develop their own research, but he is also always available for support and advice, weekends and holydays inclusive (except 10 days in the summer). James's support has been exceptional, and he reminded me that perhaps, all I needed to be successful, was to believe in myself. I am extremely gratefully to have had the chance to

study under James's supervision, certainly a role model for anyone aspiring to an academic career.

I am equally indebted to have been co-supervised by Dr Dong (Lilly) Liu. Lilly has been the balance in this project, pushing me to go forward, publish and be critical of my work, by being straightforward and direct, without holding back from constructive criticism, and I am very thankful for that.

There is a large number of people who have meant a lot to me over these four years, but instead of writing a long list of names which may not be meaningful to the reader, I shall keep them in my heart.

To my grandfather, André Zillhardt, who left us before I could complete this work, and who would have been immensely proud.

“Science and everyday life cannot and should not be separated. Science, for me, gives a partial explanation of life. In so far as it goes, it is based on fact, experience, and experiment.”

– Rosalind Franklin, pioneer of X-ray diffraction on carbons and graphite [1], letter to Ellis Franklin, 1940

TABLE OF CONTENTS

LIST OF FIGURES ..... **XI**

LIST OF TABLES ..... **XXVIII**

LIST OF ABBREVIATIONS ..... **XXX**

NOMENCLATURE ..... **XXXV**

SYMBOLS ..... **XXXVI**

GLOSSARY ..... **XXXVII**

ABSTRACT ..... **XL**

1 A CENTURY OF GRAPHITE USE, RESEARCH AND DEVELOMENT **1:1**

1.1 PREAMBLE 1:2

1.2 INDUSTRIAL RELEVANCE OF GRAPHITE 1:3

1.2.1 Advanced Gas-cooled Reactors *1:3*

1.2.2 Manufacture *1:4*

1.2.3 Next Generation Graphite and Other Uses *1:5*

1.3 GRAPHITE STRUCTURE 1:6

1.3.1 Crystal Structure and Properties *1:6*

1.3.2 Microstructure *1:8*

1.4 MECHANICAL PROPERTIES AND DEFORMATION OF VIRGIN NUCLEAR GRAPHITE 1:10

1.4.1 Deformation Behaviour *1:10*

1.4.2 Fracture Toughness *1:12*

1.4.3 Strength *1:13*

1.4.4 Notch sensitivity *1:14*

1.5 DEFECTS AT MULTIPLE LENGTH SCALES 1:16

1.5.1 Bulk *1:16*

1.5.2 Microscale *1:16*

1.5.3 Mrozowski Cracks *1:18*

1.5.4 Reorientation, Twinning, Kinking and Basal Plane Slip *1:19*

1.6 Environmental Effects 1:20

1.6.1 Thermal Expansion *1:20*

1.6.2 Irradiation *1:21*

1.6.3 Radiolytic Oxidation *1:23*

1.6.4 Combined Reactor Core Environmental Effects *1:25*

1.7 Techniques 1:26

1.8 Modelling 1:27

1.9 Objectives 1:29

2 ADVANCED EXPERIMENTAL TESTING OF VIRGIN GRAPHITE 2:1

2.1 Introduction to Experimental Characterisation 2:3

2.2 Digital Image Correlation Control 2:5

2.2.1 Preamble *2:5*

2.2.2 GOM Aramis 5M stereo-DIC (3D-DIC) *2:7*

2.2.3 PRESSOR Rig: 3D-DIC for specimen movement and deformation *2:9*

2.2.4 Neutron Radiography: 2D-DIC for specimen deformation and movement *2:11*

2.3 Laboratory X-ray Tomography 2:13

2.4 Laboratory in-situ Loading and Temperature X-ray Tomography 2:19

2.5 Synchrotron X-ray Imaging and Diffraction Mapping, Neutron Diffraction and Image Correlation for the Measurement of Elastic and Total Strains 2:20

2.5.1 Preamble *2:20*

2.5.2 ENGIN-X Neutron Diffraction Beamline *2:21*

2.5.3 Diamond Synchrotron I 12 Imaging and Diffraction Beamline *2:22*

2.6 Multi-faceted Approach to Damage and Deformation with Synchrotron X-ray Imaging and Diffraction (ESRF) 2:25

2.6.1 Preamble *2:25*

2.6.2 ESRF ID 11 Beamline *2:25*

2.6.3 High-resolution X-ray Phase Contrast Tomography and Diffraction Mapping *2:26*

2.6.4 Three-dimensional in-situ X-ray Diffraction Scanning *2:28*

2.6.5 Topo-tomography of Highly Oriented Pyrolytic Graphite Indentation *2:30*

2.7 NEUTRON BRAGG IMAGING 2:32

2.7.1 Preamble *2:32*

2.7.2 The IMAT Neutron Imaging Instrument *2:32*

2.7.3 Bragg-edge Imaging *2:34*

2.7.4 Design of the Loading Rig (PRESSOR) *2:35*

2.7.5 Experimental setup *2:37*

2.8 HIGH-RESOLUTION NEUTRON DIFFRACTION MAPPING: SALSA 2:40

2.8.1 Preamble *2:40*

2.8.2 SALSA at the Institut Laue-Langevin *2:40*

2.8.3 Compressive Loading of Drilled and Slitted Discs *2:44*

2.8.4 Tensile Loading of Notched Dog-bone Specimens *2:46*

2.9 TIME SERIES HIGH-RESOLUTION SYNCHROTRON PINK BEAM TOMOGRAPHY: SOLEIL 2:50

2.9.1 Preamble *2:50*

2.9.2 Experimental setup *2:50*

2.10 TOTAL NEUTRON SCATTERING: GEM 2:55

2.10.1 Preamble *2:55*

2.10.2 Experimental Setup *2:55*

3 EVALUATION OF DAMAGE DISTRIBUTION IN GILSOCARBON GRAPHITE 3:1

3.1 PREAMBLE 3:2

3.2 IN-SITU BULK MEASUREMENT OF ELASTIC AND TOTAL STRAINS (JEEP I12) 3:3

3.2.1 Iterative Tomography Reconstruction *3:3*

3.2.2 Local Digital Volume Correlation of Tomographies *3:6*

3.2.3 Quantification of Tensile Strains with SXRDM *3:9*

3.3 Ultra-High Resolution Digital Volume Correlation and Elastic Strain Mapping 3:13

3.3.1 Tomography Processing 3:13

3.3.2 Multi-Domain Global Digital Volume Correlation of Very Large Datasets 3:18

3.3.3 High-Resolution X-ray Diffraction Mapping 3:19

3.4 Results: Comparison of Total and Elastic Strains in the Bulk 3:22

3.4.1 Quantification of Global Deformation 3:22

3.4.2 Distribution of Large Elastic Strains 3:24

3.5 Results: Strain Evaluation at High Resolution 3:25

3.5.1 Total Strains from Multi-domain DVC of Stitched Tomographies 3:25

3.5.2 Elastic Deformation at High Resolution 3:27

3.6 Discussion: Multi-Scale Damage Evaluation and the Role of Microstructure 3:29

4 INVESTIGATION OF CRYSTAL REORIENTATION AS A MECHANISM OF DAMAGE ACCOMMODATION 4:1

4.1 Preamble 4:2

4.2 In-Situ Bragg Imaging 4:3

4.2.1 Preamble 4:3

4.2.2 Data Output and Quality, Pre-processing 4:4

4.2.3 Methodology for the Extinction Spot Tracking and Evaluation of Change in Local Coherent Scattering 4:7

4.2.4 Advanced Filtering and Segmentation 4:12

4.2.5 Image Registration 4:14

4.3 Three-Dimensional Synchrotron X-ray Diffraction (3DXRD) of a graphite cylinder 4:15

4.3.1 Preamble 4:15

4.3.2 X-ray Diffraction Finding and Fitting 4:15

4.3.3 3DXRD Tracking 4:19

4.4 Results: In-Situ Bragg Imaging 4:25

4.4.1 Preliminary Observations 4:25

4.4.2 Variation of the Correlation in the Extension Datasets *4:29*

4.5 Results: In-Situ Three-Dimensional Synchrotron X-ray Diffraction 4:34

4.5.1 Total (DVC) and elastic (XRD) strains *4:34*

4.5.2 Orientation tracking *4:38*

4.6 Discussion on Grain Orientation and Elasticity 4:40

4.6.1 Summary of Observations *4:40*

4.6.2 Potential Interpretations *4:40*

4.6.3 Experimental Aspects *4:44*

4.7 Opportunities and Future Work 4:45

5 SUB-CRITICAL MICROCRACK INITIATION, COALESCENCE AND PROPAGATION 5:1

5.1 Preamble 5:2

5.2 Data, Challenges and Methodology 5:3

5.2.1 Varied and Large Datasets *5:3*

5.2.2 Pre-processing and Shortlisting *5:5*

5.2.3 Selection and Methodology Justification *5:8*

5.2.4 Advanced Crack Identification, Detection and Tracking *5:9*

5.3 Results of Microcrack Identification and Detection 5:10

5.3.1 First Observations of Microcrack Development. *5:10*

5.3.2 Residuals from a Multi-Correlation Approach *5:15*

5.3.3 Crack Detection with Data Remapping *5:34*

5.4 Discussion on Crack Initiation and Brittle Fracture 5:40

5.4.1 Relevance of the Technique *5:40*

5.4.2 Prevalence of Microcrack Formation *5:41*

5.4.3 Preferred Microcrack Path *5:41*

5.4.4 Onsets of Brittle Fracture *5:42*

5.4.5 Outlook and Future Work *5:43*

6 ADVANCES ON THE UNDERSTANDING OF THE ROLE OF THE MICROSTRUCTURE ON ACCOMMODATING STRESS IN GILSOCARBON GRAPHITE 6:1

7 THE PROSPECTS OF NUCLEAR GRAPHITE RESEARCH 7:1

CONCLUSIONS ..... A

PUBLICATIONS ..... E

REFERENCES ..... G

APPENDIX A APPENDICES A.1-1

LIST OF FIGURES

Figure 1: Graphite crystal structure [36] 1:7

Figure 2: (a) Polarized SEM of virgin Gilsocarbon graphite, (b) TEM of unirradiated Gilsocarbon graphite [29] 1:9

Figure 3: Gilsocarbon graphite (X-ray tomography microscope Xradia 510 Versa at Oxford Materials) 1:9

Figure 4: Schematic representation of the load-displacement curve for a quasi-brittle material..... 1:11

Figure 5: Experimental setup for stereo-DIC experiments in the Oxford Materials Laboratories, with (a) the Aramis 5M system and (b) the Shimadzu mechanical loading rig 2:6

Figure 6: (a) Stereo digital image correlation setup; (b) mapping area with speckle pattern; (c) out-of-plane z-displacements of the same area; and (d) angular rotations with load of the mapped area about the X, Y and Z axes. 2:10

Figure 7: Example of vertical displacement fields calculated using LaVision DaVis on summed images from Region A. The arrows represent the vectors of displacement in the image plane. The colour represents the magnitude of the vertical displacement. Rigid body movements and displacements have been removed 2:12

Figure 8: Strains along the loading direction from summed radiographies in Region A of the energy range 2:12

Figure 9: ZEISS Xradia 510 setup (a) and close-up view of the source 2:14

Figure 10: Xradia 510 in-situ Wide Field Tomography (5.84 μm/voxel), (slice close to face of a disc compression specimen) 2:14

Figure 11: Radial and transversal tomography slices from in-situ experiments at 2.44μm/vx (a) and 0.88μm/vx (b) 2:16

Figure 12: (a) L0A - preload, (b) L1 – 80% of failure load, (c) L0B - preload. 2:16

Figure 13: Ex-situ tomography scan at high-resolution (0.3 μm/vx), transversal (a) and radial (b) slices..... 2:18

Figure 14: Xradia 510 Very High Resolution Tomography scans at 0.22 μm/voxel (a) and 0.17 μm/voxel (b)..... 2:18

Figure 15: Load and temperature regime for experiment BD050518HTB_C05 ..... 2:19

Figure 16: Deben H250 load and temperature rig (a), sample stage close-up view (b), experimental setup (c) 2:20

Figure 17: (a) Schematic (top view) of the experimental setup at ENGIN-X, with imaging of a horizontal specimen (b) and a vertical specimen (c), and example of neutron spectrum [73] 2:22

Figure 18: Presentation of the Shimadzu Rig and Pixium detector in use for experiment EE1585-2 at JEEP 2:23

Figure 19: Loading configuration for X-ray computed tomography (XCT) and X-ray diffraction (XRD) (a), area mapped by XRD (b) and variation of normal strain $\boldsymbol{\varepsilon nXRD\phi}$ as a function of azimuth angle (c) [73] 2:24

Figure 20: Rig close-up view (a), beam exit (b), sample stage and near-field detectors (c) and far-field detectors (d) 2:26

Figure 21: HR-PCT and XRDM setup, sample dimensions (a), tomography zones and overlap (b) and XRD grid (c) 2:27

Figure 22: Load steps for the 3DXRD experiment, with each ROI-A and even numbers having a different FoV for measurements 2:29

Figure 23: 3DXRD Setup with the positions of the PCT volume in yellow and the 3DXRD gauge in red 2:29

Figure 24: Topo-tomography acquisition from the near-field FreLon detector of HOPG at preload and angle 0°/10°, with two contrast and brightness adjustment to observe the diffracted grain (a) and the tomography region (b), and a schematic with the indenter in red and the HOPG in blue 2:31

Figure 25: Beam spectra for run number 15209 (Scan 5, Load 4kN, 120μA) from monitor 5 which is 49.5m from the moderator, with green bar representing wavelength for basal plane diffraction 2:33

Figure 26: Neutron imaging loading rig: (a) close up view of anvils; (b) 3D CAD 2:37

Figure 27: Experimental setup depicting a side view with rig-to-shield distance (a), overall view with robot-arm and rig fixed on tomography stage (b), detector window close-up view (c), secondary setup close-up with screw head away from top-shield (d), sample dimensions (e), and primary setup with screw head under top shield (f) 2:39

Figure 28: Experimental setup diagram for experiments 1-02-241 and 1-02-299 ..... 2:41

Figure 29: Overall instrument view (a), hexapod (b), hole-notched sample (c) and slit-notched sample (d) 2:42

Figure 30: Diagram representing the gauge volume within the sample for SALSA experiments 2:43

Figure 31: (a) Example alignment views and (b) cameras for alignment for SALSA experiments 2:43

Figure 32: (a) Map area of the slit-notched sample, (b) 36-points map at 2 × 2 × 2 mm, (c) 9-points map at 0.6 × 0.6 × 2mm, (d) hole-notched sample map at 0.6 × 0.6 × 2 mm for SALSA experiment 1-02-241 ..... 2:45

Figure 33: Loading sequences for all three samples of experiment 1-02-241 ..... 2:46

Figure 34: (a) Side view of the Instron, (b) overall setup view, (c) close-up view of the sample, (d) view of the sample and second primary collimator for SALSA experiment 1-02-299 ..... 2:47

Figure 35: Loading regime for SALSA experiment 1-02-299 ..... 2:48

Figure 36: (a) Close-up view of the right jaw, (b) jaw with alignment rings, (c) CAD rendering of the setup for SALSA experiment 1-02-299 ..... 2:48

Figure 37: Sample design and position of acquisition points in SALSA experiment 1-02-299 ..... 2:49

Figure 38: (a) Beam stop, (b) optics and monochromator, (c) data converter, (d) detector setup for SOLEIL PSICHE experiment 20190926 ..... 2:52

Figure 39: Notched DCDC sample (a) and Brazilian disc sample (b) for SOLEIL PSICHE experiment 20190926 ..... 2:52

Figure 40: (a) Tomography stage, (b) sample stage, (c) PMA tube and (d) Aluminium tube for SOLEIL PSICHE experiment 20190926 ..... 2:53

Figure 41: Diagram of the experimental setup for SOLEIL PSICHE experiment 20190926 ..... 2:53

Figure 42: Experimental setup of the GEM instrument, with (a) the sample holder, positioner and lid, (b) a close-up view of the sample, and (c) the instrument hutch..... 2:56

Figure 43: Standard gridrec tomography reconstruction (a) and magnification (b), compared with iterative CGLS reconstruction (c) and magnification (d); no filtering applied 3:5

Figure 44: Raw XRDM diffraction point acquisition (a), and its rescaled histogram (b), and a radial line profile (c) represented by a yellow bar on (a) 3:10

Figure 45: Example of strain sinusoidal fit for map point number 100 at load step 4.5 kN [73] 3:10

Figure 46: Realigned and pre-processed tomography slices of the left (a), top (b) and right (c) Regions of Interest (RoIs) for stitching with example matching features in image pairs circled..... 3:14

Figure 47: Slices of the final tomography volume after pre-processing and stitching, viewed from the XZ (a), YZ (b) and XY (c) planes 3:16

Figure 48: Volume rendering of the final stitched tomography, with an outline of the disc presented..... 3:17

Figure 49: Tetrahedral meshes used in the digital volume correlation with the global multi-domain approach, with the full grid overlaid on top of a volume rendering of the microstructure (a) and the $3 \times 3 \times 3$ mesh split used in the correlation (b)..... 3:19

Figure 50: Raw diffraction point acquisition 440 load step 6 (a), and its rescaled histogram (b), and a radial line profile (c) represented by a yellow bar on (a) 3:20

Figure 51: Radial integration and plot of an azimuthal bin after integration (a), and example of peak fitting and sinusoidal strain fitting (b) calculated as in 3.2.3..... 3:21

Figure 52: Front (i) and side (ii) views of the JEEP-i12 sample with $\boldsymbol{\varepsilon zz}$ (a) and $\boldsymbol{\varepsilon xx}$, (b) strains overlaid on top of the microstructure 3:23

Figure 53: DVC maps of (a) $\boldsymbol{\varepsilon xx}$, (b) $\boldsymbol{\varepsilon zz}$ and (c) $\boldsymbol{\varepsilon xz}$ strains for load steps 1.5 kN (i), 3 kN (ii) and 4.5 kN (iii) after interpolation on the XRD grid 3:23

Figure 54: XRD maps of (a) $\boldsymbol{\varepsilon xx}$, (b) $\boldsymbol{\varepsilon zz}$ and (c) $\boldsymbol{\varepsilon xz}$ strains for load steps 1.5 kN (i), 3 kN (ii) and 4.5 kN (iii) 3:24

Figure 55: Z- axis compressive strains from the correlation of step 2 (50N) with the reference overlaid on top of a volume rendering of the microstructure 3:26

Figure 56: Volume rendering showing initiation of a surface crack from step 5 ..... 3:26

Figure 57: High resolution XRD maps of tensile strains of all steps (100 μm slit aperture) 3:27

Figure 58: High resolution XRD maps of shear strains of all steps (100 μm slit aperture) 3:28

Figure 59: High resolution XRD maps of compressive strains of all steps (100 μm slit aperture) 3:28

Figure 60: Scatter plot of XRD and DVC tensile (b/c) and compressive (a/d) strains for a 4 × 4 mm area (c/d/e) and a 6 × 6 mm area (a/b) for the JEEP-i12 ..... 3:30

Figure 61:Scatter plot of XRD and DVC tensile (b/c) and compressive (a/d) strains for a 0.3132^2 mm2 area (c/d/e) and a 0.4176^2 mm area (a/b) for ESRF-id11 ..... 3:30

Figure 62: Maximum and minimum principal strains (a), and density plots (b) zoom (c/d) for the JEEP-i12 bulk XRD experiment 3:32

Figure 63: Maximum and minimum principal strains for the HRXD experiment on ESRF-id11 with trends (a) and density plot (b) with trendline from the JEEP-i12 experiment for comparison 3:32

Figure 64: Change in Lc parameter as function of load along the radial X-axis (a) and longitudinal Z-axis (b), and plotted as a function of point number on the map (d), with each point location overlaid on the longitudinal (compressive) strain map at 50 N 3:33

Figure 65: (a) Regions A and B are indicated on a neutron transmission spectrum averaged over the square area that is marked in (b) the raw uncorrected radiography at 2.9 A; (c) pre-processed and averaged image from Region A; and (d) from region B at the (002) Bragg-edge. [A blade with neutron absorption properties is inserted into the beam to avoid sample and detector activation when no data are collected. Even with correction for its insertion, there are residual “dips” on the transmission graph due to this ‘shutter’, as indicated in (a)]..... 4:5

Figure 66: Radiographies n°1900 (3.4 angstroms) for samples IOX20P2B7A (a) and IOX20P2D8B (b), with preliminary corrections applied (window size 28 × 28 mm^2) (see Table 5) 4:6

Figure 67: Workflow diagram presenting the NEUTRONIX program and its sub-programs 4:11

Figure 68: Original radiography N°1867, rolling median and multiplicative rotational Savitzky-Golay filter for preload (b) and maximum load (c) 4:13

Figure 69: Comparison of 5th stage (4 kN) to reference (0th pre-load stage at 0.2 kN): (a) horizontal displacements; (b) vertical displacements; (c) unregistered image; and (d) registered image 4:13

Figure 70: Diffraction image of point 110 at preload and saturated at 5%-95% for visualisation purposes (a) with rescaled histogram after saturation (b) and line profile on saturated image (c) represented by the yellow bar 4:16

Figure 71: Radial integration and plot of an azimuthal bin after integration (a), and example of peak fitting (b) 4:17

Figure 72: Diffraction acquisition with contrast adjusted to highlight higher intensities (a) and presentation of the method (b) 4:20

Figure 73: Fit of the distribution of peak intensity with regards to the azimuth angle with low (1) and high (2) angles as pictured in Figure 72 ..... 4:20

Figure 74: Peak finding (a) and fitting (b) of the low angle for ROI-A datasets of the azimuth positions with regards to the stage angle with the red curve represented the accumulation of the individual green peak fits 4:22

Figure 75: Peak finding (a) and fitting (b) of the high angle for ROI-A datasets of the azimuth positions with regards to the stage angle with the red curve represented the accumulation of the individual green peak fits..... 4:23

Figure 76: Peak finding (a) and fitting (b) of the low angle for ROI-B datasets of the azimuth positions with regards to the stage angle with the red curve represented the accumulation of the individual green peak fits..... 4:24

Figure 77: Processed radiographs from energy region B, with increasing load in observation steps from (a) to (d) (1 kN, 2 kN, 3 kN, 4 kN, with respect to stage 0) and then (e) unloading to 2 kN. The dashed square in (a) identifies the feature of interest presented in Figure 78 ..... 4:26

Figure 78: Close-up view at the centre of the specimen (90 × 80 pixels) (region indicated in Figure 77a)..... 4:26

Figure 79: Correlation values for the comparison to stage 1 difference image at 1 kN, zero values are not counted in the standard deviation or the mean 4:28

Figure 80: Result of the radiography processing for sample 3, increasing step from (a) to (e): 1kN, 2kN, 3kN, 4kN and 2kN, the circle points to the feature of interest 4:30

Figure 81: Enlarged view of the area of interest, with increasing load from (a) to (e)..... 4:30

Figure 82: Digital image correlation of all processed stages with stage 1 (1kN), correlation value (preload stage 0 and stage 1 not represented here)..... 4:31

Figure 83: Histograms of the correlation values for the digital image correlation of Figure 82 with curve representing the distribution..... 4:31

Figure 84: Median of the correlation values for the correlation of Figure 83 with the green arrow representing the succession of loading 4:32

Figure 85: Density plots of the correlation values of Figure 82 presented as curves 4:32

Figure 86: Displacements calculated by DVC and uncorrected for rigid body motion along the X-axis (a), Y-axis (b) and Z-axis (c) for ROI-A (i) and ROI-B even (ii), non-linear step scale 4:35

Figure 87: Compressive strains (along the Z-axis) computed by DVC for ROI-A (a) and ROI-B (b) sets, non-linear step scale..... 4:35

Figure 88: Z-axis total strains for both Regions of Interest (RoI) and associated error bars from the independent DaVis DVC of LR-PCT 4:36

Figure 89: Elastic strains (XRD) for ROI-A and ROI-B of the cylinder compression..... 4:36

Figure 90: Plot of XRD strains as a function of DVC strains for the cylinder compression..... 4:37

Figure 91: Linear plots of high and low angle tracking, representing the angular stage position (phi) as a function of load (in ROI-A)..... 4:39

Figure 92: Stage angle of the orientation with regards to load for ROI-B and high azimuthal angle (peak highlighted in green in Figure 76) 4:39

Figure 93: Flowchart describing the methodology of this analysis, with black stars indicating further methodologies for each advanced crack detection . 5:4

Figure 94: Tomography slices of sample SPKX2 at the reference (a) and final 44th step (b) after finding the common slice along the Z-axis, contrast adjustment and background removal (air still displayed), as well as the same 44th stage realigned for rotation and with the damage segmented using propagation thresholding..... 5:6

Figure 95: Volume rendering of the initial step (30 N preload) of disc sample SPMX1 with thresholding from the upper XY-plane (a) and side XZ-plane (b) views with the loading direction indicated by an arrow..... 5:12

Figure 96: Manually realigned tomography cross-sectional slices (XY-plane) in the centre of specimen SPMX1 at 30 N preload (a) and 355 N final load (b) with a blue frame indicating the location of a microcrack and with the loading direction being perpendicular to the plane of these slices..... 5:13

Figure 97: Manually realigned tomography cross-sectional slices (XY-plane) in the centre of specimen SPBX3 at preload (a) and prior to brittle fracture (b) with a blue frame indicating the location of a microcrack and with the loading direction being perpendicular to the plane of these slices..... 5:14

Figure 98: Top XY-plane (a) and side XZ-plane (b) views of the colourwash (overlay) of stages 1 (preload) and 88 (last load) of specimen SPMX1 after realignment using the normalised mutualised information metric (rigid translation and rotation only) with a blue frame indicating the location of the microcrack of interest which clearly appears as a difference between the two stages (everything that is not green or common porosity expresses difference – note the high levels of deformation around the filler particle)..... 5:16

Figure 99: The sub-volume for the microstructure autocorrelation was extracted from the bounding box in (a) shown here with a RoI of the volume rendering (full height of the sample along the vertical Z-axis) from which a XY-slice is presented in (b) 5:19

Figure 100: Autocorrelation of the sub-volume indicating that the average size of the microstructure is approximately 22 voxels..... 5:19

Figure 101: Displacement vectors on top of correlation grid (a) and displacements along the loading direction (b) between the preload (30 N) and the 10th step (appr. 90 N) after the coarse grid local correlation (130 voxel subset size)..... 5:21

Figure 102: Correlation value (a) and displacements vectors (b) coloured with the correlation value (1 is best) between the preload (30 N) and the 10th step (appr. 90 N) after the fine grid local correlation (60 voxel subset size)..... 5:21

Figure 103: Z-axis strains (a) and displacement (b) between the preload (30 N) and the 10th step (appr. 90 N) after the fine grid local correlation (60 voxel subset size), with (a) displayed scaled down with the axes showing the position of the slice (n°500) in the volume (same volume cut-out / ROI view for both Ezz and Uz)..... 5:23

Figure 104: The sub-volume for the microstructure DVC uncertainty measurement was extracted from the bounding box in (a) of stage 1 (and similar for stage 2 once realigned) shown here with a RoI of the volume rendering (full height of the sample along the vertical Z-axis) from which a slice is presented in (b) 5:23

Figure 105: Standard deviation of the displacements (a) and strains (b) along the X, Y and Z axis between the preload (stage 1) and the RBM scan translated by 100 µm along Y (and realigned) 5:24

Figure 106: First tetrahedral mesh for the coarse incremental global DVC calculation with an estimated 2,025 cells viewed on top of a volume rendering of the microstructure from the XY-plane (a) and the XZ-plane (b)..... 5:26

Figure 107: Second tetrahedral mesh for the fine global DVC calculation with an estimated 12,457 cells viewed on top of a volume rendering of the microstructure from the XY-plane (a) and the XZ-plane (b) 5:26

Figure 108: Displacement increment of the fine global DVC correlation between steps 1 (30 N) and 30 (approx. 230 N, 95% to failure) of sample SPMX1 with the results of the coarse incremental DVC as an input showing a fast convergence towards 0 ..... 5:28

Figure 109: ROI cut-out of the volume rendering (at slice n°500) with thresholding segmentation of the preload (30 N) of sample SPMX1 with Z-axis (a) and X-axis (b) strained colour overlays from the fine global DVC correlation between steps 1 (30 N) and 10 (approx. 90 N), sample outline and loading direction 5:30

Figure 110: Tomography slice of the same plane as presented in Figure 109 ..... 5:30

Figure 111: Correlation residuals of sample SPMX1 from the reference to stages 30 (a), 40 (b), 50 (c) and 85 (d), at loads approximatively 230 N, 250 N,

272 N and 347 N respectively with a blue frame showing the appearance of the crack after fine global correlation, the red arrows pointing at the forming crack and the green arrow showing an example of artifact due to the G-DVC limited spatial resolution 5:31

Figure 112: Crack segmented from the correlation residuals between steps 1 (30 N) and 85 (347 N) in a close-up view (a) and overlaid in the volume rendering of stage 85 after thresholding segmentation and in a blue bounding box to highlight the position in the filler particle 5:32

Figure 113: Same as Figure 112 with original porosity surrounding the crack (a), ROI in the plane of the crack (b) and close-up view (c) 5:32

Figure 114: X-axis (perpendicular to loading direction), Y-axis (along specimen thickness) and Z-axis (loading direction) strains from the correlation between the preload (L01) and the last available stage (D08) averaged over the entire SPBX3 sample tomographed Region of Interest..... 5:36

Figure 115: Tomography false colour cross-sectional slices (XY-plane) in the centre of specimen SPBX3 after correlation and remapping at preload (a) and prior to brittle fracture (b) with a blue frame indicating the location of a microcrack and with the loading direction being perpendicular to the plane of these slices 5:36

Figure 116: Same slice n°526 from the remapped volumes and after subtraction in 32-bit floating point of D01 first dimax by L01 preload (a), and D08 last dimax by L01 preload (b), with blue frames showing the extension of

the cracks and a yellow circle showing the apparition of new damage on the other side 5:37

Figure 117: Volume rendering of the crack segmented by top-hat and texture classification from the subtracted remapped volumes of the first dimax D01 (a) and the last dimax available D08 (b) by the preload, and overlaid (c)..... 5:37

Figure 118: Both segmented cracks (blue for D01-L01, red for D08-L01) overlaid and presented on top of a tomography slice (a) and a thresholded volume rendering (b), note that the segmentation did not include the entire crack as highlighted by the blue frame..... 5:39

Figure 119: Further views of the overlaid cracks showing the orientation of propagation along the specimen diameter and Y-axis (loading direction represented by a blue arrow) 5:39

Figure 120: Diagram of potential mechanism explaining the change in coherent scattering 6:5

Figure 121: Shape change of an ellipse (a) under load (area kept constant), tangential angle change as a function of azimuth (b) and angle change as a function of strain at azimuth 45° (b)..... 6:6

Figure 122: Gilsonite particles acting as stress concentrators 6:8

Fig. A 1: Diffraction maps (tensile strains) at the notch (black circle), calculated using signal cross-correlation.....A.2-3

Fig. A 2: Comparison of the control points calculated with two methods, double fitting (reference/deformed), and signel cross-correlation, showing inconsitency in the measured values A.2-3

LIST OF TABLES

Table 1: Nominal properties of virgin Gilsocarbon graphite, and for reference Magnox PGA graphite [14] 1:15

Table 2: List of completed beamtime experiments with details 2:4

Table 3: Samples table for all experiments (summary) 2:4

Table 4: Aramis 5M available configurations. 2:7

Table 5: Details of lab-XCT experiments, all used sample design C flattened disc 12 × 6 mm 2:15

Table 6: Sample specification for the neutron Bragg imaging experiments 2:39

Table 7: Camera specifications 2:51

Table 8: Peak finding (not fitting) for the preload, angle 90°, azimuth 1° ... 4:18

Table 9: Sample specifications for the PSICHE experiment, values with a star denote an engineering target, not an exact measurement, where that was not practical 5:7

Table 10: Identification of microcracking in the tomography volumes, initiating in the field of view (IFOV), in the field of view (FOV), secondary crack (2^{ND}), in the fast acquisition mode (Fast), in the continuous acquisition mode (Dimax) 5:7

Table 11: Synchronised loading of sample SPMX1 with the start load at each phase and the number of scans per phase (*percent from estimated failure, 100% is the calculated estimation of maximum load)..... 5:11

Table 12: Rigid Body Displacements between preload (30 N) and the final stage 88 (approx. 350 N)..... 5:17

Table 13: Properties of the global correlation grids..... 5:25

Table 14: Summary of results from the coarse global incremental volume correlation of sample SPMX1..... 5:27

LIST OF ABBREVIATIONS

3DXRD	Three-Dimensional X-Ray Diffraction
AG	Against Grain
AGR	Advanced Gas-Cooled Reactor
ASIC	Application-Specific Integrated Circuit
ASTM	American Society for Testing Materials
BET	Brunauer-Emmett-Teller
CEA	Commissariat à l'Energie Atomique (Fr)
CGLS	Conjugate Gradients Least Squares
CT	Computed Tomography
CTE	Coefficient of Thermal Expansion
CTE	Coefficient of Thermal Expansion
DC	Direct Correlation
DCDC	Double Cleavage Drilled Compression
DCT	Diffraction Contrast Tomography
DECC	Department of Energy & Climate Change (UK)
DLS	Dynamic Light Scattering
DOE	Department Of Energy (US)

DVC	Digital Volume Correlation
EBSD	Electron Back-Scattered Diffraction
EDF	Electricité De France (FR)
EDF	European Data Format
EDND	Equivalent DIDO Nickel Dose
EDX	Energy Dispersive X-ray spectroscopy
EELS	Electron Energy Loss Spectroscopy
ESRF	European Synchrotron Radiation Facility
ETD	Everhardt Thornley Detector
FBP	Filtered Back Projection
FEG	Field Electron Gun
FF	Far Field
FFT	Fast Fourier Transform
FPZ	Fracture Process Zone
FWHM	Full Width Half Maximum
G-DVC	Global Digital Volume Correlation
GOF	Goodness Of Fit
GPU	Graphics Processing Unit

HOPG	Highly Oriented Pyrolytic Graphite (HOPG)
HPB	Hinkley Point B
i.e.	From Latin *id est*: it is, that is to say
IAEA	International Atomic Energy Agency
IEA	International Energy Agency
ILL	Institut Laue Langevin
ISU	International System of Units
IT	Isomeric Transition
L-DVC	Local Digital Volume Correlation
LFD	Large Field low vacuum Detector
MCP	Micro-Channel Plate
NBI	Neutron Bragg-Imaging
ND	Neutron Diffraction
NDA	Nuclear Decommissioning Authority (UK)
NF	Near Field
NPP	Nuclear Power Plant
NRC	Nuclear Regulatory Commission (US)
OB	Open Beam

ONR	Office for Nuclear Regulation (UK)
PCHIP	Piecewise Cubic Hermite Interpolating Polynomial
PCT	Phase Contrast Tomography
PGA	Pile Grade-A
RBD	Rigid Body Displacements
RBM	Rigid Body Motion
RBR	Rigid Body Rotation
RGB	Red Green Blue
RMSE	Root Mean Squared Error (standard error)
RoI	Region of Interest
RSD	Relative Standard Deviation
RWM	Radioactive Waste Management board (NDA)
SANS	Small Angle Neutron Scattering
SDD	Silicon Drift Detectors
SED	Secondary Electron Detectors
SEI	Secondary Electron Imaging
SEM	Scanning Electron Microscopy
SRμCT	Synchrotron Radiation micro-Computed Tomography

TEM	Transmission Electron Microscope
TIFF	Tag Image File Format
ToA	Time-of-Arrival
ToT	Time-over-Threshold
TT	Topo-Tomography
UK	United Kingdom
VHTR	Very High Temperature Reactor
WG	With Grain
XCT	X-ray Computed Tomography
XRD	X-Ray Diffraction
XRDM	X-Ray Diffraction Mapping
XRM	X-Ray Microscopy/Microscope

NOMENCLATURE

ROMAN ALPHABET

Letter	Signification	Unit (ISU)
m	Mass	kg or g
R	Gas constant	$J.mol^{-1}.K^{-1}$
SA	Surface area	m^2
SA/V	Surface area to volume ratio	m^{-1}
T	Temperature	°C or K
t	Time	d or s

GREEK ALPHABET

Letter	Signification	Unit (ISU)
π	Pi	n/a
ρ	Density	$kg.m^{-3}$
ε	Strain	S
θ	Scattering angle	°
χ	Azimuth	°
φ/Φ	Diffraction / stage angle (3DXRD)	°

SYMBOLS

Symbol	Signification
∞	Infinity
©	Copyright
®	Registered trademark
™	Trademark
≡	Identical to
∂	Partial differential
∀	For all
∈	Element of

GLOSSARY

IM1-24/GCMB	Classification number for the Gilsocarbon graphite used in the Advanced Gas-cooled Reactors.
Diffractogram	Plot of the scattering angle as a function of intensity in a diffraction experiment.
Spectrum	Plot of the intensity (or relative intensity) as a function of wavelength or energy. Not to be confused with diffractogram.
Matlab	A programming software and language owned by MathWorks®.
Tomogram	Two-dimensional object representing a section (slice) through a 3D volume produced by X-Ray Computed Tomography (XCT/XRM)
PCEA	Specific grade designation for medium-grained extruded grade of graphite produced by GrafTech
Permanent set	Deformation that does not completely resolve when stress is removed

Disclaimer

This thesis has been prepared in the format used for dissertations at the University of Oxford. Additional information is available in the appendices.

This document was prepared as an account of work sponsored by EDF Energy UK, subsidiary of Electricité de France, hereby referred to as EDF. Neither EDF nor any institution thereof, nor the University of Oxford, nor any of their employees, makes any warranty, expressed or implied, or assumes any legal liability or responsibility for the completeness, accuracy, or usefulness of any apparatus, information, product, or process disclosed, or represents that its use would not infringe privately owned rights. Reference herein to any specific commercial process, product, or service by trade name, trademark, manufacturer or otherwise does not necessarily constitute or imply its endorsement, recommendation, or favouring by EDF or any institution thereof, or the University of Oxford. The views and opinions of the author expressed herein do not necessarily state or reflect those of EDF or any institution thereof.

All product and company names are trademarks™ or registered® trademarks of their respective holders. Use of them does not imply any affiliation with or endorsement by them. All specifications are subject to change without notice. EDF and the University of Oxford logos are used with kind permissions from EDF and the University of Oxford, respectively.

All materials and software published for or used in this Thesis, the appendices or accompanying material are protected by copyright, and are owned or controlled by or licensed to EDF or its academic partners, or the party listed as the provider of the materials. UNAUTHORIZED COPYING, REPRODUCTION, REPUBLISHING, UPLOADING, POSTING, TRANSMITTING OR DUPLICATING OF ANY OF THE MATERIAL IS PROHIBITED. You may disclose any communicable material included in the thesis or its appendices only for personal or academic, but not for commercial or informational purposes, and you must maintain and abide all copyright, trademark and other notices contained in such material.

© Copyright University of Oxford 2021, EDF Energy UK. All rights reserved.

THE EFFECTS OF MICROSTRUCTURE ON STRENGTH AND FRACTURE RESISTANCE OF NUCLEAR GRAPHITE

Thomas Zillhardt [a 1]

[a] *University of Oxford, Department of Materials, Parks Road, OX1 3PH, Oxford U.K.*

[1] Corresponding author: thomaszillhardt@cantab.net

Abstract

Cracking from stress concentrations of the graphite neutron moderator, or keyway root cracking, is a potential limit for the lifetime of the UK Advanced Gas-cooled Reactors (AGR), and there is a need to better understand how damage occurs prior to fracture. Gilsocarbon graphite is a heterogeneous and quasi-brittle material, a class that includes concretes and natural materials such as bone. This project has made use of, developed, or participated in the development of advanced neutron and X-ray synchrotron techniques to improve the understanding of the deformation of Gilsocarbon graphite. In-situ High-Resolution Tomography and X-ray Diffraction Mapping has confirmed the non-linearity of graphite deformation in compression of a flattened disc and has highlighted the heterogeneity of the microstructure's response to stress. To this extent, codes have been written to process and match the DVC and XRD strains and extract comparative strain quantities. A novel in-situ technique and associated post-processing routines have been developed with Neutron Bragg Imaging to investigate grain reorientation, and combined with In-situ Three-dimensional X-ray Diffraction (3DXRD) they reinforced indications that this mechanism is recoverable. In-situ High Speed Synchrotron Tomography provided unique time-resolved observations of crack initiation, propagation and coalescence away from a stress concentration, indicating the prevalence of lenticular cracks. With as much as 72 hours of beamtime, this project has developed reusable techniques and provided unique insights on the damage accommodation in nuclear-grade graphite.

58670 words

Chapter 1

1 A CENTURY OF GRAPHITE USE, RESEARCH AND DEVELOMENT

1.1 Preamble 1:2

1.2 Industrial Relevance of Graphite 1:3

1.2.1 Advanced Gas-cooled Reactors 1:3

1.2.2 Manufacture 1:4

1.2.3 Next Generation Graphite and Other Uses 1:5

1.3 Graphite Structure 1:6

1.3.1 Crystal Structure and Properties 1:6

1.3.2 Microstructure 1:8

1.4 Mechanical Properties and Deformation of Virgin Nuclear Graphite 1:10

1.4.1 Deformation Behaviour 1:10

1.4.2 Fracture Toughness 1:12

1.4.3 Strength 1:13

1.4.4 Notch sensitivity 1:14

1.5 Defects at Multiple Length Scales 1:16

1.5.1 Bulk 1:16

1.5.2 Microscale 1:16

1.5.3 Mrozowski Cracks 1:18

1.5.4 Reorientation, Twinning, Kinking and Basal Plane Slip 1:19

1.6 Environmental Effects 1:20

1.6.1 Thermal Expansion 1:20

1.6.2 Irradiation 1:21

1.6.3 Radiolytic Oxidation 1:23

1.6.4 Combined Reactor Core Environmental Effects 1:25

1.7 Techniques 1:26

1.8 Modelling 1:27

1.9 Objectives 1:29

1.1 Preamble

The first record of graphite in the history of mankind was for its use as a ceramic paint during the Neolithic age around the 4th millennium BCE [2]. A renewed interest in the 16th century led to its popularity in many applications, from lubricants to pencils. Its high temperature properties were recognised early on when it was used as a refractory material for the production of weapons. Graphite has entered a new age of enthusiasm in the 20th century, recognising its benefits in nuclear applications, and it has also led to the parallel development of graphene [3]. The first recorded graphite research, by von Steiger in 1922 [4], initiated modern research into the chemical and structural properties of natural graphite [5, 6]. Needless to say that graphite has been put under a microscope for almost a century. Yet, knowledge of how graphite accommodates damage in its microstructure is fairly limited, despite its current and planned use in many industrial settings, and particularly as a neutron moderator for Advanced Gas-cooled Reactors (AGR), as well as for Very High Temperature and Molten Salt Reactors (VHTR/MSR). Its study, and the methods developed in that aim may also be beneficial to other types of quasi-brittle materials. In this project funded by EDF Energy UK, the focus of the research is on the AGR neutron moderator and reflector Gilsocarbon graphite. Before presenting the different axes of this project, this chapter offers a concise overview of the graphite research that is most relevant to our area of interest. It is the only chapter whose information and data have not been produced by this project. This review is concluded by presenting and justifying the research questions and experiments of this project.

1.2 Industrial Relevance of Graphite

1.2.1 Advanced Gas-cooled Reactors

In a number of different reactor designs, graphite is used both as a structural component, allowing the coolant flow and the insertion of fuel and control rods, as well as acting as a fast neutron reflector and moderator, thanks to the high neutron scattering cross-section of carbon atoms and the high strength of the graphite structure [7]. In the reactor core of Advanced Gas-cooled Reactors (AGR), it is a specific type of graphite that is used, Gilsocarbon graphite, or IM1-24. Although Magnox reactors were the first generation of commercial gas-cooled reactors in the UK, they used a different graphite, Pile Grade-A (PGA), and thermal efficiencies were significantly lower. The cladding material also evolved, from a magnesium alloy to stainless steel, as well as the fuel itself, from uranium metal to enriched uranium dioxide. What can be noted is that although both graphites are different, and especially comparing the needle-shape filler particles of PGA to the spherical gilsonites of Gilsocarbon, their mechanical properties tend to present similarities with applied environmental stresses such as load, temperature, radiation, or weight loss. It is therefore possible to compare them with other types of graphite such as that of the now decommissioned French UNGG reactors.

A more complicated factor in trying to bridge the gap between scales, which is one of the aims of this project, is the fact that AGRs in the UK present very different designs [8]. Some have single cavity once-through serpentine boilers and others were fitted with multi-cavity pod boilers. Graphite core geometries are also different, as well as installed capacity, and this leads to different core temperature distributions, fluences, fuel burnup, oxidation, and degradation. While this has been considered as an issue in developing global fracture models, this project mainly focuses on scales from

microstructure to bulk and small notches, and it will therefore not account for design differences in the first instance. Brick designs also vary across nuclear power stations, however they have numerous similarities, one of which being the presence of filler keys in-between fuel channel bricks, which are mobile, and integral key bricks, both of which links to one of the eight keyways around a channel brick, allowing for core structural integrity [9]. It is these keyways, which act as stress concentrators, which are at the centre of graphite brick facture research, especially since the two-years shutdown of Hunterston B reactor 3 [10].

1.2.2 Manufacture

The raw materials for Gilsocarbon graphite are filler coke and pitch. The green coke is produced from coal tar. It is calcined at a high temperature between 1200°C and 1350°C, and then crushed to obtain filler particles, also called dry crushed aggregate. Spherical coke particles are used in Gilsocarbon, as opposed to the needle-shaped particles in PGA graphite. This difference is important both for the thermal expansion and the development of cracks, as presented in 1.5 and in the findings of this work. These filler particles are formed at a refining process, when spherules form during the mesophase, or liquid crystal phase, at mixing of the liquid [11]. The calcined coke is then mixed with a liquid pitch binder and heated slightly above 165°C. The mixture forms graphitizable structures and binds the filler coke particles. This is enough to allow the formation of a solid ‘green-article’ which is moulded and cooled. Extrusion used to be the main technique to manufacture graphite, but this often results in a highly anisotropic graphite, and more specifically orthotropic. This implies a material whose properties differ along three mutually-orthogonal twofold axes of rotational symmetry. Vibration moulding, when used with a green article made of spherical filler cokes, can

produce a semi-isotropic graphite, which is much more preferable with regards to thermal expansion in the reactor core [12].

The backing stage, that may last more than a month at 800°C, allows the distillation of the pitch, which will remove up to 30% of its volume through gasification. A series of three pitch impregnations is carried out to fill the interconnected porosity caused by to the volume loss, and aims at reducing the porosity below 8% of the total volume [13]. This baking stage is detrimental to the final properties of the graphite, such as thermal conductivity and expansion, strength or Young's Modulus, as this is when the porosity develops in the binder phase and most of the microstructure forms [14]. The billets are then brought to 2800°C for graphitization so that the crystals can reorder. The turbostratic carbon is converted into a three-dimensionally ordered structure, producing smaller layer distances and increasing the lattice order. Whilst the graphitization mechanism is still not fully comprehended [15], the difference between graphitizing and non-graphitising carbon has been demonstrated early on [16, 17], concluding in a model with a spectrum of materials [18], indicating that graphite contains both ordered ABA and turbostatic structures.

1.2.3 Next Generation Graphite and Other Uses

In addition to being extensively used in recent years in the anodes of lithium-ion batteries, and studied by battery researchers for its dimensional changes in-operando [19, 20], synthetic graphite has been used for many years in the steel refining industry with blocs as big as 3 m for Electric Arc Furnaces (EAF) [21] and also as electrodes in Electro-Spark Deposition (ESD) to improve corrosion resistance of metals [22]. It is now a candidate for the next generations of nuclear power reactors. Graphite's thermal properties have fostered its use in fusion reactors as a plasma facing component [23], and is currently the centre of attention for its tritium recycling capabilities [24]. Closer

to the graphite studied in this project, newer graphite microstructures are being investigated for their use in next-gen fission reactors [25], and more particularly thermal neutron versions of Very High Temperature (VHTR) [26, 27] and Molten Salt Reactors (MSR) [28], and Gilsocarbon has often been studied alongside the older anisotropic Pile Grade-A (PGA) graphite [29]. Although there are wide use differences between these graphites, such as the higher temperature and neutron fluence of VHTRs, and the particular issues of molten salt infiltration and permeation in the graphite of MSRs [30], studying one type of graphite may be beneficial to the others. For instance, spatial correlation lengths have been compared between Gilsocarbon and NBG-18 [31], and polarized light microscopy helped compare the microstructures of PGA, Gilsocarbon, NBG-18 and IG-110 [32]. This systematic combined analysis of different graphite grades have also been demonstrated with XCT and FIB-SEM [33]. Although this thesis will intend to draw links between the different graphite grades, it ha mostly experimentally investigated Gilsocarbon, and in one instance HOPG.

1.3 Graphite Structure

1.3.1 Crystal Structure and Properties

Graphite consists in layers of graphene stacked up and coupled by weak van der Waals forces. It can be rhombohedral, with alternating ABCA planes, or more commonly hexagonal ABA, as in Gilsocarbon, and as presented in Figure 1. It is a short-range order crystal structure with an interlayer spacing of 3.35 Å [34]. The unit cell parameters are 2.5 Å for the a-axis and 6.70 Å for the c-axis, while the atomic spacing is 1.42 Å. Atoms in the basal plane form covalent bonds by sp^2 hybridisation. This form of bonding involves the coupling of the valence electrons from the ‘s’, ‘p_X’ and ‘p_Y’ orbitals in both a strong σ bond and a weak π bond leading to a strength of 600 kJ/mol. This contrasts with the much lower van der Waals bonding energy of 4

kJ/mol, and this difference leads to a preferential formation of defects along the c-axis, of which the nanoscale Mrozowski cracks are the main example.

Another cause for the formation of defects is the high anisotropy of the graphite crystal. Both the difference in lattice parameters and in bonding forces result in variation of the Coefficient of Thermal Expansion (CTE). Along the c-axis, it is measured to be 27.5 μK^{-1} and 1.5 μK^{-1} in the basal plane [35]. This will not affect the bulk CTE to a great extent, but may have other effects on bulk properties such as a change in strength with temperature.

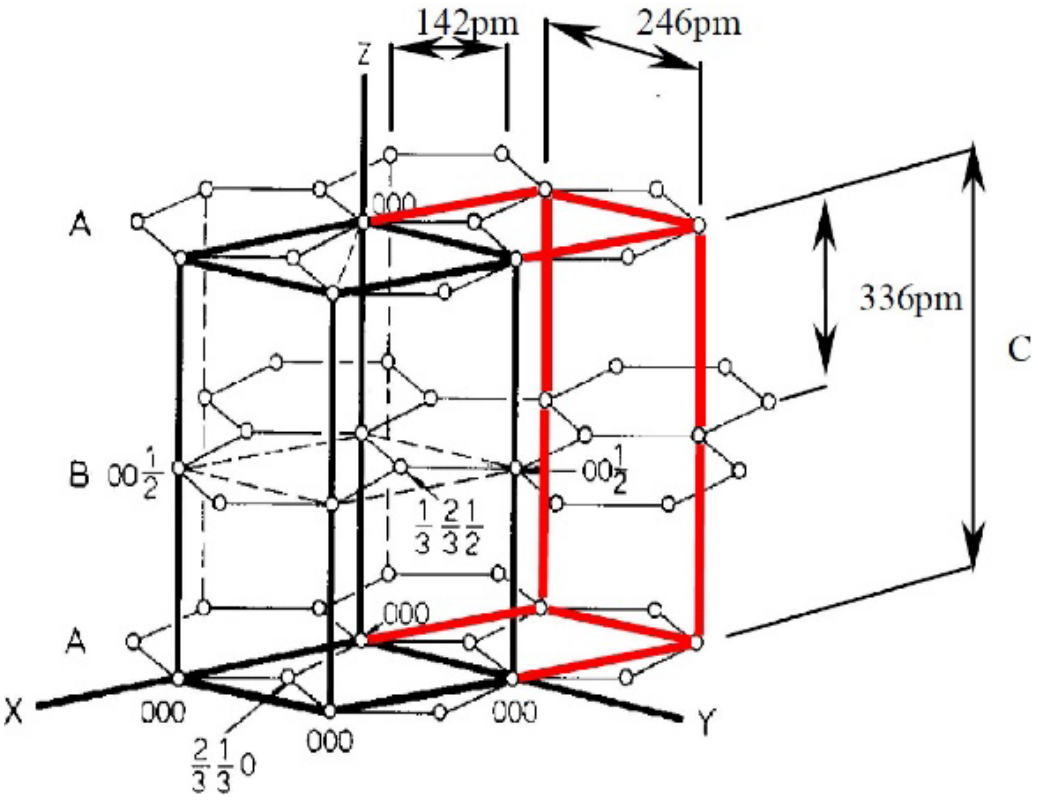


Figure 1: Graphite crystal structure [36]

1.3.2 Microstructure

As opposed to the crystal structure, the microstructure of Gilsocarbon graphite is semi-isotropic. This comes from the use of spherical filler particles. This phase can be differentiated from the binder matrix both regarding crystal orientation and porosity. In the binder, there are mostly globular pores that develop by gasification of the pitch. Some are interconnected, and the ratio of pores to crystals is higher than for the particles. In these spheres, lenticular porosity develops from nanoscale cracks, as the c-axis of the crystals is oriented radially outward from the centre, which is often refereed to as ‘onion shape’. This is a general orientation, however graphite does not strictly present grains but zones of preferred crystal orientation with folded graphite plate structures.

The thermally driven crystallite expansion of these structures defines the bulk CTE. The “grain size” of graphite is therefore more often defined by the initial starting mix and, for Gilsocarbon, is close to 500 μm. The large filler particles (~1 mm diameter) have an unusual ‘onion’-like structure with a concentric arrangement of fine, graphite crystals (~μm size) with tangentially-oriented basal planes. Figure 2 provide views of the microstructure using polarised SEM and TEM micrographs. It allows one to clearly differentiate the spherical filler particles, with “onion rings” pores and lenticular cracks from the binder phase which contains “bubbly” porosity of various sizes originating from the gasification stage. Figure 2(b) further shows the Mrozowski cracks in the basal planes. Figure 3 displays a slice of a 3D volume from an absorption contrast CT showing that the homogenous attenuation of all graphite features renders identification and differentiation difficult with conventional tomography, but nevertheless provides good contrast for porosity segmentation. As will be seen hereafter, advanced tomography techniques help improve contrast differentiation.

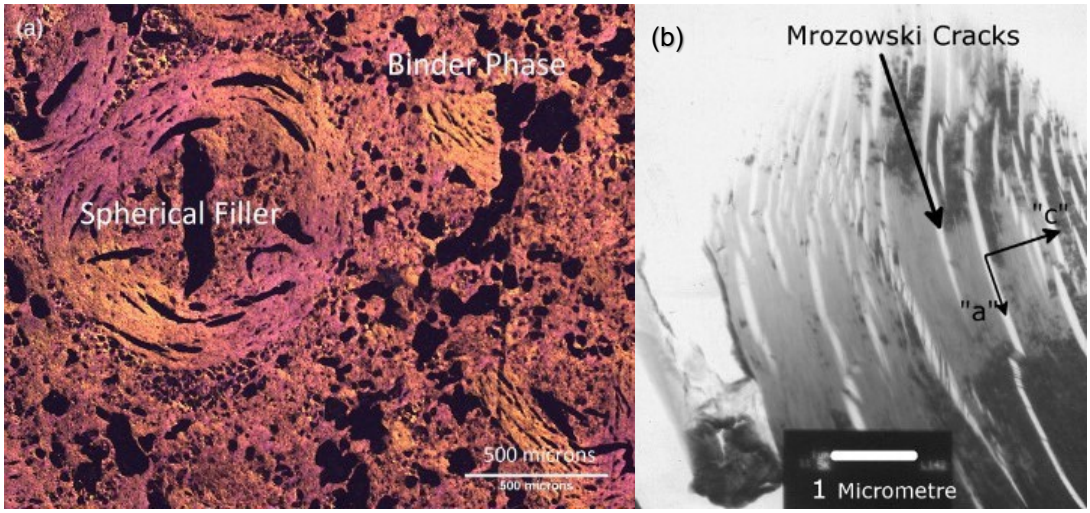


Figure 2: (a) Polarized SEM of virgin Gilsocarbon graphite, (b) TEM of unirradiated Gilsocarbon graphite [29]

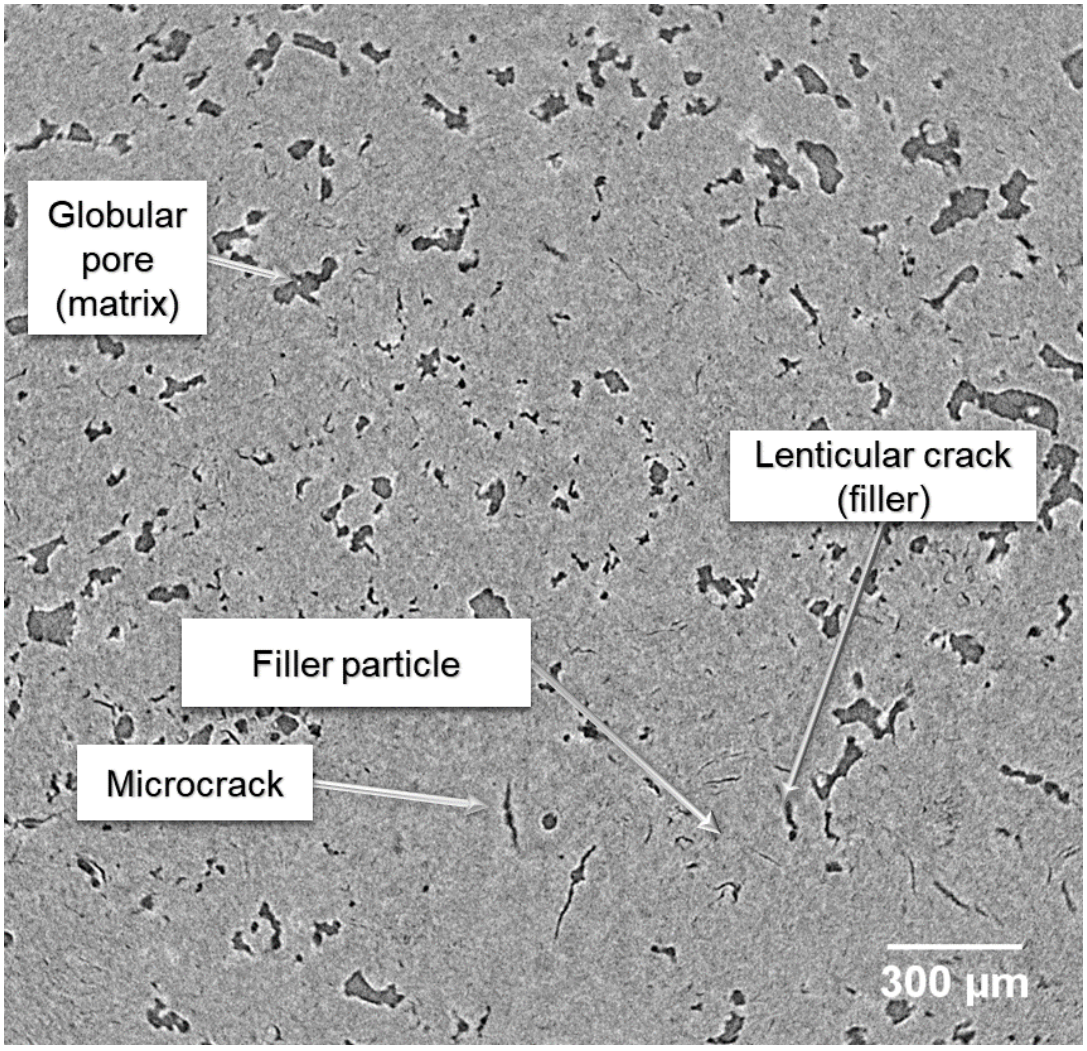


Figure 3: Gilsocarbon graphite (X-ray tomography microscope Xradia 510 Versa at Oxford Materials)

1.4 Mechanical Properties and Deformation of Virgin Nuclear Graphite

1.4.1 Deformation Behaviour

In the unirradiated state, Gilsocarbon graphite is a quasi-brittle material, i.e. almost brittle, although pseudo-brittle, and resemblance to concrete has also been suggested [37]. This is represented, in a load-displacement curve, by three regions of interest for a bending specimen, as shown in Figure 4. After an initial linear elastic region, a non-linear plastic deformation occurs, attributed to microcracking. At this stage, the released strain energy is equal to the energy required for crack growth [38]; this is stable cracking. Macro-cracks form and the resistance to crack growth is constant, or rises with increasing crack length until a critical length, after which the crack growth is unstable and leads to catastrophic brittle fracture. Inelastic deformation in graphite has been investigated with different techniques and allowed the development of new theories overcoming the limits of linear elastic models specific to more brittle materials.

Recent experiments have confirmed the development of a Fracture Process Zone (FPZ) ahead of stress concentrations in Gilsocarbon. Using synchrotron X-ray tomography and diffraction, tensile loading of the graphite was used to study how its heterogeneous microstructure deformed. The development of a permanent set was observed where localized strains occurred that were not recovered after removal of the load [2]. The different theories regarding potential reasons at a microscopic level for the development of an FPZ are detailed in section 1.5. In other quasi-brittle materials, it has been found that crack initiation is followed by an increase in fracture toughness due to plastic deformation [39]. The work of fracture can be separated in two components, the specific fracture energy and the work from the increase in deformation. In effect, most brittle materials have a form of plasticity. But some

materials like graphite, ceramic matrix composite, bones or super alloys tend to show a level of ductility that has an effect both on fracture resistance and strength.

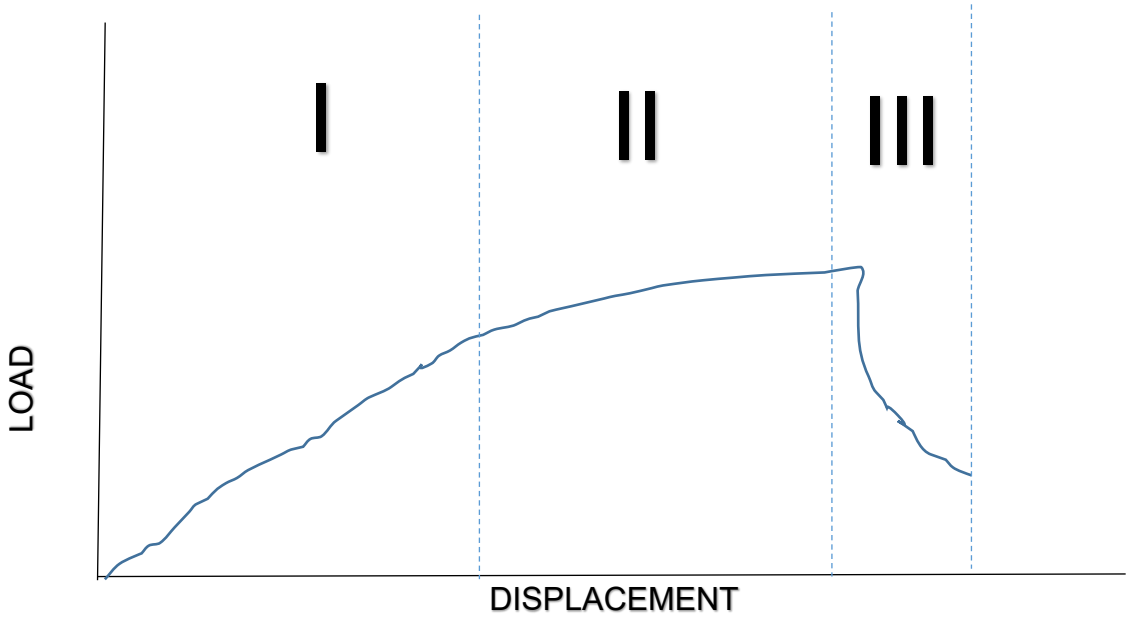


Figure 4: Schematic representation of the load-displacement curve for a quasi-brittle material.

Previous studies of Gilsocarbon fracture first used optical digital image correlation to demonstrate that inelastic strains develop prior to catastrophic brittle fracture, and that critical cracks nucleate from microstructural defects at notches [40]. Studies of deformation and damage by full strain mapping of Brazilian disc tests, i.e. in a biaxial stress state, have demonstrated the potential role of diffuse micro-cracking in the reduction of the elastic modulus perpendicular to the maximum tensile strain [41]. It has also shown that micro-crack coalescence allows stable crack propagation before brittle failure. Investigation of the behaviour ahead of a propagating crack in Gilsocarbon graphite with in-situ X-ray tomography and digital volume correlation has confirmed the presence of a fracture process zone as well as crack closure [42].

1.4.2 Fracture Toughness

The crack tip stress intensity method specifies the applied stress may be amplified in the area around the crack tip for a material whose behaviour is linear elastic [43]. The crack tip stress intensity factor 'K' reaches the fracture toughness 'K_C' at the condition of crack propagation in the specimen.

Double Torsion (DT) fracture is a technique that allows one to observe stable crack propagation. Using a finite element analysis method to calculate the J-integral at initiation and during the propagation of the crack, it was shown that the classic Linear Elastic Fracture Mechanics (LEFM) methodology may give an apparent fracture toughness due to the FPZ and wake effects that is not a material constant, highlighting non-linear behaviour in the fracture mechanics of graphite [44]. This non-linearity has been reflected in more recent neutron and synchrotron experiments particularly for tensile loading conditions. Non-linear behaviour of the crystal strains was observed both for tensile loading with X-ray diffraction and for the more complex bending observed using neutron diffraction [45], as well as Brazilian disk compression. Moreover, this latter stress state has shown to fail at higher strains and effects of differences in size are not represented in Weibull theories [46–48], but the fracture toughness criterion can be used to estimate crack growth [49].

The graphite resistance to progressive crack propagation can be represented by a tearing resistance curve, or 'R-curve', and determined with the J-integral (ASTM E1820 [50]). The 'rising R-curve' phenomenon in graphite, i.e. the increase of fracture toughness with crack extension, is proportional to temperature [51], with reported fracture toughness values of ~1–1.5 MPa.m$^{1/2}$ at 20 °C and up to ~2–3 MPa.m$^{1/2}$ at 1,000 °C for an extension of about 1 mm in a 3-points bend U-notched specimen.

1.4.3 Strength

Gilsocarbon graphite has a large number of defects at different length scales and that influences its strength. Nominal properties of virgin graphite can give a clear idea of the potential evolution of strength. In compression, the strength of Gilsocarbon is close to 70.0 MPa with or against-grain, while in tension, it is almost isotropic and equal to 20.3 MPa with-grain and 19.9 MPa against-grain [14]. It can be noted that compared to other graphites such as PGA or ATR-2E, there is little dependence on the direction, and Gilsocarbon has much more strength in compression than in tension, as reported in Table 1.

Although reactor core designs for the AGRs accounted for this weakness in tension [52], notches at keyways and cracks as well as differential volume change, due to gradients of irradiation and temperature within the core, can lead to tensile stresses on specific parts of the graphite bricks. Loading conditions are also an important factor in the change in strength. It was shown that compared to the conventional uniaxial flexural loading of a four-point bend test, the flexural strength can be reduced by 17% for the case of a equi-biaxial loading of large discs [53].

In graphites, the microstructure greatly affects strength, from 27 MPa compressive strength in PGA to 70 MPa on Gilsocarbon. Particularly, the filler grains, although detrimental to the stability in thermal expansion, constitute the weakness of artificial graphite [54]. Empirical relationships have been derived to express the averaged bend strength as a function of fractional porosity and maximum grain size, identifying the critical length for crack propagation with maximum grain size.

Another important function that needs to be accounted for when estimating strength in graphite is temperature. Although there is no phase transition, mechanical properties

of graphite do vary with increasing temperatures. For example, three-point bend samples tested at up to 1,000°C and analysed with synchrotron X-ray tomography and digital volume correlation have indicated an increase in flexural strength with temperature, which is quite unusual [51].

1.4.4 Notch sensitivity

Notch sensitivity of quasi-brittle polycrystalline materials such as graphite has been investigated for a number of years, concluding very early on that stress concentration depends on the grain size and that it is a geometric-material parameter [55]. There is however a wide variety of experimental configurations, including different notch geometries, microstructures and loading modes, and there is little global understanding of notch sensitivity in quasi-brittle materials [56].

Recent studies of quasi-static crack propagation in graphite correlated micro X-Ray Computed Tomography (μXRCT) measurements of the total strain field with the elastic strains that were mapped by synchrotron X-ray diffraction [57]. This confirmed that stress relaxation occurred in the fracture process zone ahead of the crack tip. Similar stress relaxation is expected to occur when a notch such as the keyway root is loaded close to failure, and this will affect the failure strength. The stress relaxation is attributed to stable micro-crack propagation from defects. Oxidation and irradiation of graphite have very significant effects on porosity [58], and this is also expected to affect the notch strength. Early work on model laws for notch sensitivity of brittle materials indicate that notch sensitivity decreases with increasing fracture toughness [59]. More recent modelling work looking at V- and U- notched tips specifically in quasi-brittle materials have highlighted the importance to consider the small plastic zone in predicting the failure initiation at the tip, and that the damage zone grows first with the square of the applied load [60, 61], and this has been confirmed experimentally.

Table 1: Nominal properties of virgin Gilsocarbon graphite, and for reference Magnox PGA graphite [14]

Graphite Grade	PGA	Gilsocarbon
Method and coke	Extrusion-Needle	Moulding-Gilsonite
Grain size (μm)	800	500
Density (g/cm3)	1.7	1.8
Young's modulus (WG - GPa)	11.7	10.9
Young's modulus (AG - GPa)	5.4	10.8
Flexural strength (WG – MPa)	19.0	26.7
Flexural strength (AG – MPa)	12.0	26.9
Compressive strength (WG – MPa)	27.0	70.0
Compressive strength (AG – MPa)	27.0	70.0
Tensile strength (WG – MPa)	17.0	20.3
Tensile strength (AG – MPa)	11.0	19.9
CTE (WG – $E^{-6}K^{-1}$) [2]	0.9	4.7
CTE (AG – $E^{-6}K^{-1}$)	3.0	4.9

[2] The CTE is evaluated between 20°C and 120°C.

1.5 Defects at Multiple Length Scales

1.5.1 Bulk

It is crucial to understand that graphite is a heterogeneous material. The structure of nuclear graphite contains a large number of defects at multiple length scales. Lenticular porosity appears at calcination (1,300°C) in filler particles while large circular pores develop during carbonization baking at 800°C. Upon cooling from graphitization at 2500°C, lenticular cracks form both in filler particles and in the binder matrix.

Graphite is also a quasi-brittle material, and its bulk elastic deformation is mostly non-linear [62]. The large number of defects, at all scales, ranging from nanometres to millimetres, imply that the microstructure contains residual elastic strain [45], most of which may be due to cooling from the graphitization temperature during manufacture [51]. Raman spectrometry indicated that both the binder and filler particles of Gilsocarbon graphite have high residual stresses [63], which are due to the highly anisotropic properties of the graphite crystals and the high temperatures of graphite manufacture.

Furthermore, it was shown that scale has an effect on the elastic modulus, with up to an 80% decrease for specimens whose cross-sections are increased from millimetres to centimetres, as well as on the failure strain which increases from the meso to the macro-scale [64].

1.5.2 Microscale

After moulding and graphitization at high temperatures, Graphite has bulk semi-isotropic properties and contains many microcracks that reduce its elastic modulus and thermal expansion to give excellent thermal shock resistance. Current theories

attribute the stress relaxation to stable micro-crack propagation and coalescence. However, this process has not yet been observed directly. Such studies are needed to understand how microstructural features such as porosity affect the mechanical properties.

Some researchers have made observations by confocal laser microscopy of how the closure of pores and micro-crack accommodates compressive strains at low loads [65], but this was only achieved in two dimensions with a minimum observable pore size of 50 μm^2. To study how high levels of tensile strain are accommodated in the microstructure, it is necessary to make high resolution, three-dimensional observations as the microstructure approaches the onset of failure, which could be done with time-resolved synchrotron observations.

Recent work has combined neutron diffraction and in-situ digital image correlation of Gilsocarbon graphite to study the stress relaxation due to mechanical damage at high temperatures, up to 850°C [51]. It was observed that the applied tensile bulk strains are accommodated by relaxation of stress in the graphite crystals. This is sensitive to temperature, and the key question is how this stress relaxation occurs. It has been attributed to finely distributed microcracking, but the necessary degree of damage has not yet been observed, even with sub-micron resolution X-ray tomography.

These microcracks are important for damage development and are responsible for the relatively good damage tolerance of graphite that affords some insensitivity to notches. Small Angle Neutron Scattering has further related the Mrozowski cracks with thermal expansion and indicated that this type of crack or porosity dominates the volume change with temperature [66], something that is difficult to measure with conventional low resolution tomography techniques.

1.5.3 Mrozowski Cracks

This type of cracks is often found in the spherical filler particles, and more generally in all graphitized graphite material. It extends over a few micrometres and they are on the order of 10 nanometres in width. They are the result of anisotropy of the graphite, with weaker bonds between the basal planes and different lattice parameters, and appear at the cooling from graphitisation [67]. A number of experiments have highlighted the roles of these nanoscale cracks.

It was demonstrated very early on that these cracks can accommodate both thermal expansion and irradiation creep, and especially the change of CTE during irradiation can be attributed to the closure of these cracks [68]. Three-dimensional characterisation of these defects is difficult, and two-dimensional Transmission Electron Microscopy can lead to diverging conclusions. A study determined that the Mrozowski cracks may be filled with a disordered amorphous carbon material with a lower density and graphitic character [69]. The composition of the content was confirmed by Electron Energy Loss Spectroscopy (EELS), Energy Dispersive X-Ray (EDX) and Energy Filtered TEM (EFTEM), concluding that Mrozowski cracks may act as vacancy sinks during irradiation. This was also found in PGA (Pile Grade-A), Highly Oriented Pyrolytic Graphite (HOPG) and Gilsocarbon samples [70]. Others have challenged this theory using High Resolution TEM (HRTEM) observations, suggesting that some cracks are in fact the termination of platelets, and that most of them are empty or only partially filled [71]. This is in contradiction with the initial theory of irradiation creep, where after shrinking the nano-cracks become completely filled at a specific fluence and the graphite expends back to its original state [72].

1.5.4 Reorientation, Twinning, Kinking and Basal Plane Slip

There is a lack of evidence for the mechanisms of deformation of bulk polygranular graphites such as Gilsocarbon, which exhibits a change in deformation behaviour at elevated temperatures, leading to improved toughness and tensile strength [73]. Due to its polycrystalline nature and the ABAB stacking in hexagonal graphite crystals, shear by basal dislocation glide occurs readily [74] and graphite crystals also exhibit kink band formation [75]. Twinning in graphite is a known, but little-studied, deformation mechanism. Its importance in the accommodation of strain has not been investigated before, because twinning has been difficult to detect in post-test characterisation techniques that study unloaded material. Twinning, first reported in [76] and observed by optical microscopy [77], is theorised as a rotation of approximately 20° about $< 1\bar{1}01 >$ [78]. Twinning under load in natural graphite flakes has been demonstrated with electron microscopy [79] and it has also been reported, for neutron-irradiated synthetic graphite, that twins recover once the load is removed [80] so twinning may be an elastic deformation mechanism. Conventional in-situ neutron diffraction studies, which sample a gauge volume of many cubic millimetres, do not provide sufficient resolution to detect the location of the twins. Observations of the local changes in coherent scattering may provide a way to obtain quantitative data on the mechanisms of grain reorientation by twinning, and the role of plastic deformation. This would provide essential information for the microstructural models that are needed to understand the effects of irradiation and temperature on graphite properties in order to support the design and operation of advanced fission reactors.

The graphite microstructure contains a high level of thermally induced residual stress due to the strong crystal anisotropy, and synchrotron X-ray diffraction studies have shown that these stresses may be relaxed by mechanical loading [45]. Local variations

in residual stress are expected to affect the onset of twinning and its distribution in the microstructure. This can only be studied by high-resolution observations of bulk samples but cannot be achieved by conventional synchrotron X-ray diffraction. Two-dimensional studies of deformation twinning are also not possible.

For instance, previous experiments have demonstrated that EBSD cannot be performed on graphite due to the difficulty of obtaining a deformation-free surface [81]. Nonetheless, grain mapping by Diffraction Contrast Tomography (DCT) might provide a solution as it allows mapping of the orientation of crystals with high resolution. DCT is a recent but reliable method combining Bragg diffraction with μXCT, and has been used to study metals and ceramics [82, 83]. This can be applied to single grains, as for instance in Highly Oriented Pyrolytic Graphite (HOPG), using the more advanced version Topo-Tomography (TT) [84], Similar investigation in the bulk of graphite samples are also possible using Three-Dimensional X-Ray Diffraction (3DXRD) [85].

1.6 Environmental Effects

1.6.1 Thermal Expansion

Length Scales are important when considering thermal expansion. At a structural level, Mrozowski cracks tend to be responsible for most of the thermal expansion along the c-axis, as found in Gilsocarbon and HOPG by high temperature TEM [70]. These defects tend to close upon heating which usually leads the graphite structure to shrink in that direction.

It was demonstrated that the Coefficient of Thermal Expansion (CTE) is susceptible to change with a number of factors. It is a function of loading, as compressive conditions increase the CTE parallel to the loading direction while tension decreases the CTE in that direction [86]. A potential explanation for this, as well as for changes in CTE

transverse to the loading direction, is a change in crystal orientation, in addition to the well-known closure and opening of cracks. A change in orientation factor was measured with compression at high temperature for fusion-grade graphites [87].

Another important element influencing CTE is irradiation. Data from Materials Test Reactors (MTRs) as well as trepanned samples for AGRs have been used to develop models on the effects of irradiation on the change in CTE. The recent data showed an unexpected increase in CTE up to an ‘upper shelf’ with irradiation, followed by a decrease with increasing doses [88]. Other models include representations of the underlying crystal dimensional change and representation of the accommodation porosity distribution [89]. Creep strain is also a factor in the change of CTE, supporting a correlation with elastic deformation in virgin graphite [90]. More recently, high temperature Synchrotron X-ray Tomography (at up to 1000°C) and Raman spectroscopy have demonstrated an increase in strength and fracture toughness with temperature, coincident with processing residual stresses being relaxed in the microstructure [51].

1.6.2 Irradiation

The scattering of fast neutrons displaces carbon atoms when the neutron energy is higher than that of the atomic bonding. Vacant lattice sites are created as well as interstitial atoms most probably in between the graphene layers, increasing the c-axis parameter, while shrinking along the a-axis [52, 62]. The energy transferred to form the defect is called the Wigner energy and can be removed after annealing of the graphite at higher temperatures [91]. This dimensional change of bulk graphite caused by interstitial atoms displacements depends on doses [52]. Isotropic graphite such as Gilsocarbon shrinks at low doses, because the c-axis expansion is accommodated in the porosity but the shrinkage along the a-axis is reflected in the bulk [92]. At higher

doses, new porosity is generated by crystal strain [72, 93] and the graphite expands if the neutron fluence is above the critical dose of 10×10^{20} n.cm^{-2} EDND [29].

In general, Gilsocarbon is capable of withstanding large internal crystalline strains while maintaining its properties relatively constant under irradiation and this is probably due to basal slip and generation parallel to basal planes of Mrozowski and shrinkage cracks [94]. Irradiation creep, which is the difference of dimensional change between an unloaded and a loaded specimen in compression at equivalent doses, tends to reduce the stress from dimensional changes as well as thermal stresses, has an effect on the CTE, and is itself dependent on the modulus change due to weight loss [95–97]. The creep rate is accelerated by higher temperatures and decreases with creep strain as higher neutron fluences are reached, up to 1.2×10^{26} n.cm^{-2} at which point the creep rate increases again. The secondary creep rate is highly dependent on the change in modulus as well as applied stress.

Past the turnaround point, graphite expands with irradiation dose [89], however due to the more intense radiation at the bore than at the periphery, internal compressive stresses become more important there. Bromine intercalation has been used to replicate this phenomenon which leads to cracking [98]. More recently, experimental work has been completed on neutron irradiated graphite, thereby partially representing reactor damage. Specimens of PCEA irradiated in the High Flux Isotope Reactor (HFIR) to doses from 6.6 to 10.2 dpa[3] at 900°C have demonstrated an irradiation induced volume shrinkage of 5-6% as well as an increase in dynamic and shear modulus [99]. Tests on small graphite disc specimens of IG-11 and HCB-18 irradiated to fluences of $(1.1 \sim 2.3) \times 10^{21}$ n.cm^{-2} in the Japanese Materials Testing Reactor have

[3] By definition in graphite, 1 n.cm^{-2} EDND = 1.313×10^{-21} displacement per atom (dpa). EDND: Equivalent DIDO Nickel Dose.

indicated despite a noticeable increase in mechanical strength, thermal shock resistance and fracture had decreased after irradiation [100, 101].

1.6.3 Radiolytic Oxidation

Gilsocarbon GCMB graphite is used in reactors cooled by gas. As such, the carbon dioxide coolant can permeate through the brick assembly via a complex network of open porosity and react with the carbon atoms. Thermal oxidation of graphite is a complex mechanism consisting of a series of chemical and physical processes which depends on the availability of oxygen in the coolant and with a 6-fold increase in oxidation rate between 700°C and 800°C [102]. As such, it is often regarded as insignificant at the temperatures of AGRs [103], as its rate is fairly low [104]. In contrast, radiolysis of carbon dioxide produces ionised groups and radicals that increase the rate of the oxidation of graphite. It can be simplified to the following equation:

$$CO_2 \rightsquigarrow O^- + CO\ (and\ other\ products)$$

$$O^- + C \rightarrow CO \qquad (1)$$

$$O^- + CO \rightarrow CO_2$$

where $\rightsquigarrow$ represent a radiation-induced process.

This oxidation results in weight loss reducing the fracture resistance of the graphite bricks as well as their capacity to moderate neutrons efficiently. It also promotes the growth and coalescence of internal voids, and this may affect the rate of dimensional change. It has been shown that the elastic modulus and strength exponentially decay with the weight loss [14]. Nuclear graphite is made of 99% carbon atoms, and impurities are removed in order to avoid unwanted activation by irradiation. There are

different manufacturing processes leading to isotropic or anisotropic grades of graphite, but this mainly has an effect on thermal expansion. There is little that can be done on the graphite structure itself, but the use of methane to inhibit the oxidation can be particularly efficient in reducing oxidation rates. In particular, methane transport channels are drilled in modern gas-cooled power plants to shorten the diffusion distance and thereby reduce the required methane concentration [72]. Trepanning can be done to remove a sample of graphite that can then be analysed with different techniques to obtain weight loss information. It is also feasible to periodically withdraw carriers of pre-characterised specimens, which has the advantage of being able to be comparable with the virgin state, but such carriers are generally exposed to a lower dose rate than the structural parts of the reactor.

The evolution of porosity can be tracked by segmentation of three-dimensional X-ray scans, by Brunauer–Emmett–Teller (BET) gas absorption analysis [105] and mercury porosimetry or helium pycnometry [106]. Tomography segmentation is dependent on the scan resolution, which is often limited to resolving the larger pores, and can be biased and subjective when comparing different scans and without the appropriate method in place. On the other hand, direct porosity measurement techniques are limited to the open porosity of the microstructure. A number of models exist for radiolytic oxidation of graphite bricks, and they account for the differential corrosion rates that occur due to the uneven diffusion of the methane. It is also possible to perform studies that measure the effects of oxidation and oxidation rates with separated oxidation and irradiation steps to predict strength. A reduction in strength is generally observed and is exponentially proportional to the increase in porosity [107]. The rate of oxidation is a function of radiation intensity as well as gas pressure and is therefore proportional to the production of the oxidising species. Because AGR

designs are slightly different, there is a variable degree of “aggressiveness” in each reactor, mainly dependent on gas pressure [72]. In general, weight loss greatly reduces the mechanical properties of graphite, such as Young’s modulus, thermal conductivity and strength, up to 50% at 20% weight loss [108].

1.6.4 Combined Reactor Core Environmental Effects

Although it is possible and can be more practical to advance the understanding of the graphite mechanical properties and microstructure studying virgin specimens and each environmental effect independently, in-operando realistic conditions imply a combined effect which some have intended to elucidate. Trepanned samples from AGR cores (Hinkley Point B and Dungeness B) machined in chevron specimen with varied doses and densities have indicated that porosity may be the most influent factor in the changes of graphite properties in-operando [109]. Advanced methods have been developed to further study these samples, including with synchrotron light [110]. Indeed, recent work also on trepanned samples from HPB (neutron dose 19.7×10^{20} neutrons cm^{-2},2.6 dpa) but manufactured as Double-Cleavage Drilled Compression (DCDC) specimen has theorised the fracture in an irradiated specimen was affected by suppression of microcracking and pore-related crack-tip blunting [111]. Further analysis of these datasets showed a predominant mode I fracture propagation with a constant crack opening angle that was 50% lower for the irradiated specimens, and finite element simulation with non-linear and linear elastic models using the experimental boundary conditions provided a comparison of the critical strain energy release rate [112]. Although the objectives of this thesis outreach the current available technical apparatus available (at the time of writing), and only focused on non-irradiated specimens, links with irradiation, temperature and radiolytic oxidation will be made in the concluding chapters.

1.7 Techniques

As graphite has been studied for the most part of the last century, including with optical, electronic and transmission microscopy as well as many other laboratory techniques, the scientifically interesting research questions to be analysed for this project required uncommon and advanced tools. X-ray tomography forms an integral part of this work. Worth noting is the difference between conventional absorption contrast Computed Tomography (CT) and Phase Contrast Tomography (PCT). There are many PCT techniques, such as interferometer or grating-based PCT, with the aim to improve the contrast difference for phases or microstructural elements which have a very similar attenuation. Of particular interest due to its practicality, and used in this project, is Propagation Based Imaging (PBI), also called in-line holography. With synchrotron based hard X-ray radiation, the wave front is deformed and leads to both a phase shift and an angular deflection [113]. A simple way to retrieve this additional information is to place the sample at some distance and use phase-retrieval reconstruction techniques [114], providing enhanced edge-contrast, which can be improved by acquiring multiple radiographies at different distances so that the absorption effect can be differentiated from the phase effect [115]. This PCT technique was particularly developed at the ESRF and is suitable for improved graphite tomography.

Tomography volumes acquired at different stress states can then be compared using Digital Volume Correlation (DVC). The fundamentals of DVC are similar to Digital Image Correlation (DIC) pattern matching principles, which are detailed in 2.2, but a particular point can be made here. DVC gives displacement and strain information for a volume, which can be used to calculate the corresponding material properties during in-situ experiments and observe with high fidelity the localisation of damage within the

microstructure. There are two main approaches, global and local. The global approach uses a discrete mesh and computes the correlation residual over the entire region of interest, while the local approach compares interrogation volumes to find a correlation coefficient. It is generally admitted that both methods can provide displacements with a high accuracy, but recent work on bone using SRμCT has shown a lower error rate with the global approach [116]. This method also offers the opportunity to obtain data closer to defects and cracks, refining the mesh at boundaries, but is less well implemented in commercial software products. Apart from a number of open-source codes such as TomoWarp [117], the local approach is commercialized by LaVision and the global approach by Thermofisher Scientific.

1.8 Modelling

A number of computational models have been developed to predict the fracture behaviour of Gilsocarbon, in particular, as well as other changes such as weight loss. These models are primarily Finite-Element Method (FEM) based. Multi-phase models, as opposed to two-phase ones, have been developed for density based methods to avoid dependence on arbitrary elements to segment the microstructure [118]. Density based models use the step-wedge method to calibrate the density as well as tomography data to generate meshes for finite element analysis. Site-bond models offer an alternative by constructing a large scale composite from microstructure-informed lattice models [119]. The advantage is that this multi-scale model does not require pores to be explicitly modelled. Cellular Automata (CA) models have allowed morphological analysis of the porosity while reducing computational demand [120]. This has shown a dependence on pore shape of microstructural strength as well as a difference in fracture behaviour and strength between filler particles and binder matrix.

While the models aforementioned mainly focus on the microstructure, some models focus on the interaction between graphite bricks with a reactor core. Using finite-elements, and accounting for fluence, irradiation temperature and weight loss, it was concluded that multilayer models more accurately represent the evolution of the ovality of the bore as well as the contact interaction between bricks [121]. However, it does not account for the role and evolution of the microstructure with dose and temperature. Models simulating keyway root crack arrest, also using finite-element analysis, and giving indication on whether a crack is likely to arrest depending on stress reversal at methane holes, have not included the evolution of microstructure either [122]. This tends to show that multiscale models are required in order to represent the fracture behaviour and dimensional change with fidelity.

An attempt to this consisted in combining CA, FEM as well as mesh-free models to obtain information at both macro-structural and microstructural scales [123]. This allowed accurate calculation of strain development with a more computationally efficient coarse mesh, while still representing the microstructure with fidelity. At the microstructure level, the nodal solutions of the mesh-free model are used for the CA analysis which then produces the mechanical properties used for the FEM model at the macrostructure level. This has been further developed for complex geometries by using a tetrahedral FE mesh for the cells of the CA model in the same multiscale analysis, better defining complex microstructures [124].

Another attempt focused on a model based on continuum damage mechanics [125]. At the scale of the macrostructure and using a FEM approach, an interface is introduced into the continuum solids at potential crack positions, and a non-dimensional damage parameter is used to account for the growth of micro-defects and coalescence into macro-cracks and particularly stable crack propagation. It does not

however account for the change of mechanical properties at different length scales or the effect of temperature and irradiation.

1.9 Objectives

As seen, the current challenge of graphite research is to be able to better predict its failure and state of damage, in order to provide more efficient preventive maintenance and lifetime assessments. This will be done by developing models based on theoretical knowledge and empirical data representing the deformation and damage accommodation of nuclear graphite.

The many defects in graphite, together with the interaction between filler and binder matrix, define the deformation behaviour under load at the macroscopic and microscopic scales. It is particularly important to have a clear idea of what helps graphite accommodate the load during the quasi-elastic deformation, and whether it is possible to evaluate and quantify the mechanisms by which it deforms. To fulfil this objective, use will be made of Digital Volume Correlation (DVC) of high-resolution Phase Contrast Tomography (PCT) datasets and X-Ray Diffraction Mapping (XRD).

Of particular interest is the crack initiation, coalescence and propagation, which has not yet been observed *in-situ* and in real time in a volume of graphite. It is expected that most of the sub-critical microcracking occurs within the last few stages prior to fracture. To that end, high-speed continuous tomography will be employed to probe the graphite microstructure for crack initiation within the last 20% of brittle fracture.

At the scale of the crystal lattice, twinning, kinking and grain reorientation might be ways by which graphite deforms elastically, and although post-mortem analysis has proven the existence of twins and kink bands, this has never been observed in-situ as the load is applied and subsequently removed. To that extent, neutron Bragg-edge

imaging and three-dimensional synchrotron X-Ray Diffraction (3DXRD) are used to investigate the effects of load on grain arrangement and crystal parameters.

Predicting keyway root cracking requires understanding deformation at notches and other stress concentrators. Extensive research has proven the existence of a fracture process zone, however there is still a considerable amount of uncertainty on how cracks propagate and deflect, and on how stresses are relaxed due to loading. Detailed in-situ tomography and neutron diffraction are used to probe these questions.

The multi-scale approach employed in this work help answer essential questions on how the microstructure affects the fracture resistance of graphite, and improve the fundamental understanding of graphite deformation. It will help design better models and it paves the way for similar experiments on neutron irradiated or oxidised samples at temperature to factor-in the environmental effects.

Chapter 2

2 ADVANCED EXPERIMENTAL TESTING OF VIRGIN GRAPHITE

2.1 Introduction to Experimental Characterisation 2:3

2.2 Digital Image Correlation Control 2:5

2.2.1 Preamble 2:5

2.2.2 GOM Aramis 5M stereo-DIC (3D-DIC) 2:7

2.2.3 PRESSOR Rig: 3D-DIC for specimen movement and deformation 2:9

2.2.4 Neutron Radiography: 2D-DIC for specimen deformation and movement 2:11

2.3 Laboratory X-ray Tomography 2:13

2.4 Laboratory in-situ Loading and Temperature X-ray Tomography 2:19

2.5 Synchrotron X-ray Imaging and Diffraction Mapping, Neutron Diffraction and Image Correlation for the Measurement of Elastic and Total Strains 2:20

2.5.1 Preamble 2:20

2.5.2 ENGIN-X Neutron Diffraction Beamline 2:21

2.5.3 Diamond Synchrotron I 12 Imaging and Diffraction Beamline 2:22

2.6 Multi-faceted Approach to Damage and Deformation with Synchrotron X-ray Imaging and Diffraction (ESRF) 2:25

2.6.1 Preamble 2:25

2.6.2 ESRF ID 11 Beamline 2:25

2.6.3 High-resolution X-ray Phase Contrast Tomography and Diffraction Mapping 2:26

2.6.4 Three-dimensional in-situ X-ray Diffraction Scanning 2:28

2.6.5 Topo-tomography of Highly Oriented Pyrolytic Graphite Indentation 2:30

2.7 Neutron Bragg Imaging 2:32

2.7.1 Preamble 2:32

2.7.2 The IMAT Neutron Imaging Instrument 2:32

2.7.3 Bragg-edge Imaging 2:34

2.7.4 Design of the Loading Rig (PRESSOR) 2:35

2.7.5 Experimental setup 2:37

2.8 HIGH-RESOLUTION NEUTRON DIFFRACTION MAPPING: SALSA 2:40
2.8.1 Preamble *2:40*
2.8.2 SALSA at the Institut Laue-Langevin *2:40*
2.8.3 Compressive Loading of Drilled and Slitted Discs *2:44*
2.8.4 Tensile Loading of Notched Dog-bone Specimens *2:46*
2.9 TIME SERIES HIGH-RESOLUTION SYNCHROTRON PINK BEAM TOMOGRAPHY: SOLEIL 2:50
2.9.1 Preamble *2:50*
2.9.2 Experimental setup *2:50*
2.9.2.1 Stepwise tomography acquisition 2:54
2.9.2.2 Sequential Synchronous Continuous Tomography 2:54
2.9.2.3 Time-resolved Trigger-based Acquisition 2:55
2.10 TOTAL NEUTRON SCATTERING: GEM 2:55
2.10.1 Preamble *2:55*
2.10.2 Experimental Setup *2:55*

2.1 Introduction to Experimental Characterisation

The objectives addressed in this thesis require the use of advanced techniques and the development of new experimental methods. Some of these techniques are combined for specific research objectives, in one or multiple experiments. This chapter therefore presents the main techniques used and the setups of the experiments that have been completed for this research project.

Pre-characterisation and preliminary analyses have made extensive use of the laboratory facilities in Oxford, and in particular the mechanical testing rigs, stereo-DIC system and X-Ray Microscope (XRM). However, as these tools faced inherent limitations to answer the research questions laid out earlier in this thesis, experimental time was applied for at national and international synchrotron radiation facilities and neutron sources. In total this project was awarded by peer review 72 shifts (8-hours each) of beamtime in four main experiments and two extensions of these, as summarized in Table 2, and a list of sample designs is available in Table 3. Experiment ME1504 [126] was completed on the ID11 beamline at the European Synchrotron Radiation Facility (ESRF), and used a number of techniques including Phase-Contrast Tomography (PCT), Three-dimensional X-Ray Diffraction (3DXRD), High-Resolution X-ray Diffraction Mapping (HR-XRDM) in Gilsocarbon specimens, as well as Topo-Tomography / Diffraction Contrast Tomography (TT/DCT) of HOPG, to investigate the effects of mechanical stress on the accommodation of damage in the microstructure and on crystal reorientation or twin formation. Experiment 1-02-241 [127] and its extension 1-02-299 [128] on the SALSA instrument at the Institut Laue-Langevin looked at the evolution of tensile stress in notched specimens. Experiment 20190926 [129] on the PSICHE beamline at the Soleil Synchrotron offered for the first time qualitative and quantitative evaluations of microcrack initiation, coalescence and

propagation in the bulk. Finally, experiments RB1910517-1 [130] and RB1910517-2 [131] on the IMAT instrument at the STFC-ISIS neutron and muon source have brought valuable information on crystal reorientation in graphite. Data from an experiment carried out prior to the start of this project, EE12585-2 [132] on the JEEP-i12 beamline at Diamond Light Source, has also been processed and analysed.

Table 2: List of completed beamtime experiments with details

Experiment n°	Date	Centre / Instrument	Specimen Geometry / Size	Loading	Mode	Objective
ME1504	2018 Q4	ESRF ID11	Variable Small	Compression	XRD PCT DCT TT	Damage accommodation and grain reorientation
1-02-241	2019 Q2	ILL SALSA	Disc (notched) Large	Compression	ND	Notch sensitivity
20190926	2020 Q1	SOLEIL PSICHE	Disc Small	Compression	HS-XCT	Microcracking
RB1910517-1	2020 Q1	ISIS IMAT	Disc Large	Compression	NBI	Novel technique
RB1910517-2	2020 Q4	ISIS IMAT	Disc Large	Compression	NBI	Grain reorientation
1-02-299	2021 Q1	ILL SALSA	Dog-bone Large	Tension	ND	Notch sensitivity

Table 3: Samples table for all experiments (summary)

Design ID	Sample design	Grade	Dim1[4] (mm)	Dim2 (mm)	Dim3 (mm)	Experiment	Number tested	Number analysed	Details
H6D3	Cylinder	GCMB	6	3	NA	ME1504	1	1	NA
BX1	Disc	GCMB	3	1.27	NA	ME1504	1	1	NA
D4O/H	Disc	GCMB	50	25	NA	1-02-241	3	3	NA
Varies	Disc	GCMB	Varies	Varies	NA	20190926	22	3	Table 9
C1	DC	GCMB	30	10	10	20190926	4	0	NA
D7	Disc	GCMB	20	10	NA	RB1910517-1/2	3	2	NA
D6	Disc	GCMB	25	12.5	NA	RB1910517-2	2	1	NA
T2B	Dog-bone	GCMB	300	30	10	1-02-299	2	2	NA
HSOXE	EM sample	HOPG	10	10	2	ME1504	2	1	NA

[4] [Dim1, Dim2, Dim3]: Cylinder [length, diameter], Disc [diameter, thickness], DC [length, width, thickness], Dog-bone [length, width, thickness], EM sample [length, width, thickness]. Figures available in respective experimental methods.

2.2 Digital Image Correlation Control

2.2.1 Preamble

Digital Image Correlation (DIC) has been in use since the 1970s when it was first developed for pattern recognition and scene classification [133], and many projects have made use of the strain measurement technique to measure the two-dimensional deformation of graphite samples, from Brazilian disks [73] to tensile specimens (e.g. [48]) and multi-point bending setups [46].

DIC is a non-contact strain measurement technique based on pattern-matching of time-series greyscale images [134–136], which has only picked up momentum in the past couple of decades with the evolution of hardware and software [137]. Subsets containing tens of pixels of an image are compared to a reference image by homogeneous linear mapping of the intensity pattern. This allows tracking of relative displacements that are smaller than a pixel and mapping of the displacement field, from which the strain field can be derived. Stereo-DIC, using two synchronised cameras, is able to provide in-plane and out-of-plane displacements within the range specified by the measured volume and the depth of field. Full field 3D measurements are done by treating each camera independently and then combining the results to obtain the ‘third dimension’ [138]. This has limitations due to difficulties with the presence of discontinuities on the specimen [137] such as within the regions of cracks [136], and grating or prism based single-camera 3D-DIC techniques have been developed as suitable alternatives [139]. There has also been concerns about the accuracy of the calculated strains with regards to the handling of noise and filtration of outliers, and recently an FE-based outlier filter using the force vector data has been developed [140]. Nonetheless, DIC experimental work on graphite is plentiful [40, 44,

45, 53, 73], offering a large number of case-study for comparison, and conventional single-camera and stereo-camera techniques are used throughout this project.

In this project, DIC is used to obtain full-field strain measurements for co-modality experiments or control tests in the laboratory. Two different setups have been used in this project, and their benefits and limitations are evaluated here.

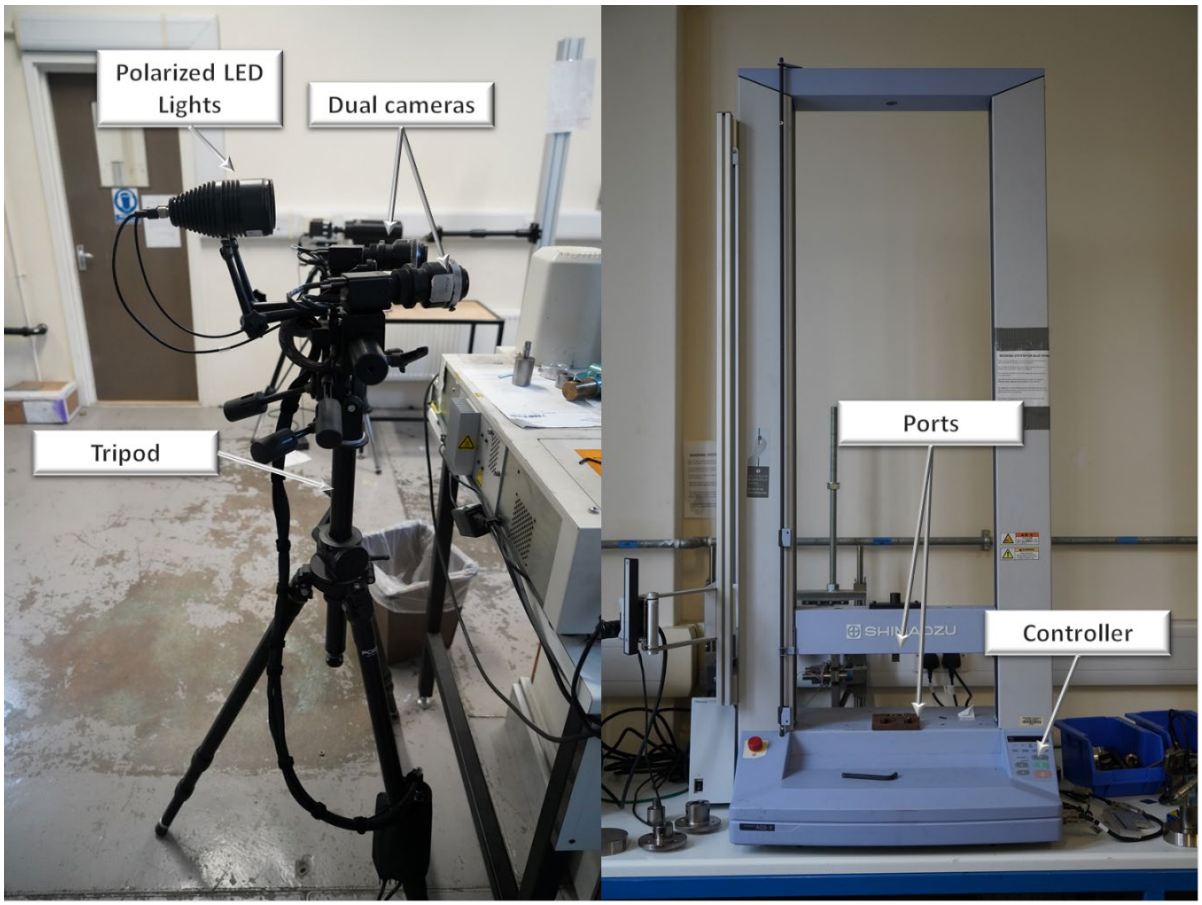


Figure 5: Experimental setup for stereo-DIC experiments in the Oxford Materials Laboratories, with (a) the Aramis 5M system and (b) the Shimadzu mechanical loading rig

2.2.2 GOM Aramis 5M stereo-DIC (3D-DIC)

The Aramis system used throughout this project, pictured in Figure 5, is a stereo-DIC setup manufactured by GOM Gmbh composed of an acquisition computer with 24 GB of RAM connected to the cameras by Cameral-Link®. The cameras are fixed on a tripod assembly which allows for different camera distance, angle and focus to define the measured volume. The progressive scan cameras are two 2448 × 2050 pixels Baumer TXG50 with a scan area of 8.45 × 7.07 mm and a pixel size of 3.45 × 3.45 µm. They are equipped with 75 mm lenses with adjustable focal distance and aperture.

Table 4: Aramis 5M available configurations.

Sensor	Lens	Measuring volume [mmxmm]	Min. length camera support [mm]	Distance ring [mm]	Measuring distance [mm]	Slider distance [mm]	Camera angle [°]	Calibration Object	Aperture dependent depth of field [mm]				
									5,6	**8**	11	16	22
ARAMIS 5M	Titanar A 75mm	**10 x 8**	500	50	**285**	88	25	CQ 10x 8	n.a.	**n.a.**	n.a.	n.a.	0,9
		15 x 13	500	30	**310**	98	25	CQ 15x 12	n.a.	**n.a.**	n.a.	0,9	2,5
		25 x 21	500	20	**385**	132	25	CQ/CP20 30x 24	n.a.	**n.a.**	1,4	4,6	8,5
		35 x 29	500	10	**470**	170	25	CQ/CP20 30x 24	n.a.	**1,5**	5	11	18
		Legend							n.a.: It is not possible to focus the complete measuring volume.				

The GOM Correlate algorithm which provided 3D-DIC measurements in this study uses the principle of 3D mesh correlation and parametric inspection. The grey value distribution in each facet of the right and left camera images are reidentified to a reference set of images and 3D coordinates are triangulated [141]. This stereo-DIC system is calibrated using a calibration cube for each of the three available measuring

volumes. The CQ15x12 calibrates the 15 × 13 mm volume with a camera angle of 25°, three pre-lens focus rings of 30 mm, giving a sample to camera distance of 310 mm and a depth of field of 0.3 to 5 mm for apertures between 8 and 22 mm. The larger 25 × 21 mm and 35 × 29 mm volumes are calibrated with CQ/CP20 30 × 24 and adjusting the camera distances, angles, and number of rings according to Table 4. LaVision DaVis Camera and DaVis StrainMaster for 2D-DIC

This single camera was used for strain measurements in experiment 1-02-41 [127] and was on loan from STFC-ISIS ENGIN-X. The camera is a Basler Pilot PIA2400-17 GM with a Sony ICX625 sensor and a LaVision DaVis housing. It is certified for use with the LaVision DaVis StrainMaster software. The sensor offers a 2456 × 2058 array with a raw pixel size of 3.45 × 3.45 µm (without magnification) and a maximum frame rate of 17 fps. The camera is controlled by Gigabit ethernet.

DaVis StrainMaster 8.4 was used to process the acquired images for this experiment, and a number of other datasets in this project. Although StrainMaster is also capable of handling stereo-DIC, the newer GOM Correlate 2020 software was chosen for those cases. Deformation and movement information was calculated from optical images, with straight-on and angled imaging, as well as from neutron and X-ray radiographies where the contrast offered a sufficient pattern. After discretising the image in windows or facets of tens of pixels, the program deforms and displaces each sub-cell to obtain a best match or correlation peak.

2.2.3 PRESSOR Rig: 3D-DIC for specimen movement and deformation

In an experiment presented hereafter in 2.7 and detailed in 4.2, a novel loading apparatus was used to apply compressive strain on disc specimens whilst making observations by neutron imaging close to the Bragg condition on the IMAT beamline. Due to the sensitivity of the diffraction imaging measurements, it was important to ensure there was no other reason for the apparition of new features, other than local change in the microstructure such as grain reorientation or deformation. In particular, crystals could enter or leave the Bragg condition if the torque from the mechanical loading led to the sample rotating sufficiently. In order to check for out-of-plane movements and sample rotations with the application of load, 3D Digital Image Correlation (DIC) was employed in laboratory tests at Oxford University, using the GOM Aramis 5M setup with a 75 mm focal lens and the same loading conditions as in the beamline experiment. Figure 6(a) shows the image correlation setup, with the test specimen coated with a speckle pattern using an airbrush with a 0.3 mm nozzle.

The measuring area was 15 × 13 mm with a calibration deviation of 0.028 pixels and a depth of field of 5.4 mm (Figure 6b). The displacement field was computed using a 32-pixel facet size and a point distance of 19 pixels. The out-of-plane displacements, for an applied load of 5.2 kN (close to failure of the specimen) are presented as an example (Figure 6c) that also shows the local effects of the contact load. The average 3D tilts of the specimen surface (Figure 6d) show there is a maximum rotation of 0.1° about the vertical axis, and a forward tilt of less than 0.2° even at high load as failure is approached. The angular width of the investigated Bragg edge is approximately 3.9°, so sample rotations during the experiment will have a marginal effect.

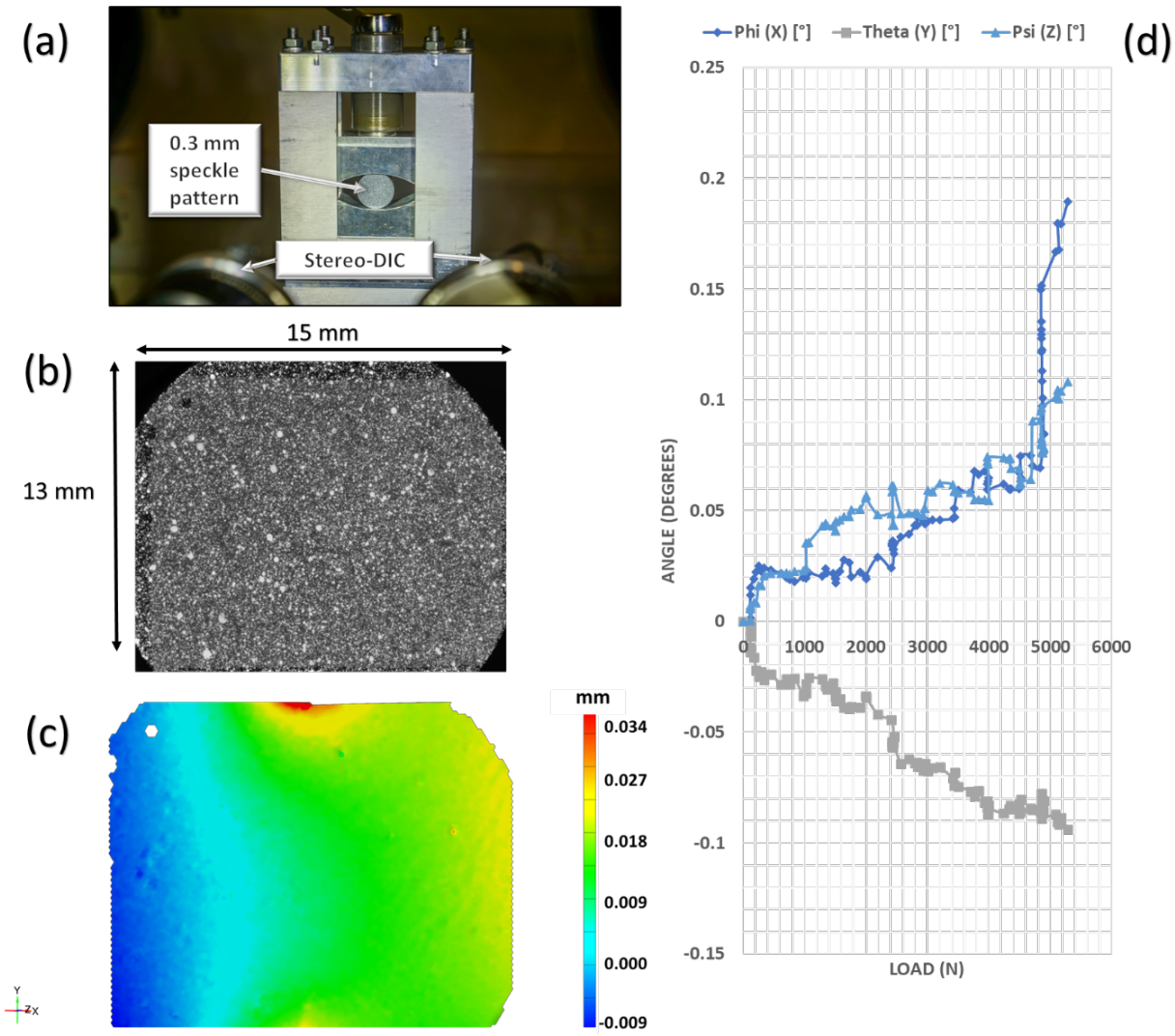


Figure 6: (a) Stereo digital image correlation setup; (b) mapping area with speckle pattern; (c) out-of-plane z-displacements of the same area; and (d) angular rotations with load of the mapped area about the X, Y and Z axes.

2.2.4 Neutron Radiography: 2D-DIC for specimen deformation and movement

In order to verify the deformation and the registration method of the neutron imaging experiment presented hereafter [130], it was necessary to obtain full field displacements and strains. Figure 7 presents the results from the digital image correlation software LaVision DaVis (Version 8.4). For this analysis, neutron radiographs were combined over a range of approximately 1.5 Å from the lowest energy which offer sufficient microstructural contrast for use as a pattern in the correlation algorithm (see chapter 4). The six images, one for each load step, were imported as non-compressed pre-processed TIFF files to avoid losing information. The correlation parameters set at the facet size of 39 pixels with a step between facets of 3 pixels. A shift correction was performed with a 16 × 16 pixels translation and a 32 × 32 pixels rotation windows relative to first image with intensity normalisation. This allowed calculation and removal of rigid body motions to validate the true deformation displacement fields.

Both correlation and registration approaches offer similar results for this specimen. For example, considering the strain values, as pictured in Figure 8, within a 4 × 4 mm region at the centre of the sample for the 3 kN load step, relative to the reference observation, DaVis finds average vertical strains of -2848 μS, while the built in radiography correlation algorithm (see section 4.2.2) finds -2139 μS respectively as calculated from pixel displacements. A correlation of the radiographs without initial shift correction and with a subset size of 39 pixels and a step size of 5 pixels was to measure the relative rotation using a Matlab code that implemented Shoemake's Euler angle conversion [142]. It was found for the highest load that the rotation angle around the beam axis, based on summed radiographies, was 0.156°.

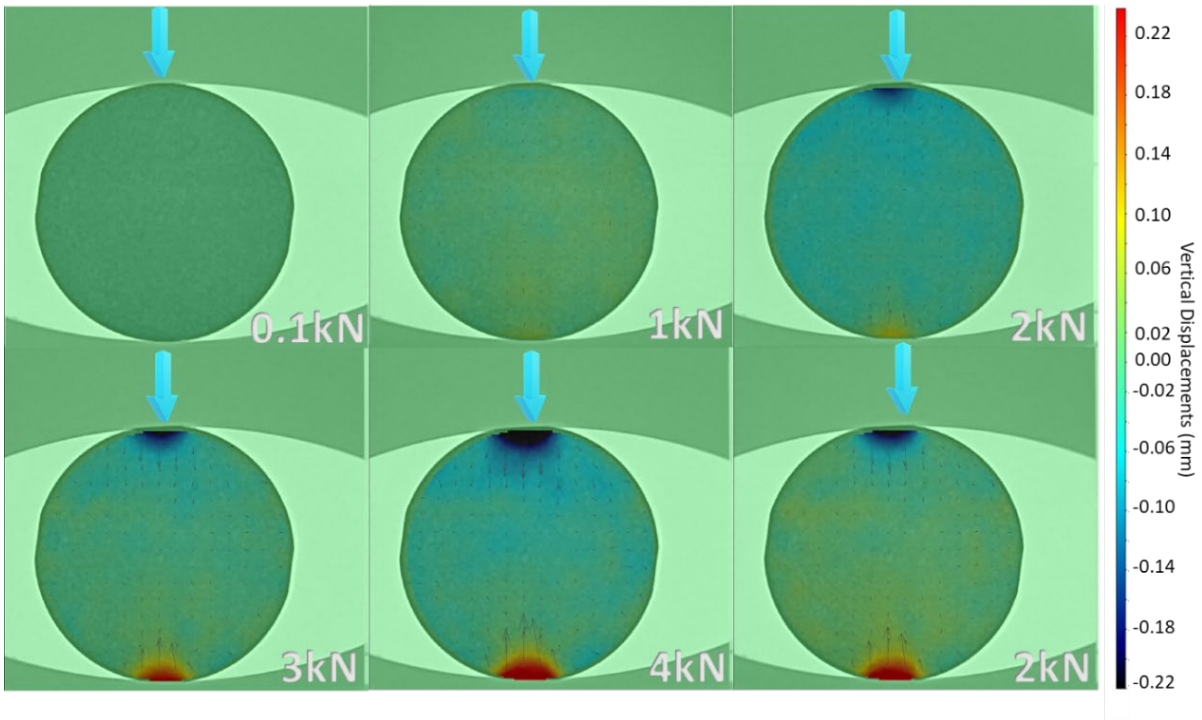


Figure 7: Example of vertical displacement fields calculated using LaVision DaVis on summed images from Region A. The arrows represent the vectors of displacement in the image plane. The colour represents the magnitude of the vertical displacement. Rigid body movements and displacements have been removed

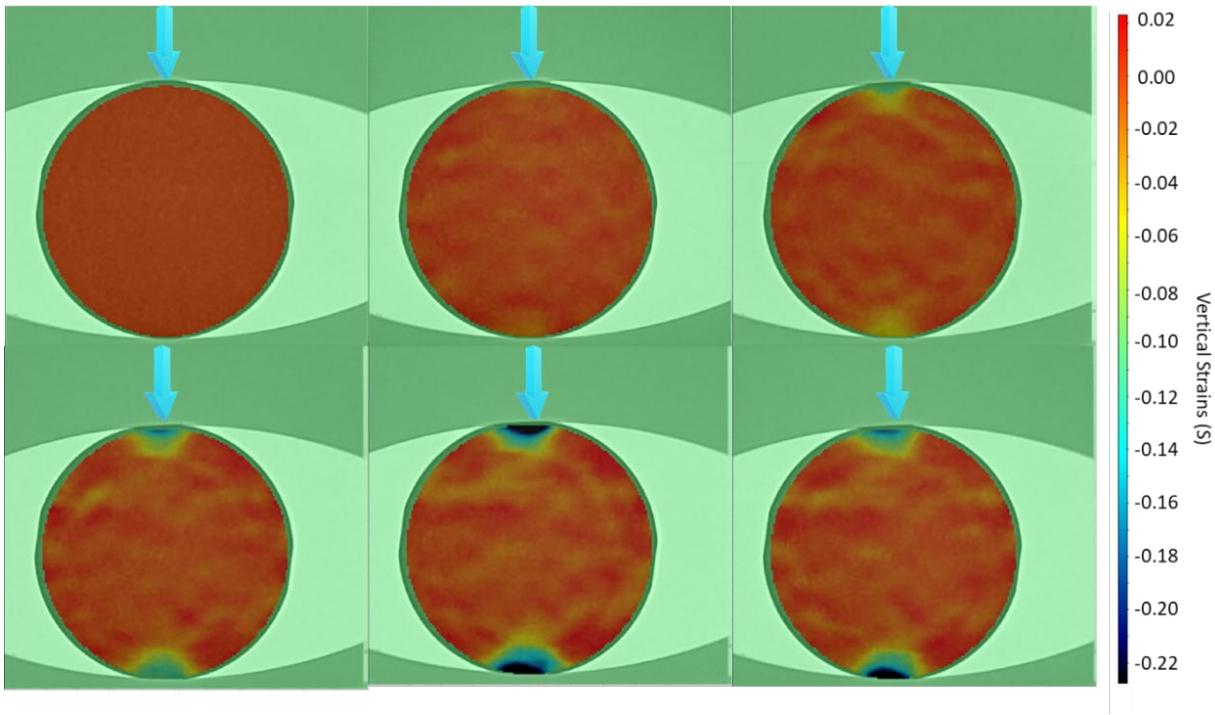


Figure 8: Strains along the loading direction from summed radiographies in Region A of the energy range

This is comparable to the control experiment in the lab using 3D digital image correlation (see Figure 6 in 2.2.4). These results are presented here as this is a control DIC test that do not bring any other valuable information than the ability to confirm the code and method presented in 4.2.2, and readers should refer to that section for more information on the energy ranges. The technical details of the Bragg imaging experiment are also presented in 2.7.

2.3 Laboratory X-ray Tomography

Early experiments were carried out for this project that aimed at finding the limits of the available laboratory equipment and identify the scale at which it was necessary to investigate the effect of the microstructure on the strength of graphite. The Zeiss Xradia 510 at the University of Oxford, Department of Materials, which upgraded to a 610 after the experimental work of this thesis was completed, offers a 160 kV 10 W tungsten source on a guide rail. As presented in Figure 9, four lenses are available. The macroscopic lens is in fact simply a flat panel scintillator which results in a 0.4x zoom, and the turret assembly offers three microscopic lens and scintillator setups for 4x, 20x and up to 40x zoom. This being a point-based source, the system works on the fundamentals of cone-beam tomography, meaning that a wide range of pixel size is achievable by adjusting the source-sample-detector distances. A set of high-energy or low-energy filters can improve image reconstruction by removing X-rays not appropriate for the material. Experimental details are provided in Table 5.

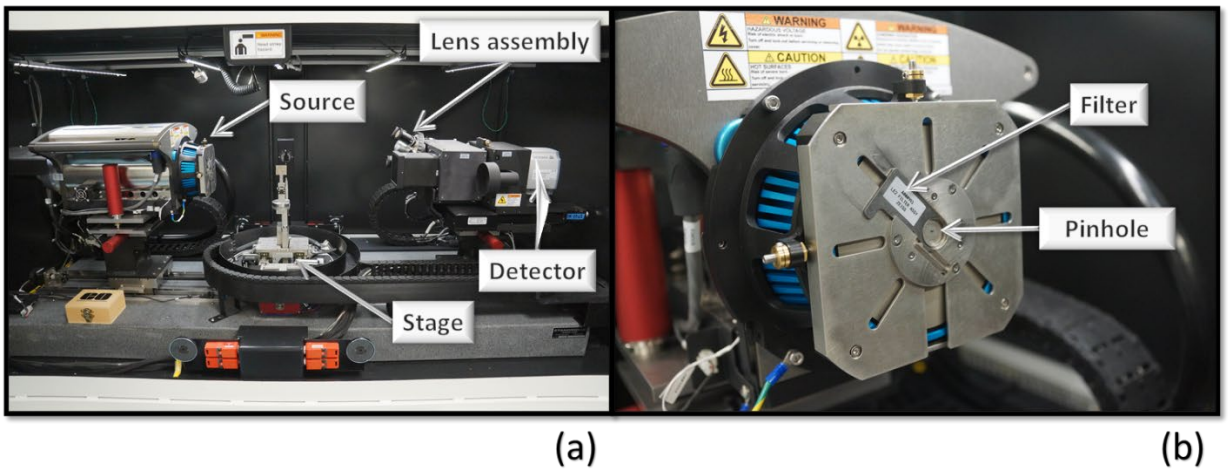


Figure 9: ZEISS Xradia 510 setup (a) and close-up view of the source

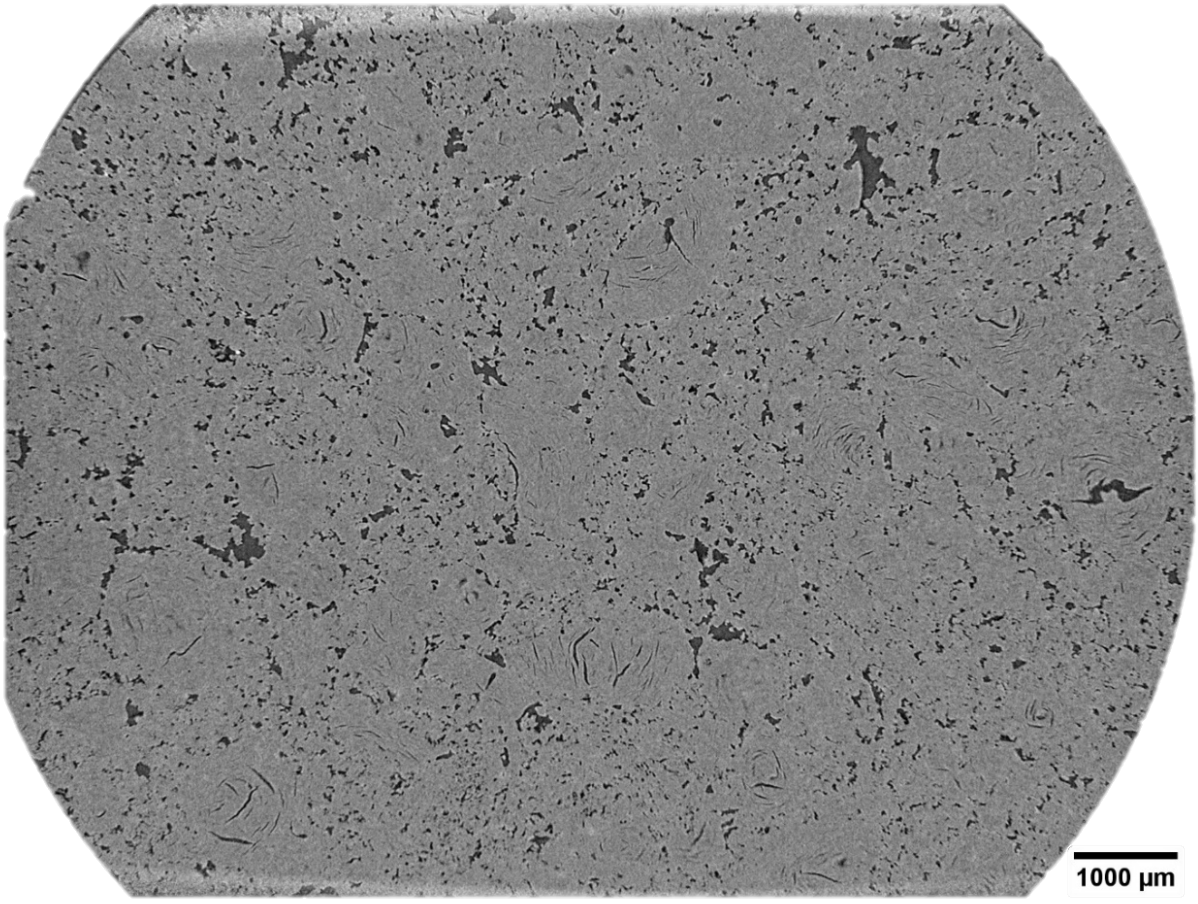


Figure 10: Xradia 510 in-situ Wide Field Tomography (5.84 µm/voxel), (slice close to face of a disc compression specimen)

Figure 10 presents an example of low-resolution wide-field scan completed for an in-situ loading of a disc. As one zooms in to the material with higher resolution scans, it is possible to resolve smaller features which play an essential role in the deformation of graphite, such as lenticular cracks, however this also reduces the field of view and decreases the signal to noise ratio. Figure 11 presents a further two in-situ experiments using the Deben loading stage and Region of Interest (RoI) tomography down to sub-micron resolution. The signal to noise ratio for the scans at the highest resolution is relatively low and it took more than 40 hours per scan to complete. As presented in Figure 12, there are significant movements of the sample between images, but no visible microcracking or significant deformation. These in-situ lab tomography experiments helped define the proposals for beamtime.

Table 5: Details of lab-XCT experiments, all used sample design C flattened disc 12 × 6 mm

Experiment identifier	Experiment type	N° of steps	Pixel size (µm)	Maximum temperature (°)
BD190418A_C02	Wide angle Deben	5	5.84	Room
BD181217A_SBD17C1	Deben scan	6	2.44	Room
BD181217B_SBD17C2	Deben scan	4	0.88	Room
BD190418BHR_C04	Scan	1	0.32	Room
BDHR090218B	Scan	2	0.22	Room
BDHR090218A	Scan	3	0.17	Room
BD050518HTB_C05	Deben Temperature	4	1.46	250
BD0119D2HTA	Stitch Deben Temp	5	2.00	250

Experiment identifier	Voltage (kV)	Power (W)	Lens (X)	Bin	Angles	Filter
BD190418A_C02	80	7	0.4	1	1891	Air
BD181217A_SBD17C1	80	7	4	2	2001	Air
BD181217B_SBD17C2	140	10	20	2	2001	Air
BD190418BHR_C04	110	10	4	1	2001	Air
BDHR090218B	110	10	20	1	3001	
BDHR090218A	110	10	20	1	3001	
BD050518HTB_C05	110	10	4	1	2001	Air
BD0119D2HTA	140	10	4	1	2001	Air

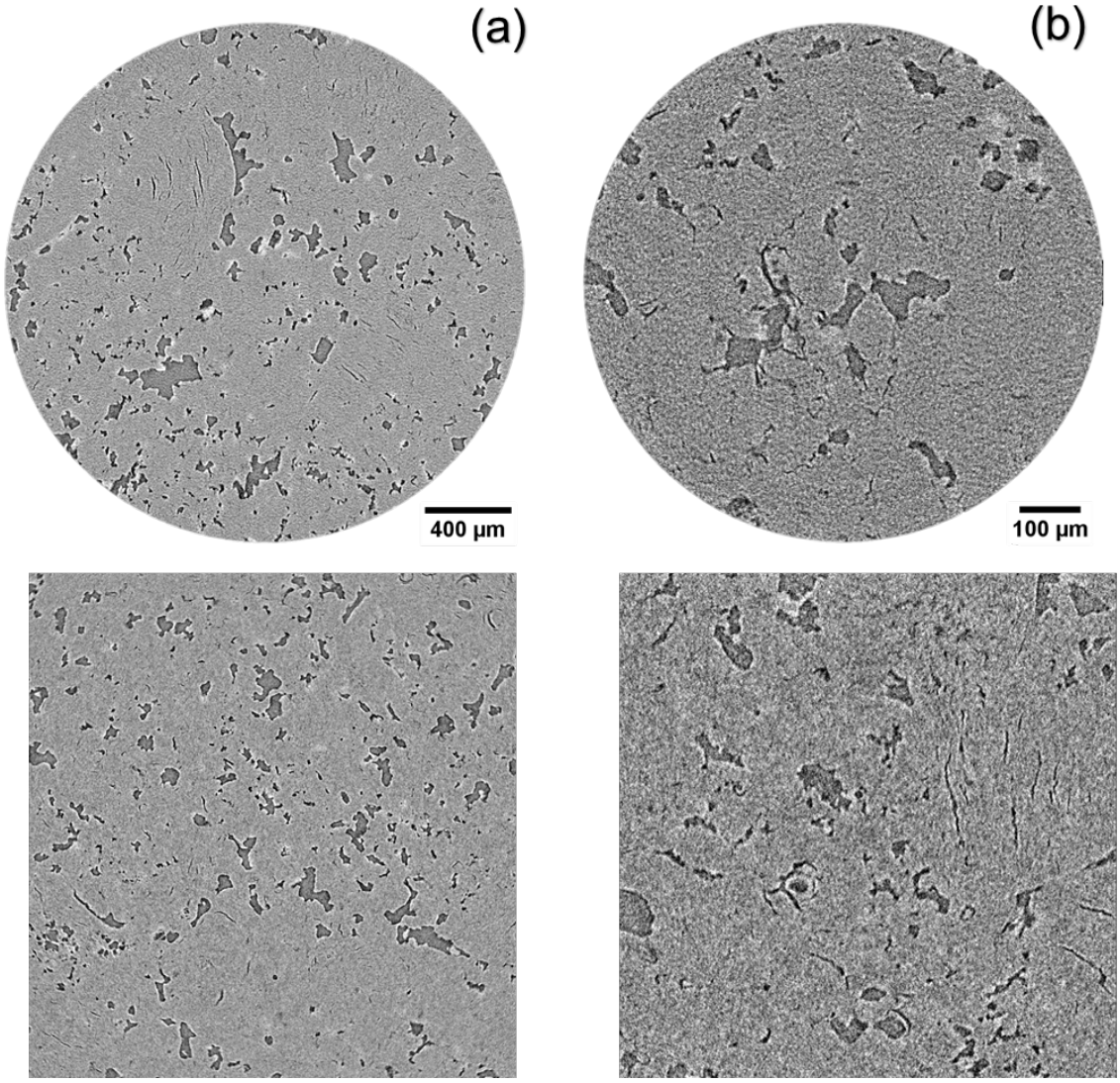


Figure 11: Radial and transversal tomography slices from in-situ experiments at 2.44µm/vx (a) and 0.88µm/vx (b)

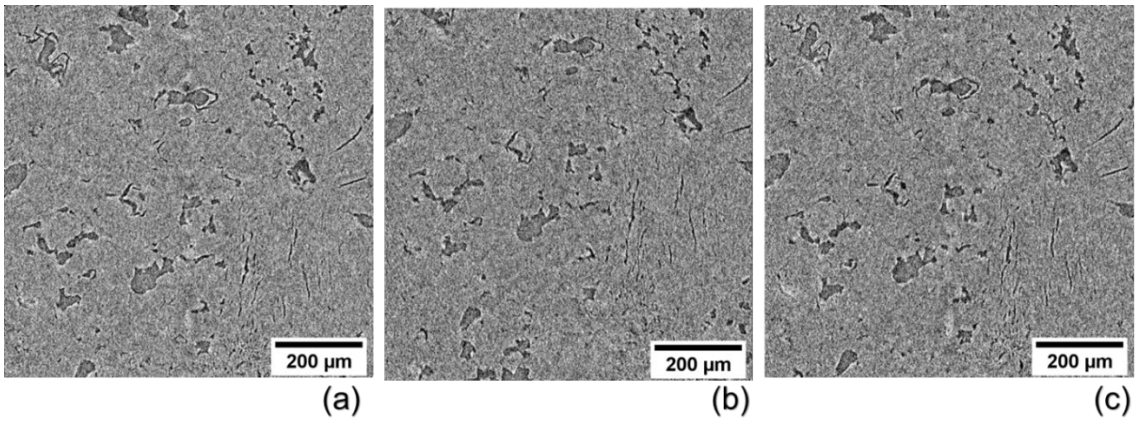


Figure 12: (a) L0A - preload, (b) L1 – 80% of failure load, (c) L0B - preload.

The maximum practical resolution of this instrument is around 0.7 µm, however as indicated in the manual, smaller pixel sizes can be achieved, and trials have been made on graphite to push the limits of the Xradia 510. Figure 13 pictures transversal (a) and radial (b) tomography slices of an ex-situ scan carried out at 300 nm/voxel using careful alignment and the 20x objective. Sub-micron size cracks and pores can be spotted, however it appears that solely the binder matrix is probed without having a single Gilsonite particle in the final volume. There is no visible artefact, however the noise levels are high and the contrast ratio quite low. These scans helped define the multi-scale experimental approach of this project, as there is always a significant trade-off between Field of View (FoV) and the size of the smallest resolvable features. Due to not insignificant attenuation from the Deben CT5000 glassy-carbon tube, this scan would not be possible in-situ. It is also important to note here the time it took (over 30 hours) for one sub-micron scan as a comparison with the high-speed tomography presented in 5.

Two very high-resolution tomography scans were acquired using the 40x lens and are presented in Figure 14 on small 6 × 3 mm cylinders. Even though features that are a few hundred of nanometres can be noticed, one cannot resolve features of the size of a few tens of nanometres and in particular Mrozowski cracks would not be visible. Although Coherent Bragg Imaging (CDI) or X-ray ptychography might be able to resolve these features [143], it would prove very complex to prepare Gilsocarbon graphite specimens of the size required for these techniques, and test them in-situ.

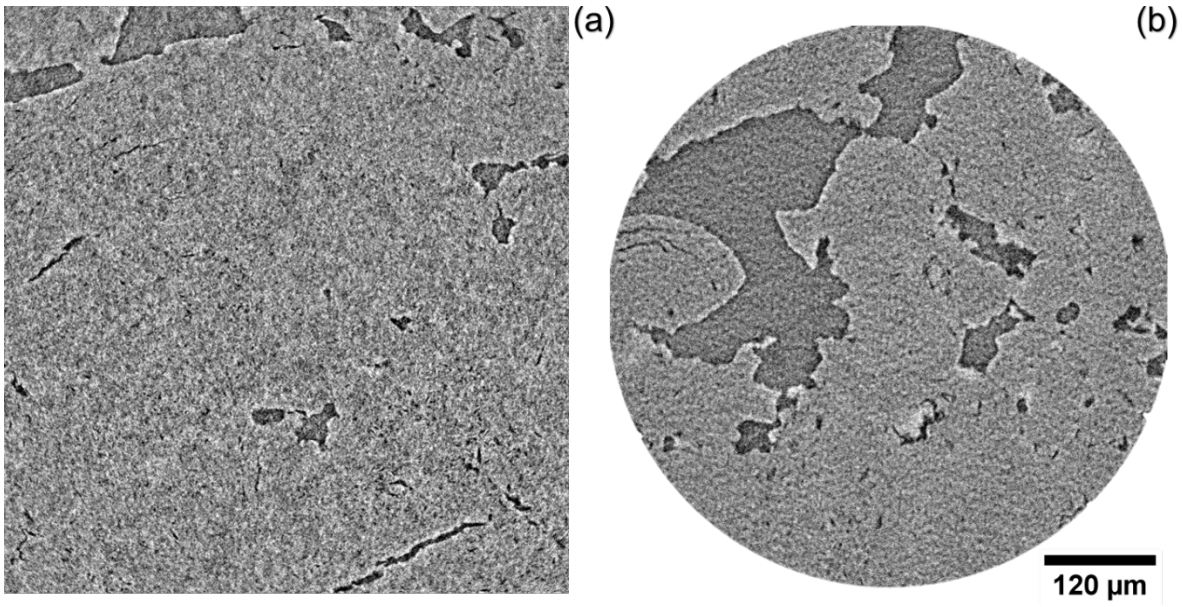


Figure 13: Ex-situ tomography scan at high-resolution (0.3 µm/vx), transversal (a) and radial (b) slices

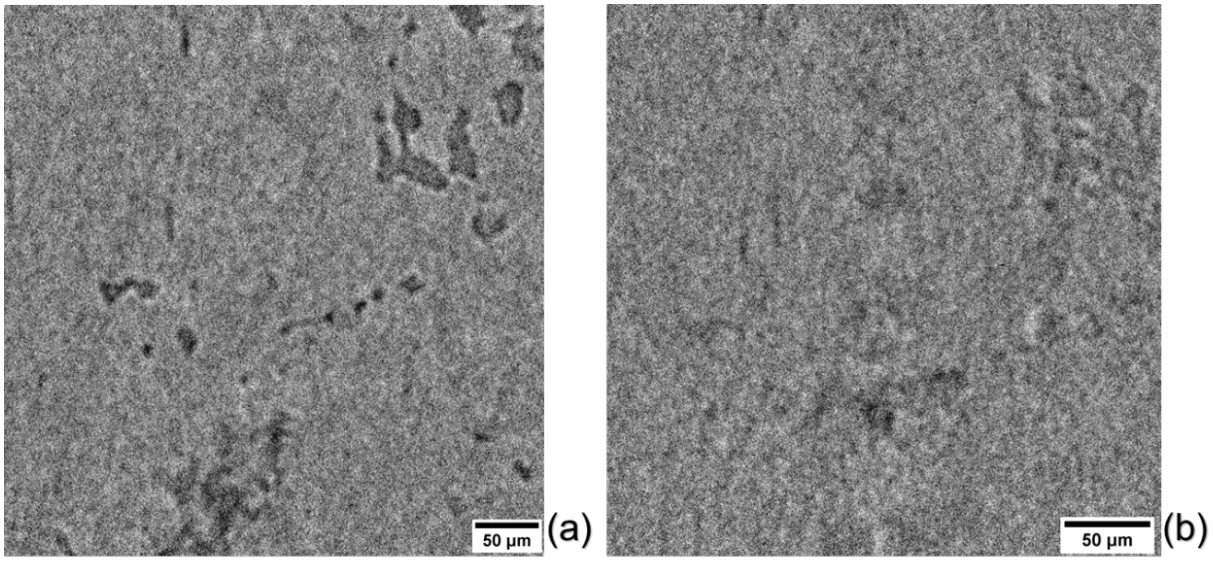


Figure 14: Xradia 510 Very High Resolution Tomography scans at 0.22 µm/voxel (a) and 0.17 µm/voxel (b)

2.4 Laboratory in-situ Loading and Temperature X-ray Tomography

The Xradia lab in Oxford offers two Deben loading devices for in-situ 4D imaging. Both of these rigs can provide load and temperature control. The TEC uses Peltier stages to provide a temperature range between -10° and 160°C while the H250 has simple heating platens to reach higher heating temperatures of up to 250°C but at the expense of not being able to go under room temperature.

The samples were flattened Brazilian discs with a 2:1 diameter to thickness ratio. The loading and temperature regimes of the samples analysed are presented in Figure 15. Since this is not a furnace, the maximum temperature is only indicative and likely to be reached at the contact points. However as small samples were used and graphite is a good thermal conductor, one can expect that the temperature gradient between the two platens will be small. Experimental details are provided in Table 5, and Figure 16 presents different views of the apparatus before the cooling pipes are connected.

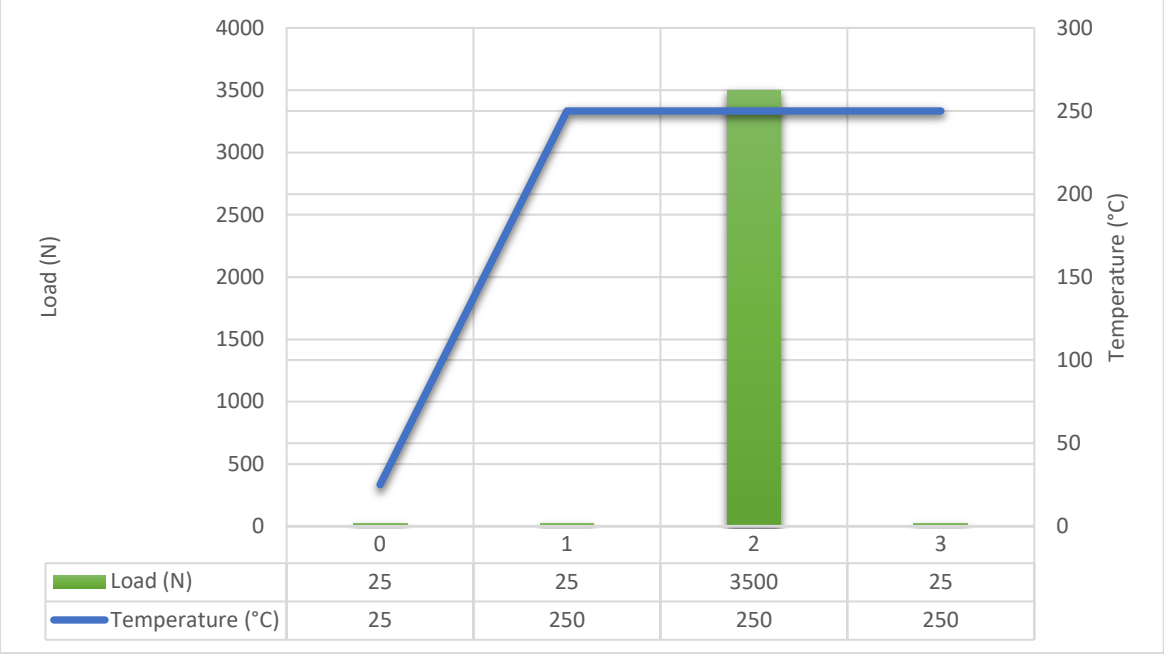


Figure 15: Load and temperature regime for experiment BD050518HTB_C05

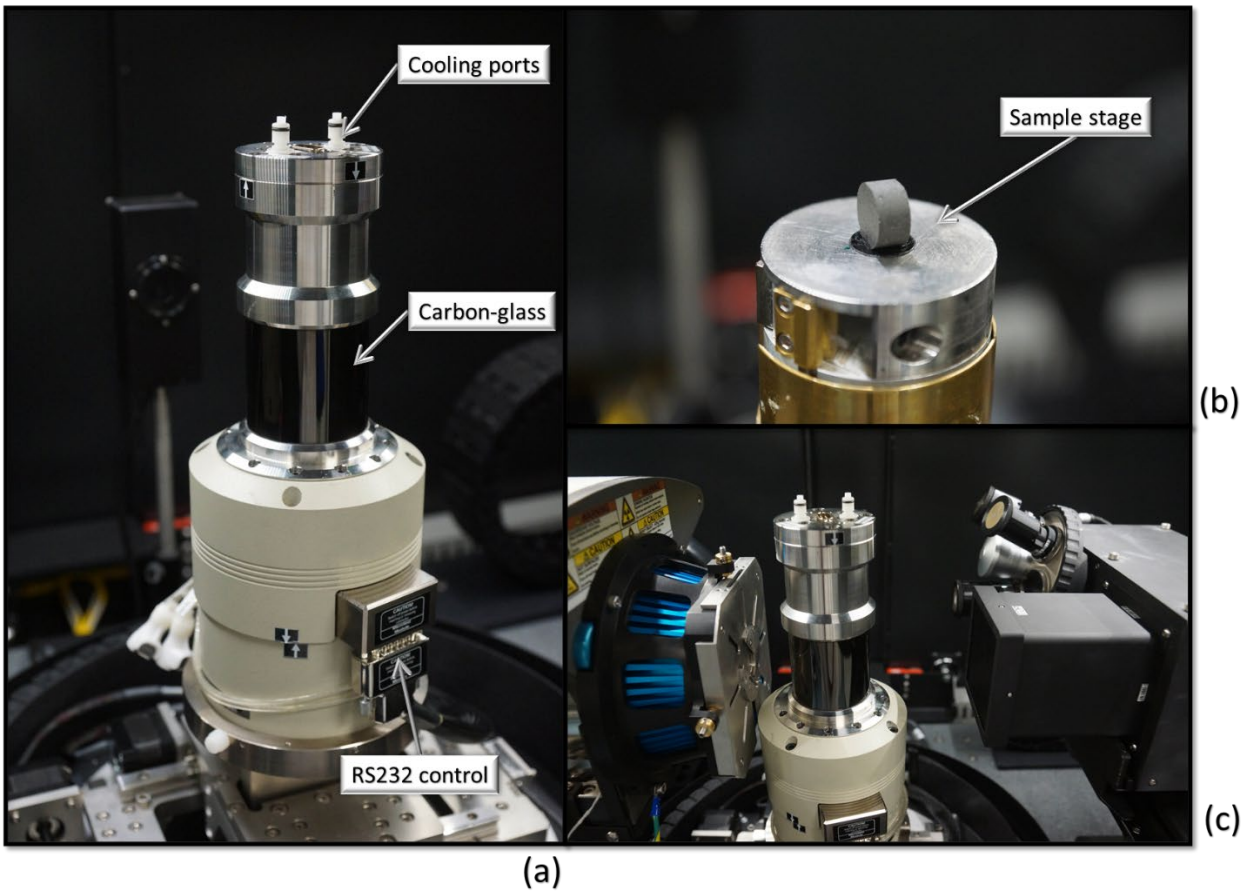


Figure 16: Deben H250 load and temperature rig (a), sample stage close-up view (b), experimental setup (c)

2.5 Synchrotron X-ray Imaging and Diffraction Mapping, Neutron Diffraction and Image Correlation for the Measurement of Elastic and Total Strains

2.5.1 Preamble

The objective of this combined neutron and x-ray diffraction Brazilian disc compression experiment is to quantify the evolution of elastic strains with temperature. The synchrotron experiment was performed at the I12 beamline of Diamond Light Source prior to this thesis from the 1st of October 2016 for 12 shifts [132]. Two shifts were dedicated to the acquisition of a series of tomography scans and diffraction maps under load of Brazilian discs of Gilsocarbon. The results obtained were combined with

a high-temperature neutron elastic scattering experiment at the ENGIN-X instrument of the STFC-ISIS neutron and muon source, and published in Carbon [73].

The author of this thesis did not participate in the experiments (from 2016) and did not analyse the neutron diffraction data from the high-temperature neutron elastic scattering experiment. However, as part of this DPhil project and contributing also to the publication, the total strains were extracted after improving the quality of the tomography reconstruction using iterative reconstruction algorithms, the X-Ray diffraction data was re-processed to obtain the elastic strains and interpolated with the total strains to investigate their relation. An important piece of work consisted in developing the DIFFRACTX code to process XRDM datasets, output strain maps, and combine them with the DVC strains. Furthermore, the author computed the DIC strains from the neutron experiment at ENGIN-X.

2.5.2 ENGIN-X Neutron Diffraction Beamline

STFC-ISIS is a neutron and muon spallation source. Hydrogen ions are produced by electric discharge and accelerated to 37% of the speed of light by copper drift tube electrodes. After being stripped of their electrons, the hydrogen protons are further accelerated to 87% of the speed of light in a synchrotron by ten accelerating cavities. Two bunches of protons are then rerouted to each of the two target stations by fast kicker magnets. The proton beams collide with a tungsten target producing a neutron pulse. The neutron diffraction data were acquired on the ENGIN-X instrument [144] at the STFC-ISIS spallation neutron and muon source from ambient temperature to 850°C, and are presented in Figure 17 for information. Gilsocarbon graphite discs were loaded in compression at each temperature, and both elastic and total strains were investigated. Neutron diffraction data were collected by two opposite detector banks perpendicular to the beam, with two sample orientations and up to a count

current of 15 μA, however only the radial and transversal strains were used in the subsequent analysis. In the orientation where the orthogonal strains were also collected, the disc circular plane was facing the camera which allowed to record the total strains by Digital Image Correlation (DIC) using the Basler Pilot PIA2400-17 GM LaVision DaVis camera. Out-of-plane movements were estimated by performing a dual setup DIC experiment in the lab with the stereo GOM-Aramis system on one face of the disc and the single camera DIC on the other (see sections 2.2.3 and 2.2.2).

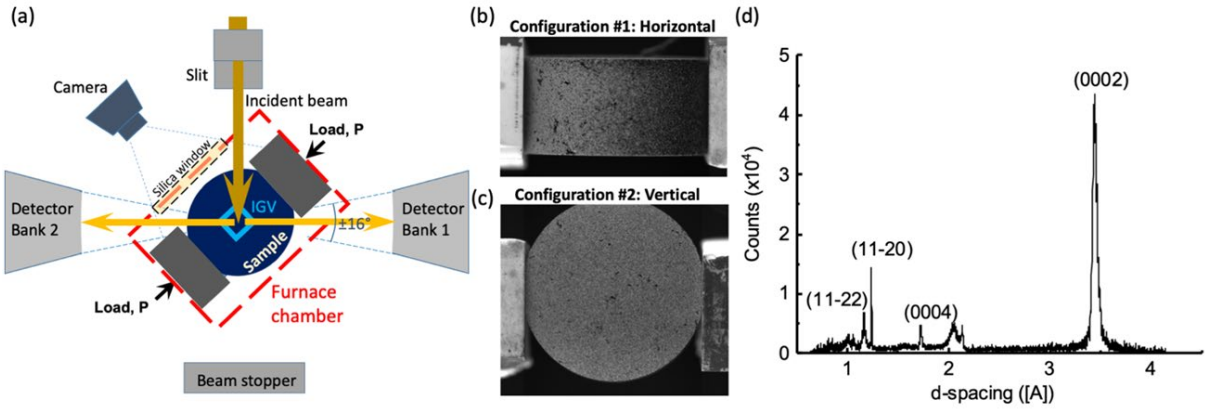


Figure 17: (a) Schematic (top view) of the experimental setup at ENGIN-X, with imaging of a horizontal specimen (b) and a vertical specimen (c), and example of neutron spectrum [73]

2.5.3 Diamond Synchrotron I 12 Imaging and Diffraction Beamline

The synchrotron experiment was performed at the I12-JEEP beamline of the Diamond Light Source (DLS) synchrotron in Oxfordshire. The team installed one of the Oxford Materials Shimadzu loading rigs AGS-10kNX and acquired tomography and diffraction maps for four steps, a 200 N preload, 1.5 kN, 3 kN and 4.5 kN (as presented in Figure 18). A super-conducting 4.2 T wiggler source provided the X-ray white beam which was then reduced to a narrow energy band around 61.86 keV using a double bent crystal Laue monochromator. The PCO-EDGE 5.5 CMOS camera combined with the

Module 2 scintillator-lens assembly provided radiographies of 2,560 × 2,160 pixels at a pixel size of 7.9 µm/pixel, and with an exposure time of 0.05 seconds, an acquisition rate of 100 fps and 2,500 projections collected over a 146.2° range. This limited angle tomography configuration was required due to the shadowing from the close Shimadzu pillars. The large-area Thales Pixium RF4343 detector was used to obtain partial Debye-Scherrer diffraction rings at a distance of 2.46 m and a resolution of 2,880 × 2,881 (pixel size 148 µm), using 1 × 1 mm beam-defining slits and after calibration with a CeO_2 powder sample, at 4 s exposure.



Figure 18: Presentation of the Shimadzu Rig and Pixium detector in use for experiment EE1585-2 at JEEP

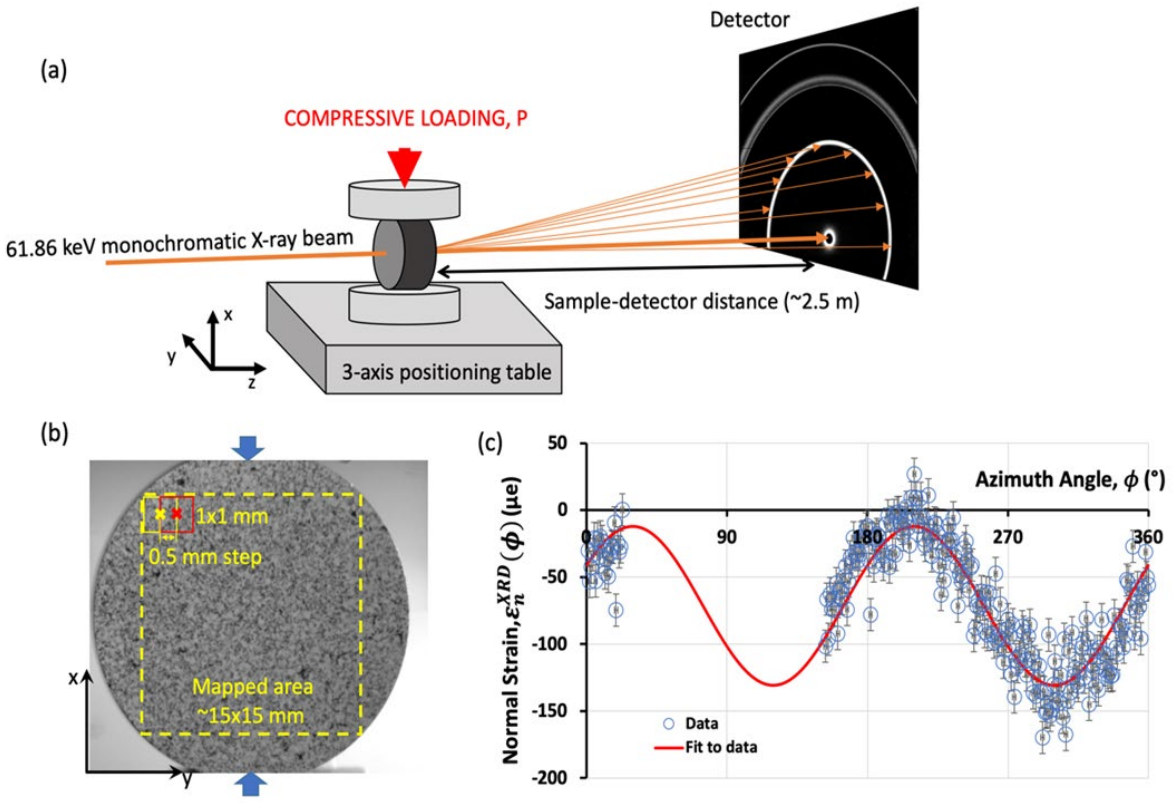


Figure 19: Loading configuration for X-ray computed tomography (XCT) and X-ray diffraction (XRD) (a), area mapped by XRD (b) and variation of normal strain $\varepsilon_n^{XRD}(\phi)$ as a function of azimuth angle (c) [73]

After reconstruction, cropping and background correction, the X-ray datasets consisted of 15 × 15 mm (29 × 29 points) diffraction maps and tomographies with dimensions 2501 × 2150 × 1171 voxels (19.8 × 17.0 × 9.1 mm) at 11, 1500, 3000 and 4500 N. Figure 19 presents the configuration of the X-ray mapping and the mapped area, as well as an example of normal strain calculated from d-spacings variation with respects to the azimuth for an acquisition point at the centra of the map. The results from this experiment are presented in Chapter 3.

2.6 Multi-faceted Approach to Damage and Deformation with Synchrotron X-ray Imaging and Diffraction (ESRF)

2.6.1 Preamble

This experiment (number ME1504) was carried out at the ID11 branchline of the European Synchrotron Radiation Facility (ESRF) in Grenoble, France, from the 28th of November 2018 [126]. A total of twelve shifts of 8 hours were allocated to this project under four main objectives, which made use of three different detectors, a small in-situ loading device and five different techniques. The ESRF was, at the time of the experiment, a third-generation synchrotron, prior to the ESRF-EBS (Extremely Brilliant Source). It has a storage ring circumference of 844 m maintaining electrons at 6 GeV.

2.6.2 ESRF ID 11 Beamline

The ID 11 beamline is located on port 11 of the electron storage ring and provides synchrotron light through a choice of two in-vacuum undulators (U22 and CPM18) offering a flux of up to 10^{14} photons/s/mm^2. The experiment was conducted in Experimental Hutch 3 (EH3) which is the last hutch on the line. Depending on the technique, either a monochromatic beam of 40 keV using a Laue-Laue double bent silicon crystal monochromator was used, or alternatively a high-energy 60.1 keV pink beam (filtered white beam).

Figure 20 pictures the experimental setup. The Nanox loading rig is composed of a screw driven by a hex-key and linked to the top compressive platen by a ball bearing. The load cell is located at the bottom of the rig and is connected to a multi-meter. The load is read as a function of the voltage on the device. The sample stage can be rotated 360° and tilted from -10° to +10°. It is surrounded by two near-field detectors aligned with the perpendicular to the beam direction. As needed the scintillators are placed into the beam to collect radiographies. These two detectors can be used for

many near-field techniques such as Phase-Contrast Tomography (PCT) or Diffraction-Contrast Tomography (DCT). During this beamtime, four different experiments were conducted as described in the following sections.

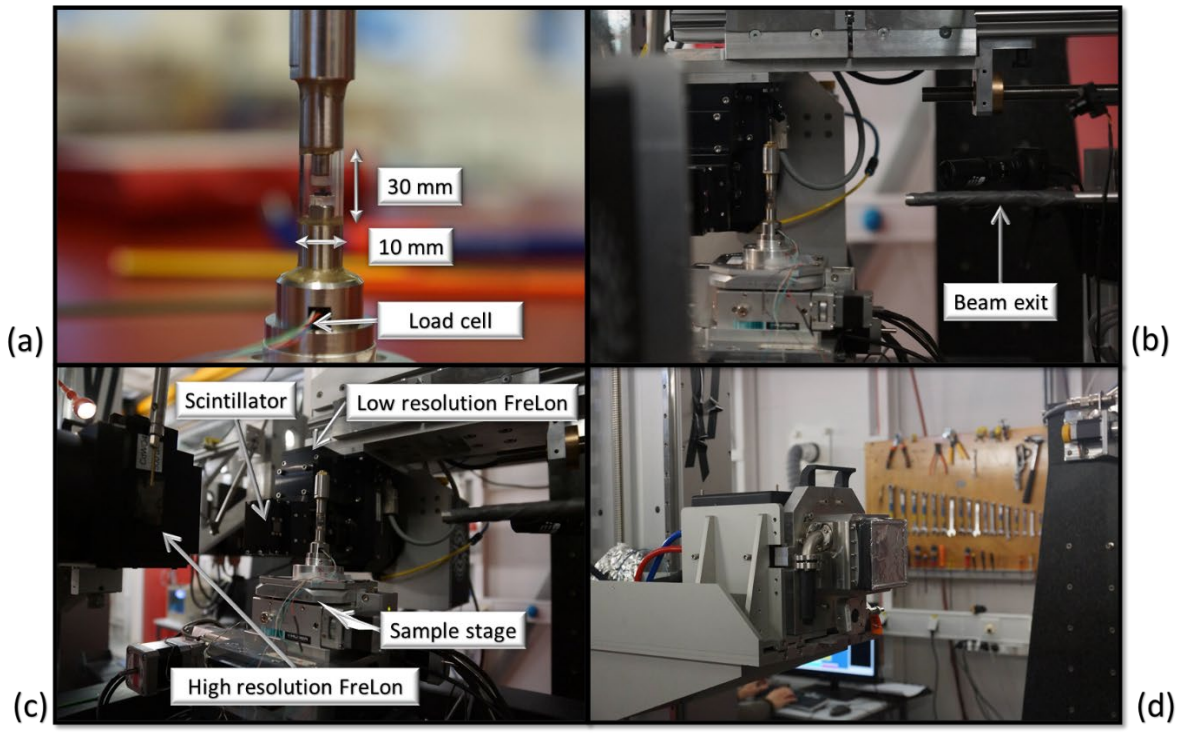


Figure 20: Rig close-up view (a), beam exit (b), sample stage and near-field detectors (c) and far-field detectors (d)

2.6.3 High-resolution X-ray Phase Contrast Tomography and Diffraction Mapping

In this part, the interest is in quantifying deformation using a method similar to the experiment presented in 2.5, but with a much higher resolution. The aim is to identify zones of tensile stresses, whether particular features act as stress concentrators and how filler particles and matrix share the strain distribution, by sampling a thin sample (3 mm diameter) of about 1.3 mm thickness. Considering the size of the Gilsonite

particles compared to the FoV, there is a higher probability of averaging across just matrix or filler, than in a bigger sample, and this can be confirmed by tomography. The compressive load was applied within the Nanox rig in 6 steps: 20 N, 50 N, 100 N, 150 N, 180 N, and 200 N after which the sample failed.

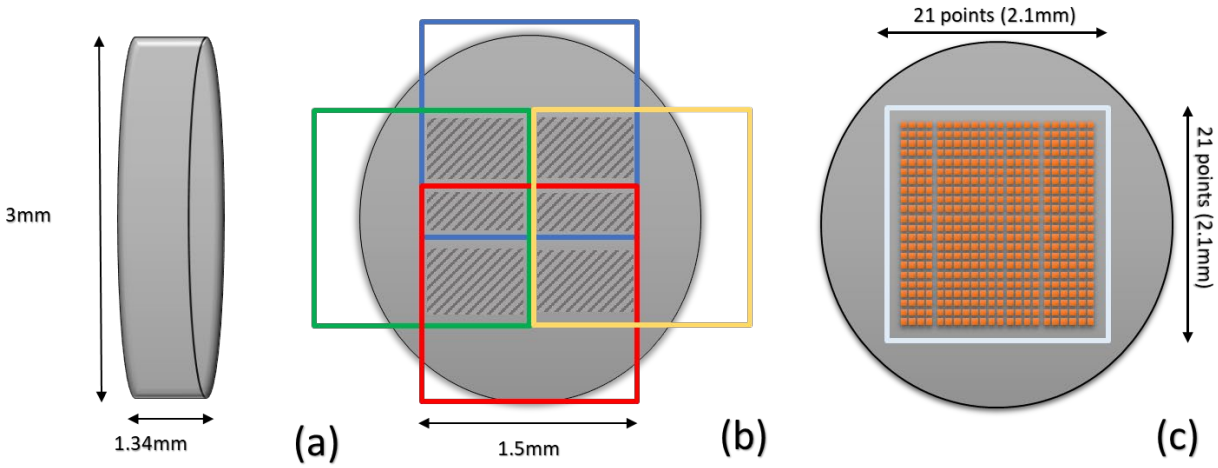


Figure 21: HR-PCT and XRDM setup, sample dimensions (a), tomography zones and overlap (b) and XRD grid (c)

Use was made of the high-resolution FreLon assembly which, thanks to a set of optics, offers $2{,}000^3$ voxels at 0.75 micrometres per voxel. In order to collect information on the major parts of the sample, four Regions of Interest (ROI) were defined with sufficient overlap to be stitched post-reconstruction; this is pictured in Figure 21.

For the X-Ray Diffraction Mapping (XRDM), beam defining slits were used with a 100 µm opening. A square map was defined of 441 points with no overlap or spacing between the points, meaning that the map covers an area of 4.41mm^2 which spans over almost two-thirds of the area of the disc; there are no points outside of the sample. The results from this experiment are presented in Chapter 3.

2.6.4 Three-dimensional in-situ X-ray Diffraction Scanning

In this experiment, the Nanox rig was used to apply a load to a 6 × 3 mm graphite cylinder. The beam was configured to be monochromatic at an energy of approximately 40 keV using a double-bend silicon crystal monochromator. Figure 22 presents the experimental setup. The Far Field detector FReLoN-4M (effective pixel size 50 × 50μm, 2048 × 2048 pixels, in-line fibre channels) was used to collect diffraction patterns while rotating the sample 360° and taking one acquisition at each angle. The exposure time was approximately 0.15 s and the loading regime is presented in Figure 23. Each loading step was followed by a wait time to stabilise before beginning to acquire data. At each load step, and after the full 3DXRD acquisition had completed, the scintillator of the near field FreLon detector was placed in the beam and the slits were opened for tomography mode. With the set of optics installed, one tomography was acquired per load step at $2{,}000^3$ voxels and 1.5 μm/voxel. The yellow volume in Figure 22 represents the tomography Region of Interest (RoI) and the orange cube identifies the gauge window for the diffraction, centred in the middle of the specimen and with a slit opening of 300 × 300 μm. The Phase Contrast Tomography (PCT) mode was used to control and quantify sample movements. The odd step numbers (1, 3, 5, etc.) had a Field of View (FoV) positioned in the centre of the specimen, and will be referred to as ROI-A, however the even numbers (2, 4, etc.) had a FoV centre shifted by about 200 μm along the X-axis, and it will be called here ROI-B. This was not intentional and was due to a python script error carried from another setup (and not visible on the radiographies during the experiment). It means both sets cannot be analysed together, but it does provide the ability to compare the results obtained from two different regions in the specimen. Results of this experiment are presented in Chapter 4.

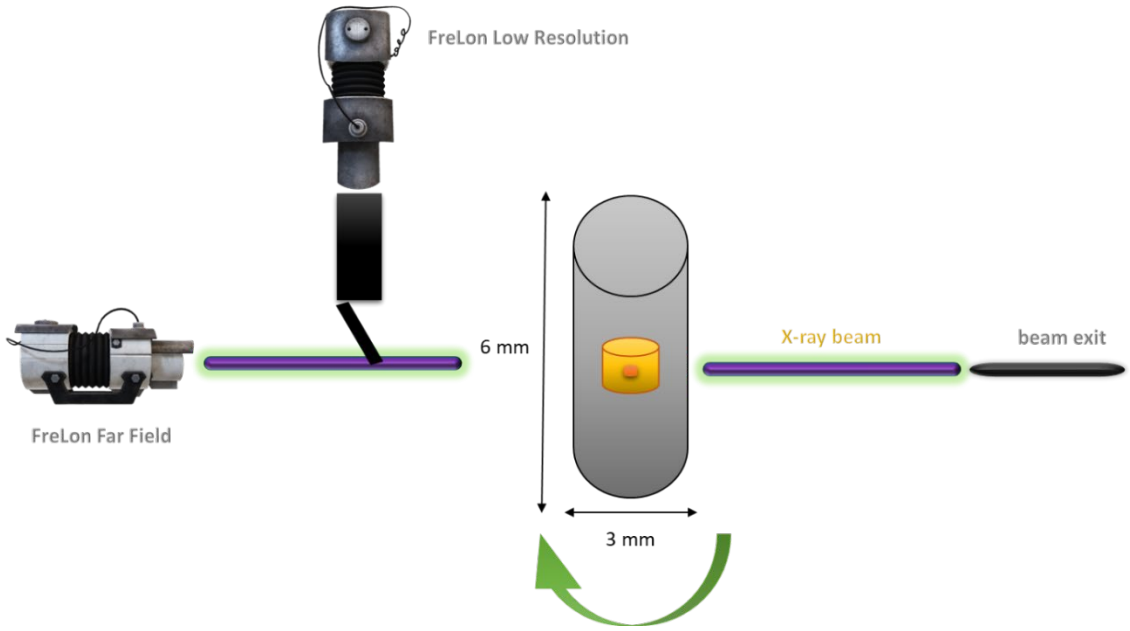


Figure 22: 3DXRD Setup with the positions of the PCT volume in yellow and the 3DXRD gauge in red

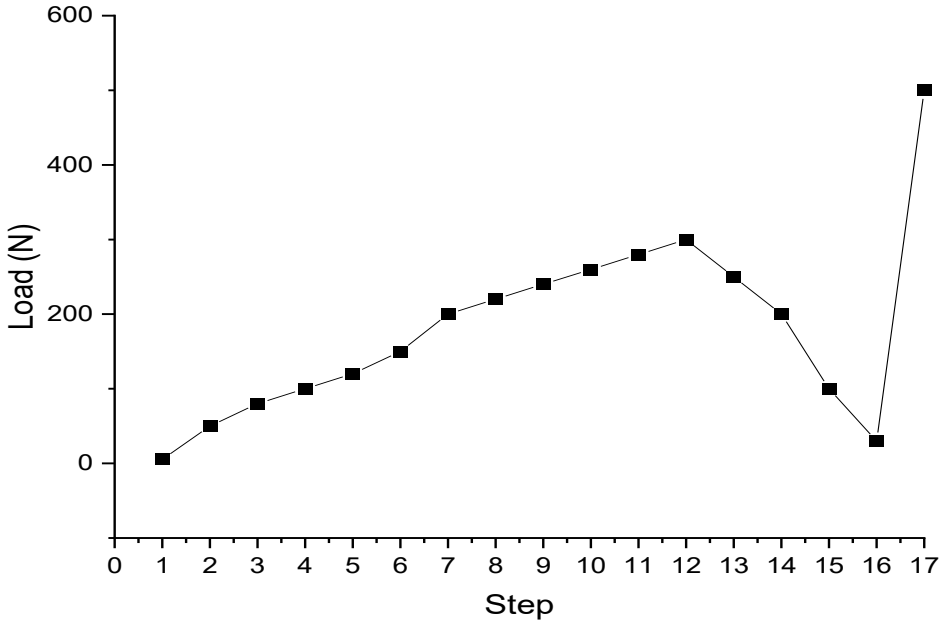


Figure 23: Load steps for the 3DXRD experiment, with each ROI-A and even numbers having a different FoV for measurements

2.6.5 Topo-tomography of Highly Oriented Pyrolytic Graphite Indentation

Whilst 3DXRD is a Far-Field (FF) technique of the order of hundreds of micrometres in resolution, Near-Field (NF) diffraction techniques can resolve grains at a sub-micron resolution. The typical distances for the in-line FreLon 4M fibre-optic diffraction detector (FF techniques) is over 150 mm (206 mm in this experiment) whilst NF techniques using the out-of-beam F2K14 detector (with scintillator, 2048 × 2048 pixels, 7.0 µm pixel size with 1.0 eyepiece and 2x objective length) is usually positioned less than 10 mm from the sample [145], and in this case this was set at 8 mm for both high (PCT) and low (TT/DCT) resolution detectors (same cameras but two different magnifying lenses and installed on opposite sides of the beam).

Diffraction Contrast Tomography (DCT) and Topo-Tomography (TT) are complementary techniques offering faster acquisition times than focused-beam scanning 3DXRD while also providing higher resolution. In both methods, a Near-Field tomography (as in PCT) detector is used to collect both diffracted spots and radiographies with extinction spots originating from the grains. DCT is setup to acquire the 2-5 innermost *hkl* families whilst TT focuses on a single grain, rotating around the orientation vector for a few tens of degrees at most; here from -10° to +10°. Combining DCT and TT enables orientation microscopy [84]. In this experiment, the surface of a 1 × 1 mm Highly Oriented Pyrolytic (HOPG) graphite sample was indented to investigate possible twinning. Three acquisitions were performed in sequence for each displacement increment: PCT, FF-XRD and TT/DCT. An example of TT/DCT acquisition is presented in Figure 24, with the same image shown with two contrast and brightness adjustments. It was acquired at preload (contact) at stage angle 0°/360° and tilt angle 10°. In (a) the diffracted grain is visible on the top of the image,

and in (b) the ball indenter can be seen just below the top platen from which the load is applied (Nanox rig).

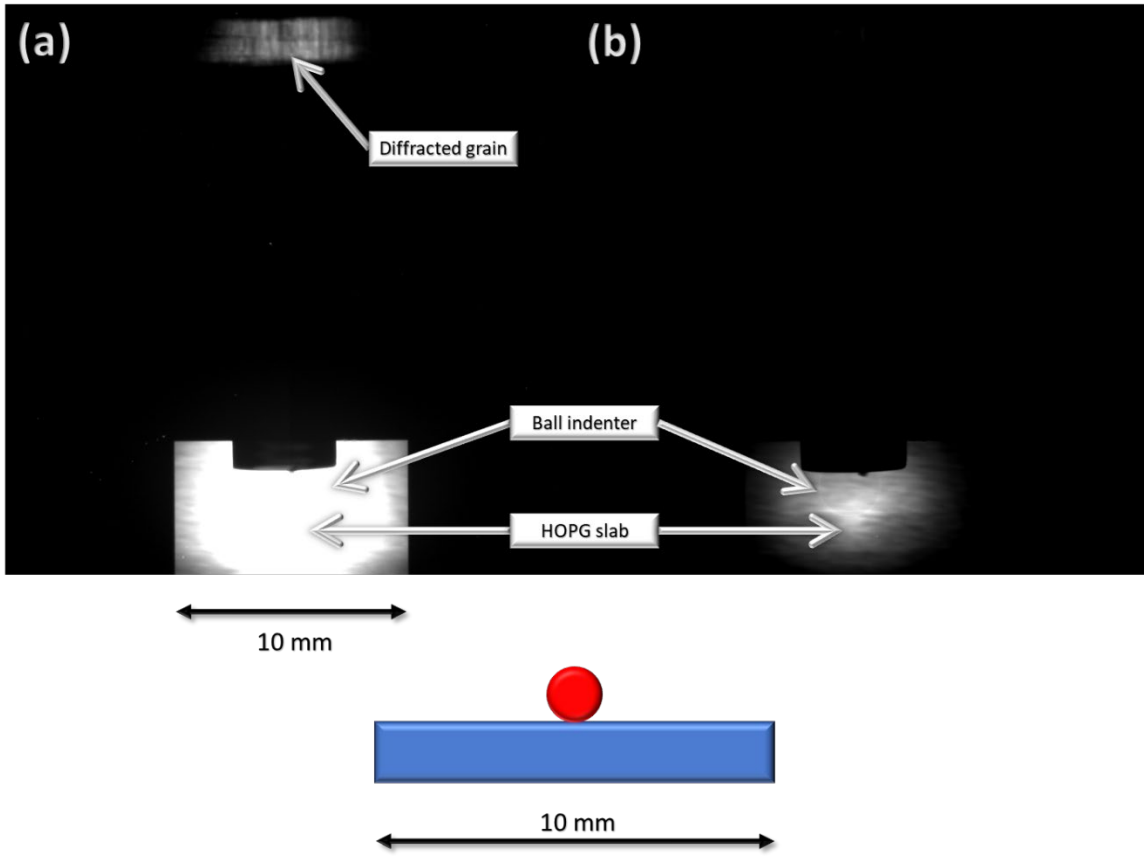


Figure 24: Topo-tomography acquisition from the near-field FreLon detector of HOPG at preload and angle 0°/10°, with two contrast and brightness adjustment to observe the diffracted grain (a) and the tomography region (b), and a schematic with the indenter in red and the HOPG in blue

2.7 Neutron Bragg Imaging

2.7.1 Preamble

In this section, a novel method is proposed that is suited to investigate the effects of grain reorientation and deformation in polycrystalline samples with coarse grain size or grain domains (from ~100 μm) using in situ time-of-flight energy-resolved neutron imaging on the IMAT instrument of the STFC-ISIS neutron and muon spallation source. A novel mechanical loading device for high resolution imaging has been designed (see 2.2.4), and tools for advanced image analysis have been developed, to detect the response to applied mechanical stress of microstructural features that are close to the Bragg condition. This method was applied to Gilsocarbon graphite, first with proof-of-concept experiment RB1910517-1 [130] to demonstrate the feasibility of the method and subsequently with an extension beamtime RB1910517-2 [131] after adjusting parameters to provide better conclusions on grain reorientation in Gilsocarbon graphite.

2.7.2 The IMAT Neutron Imaging Instrument

Installed on a 'broad pulse' liquid hydrogen moderator connected to Target Station 2, IMAT is an imaging beamline that offers a time-integrated neutron flux of 4 $\times 10^7$ n/cm^2/s with a 40 mm pinhole aperture thanks to a straight neutron guide [146, 147]. Between the source and the sample stage position, distanced by 56 m, a 20 Hz T_0 chopper filters the fast neutrons and gamma radiation at 12.75 m from the moderator while two 10 Hz double-disc choppers at respectively 12.2 and 20.4 m from the moderator are used to select the wavelength bands and avoid frame-overlap. They allow users to define and shift the pulse spectrum as required to suit the material being studied. The supermirror neutron guide ends just before the experimental hutch with a pinhole selector offering apertures of 20, 30, 40, 60 and 80 mm, which provides a

quasi-parallel beam with a L_P/D specific divergence, where D is the aperture and L_P the length to the neutron camera from the pinhole. The resolution, r, is independent of the camera pixel size and can be calculated with equation (2), where l is the distance from the active area of the detector to the centreline of the sample.

$$r = \frac{l}{L_P/D} \tag{2}$$

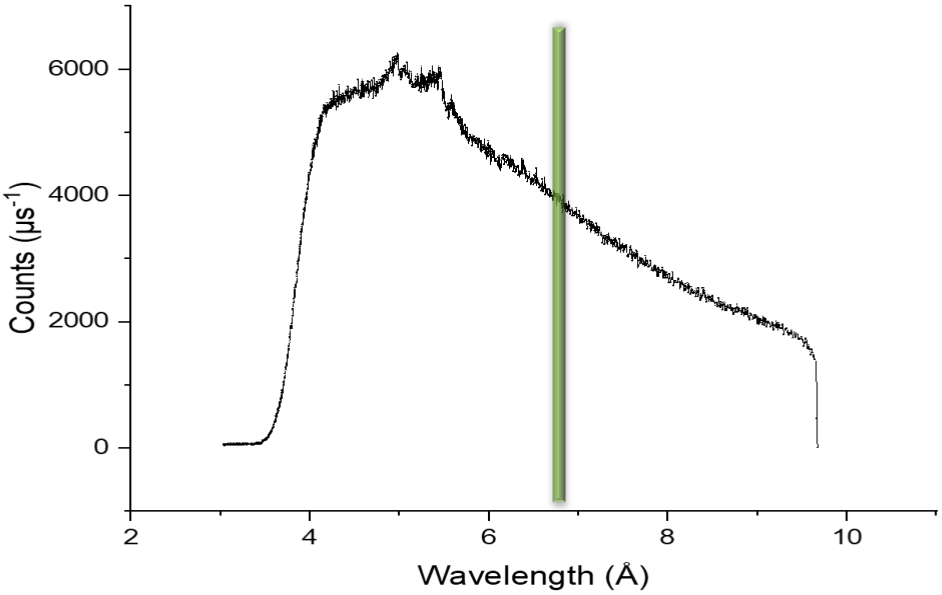


Figure 25: Beam spectra for run number 15209 (Scan 5, Load 4kN, 120μA) from monitor 5 which is 49.5m from the moderator, with green bar representing wavelength for basal plane diffraction

Within the hutch, an in-vacuum tube carries the neutrons to the sample area and comprises a set of 5 beam-limiting boron carbide jaws. The last retractable neutron monitor on the beam, M5, is located just before the end of the tube, and allows to check the shape of the flux. Figure 25 is an example of the neutron count from Monitor 5 (M5) on IMAT. Although it is possible to use a white beam and shift the pulse with

appropriate chopper parameters, this has limitations that need to be accounted for when studying materials with energies away from the peak flux. This is due to the need to avoid neutron pulse overlap, and the maximum wavelength band, $\Delta\lambda$, is set by equation (3) [147].

$$\Delta\lambda = \frac{3957}{L_S f} \tag{3}$$

where f is the repetition rate and L_S is the distance from the source to the detector.

2.7.3 Bragg-edge Imaging

Bragg-edge imaging is a fast-developing acquisition tool that provides energy-resolved information of internal structures in engineering components. Time-of-flight energy-resolved neutron imaging using different sensors has been initially used for in-situ strain analysis and 2D single crystal Bragg-dip mapping [148–151]. More recent developments of in-situ wavelength-dependent neutron imaging has been able to accurately determine the lattice spacing, lattice strains and coefficient of thermal expansion of metallic powder samples [152]. This has been made possible by the development of Microchannel Plate (MCP) -based detectors capable of time resolutions below 10 ns. The MCP detector on IMAT, developed at the University of California at Berkley [153], is composed of an array of four Timepix ASIC sensor chips offering a field of view of 28 × 28 mm with a pixel size of 55 µm at event rates up to 200 MHz.

A relatively unexplored use of Bragg-edge imaging is direct image processing and analysis of extinction spots for crystals in the Bragg-condition. This use of energy-resolved neutron radiographs is particularly sensitive to the resolution defined by equation (2) and is most suitable for materials with grain sizes or domains over 100 µm. Several methods can be used to investigate grain orientations. Electron Back-

Scattered Diffraction (EBSD) has a number of limitations including sample size and the requirement to polish the examined surface, and it is not very suitable for bulk samples of materials such as graphite [154]. For characterisation of grains within the microstructure, Three-Dimensional X-Ray Diffraction (3DXRD) grain reconstruction, as well as Diffraction Contrast Tomography (DCT), have proven effective for metals and materials with a low mosaic spread [82, 83, 155, 156]. DCT can be applied with in-situ loading or heating and has the potential to provide information on the grain strain state [157]. The DCT technique has been generalized to neutron imaging with the development of the ToF-3DND grain mapping method [158].

2.7.4 Design of the Loading Rig (PRESSOR)

The method consists of a neutron energy-resolved acquisition of a specimen while applying mechanical compression. The rig is used to apply a small preload to the sample and subsequently proceed to a neutron radiography acquisition. This is followed by a series of loading stages, each associated with a radiograph acquisition of equal duration.

The radiograph image resolution is independent of the detector pixel size and varies principally with the sample to detector active area distance, as discussed. The distance from the pinhole to the detector is fixed and the pinhole aperture determines the neutron flux, which affects the acquisition time for sufficient signal (i.e., neutron count). This means that the main way to reach a suitable resolution for image analysis whilst maintaining a high neutron flux is to reduce the sample to active area distance and bring the sample as close to the detector as possible. Preliminary acquisitions are necessary to determine the most appropriate configuration (i.e., pinhole size, collection time, sample-to-detector distance and chopper speed).

A proof-of-concept loading apparatus was designed to suit the requirements of close proximity to the detector, low neutron absorption, limited image shadowing and controlled loading capabilities. The rig is a manually loaded, screw driven device for compressive loading (Figure 26). In this work, diametral compression was applied for comparison with other studies of graphite [24, 25]. Other samples suited for compressive loading can be studied using the same rig.

The overall thickness of the rig was minimised to allow a short sample to active area distance. The top assembly, or loading head, can be positioned in the neutron beam whilst avoiding potential contact with the MCP detector, which is introduced via a robotic arm. Figure 26 presents the top assembly with its main components. A loading cell (20 kN) is located on the lower top assembly and is connected via universal serial bus to a computer for direct monitoring of the load. All the structural components, other than stainless steel fixing screws and bolts that are not in the beam path, are made of aluminium alloy (HE30-6082T6) for neutron transparency and sufficient mechanical strength. The curved surface of the secondary anvils is suitable for discs with a diameter between 15 and 25 mm, maintaining the contact surface within the range specified by ASTM D8289-19 [159]. In the main configuration, the flat surface of the secondary anvils is loaded by the primary anvils. Both anvil pairs slide on two cylindrical pillars attached to the top and bottom parts of the assembly. The secondary anvils can be inverted to offer a flat loading surface for flattened discs [41] or other flat-ended compression samples.

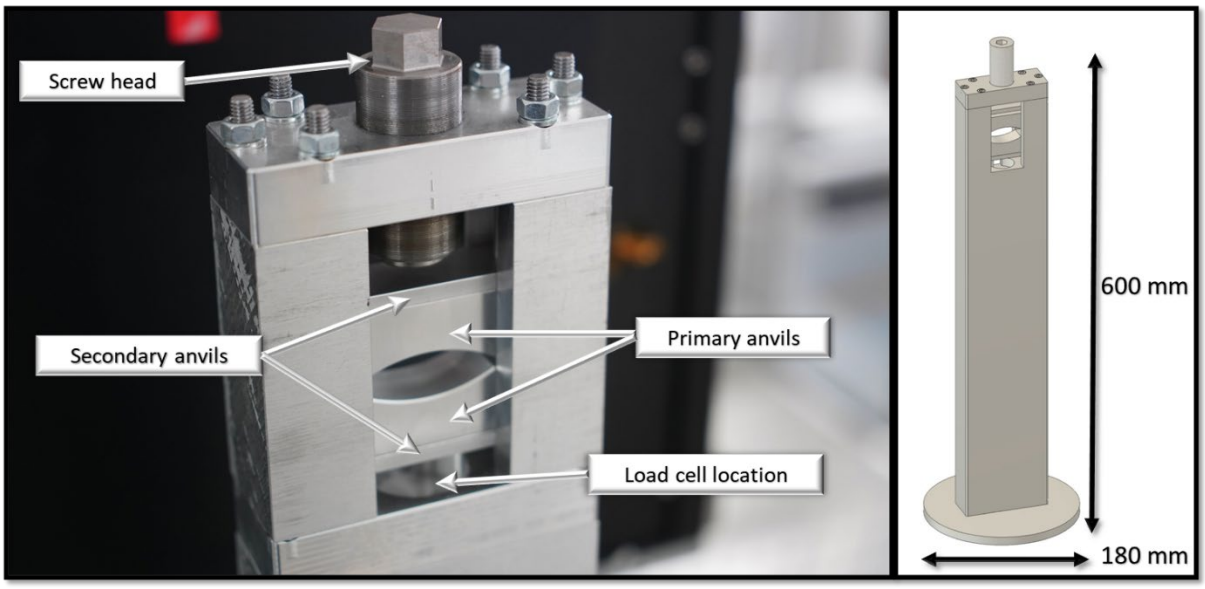


Figure 26: Neutron imaging loading rig: (a) close up view of anvils; (b) 3D CAD

2.7.5 Experimental setup

Three days of beamtime were allocated on IMAT under experiment number RB1910517-1 and a further three days for the extension experiment RB1910517-2. The neutron wavelength at which the graphite basal planes will enter the (002) Bragg condition is significantly away from the 2.6 Å pulse maximum at 6.7 Å, so for the proof-of concept experiment a pinhole aperture of 40 mm was selected to collect radiographs with a resolution sufficient to identify extinction spots and the loss in flux was compensated with an acquisition time of 120 µA to ensure sufficient neutron count in the energy band of interest. In the extension experiment, data were acquired for two samples. The first was a repeat of the original experiment with double the neutron count at 240 µA whereas the second sample was a larger flattened disc scanned with the same 120 µA current but with the larger 60 mm pinhole aperture. The disk choppers were configured for a 10 Hz frequency and a phase delay of 20 ms moving the Time-of-Flight (ToF) range to 30-130 ms which is equivalent to approximately 2-

10 Å; the suitability of this range is illustrated by the neutron count in Figure 25. The data is binned and saved as a stack of images in the FITS format (Flexible Image Transport System), each image representing an approximate energy. In this experiment, the data collected has been divided in 2,474 bins.

Figure 27 presents the experimental setup inside the hutch. In order to avoid the risk of collision with the detector, a minimum of 5 mm distance was maintained between the rig and the lower reflector shield, and for the preliminary experiment the default distance was set to be 9 mm. The distance from the rig surface to the centreline of the sample being 20 mm, and the active area of the detector being 17 mm behind the shield, the total detector to sample centreline distance is 46 mm giving a resolution of approximately 184 µm. On the first part of the extension experiment, the sample came closer to the shield at 5 mm giving a resolution of 168 µm, whilst for the second part, to avoid the top screw from colliding with the top shield due to the reversed anvil configuration and the larger sample, the distance was increased, giving a resolution of 276 µm. The detector is held by a robotic arm at a fixed position defined by the beamline arrangements, and at a fixed distance of almost 56.4 m from the moderator. The rig sits on the tomography stage that can be used for vertical rotation, which is attached to the heavy-duty sample stage used for all translations.

The control of sample rotation under load has been presented in the DIC section 2.2.4, and the results of these Bragg imaging experiments are presented as part of the study on grain reorientation in Chapter 4. The geometry and identification number of each sample studied are available in Table 6.

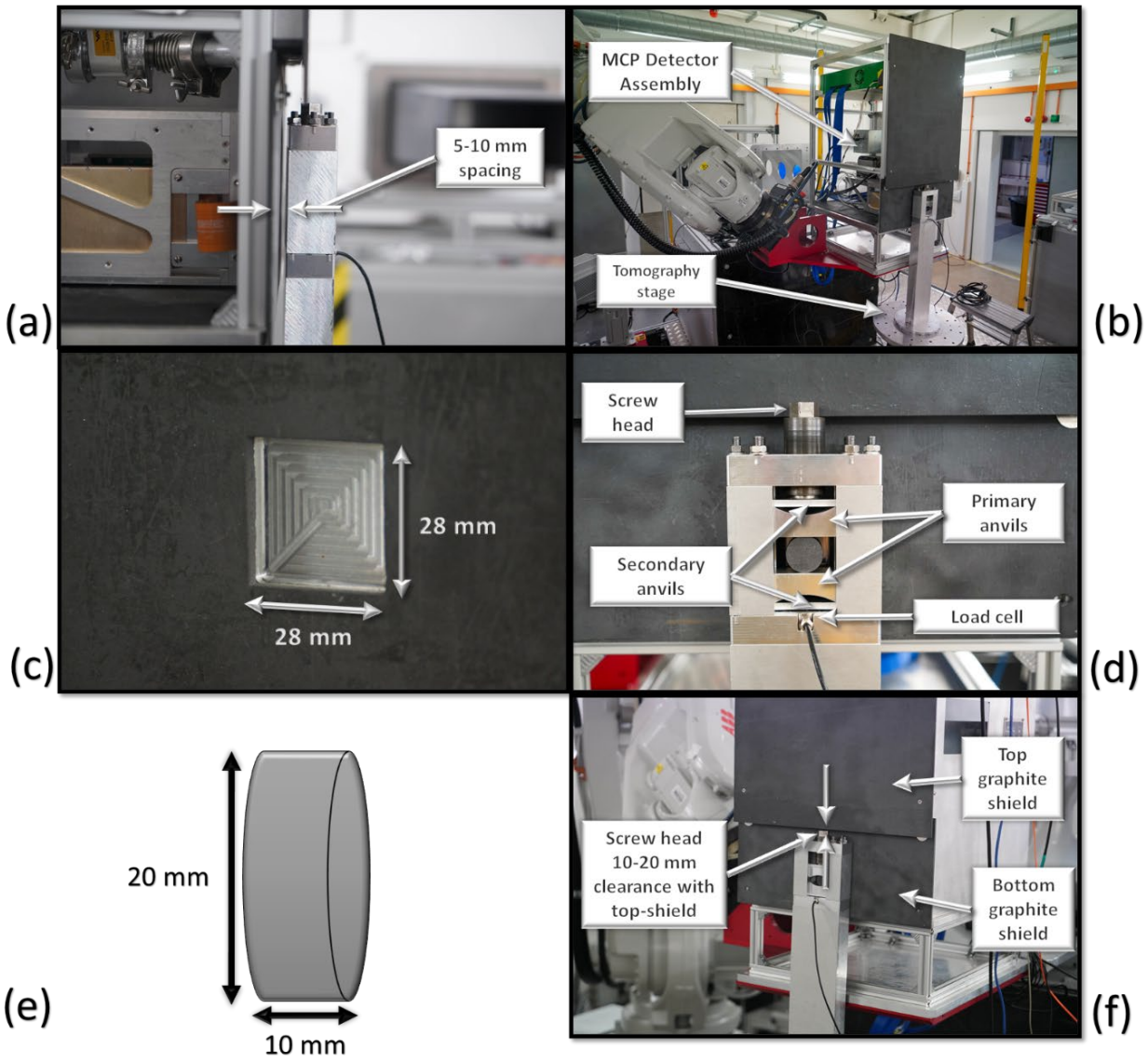


Figure 27: Experimental setup depicting a side view with rig-to-shield distance (a), overall view with robot-arm and rig fixed on tomography stage (b), detector window close-up view (c), secondary setup close-up with screw head away from top-shield (d), sample dimensions (e), and primary setup with screw head under top shield (f)

Table 6: Sample specification for the neutron Bragg imaging experiments

Sample ID	Geometry	Flattened	D	H	Anvil
IOX20D7B	Disc	No	10	20	Curved
IOX20P2B7A	Disc	No	10	20	Curved
IOX20P2D8B	Disc	Yes	12.5	25	Flat

2.8 High-resolution neutron diffraction mapping: SALSA

2.8.1 Preamble

Two experiments were carried out at the SALSA instrument for this project. The first 2019 experiment, 1-02-241 [127] investigated disc specimens with slit and hole stress concentrations in their centres, retrieving the radial component (or along the loading axis) with compressive stress. A global cooling failure led to the Instron pumps being offline for about two shifts, and this limited the time available to switch to the second configuration. An application for extension was accepted, and designed, planned and completed as experiment 1-02-299 in March 2021 [128]. This extension saw a revised experimental setup prepared. Instead of discs, dog-bone tensile specimens with a notch along their centreline, and deep by about 1/3 of the cross-section width, were loaded in tension, with new grips specifically designed for that purpose[5].

2.8.2 SALSA at the Institut Laue-Langevin

The Institut Laue-Langevin is a pool-type, heavy-water cooled 63 MW high-flux reactor located on the European Photon and Neutron (EPN) Campus in Grenoble, France. It offers a flux of $1.5x10^{15}$ neutrons per second per cm^2, the brightest in the world. Although reactor-type neutron sources have limited Time-of-Flight capabilities, the brightness of the flux offers the fastest possible speed of acquisition. As a comparison, a single neutron diffraction acquisition at STFC-ENGINX, which does not require ToF, takes approximately 20 minutes for a final beam-defining window of 4 × 4 × 4 mm and a reasonable count of 2,000 detections. For a similar count and a beam defined at a 2^3 mm gage volume at SALSA the acquisition takes 2 minutes, which is a x10

[5] Please note that this is presented in this section as a main experiment, however due to the limited space in this thesis and the modest conclusions brought by the current stage of analysis, the results are presented in the appendices. This is partly due to a combination of COVID-19 delays and equipment failures, and further work will be continued beyond this thesis. This is not one of the main original experiments, and it is not a limitation to the conclusions of this work.

improvement. This speed of acquisition is essential to time-resolved experiment considering that access to beamtime is limited.

The SALSA Instrument is second on a guide providing thermal neutrons to three instruments, including D1B and FIPPS, and it is therefore able to provide a high and constant flux throughout the experiment. The neutron beam is diverted using a double-focusing bent Si-crystal monochromator composed of 39 elements to one of the beam-exit ports with a take-off angle between 55° and 125°. As presented in Figure 28, the beam is delivered by a set of two primary collimators which define the vertical length of the gage volume as well as its horizontal width.

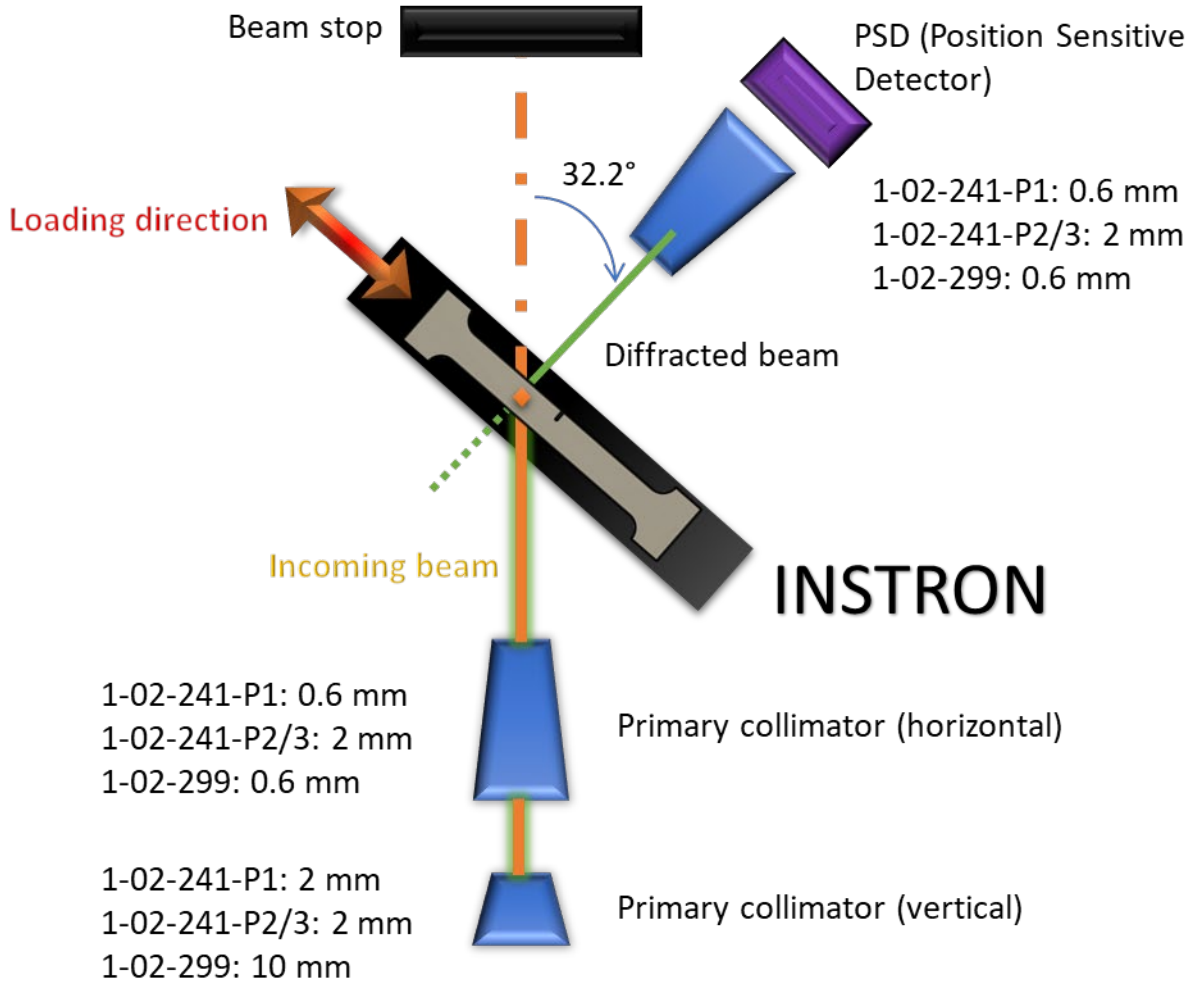


Figure 28: Experimental setup diagram for experiments 1-02-241 and 1-02-299

For all experiments presented here and with the take-off angle (of the monochromator) and the wavelength of about 1.61 Å, the diffraction angle (position of the detector) was set at 32.2° to capture the 002 ring. The detector, sample table and hexapod have air-cushion pads, allowing for relatively precise alignment, and views of the instrument are displayed in Figure 29. The detector is a 2-dimensional Position Sensitive microstrip Detector (PSD) with an active area of 80 × 80 mm^2 and 256 × 256 channels. This detector offers flexibility in the positioning and is able to accurately resolve part of the Debye-Scherrer cone. Its main limitation however is that it can only record one strain component at a time, requiring to either select one or change the sample position at each step, where possible.

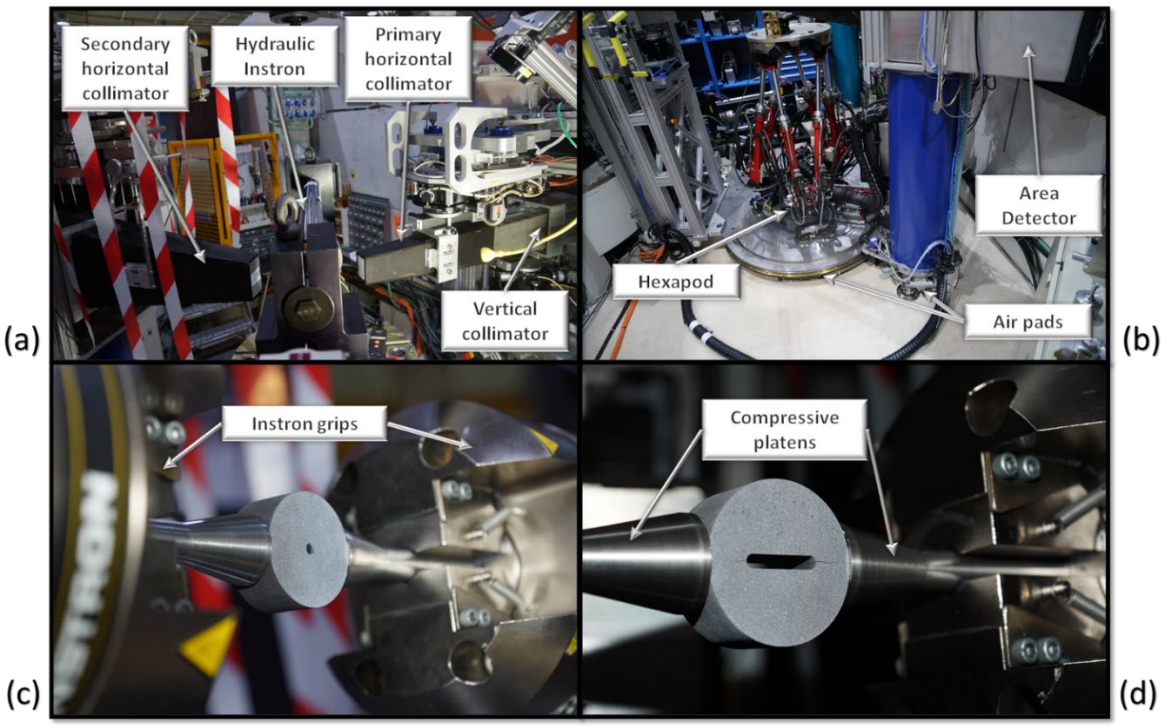


Figure 29: Overall instrument view (a), hexapod (b), hole-notched sample (c) and slit-notched sample (d)

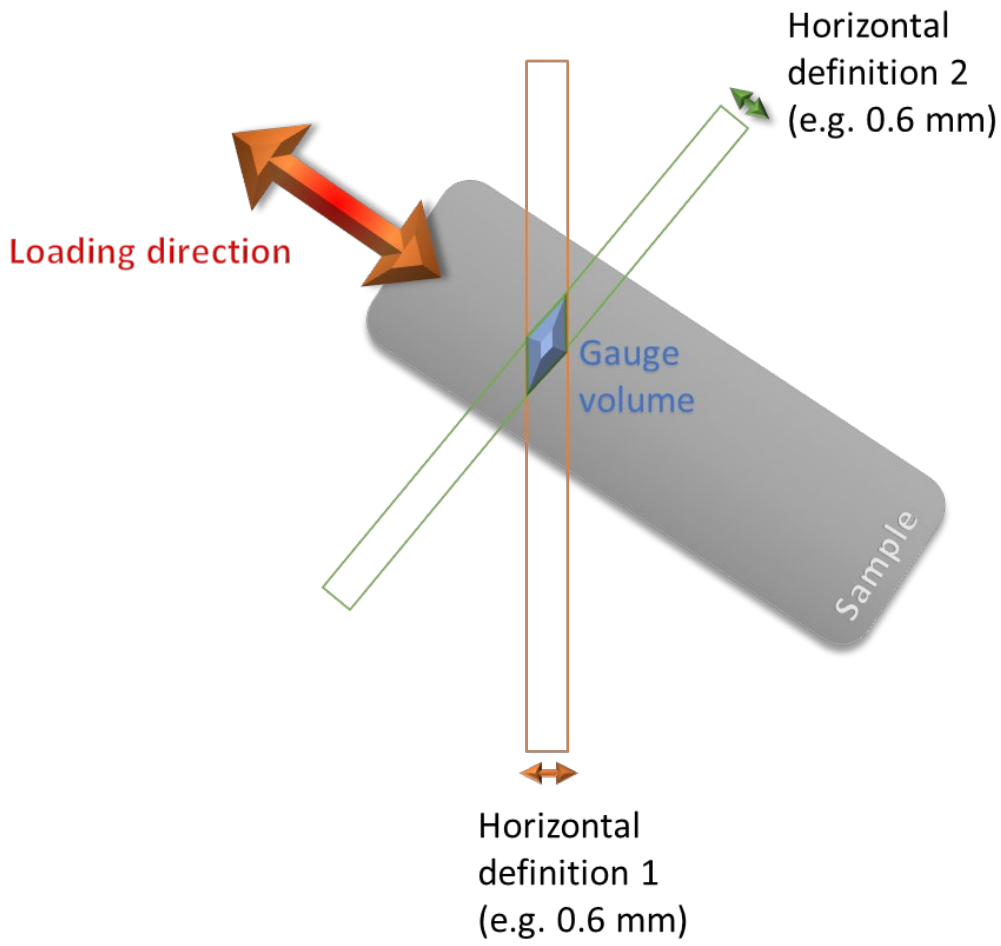


Figure 30: Diagram representing the gauge volume within the sample for SALSA experiments

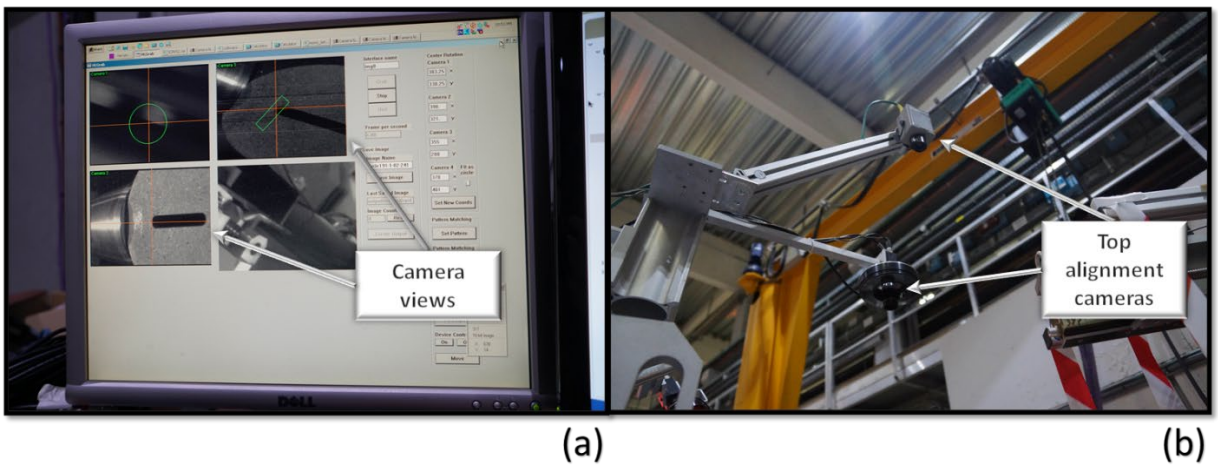


Figure 31: (a) Example alignment views and (b) cameras for alignment for SALSA experiments

The hexapod positioning table has six degrees of freedom. It can roll and pitch by ±30° and rotate yaw by about ±45°. It has a horizontal plane translation of ±300 mm and vertical translation of 150 mm at maximum. The hexapod can also translate on its air-pads up to 700 mm. Prior to installing the Instron loading rig, the collimators and table alignment were calibrated using a single crystal copper sample. Entry scans can take a long time due to the requirement of count and time wait in the Nomad program and are mostly reserved for interfaces, so the notches were aligned using the alignment cameras as pictured in Figure 31. The upper cylindrical bar of the Instron hides the view from both top cameras, and only the remaining 2-3 cameras could be used. Due to the directions of the incoming and diffracted beams, and the required sample positioning, the gauge volume has the shape of a rhombus in the horizontal plane, whose size depends on the detector angle and on the aperture of the horizontal collimators, as diagrammed in Figure 30. Hereafter, dimensions of the gauge volume will be given as “longer diagonal” × “shorter diagonal” × “height”.

2.8.3 Compressive Loading of Drilled and Slitted Discs

The first experiment is presented in Figure 32. Two types of Brazilian discs were studied, both 50 × 25 mm, with either a hole or a slit in their centres to act as stress concentrators. As can be seen in picture Figure 32(a) the 0.6 mm collimators reduce the space of the sample volume and the manoeuvrability of the Instron hydraulic loading rig. Sample installation and sample changes were performed by a rigid translation of the hexapod on its air pads. Two conical platens were used to hold and apply compression to the specimens, and they were held by the Instron tensile grips. The alignment of the grips was preformed prior to the experiment by placing the platens in contact and applying a load of 500 N while adjusting the five degrees of

freedom of the main grip. A thin paper was passed in between the platens to determine any remaining misalignment. The Instron PID was calibrated using a dummy graphite sample and the autocalibration for graphite.

This experiment was composed of three parts. The first configuration used the 0.6 × 0.6 mm horizontal collimators and the 2 mm vertical collimator for sample D4H-S2. This offered a rhombus gauge volume of approximately 2.16 × 0.62 × 2 mm, and a 9-points map. For the other two specimens (D4O-S3, D4H-S4), to save time and acquire more points, a switch was made to the 2 × 2 mm horizontal collimators providing a gauge volume of 7.21 × 2.08 × 2 mm, at the expense of a larger sampling area, but with up to 36 points. The loading steps for all samples are presented in Figure 33.

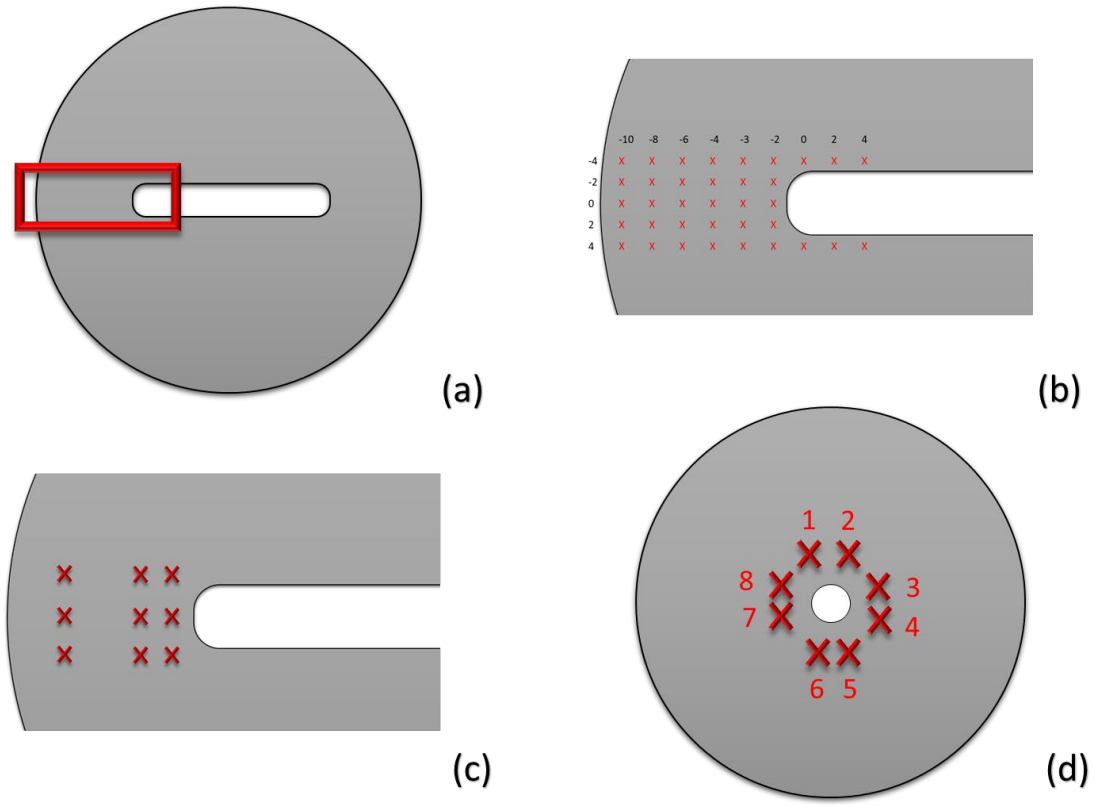


Figure 32: (a) Map area of the slit-notched sample, (b) 36-points map at 2 × 2 × 2 mm, (c) 9-points map at 0.6 × 0.6 × 2mm, (d) hole-notched sample map at 0.6 × 0.6 × 2 mm for SALSA experiment 1-02-241

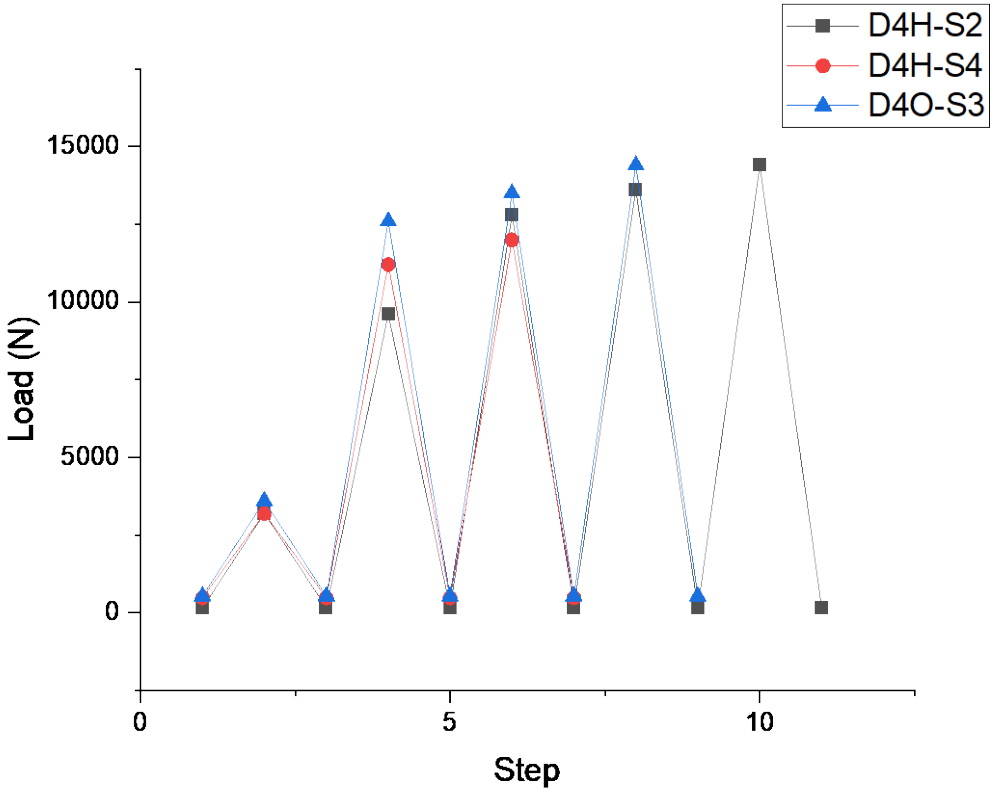


Figure 33: Loading sequences for all three samples of experiment 1-02-241

2.8.4 Tensile Loading of Notched Dog-bone Specimens

In order to observe tensile strains at a notch, the experimental setup was modified by using notched dog-bone specimens loaded in tension, whilst keeping the Instron position in the same orientation with respects to the beam. The strain component direction is still radial, but the tensile setup implies that it is the tensile strains that are being resolved in this alternative arrangement. The experimental setup is presented in Figure 34, and the loading scheme in Figure 35.

Due to the brittleness of Graphite, the existing Instron tensile grips could not be used, and instead specific jaws were designed and manufactured to apply the load on the shoulders of the dog-bone specimens. These jaws limit the risk of sample sliding as well as potential brittle fracture from overtightening at the contact points. The jaws and

the specimens were designed to be compatible, the shoulder curvature and the jaw spacing matching precisely to the dimensions of a sample, and accounting for the maximum and minimum port distances on the Instron as well as the adjustment pieces. The jaws were connected directly to the M30 screw of the Instron ports. The adjustment pieces are a set of curved rings which allow tightening and auto-alignment of the jaws or grips. Detailed views for the jaws and the alignment pieces can be seen in Figure 36.

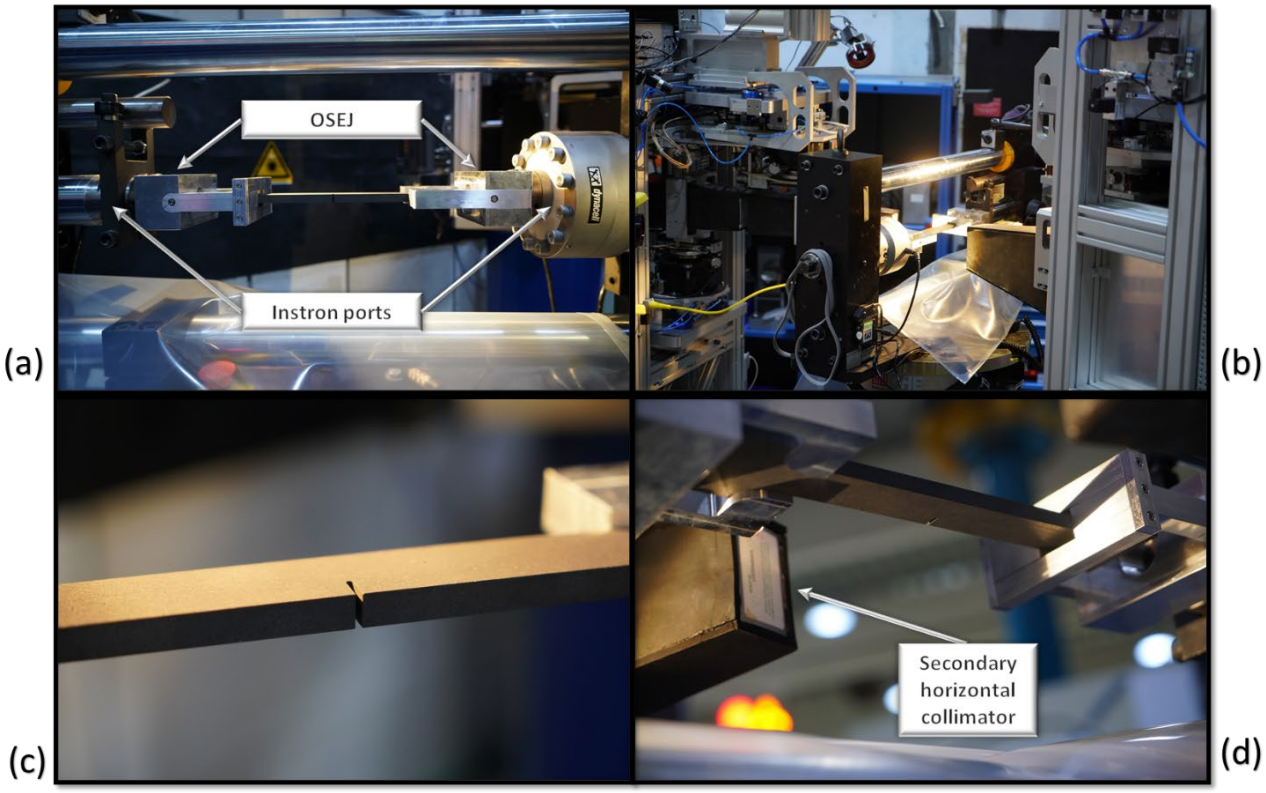


Figure 34: (a) Side view of the Instron, (b) overall setup view, (c) close-up view of the sample, (d) view of the sample and second primary collimator for SALSA experiment 1-02-299

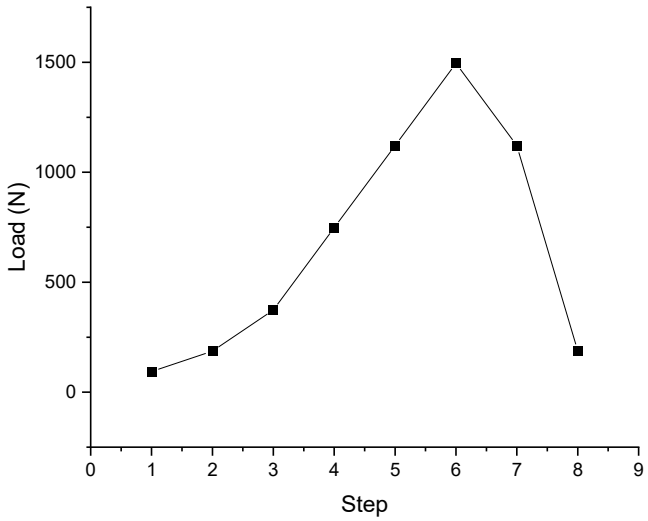


Figure 35: Loading regime for SALSA experiment 1-02-299

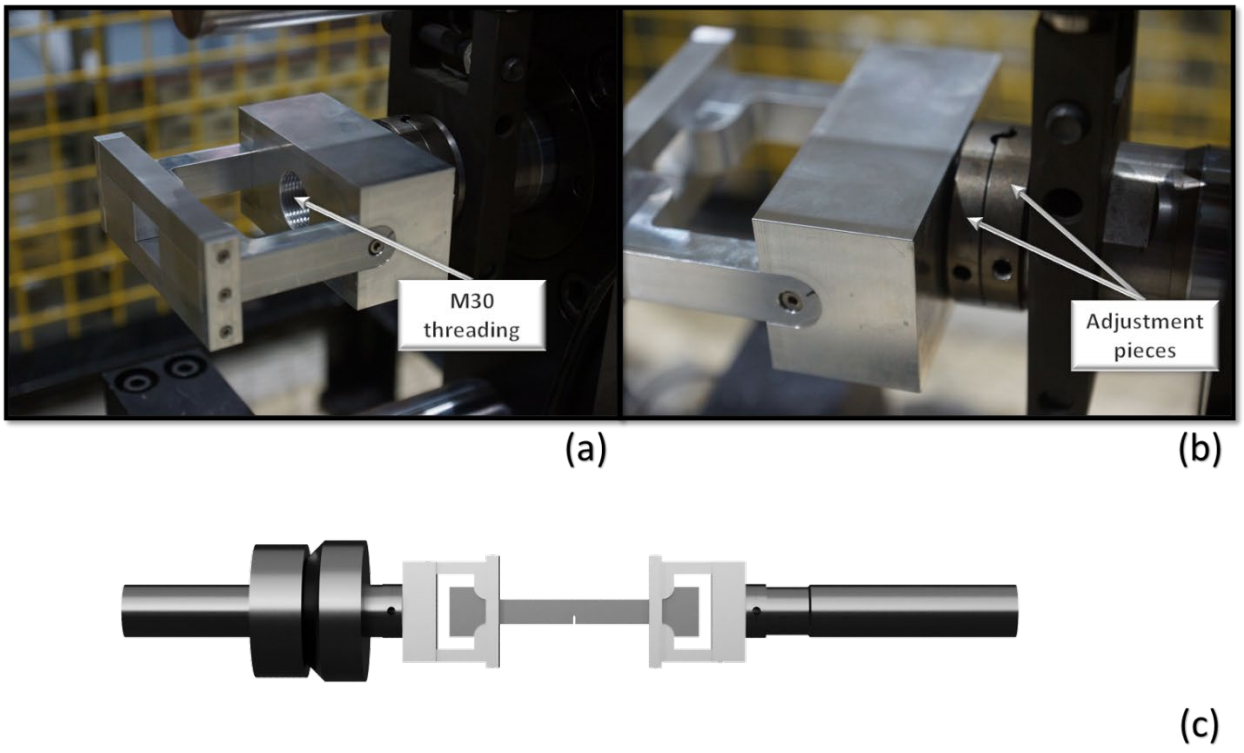


Figure 36: (a) Close-up view of the right jaw, (b) jaw with alignment rings, (c) CAD rendering of the setup for SALSA experiment 1-02-299

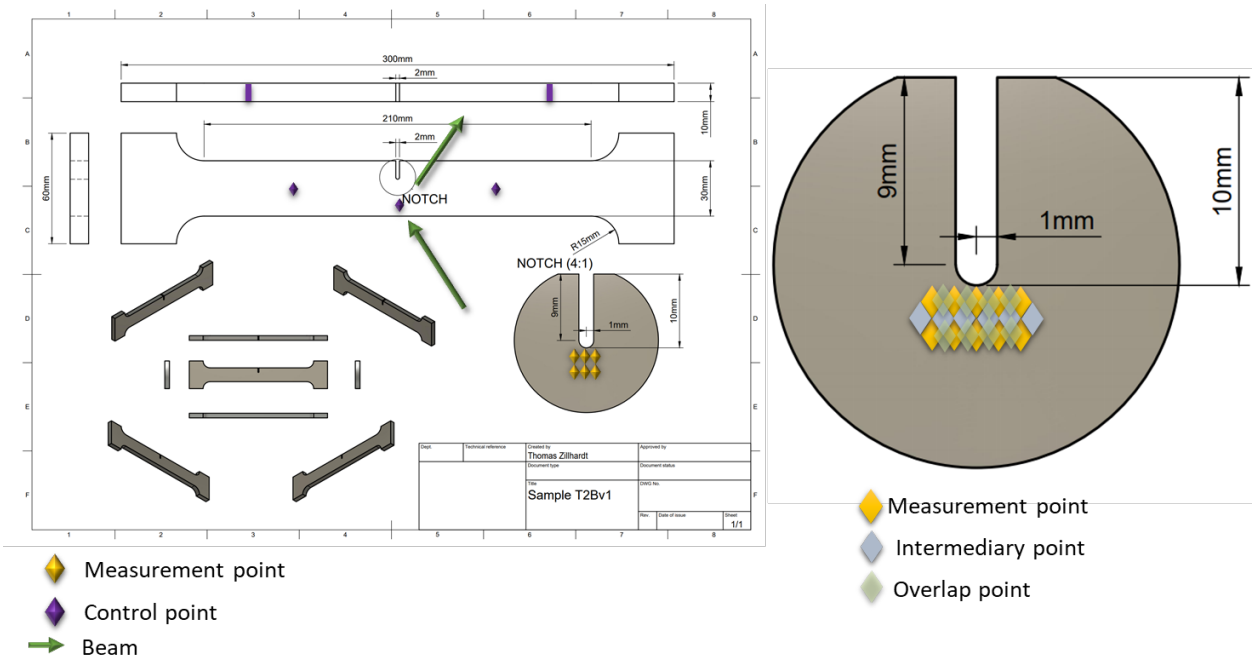


Figure 37: Sample design and position of acquisition points in SALSA experiment 1-02-299

Figure 37 provides the sample dimensions as well as the location of the map below the notch. As the high-resolution 6 mm horizontal collimators were used, the rhombus gauge volume measured 2.16 × 0.62 × 2 mm. Here the speed of acquisition and the large number of points (27) was made possible at high-resolution by sampling over a height of 10 mm. The map is made of an irregular grid composed of two main lines (yellow measurement points) of 10 points each, which are then overlapped by four points each. The intermediary line is shifted, so that all the area below the notch is covered. Two control points are located on the centreline of the specimen at ± 40 mm and a third control point is located directly opposite the notch, at the same distance from the side surface. As the first primary collimator defining the vertical beam length has a 10 mm aperture, the entire specimen thickness fits in the gauge volume.

2.9 Time series high-resolution synchrotron pink beam tomography: SOLEIL

2.9.1 Preamble

The Soleil Synchrotron is France's national synchrotron radiation facility located on the CEA site of Saint-Aubin Paris-Saclay, south-west of Paris. Soleil is a third-generation synchrotron with a 354 m storage ring and electron energy of 2.75 GeV. It operates 29 beamlines for engineering, biosciences and condensed matter physics. The PSICHÉ (Pression Structure Imagerie par Contraste à Haute Énergie) uses an in-vacuum multi-pole wiggler source, offering an X-ray energy range between 15 and 100 keV. It is one of the very few beamlines in the world to offer in operando high-speed and high-resolution continuous time-resolved tomography.

Microcrack initiation, propagation, and coalescence away from a stress concentration (such as a notch) has not yet been observed in the graphite 3D microstructure. Because graphite is quasi-brittle, its plastic transition before failure is relatively short. Furthermore, there is a range of uncertainties in graphite's failure strength for a given specimen, and commonly brittle fracture occurs before any 3D microstructural information can be observed. In this experiment, different high-speed and high-resolution time-resolved tomography methods are used with a filtered white X-ray beam to observe for the first time subcritical microcrack development and critical brittle fracture. The experimental number is 20190926 [129].

2.9.2 Experimental setup

Figure 38 provides detailed views within Optical Hutch 1, where the experiment was conducted. The experimental stage positioned just after the optics and filters benefits from an extremely bright flux as it is closest possible from the wiggler source. The beam-stop is located before the sample and just after the monochromator, and it is

used to avoid damaging the sample and the optics when no acquisition is made. The double silicon crystal monochromator was moved out of the beam as fast acquisition requires a short exposure time and hence a bright X-ray flux.

The high-speed camera is pictured in Figure 38(d) and its details are presented in Table 7. The PCO Dimax HS4 employs a CMOS sensor with a 12-bit dynamic range and it is capable of 7,039 frames per second (fps) at a factor-2 binned 1 megapixel (MPix) resolution and 2,277 fps at full 4 MPix resolution (2,000 × 2,000 pixels). This allows in theory for tomographies of 1,000 projections to be acquired in less than a second. The limit is set by the maximum rotational speed of the tomography stage and the maximum exposure achievable, which led to tomography acquisition times of 1-2 seconds. The system's bottleneck is the on-board memory of 36 GB which only allows for about 6,000 projections at full-resolution and up to 24,000 projections with a factor-2 binning. Different methods have been investigated to account for the benefits and limitations of the experimental setup.

Table 7: Camera specifications

Model	**Dimax HS4**
Manufacturer	PCO
Sensor type	CMOS
Sensor array size	2000×2000
Sensor pixel size	11.0 µm
Max. frame rate[(a)]	2277 fps[(c)]
Exposure time per frame	1 µs to 40 ms
Frame buffer size	36 GB[(e)]
ADC bit depth	12-bit
Max. SNR	1600
Peak quantum efficiency	47 %

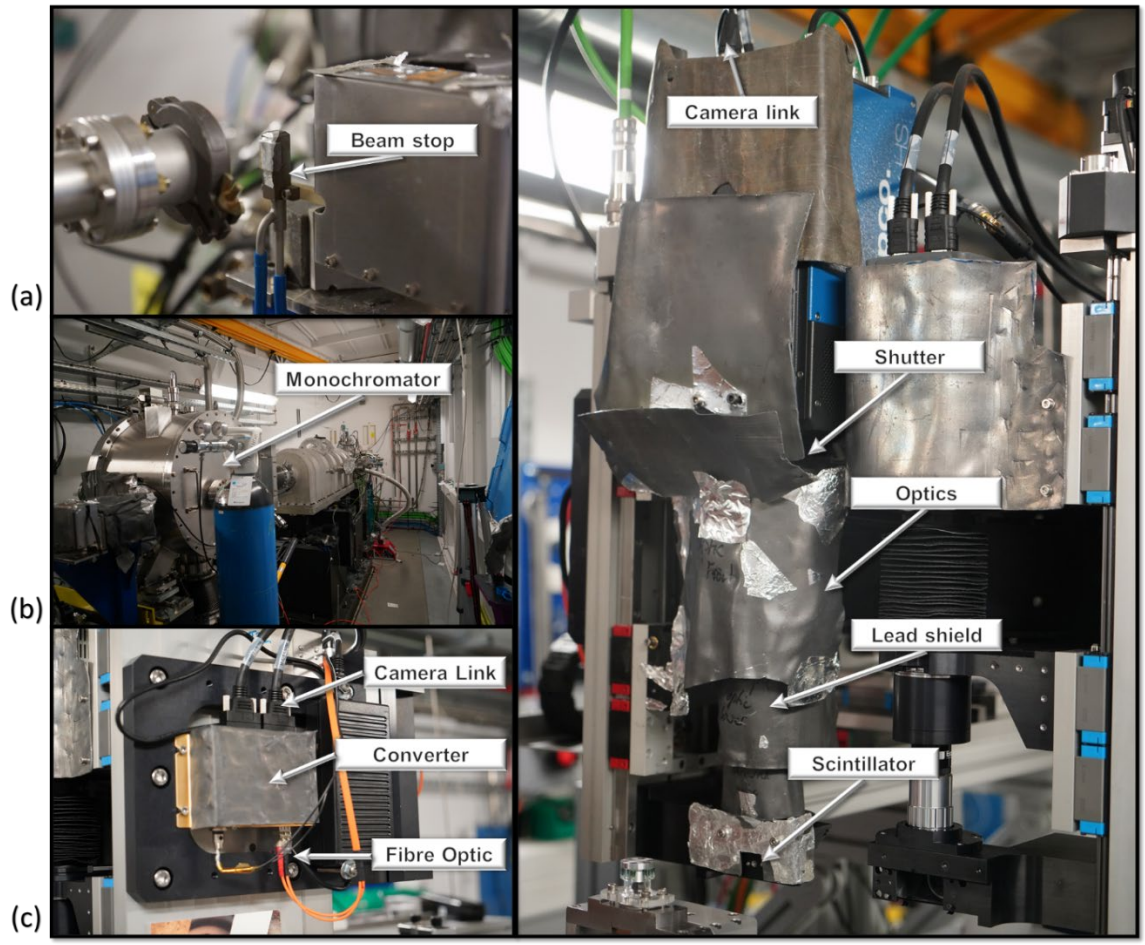


Figure 38: (a) Beam stop, (b) optics and monochromator, (c) data converter, (d) detector setup for SOLEIL PSICHE experiment 20190926

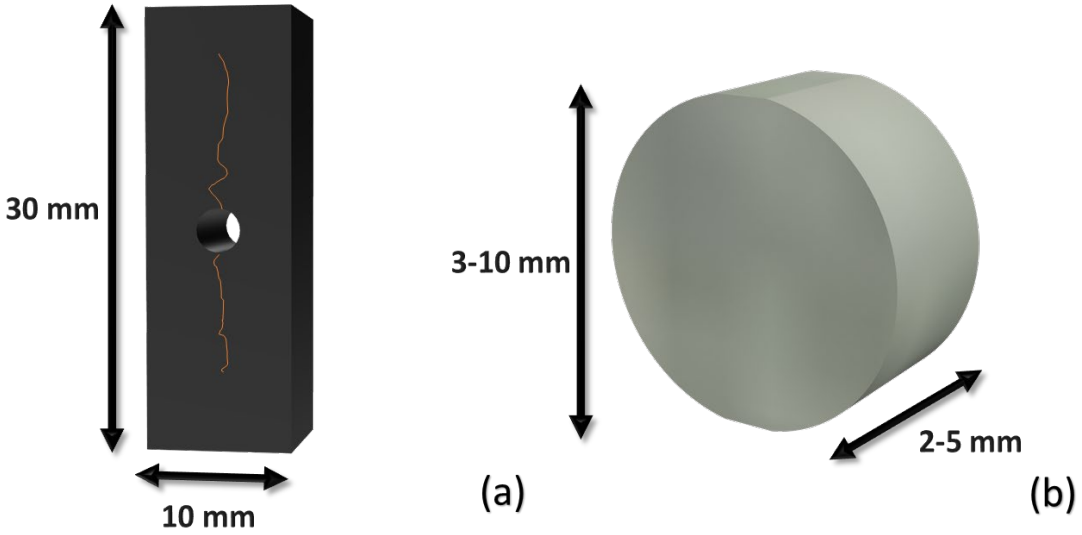


Figure 39: DC sample (a) and Brazilian disc sample (b) for SOLEIL PSICHE experiment 20190926

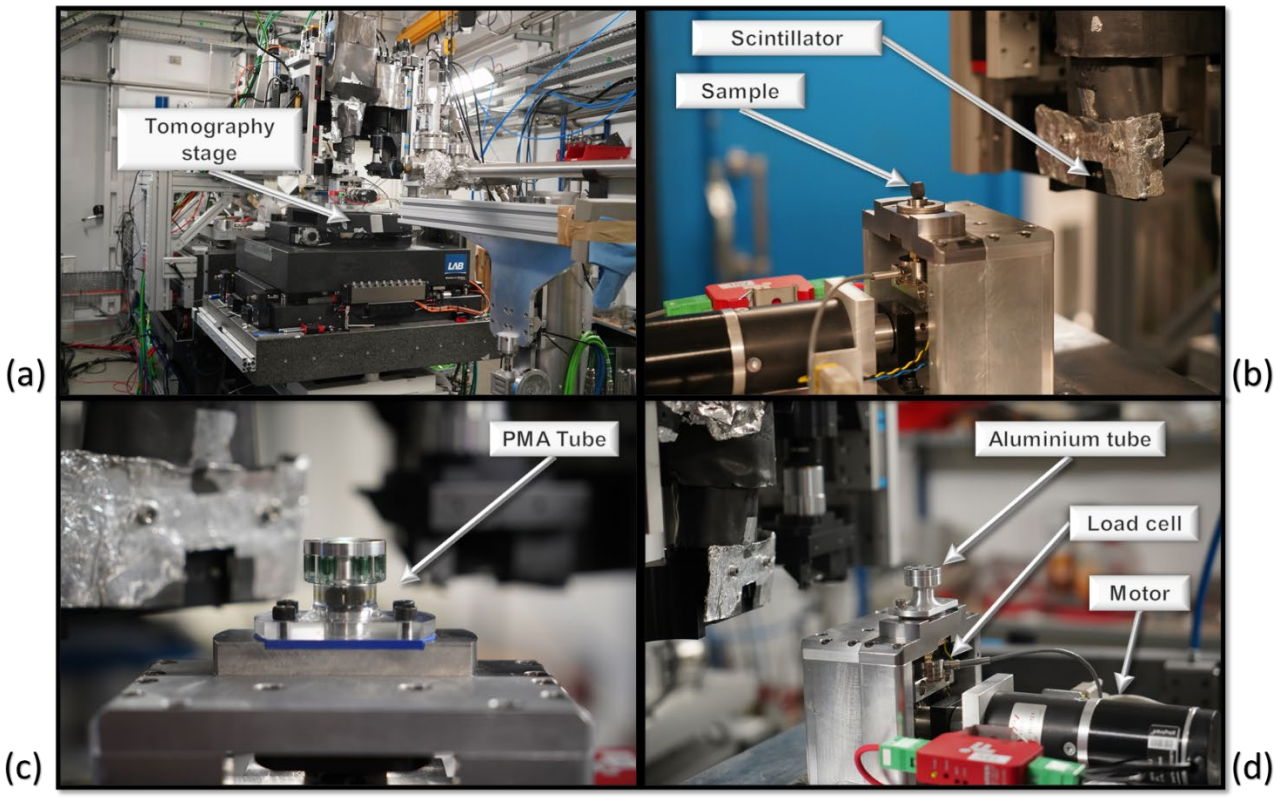


Figure 40: (a) Tomography stage, (b) sample stage, (c) PMA tube and (d) Aluminium tube for SOLEIL PSICHE experiment 20190926

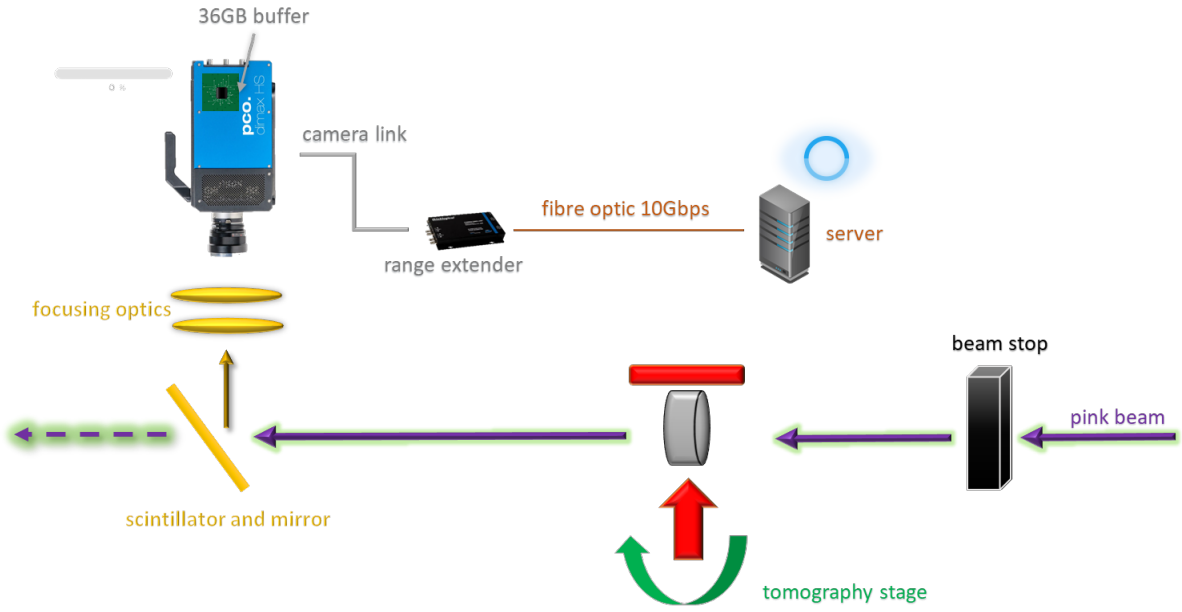


Figure 41: Diagram of the experimental setup for SOLEIL PSICHE experiment 20190926

The samples used were flattened Brazilian discs of varying sizes, to investigate sub-critical microcracking away from stress concentrators, and Drilled-Compression (DC) samples for the observation of subcritical macrocrack initiation and growth; they are presented in Figure 39. Figure 40 and Figure 41 present the experimental stage and setup. The loading rig on loan from Mines Paristech is made of an electric motor driving a piston into a small PMA or aluminium tube. A load cell is placed directly between the piston and the driving screw.

2.9.2.1 Stepwise tomography acquisition

This configuration is akin to lab-based in-situ tomography, and the faster tomography was used to acquire more steps and at smaller load increments. Each tomography was captured at full resolution once a stable load had been reached and offloaded immediately to the servers before another loading step or tomography was initiated. This leads to actual tomography acquisitions of approximately 36 seconds after factoring the data transfer. This configuration was used for the DC specimen loading. Three to five tomographies were taken at each load step along the crack path, on either or both sides of the centre hole. An overlap of approximately 200 voxels along the overlap direction allows for subsequent tomography stitching.

2.9.2.2 Sequential Synchronous Continuous Tomography

In addition to observing microcracking in the graphite microstructure, the objective was also to be able to track its development from initiation to merging with other microstructural features. This objective and the risk of brittle fracture required the use of Sequential Synchronous Continuous Tomography (SSCT). The beam-stop, camera trigger and loading rig are synchronised by a python code with inputs start load, end load and sampling rate. The camera acquires projections as the stress on the sample is increased and until its buffer memory is filled, which will trigger the end of the

sequence. As the speed of acquisition remains fast compared to the microstructure movement and deformation, artefacts in the reconstructed tomographies were negligeable.

2.9.2.3 Time-resolved Trigger-based Acquisition

Past 90% of the failure, the uncertainty of brittle fracture overweighs the advantages of the aforementioned acquisition methods, especially when looking at identifying which microcrack may extend to a critical crack. The control software of the camera was set in a ring-buffer acquisition mode, where projections are acquired until the onboard memory is full, after which point earlier projections are overwritten by latest acquired images. As a result, the latest 6,000 to 24,000 projections are in memory at any given time until the trigger is activated.

2.10 Total Neutron Scattering: GEM

2.10.1 Preamble

The General Materials Diffractometer (GEM) instrument at the STFC-ISIS neutron and muon spallation source is located on Target Station 1 and contains in excess of 7,270 elements for powder diffraction texture analysis. Although experiment RB1810071 was granted for the study of cast alpha-uranium, some remaining beamtime was used to acquire diffraction data on two samples of Gilsocarbon graphite [160].

2.10.2 Experimental Setup

Figure 42 presents the instrument and experimental setup. Gilsocarbon graphite 10 × 4 mm cylinders were glued to the sample holder after being aligned with a laser pointer. The sample holder can translate along the vertical axis and also acts as lid when inserted in the experimental hutch. The beam size was 4 × 4 mm and the sample

was not tilted with regards to the beam direction. The air was vented from the chamber as the experiment was carried out in vacuum.



Figure 42: Experimental setup of the GEM instrument, with (a) the sample holder, positioner and lid, (b) a close-up view of the sample, and (c) the instrument hutch.

Chapter 3

3 EVALUATION OF DAMAGE DISTRIBUTION IN GILSOCARBON GRAPHITE

3.1 PREAMBLE 3:2

3.2 IN-SITU BULK MEASUREMENT OF ELASTIC AND TOTAL STRAINS (JEEP I12) 3:3

3.2.1 Iterative Tomography Reconstruction 3:3

3.2.2 Local Digital Volume Correlation of Tomographies 3:6

3.2.3 Quantification of Tensile Strains with SXRDM 3:9

3.3 ULTRA-HIGH RESOLUTION DIGITAL VOLUME CORRELATION AND ELASTIC STRAIN MAPPING 3:13

3.3.1 Tomography Processing 3:13

3.3.1.1 Reconstruction and Pre-processing 3:13

3.3.1.2 Vertical and Horizontal Stitching 3:14

3.3.2 Multi-Domain Global Digital Volume Correlation of Very Large Datasets 3:18

3.3.3 High-Resolution X-ray Diffraction Mapping 3:19

3.4 RESULTS: COMPARISON OF TOTAL AND ELASTIC STRAINS IN THE BULK 3:22

3.4.1 Quantification of Global Deformation 3:22

3.4.2 Distribution of Large Elastic Strains 3:24

3.5 RESULTS: STRAIN EVALUATION AT HIGH RESOLUTION 3:25

3.5.1 Total Strains from Multi-domain DVC of Stitched Tomographies 3:25

3.5.2 Elastic Deformation at High Resolution 3:27

3.6 DISCUSSION: MULTI-SCALE DAMAGE EVALUATION AND THE ROLE OF MICROSTRUCTURE 3:29

3.1 Preamble

The diversity of defects and features in polygranular graphite makes it crucially important to understand how stress and damage is accommodated in the microstructure. This requires a multiscale approach, whether direct or indirect, as the feature size can range between 1 mm for the largest Gilsonite particles to a few nanometres for the smallest interplanar Mrozowski crack. Although microcracking has been attributed to cause the saturation of tensile stresses [45, 73], it has not yet been observed in the microstructure and in sample geometries with engineered stress concentrations. Graphite manufacture, as presented in 1.2.2, presents similarities across all grades, however specific differences such as the forming process or the type of filler increases the need to evaluate how the microstructure deforms to accommodate tensile, compressive and shear stresses.

Synchrotron X-Ray Diffraction Mapping (SXRDM) is a two-dimensional technique that uses the valuable quantification of elastic strains across a 2-D regular grid, providing information on the variation of these strains across the sample. This technique is only helpful for samples with symmetric or 2D-averaging geometries such as dog-bones or discs. Combined with the total strains obtained with Digital Image or Volume Correlation (DIC/DVC) from grayscale images or tomographies, it can provide information on where plastic and non-recoverable deformation occurs in the sample. Due to the configuration of the synchrotron beamlines, tomography-DVC is usually preferred to compute total strains.

This chapter looks at the variation of strains across flattened discs specimens and tries to identify the relationship between the different elements of the microstructure. It presents the results from an experiment carried out in 2016 at the Diamond Light Source JEEP-I12 beamline whose data has been processed and published in 2019

[73], and that from a similar experiment with a smaller specimen on ID11 at the European Synchrotron Radiation Facility [126].

3.2 In-situ Bulk Measurement of Elastic and Total Strains (JEEP i12)

3.2.1 Iterative Tomography Reconstruction

As mentioned in section 2, tomography relies on a number of angular views or radiographies to be able to reconstruct the 3D volume. The initial and fastest reconstruction method used at synchrotrons and on JEEP-I12 is the fast re-gridding algorithm [161]. It is a highly CPU optimised code based on the Fourier Transform Method (FTM), by convoluting the data in the Fourier domain. This decreases the reliance on high-performance GPU enabled systems, offering the highest throughput of all available algorithms while maintaining a high accuracy, at the expense of a dependence on very-well sampled datasets. This algorithm is particularly efficient for fast, continuous tomography, but not adapted to datasets with missing angular views, due to the requirement of interpolation in the 2D Fourier domain. The standard method of reconstruction, and the baseline for medical imaging, is the Filtered Back Projection (FBP). The attenuation profile is back-projected across the image space and repeated at each angle, after having applied a spatial frequency filter to the attenuation profiles. Because the FBP method assumes that the sinogram is a perfect representation of the sample [162] and requires as many angular views as possible for the back-projection, it presents limitations for low-dose and limited-angle tomography.

Recent improvements in the availability of processing power and the interest in low-dose fast tomography has led to a renewed incentive to develop and use iterative reconstruction algorithms, which are more computationally intensive due to their requirement of convergence. Whilst ESRF has developed the python and UNIX based

pyHST2 reconstruction code [163], Diamond Light Source has implemented the SAVU program based on the Astra Toolbox [164]. In this revision of the tomography reconstruction, direct use was made of Astra together with the advanced ring and artefact removal code Sarepy [165]. The toolbox has three iterative reconstruction algorithms: the Simultaneous Iterative Reconstruction Technique (SIRT), the Simultaneous Algebraic Reconstruction Technique (SART) and the Conjugate Gradient Least Squares (CGLS) algorithm. Although pyHST2 offers regularisation capabilities to the optimisation problem such as with the Total Variation (TV) or Dictionary Learning (DL) algorithms, the Astra toolbox is sufficient for this case as long as the convergence is carefully determined. This is due to the fact that noise may be overrepresented if the number of iterations has passed the convergence.

In the JEEP-i12 experiment, the Shimadzu loading rig has two pillars supporting the frame which are close to the sample stage. This required the tomography to be taken from -73.1° to +73.1, as the metal frame was opaque to X-rays. After determining the optimal number of iterations and comparing the FBP, SIRT, SART and CGLS algorithms qualitatively and quantitatively through Digital Volume Correlation, all the datasets were reconstructed with CGLS and 50 iterations. Figure 43 presents a qualitative comparison of the higher signal to noise ratio with the CGLS reconstruction, which is clearly visible on the zoomed image of a filler particle[6]. It is also possible to appreciate how the distribution of grey values is more uniform. Pores in the gridrec reconstruction appear dark at the edges, and lighter in the middle, which is an issue both with simple segmentation (such as thresholding or top-hat), and for DVC, as these areas do not represent the microstructure. On the other hand, pores

[6] No other form of pre-processing has been applied

reconstructed with the CGLS method appear dark with a close to 0 value on an unsigned 16-bit scale[7].

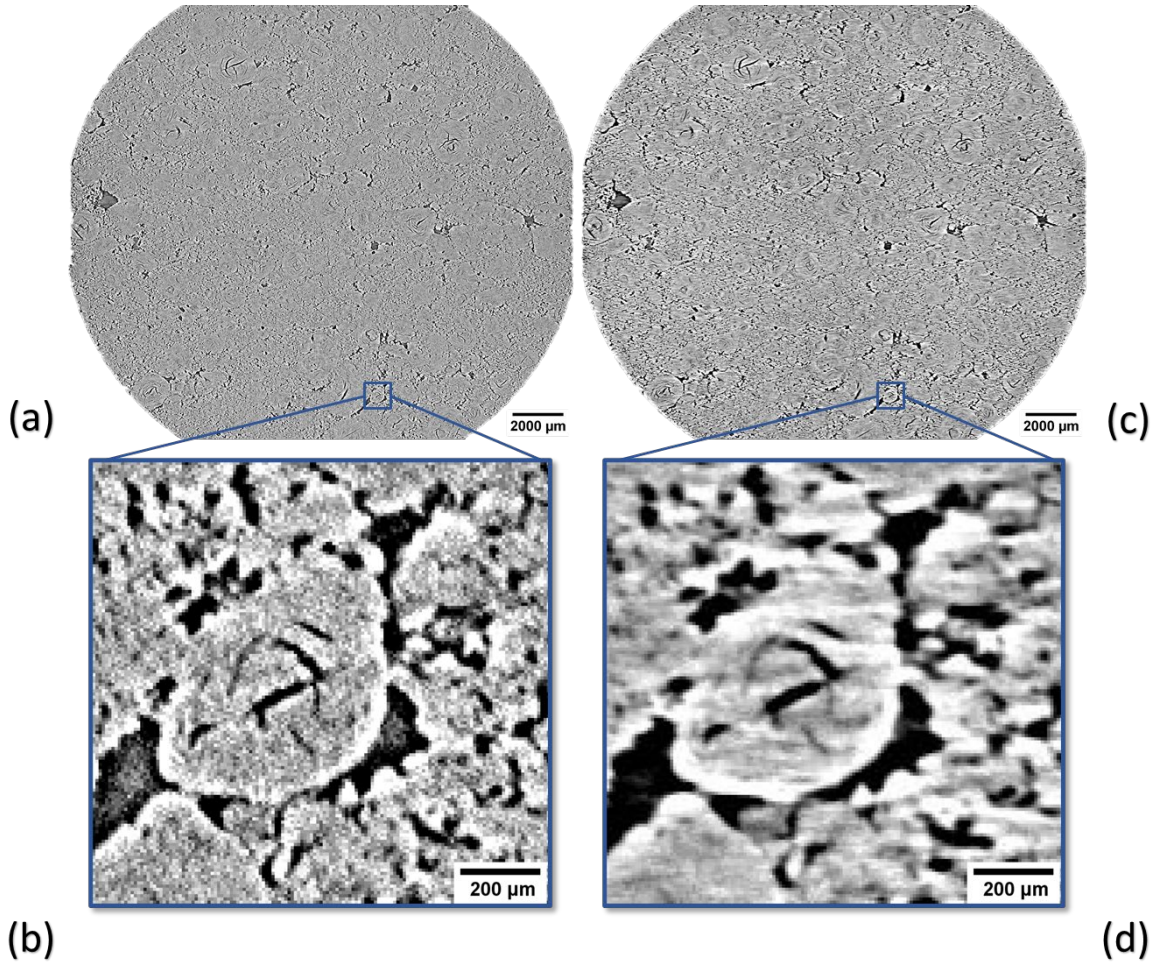


Figure 43: Standard gridrec tomography reconstruction (a) and magnification (b), compared with iterative CGLS reconstruction (c) and magnification (d); no filtering applied

[7] 16-bit unsigned is from 0 (darker) to 65,535 (lighter) and is the bit range used in tomography throughout this thesis unless otherwise specified.

3.2.2 Local Digital Volume Correlation of Tomographies

Digital Volume Correlation (DVC) analysis on the reconstructed tomography of the JEEP-I12 experiment scans was performed using LaVision DaVis software (Version 8.4.0). Each of the scans at higher load was compared with the pre-load (11 N) dataset. The datasets were cropped in ImageJ beforehand in order to remove most of the rigid body translation along the loading Z-axis. Contrast was adjusted and matched over the volumes to obtain the best possible grayscale range in 16-bit unsigned and the datasets were saved in 3D RAW(W) format, little endian order[8]. There is no published research comparing the precision and accuracy of 8-bit (0 to 255) and 16-bit DVC, however it is widely understood that the latter is preferable for the local correlation approach as it offers a much wider range of values for the correlation[9]. It is also best for the DaVis program, due to the conversion to 32-bit floating point before the correlation process in this algorithm, and it being more efficient from 16-bit, as well as for algorithmic masking[10], as a conversion from 16 to 8-bit will give the value 0 to all pixels from 0 to 256 and in turn induce masking noise.

There is an important but mostly unreported consensus by tomography correlation experts that reconstruction quality is essential and should be sufficient so that no further filtering needs to be applied. A number of studies [111, 112] have mentioned the use of Gaussian or median (3D or worst, slice by slice) filters before correlation. Even though filtering may reduce the statistical image noise, it also ‘blurs out’ features

[8] Little endian (as opposed to big endian) is a data addressing mechanism for data storage by which the least significant value is stored first. Although big endian is often used across everyday computing, little endian is most efficient for large datasets (and especially 16-bit tomographies) as the operations are faster to perform.

[9] This has also been informally compared for this project, and most DVC analysis here use 16-bit datasets.

[10] Algorithmic masking is done by masking pixels below or above specific values (outside a specified range). Smoothing can be applied to avoid single-masked pixels which most likely represent masking noise.

and there is currently no 3D deep learning technique, so that filters will always work over the same range (3 to 9 voxels for instance), irrespective of the location. In this study, the work has instead revolved around reducing noise by employing more appropriate reconstruction techniques, as well as using projection-based density filters (pre-reconstruction). Paganin filtering, essentially a low-pass Fourier filter, has been used, as it is preferable to post-filtering, especially for the phase retrieval process.

A Fast Fourier Transform (FFT) correlation with a large cubic subset (224 × 224 × 224 voxel dimension) at 50% overlap was used to determine the rigid body motion and large deformations in the tomography volumes. As most of the sample in the JEEP-I12 experiment was in the field of view, it was decided to maintain as much of this volume in the correlation as possible and this required the use of two different masking techniques. An algorithmic mask was applied to remove all voxels with an intensity equal to or below that of the air surrounding the sample and the '0' value of the unreconstructed region. This also smoothed the contrast changes within pores, and particularly the 'upper valley' effect, a peak in the middle of the pore due to lower attenuation, but excluded in the mask the edges of the pore which are the most essential for correlation; for pores where the new reconstruction was not sufficient. A 2D circular geometric mask was applied in the XZ-plane to exclude the edges of the specimen which can lead to correlation 'smearing'.

After the initial coarse FFT correlation, a series of four Direct Correlations (DC) with decreasing peak search radius[11] were performed, from 16 voxels at 4 × 4 × 4 binning down to 2 voxels with no binning. This was selected based on the estimated maximum displacement after registration and the average size of the microstructure. Passes

[11] Peak search is the maximum distance by which the subset is displaced to find a matching pattern. A low value may lead to no correlation and a higher value increases the computation time significantly.

were increased from 1 to 4 so that the latest level is most precise. The larger first pass used cubical sub volumes and the following three steps employed Gaussian weighted spheres. The spheres are about twice the size of the defined subvolume, however the weighting implies that the spatial resolution is preserved and this improves the accuracy of the vector field due to the fact that voxels near the centre will have more weight than those further away. The last step has a subset size of 88 × 88 × 88 voxels at 75% overlap and as such the calculated displacement vectors were mapped on a 3D spatial grid of approximatively 348 × 348 × 348 μm. Note that although overlap increases the spatial resolution at no computational cost, which in effect helps 'smooth' the result, it does not change the actual displacement accuracy.

The rigid body movements of the specimen between the datasets were determined relative to the centre of mass in the DVC and they were found to be relatively small compared to the dimensions of the 1 × 1 mm^2 collimated X-ray diffraction beam. For instance, the downwards rigid body translation along the z-axis (compression) of applied load was less than 100 μm each load step, with a total movement of 370 μm at 5800 N. The displacements in the horizontal XY-plane are more important, as they will inform on how much of the sample has remained in the Field of View (FoV) and is usable for correlation. The horizontal movement in the *x-axis* perpendicular to the X-ray beam was less than ±15 μm each step, with zero net displacement overall and the horizontal rigid translation along the *y-axis* parallel to the X-ray beam was less than 3 μm per step, except for the final step at 5800 N where a displacement of 42 μm was observed. However, this final step was not included in the study, due to lacking a corresponding strain map. The Rigid Body Rotations (RBR) were separated from the vector field deformation by polar decomposition, and they were all less than 0.3° (all axes considered). Rigid Body Displacements (RBD) were removed from the final 3D

displacement fields, which had a displacement measurement precision estimated to be 0.065 μm. The 3D strain field was then computed from the gradients of the displacement field, with a precision of 264 με or 0.03% strain estimated from the displacement precision according to the final DVC subset size.

3.2.3 Quantification of Tensile Strains with SXRDM

The large 2D Thales Pixium detector was installed in Experimental Hutch 2 (EH2) of JEEP-I12 so that most of the 002 Debye-Scherrer ring of the basal plane of graphite was recorded. This is pictured in Figure 44, which shows the sharpness of the 002 ring on the line profile, due to the detector exposure time and the fine tuning of the beam wavelength. This leads to a very good peak-fitting for that particular peak as there is little background noise, however it also implies that the signal of all other peaks is weaker. Furthermore, the 002 ring is the only one fully in the Field of View from which radial horizontal and vertical strains can be computed, however the latter cannot be averaged over the lower 70-100° angular range as the ring is cut off. Transversal strains (along the y-axis) are of little interest for this study, and it is estimated that the elastic and total strain gradient along this direction is negligible.

The XRD maps were processed individually point-by-point using an early version of the DIFFRACTX code. It employs a cross-correlation based method which improves strain measurement precision in graphite compared with the conventional strain computation from double peak-fitting. Usually, for a single point location both diffractograms of the reference and deformed volumes are fitted to obtain the scattering angle and compute the strain.

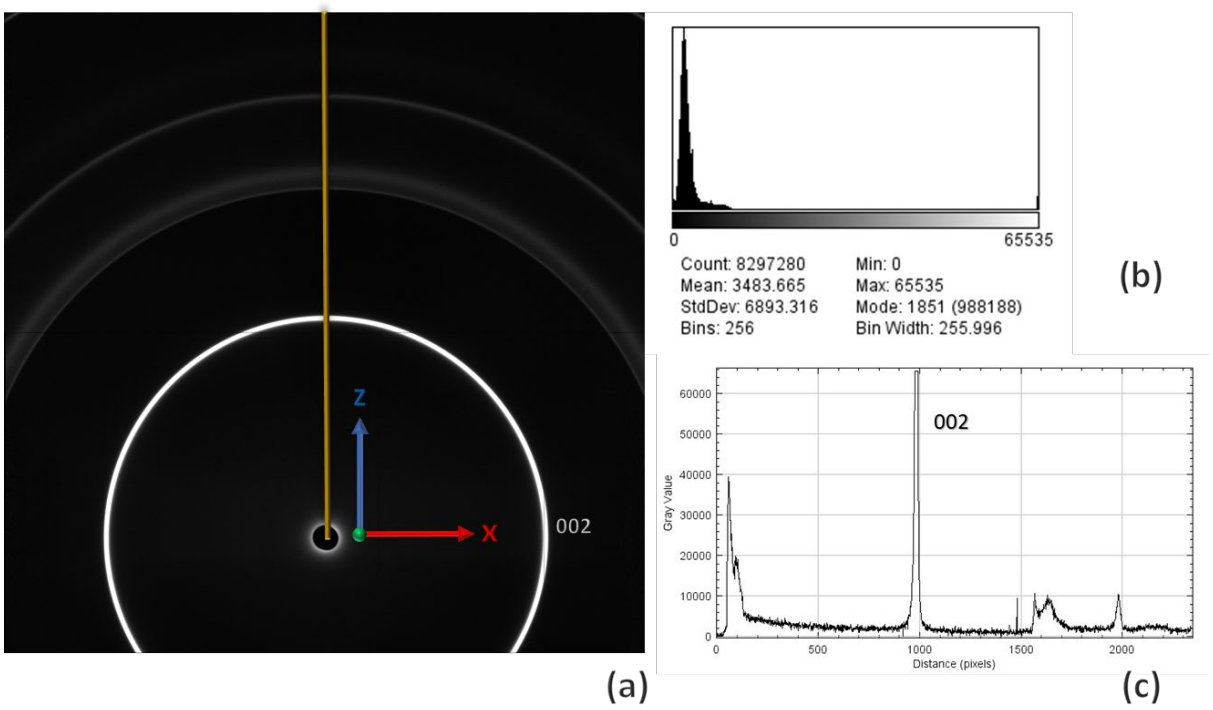


Figure 44: Raw XRDM diffraction point acquisition (a), and its rescaled histogram (b), and a radial line profile (c) represented by a yellow bar on (a)

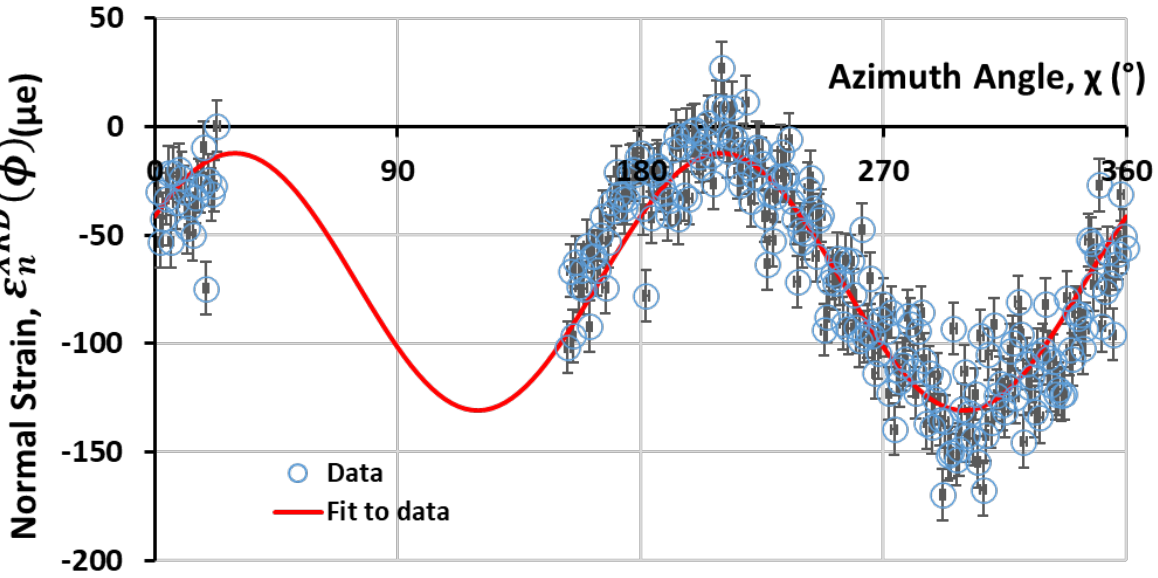


Figure 45: Example of strain sinusoidal fit for map point number 100 at load step 4.5 kN [73]

In a first step of the data processing (INTEGRX code[12]), an ellipse was fitted to the partial (0002) Debye ring to identify its centre. Flat and dark field corrections were applied before radial (2θ) integration (straightening of the rings). The intensity and position data were then binned into 1° azimuth sectors (χ) to obtain a set of 360 intensity profiles generated by azimuthal integration between $\chi = 0°$ and $\chi = 360°$. Each diffractogram obtained was then saved as Matlab datafiles with 360 diffractograms for each point file.

In the next step of this process (COREX), the diffractograms were loaded one by one in the memory and the diffractograms of the reference were fitted in a parallel loop with around 18 worker-cores (previous iteration of DIFFRACTX). An upgraded version of the cross-correlation routine applied for XRD mapping, first developed by Buck et al for Matlab r2005 [166, 167], and first adapted for diffractogram signals in XCORR [45], determined the signal shift with regards to the load-free reference (i.e. 11 N pre-load). This shift was added to the fit of the reference to obtain a more accurate peak position, without however any other information such as peak FWHM, height or prominence. This also offered faster processing as peak fitting is the most time-consuming step.

The peak positions were first obtained as a function of bin (the number of points in the radial direction) for each of the 360 azimuthal bins. This was converted first to angle using a linear interpolation of the corresponding radial integration range, and then in d-spacing using Bragg's law, from which strains were computed for each bin between the deformed and reference stages. A least-squares fit of Mohr's circle to the azimuthal

[12] This integration code was written and used for the JEEP-i12 data only and not for the ESRF-ID11 data where pyFAI was used instead (pyFAI is written by the ESRF computation group)

variation of normal strain $\varepsilon_n^{XRD}(\chi)$ (Figure 45) using equation (8) was used to extract each of the strain components ε_{xx}^{XRD}, ε_{zz}^{XRD} and ε_{xz}^{XRD} :

$$\varepsilon_n^{XRD}(\chi) = \frac{\varepsilon_{xx}^{XRD} + \varepsilon_{zz}^{XRD}}{2} + \frac{\varepsilon_{xx}^{XRD} - \varepsilon_{zz}^{XRD}}{2}\cos 2\chi + \varepsilon_{xz}^{XRD}\sin 2\chi \quad (4)$$

where χ is the azimuth, Z is the axis of the compressive strains and X is the axis of the tensile strains.

One may note the potential reading of deviations between the points and the fit of Figure 45, and more particularly at the points of inflection and at 180°. Due to the number of azimuthal angles for each of which a Voigt (variable alphas) fit with an average 6% error is combined with a signal cross-correlation, the potential fitting error introduced by the Mohr analysis must be read together with the accuracy of the strain calculation. For the point extracted in Figure 45, the RMSE returned by the GOF is 4×10^{-4}. Further, this method for extracting the strain components reduces the global error as it encompasses the strain results at many binning angles, and the original cross-correlation method has already demonstrated a strain error below 12 με [45]. The relative elastic anisotropy of the graphite crystal may indicate an incompatibility with the Mohr circle analysis. It is nonetheless essential to note that in this study we are comparing XRD and DVC strains in a material with a complex crystallography and in a biaxial stress state, with many grains in the diffraction volume and individual crystals bending and contributing to more than one direction. This high degree of deformation and orientation combined with a disc geometry is considered sufficient to validate the applicability of Mohr's circle in this particular case, where elastic strain results can be compared to previous studies which have used different methods.

3.3 Ultra-High Resolution Digital Volume Correlation and Elastic Strain Mapping

3.3.1 Tomography Processing

3.3.1.1 Reconstruction and Pre-processing

At about 24 Giga Pixel (Gpix), and a sub-micron pixel size of 750 nm/voxel, the datasets acquired in the ESRF-ID11 High-Resolution Phase Contrast disc compression experiment are by far the highest 3D resolution ever obtained for an in-situ experiment of nuclear graphite, all grades included (see section 2.6.3 for experimental details). This was made possible using high-resolution optics and vertical/horizontal volume overlapping (four regions in this case). This poses a number of challenges and in particular relating to the size of the datasets and the average size of the microstructure compared with the Field of View. Furthermore, the interesting aspect of this experiment is to be able to compare total strains from the DVC and elastic strains from the XRD mapping, which required appropriate methodology. An option would have been to process all four tiles of the stitch individually, correlating with regards to the reference using the local approach in DaVis for instance. As however the XRD map includes the four regions of interest, it was decided instead to homogenize and stitch the volumes together before correlation. Although stitching can introduce discontinuities, it can be done with a sufficient accuracy so that the errors introduced are less than when trying to ‘stitch’ displacement or strain volumes, of which the exact position with regards to each other and the XRD map may not be known.

As presented in Chapter 2.6.3, this experiment used a 61.4 keV pink (filtered white) beam. This allowed for faster speed of acquisition for the Ultra-High-Resolution Tomography and offered sufficient signal for X-ray Diffraction acquisitions with a very

small slit beam-defining aperture of 100 µm. On the other hand, although less problematic than with a white beam, pink beam leads to a number of complications in the datasets, and particularly high background noise which is particularly problematic in the XRD data, and beam hardening and ring artifacts in the tomography. Advanced reconstruction and ring removal methods have therefore been used to obtain the final volumes as presented by the realigned slices in Figure 46. The striped area posed an issue during stitching of the right and left volumes as the usual merging process does not consider 'zero' count as transparent.

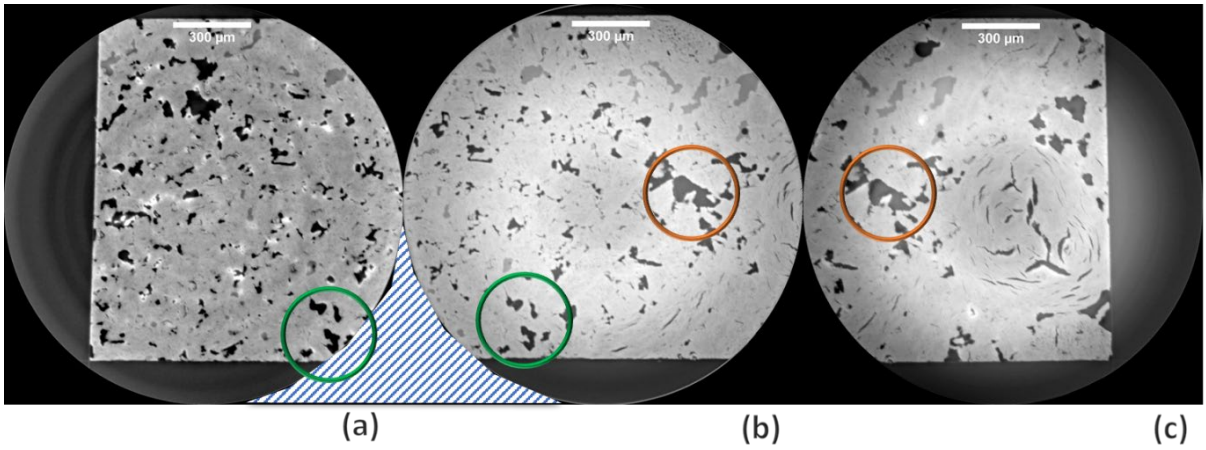


Figure 46: Realigned and pre-processed tomography slices of the left (a), top (b) and right (c) Regions of Interest (RoIs) for stitching with example matching features in image pairs circled

3.3.1.2 Vertical and Horizontal Stitching

Each of the seven load steps consisted in four Regions of Interest (RoI), covering about 80% of the sample volume. Total strains have been obtained for all four parts individually using the local approach and Direct Correlation (DC) in DaVis 8.4, however it proved not efficient to continue the analysis using four different correlation sets. Indeed, the geometric masking required in the local approach uses a 70% minimum inclusion, meaning that at least 70% of the voxels of a subset must be inside the mask

to allow for correlation, and this can change the position and number of correlated subsets from a series to another. As this was also necessary for segmentation and visualisation, the four volumes of each step were stitched together in Avizo 2020.3.1.

The stitching of the top and bottom volumes was straightforward as they had a complete overlap in the Z axis of approximately 300 usable voxels (300 shared 2048 × 2048 full size vertical slices). For these volumes, and after manual alignment using colour washes, the reference subvolume was subsampled by two for the coarsest alignment level, and a correlation algorithm was used to align the datasets with a quasi-Newton optimizer with final step at $1/6^{th}$ of the voxel size. As seen in Figure 46, the left and right volumes overlap with the central ones with a partial semi-cylindrical region. A similar registration method was used, but by choosing smaller sub-volumes within each dimension, without subsampling and using normalised mutual information, which is a more robust metric that minimises a computed entropy to maximise the mutual information between both datasets. In both cases, registration only had the three translation degrees of freedom and hence the volumes were not rotated or scaled. Once all four volumes had been registered, their contrast ranges were adjusted by a 3D matching algorithm (Avizo match contrast module) to that of the top volume, and they were merged altogether with a standard interpolation after a resampling of the volumes to apply the transformation. The results are presented in Figure 47 with views from the three planes. To avoid the dark ‘zero count’ areas around the reconstructions being merged with the other volumes, all four volumes were cropped and merged to a fifth volume by merging the top and bottom region, cropped so that its height is only that of the left and right. This was possible as the left and right volumes had an overlap with the top and bottom of about 400 voxels.

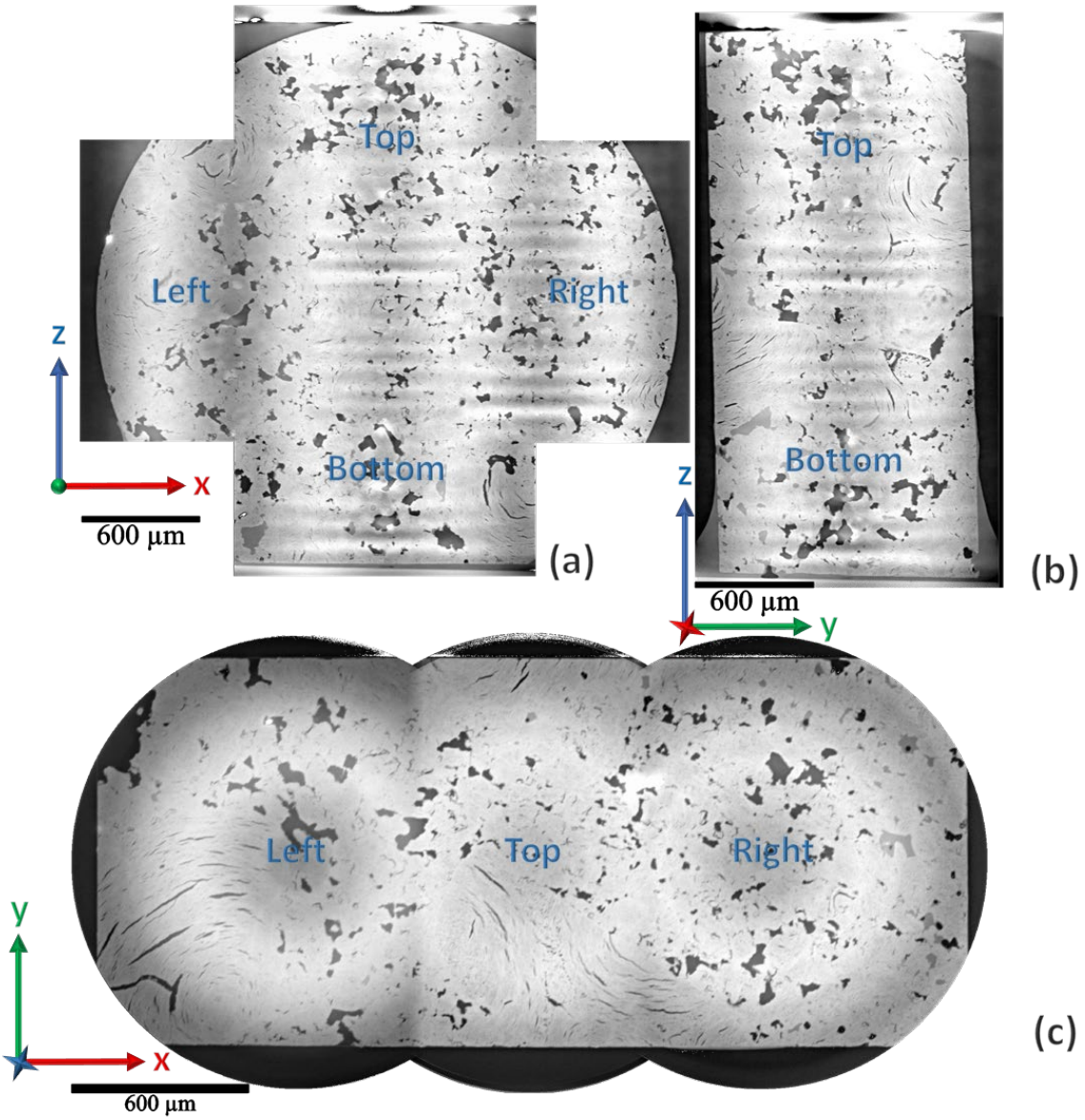


Figure 47: Slices of the final tomography volume after pre-processing and stitching, viewed from the XZ (a), YZ (b) and XY (c) planes

The remaining 'contrast' ring artefacts are from each individual volume due to the attenuation of the pink beam and the quality of the detector and it was not possible to completely correct them. Figure 48 presents an XZ-plane view of a volume rendering of the stitched datasets with an outline of the sample. It allows one to appreciate the importance of efficient stitching techniques to be able to observe features spread in two different volumes such as the large filler particle in the top left corner.

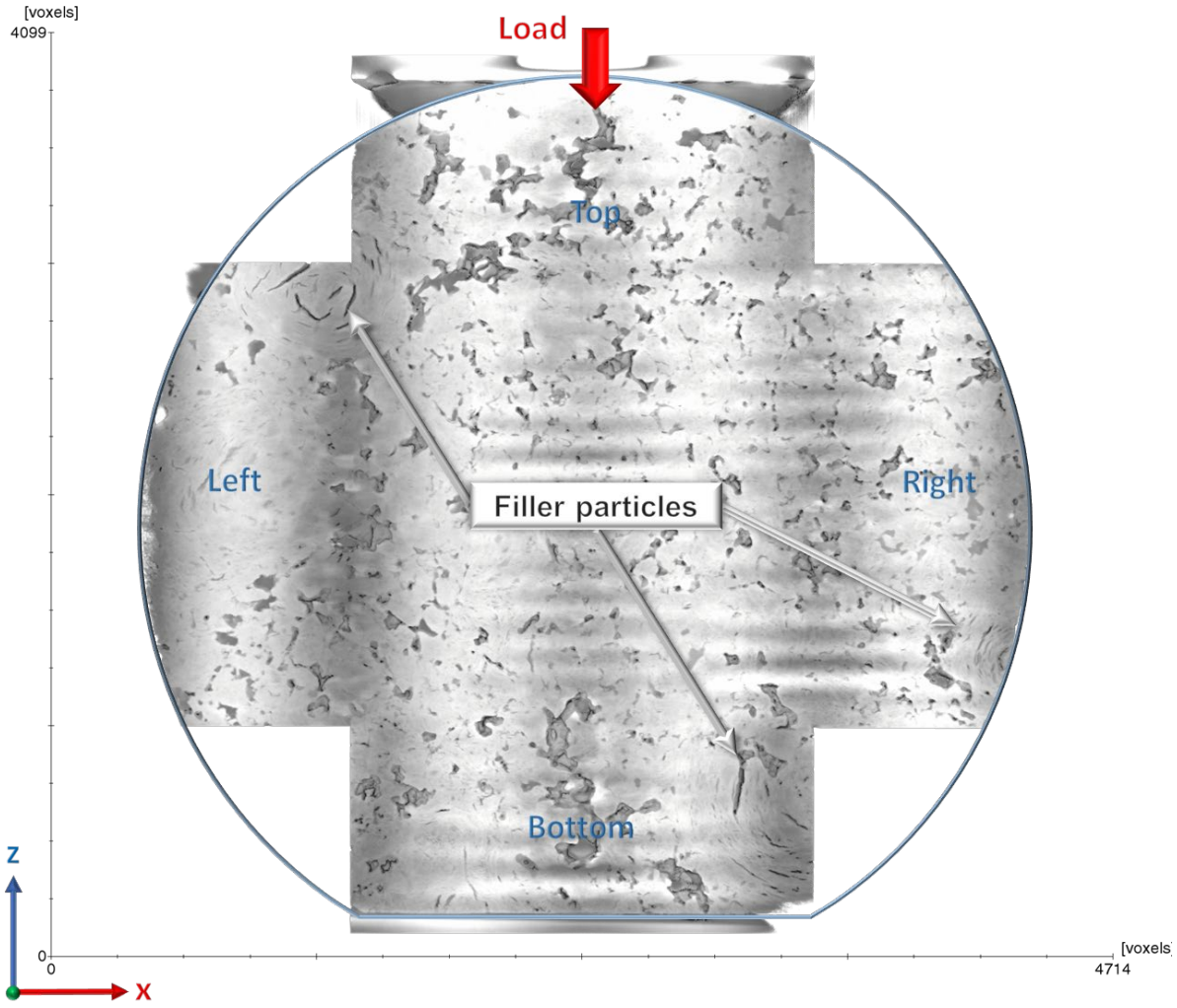


Figure 48: Volume rendering of the final stitched tomography, with an outline of the disc presented

3.3.2 Multi-Domain Global Digital Volume Correlation of Very Large Datasets

The stitched volumes had a total resolution of to $4031 \times 2078 \times 3872$ voxels and a voxel size of 750 nm, with an irregularly cross-shaped zone of interest, which prevents the use of conventional correlation algorithms such as DaVis due to the large volume size (exceeding 512 GB of RAM when correlating) and their limited 2D masking capabilities. Instead, the XDVC extension in Avizo 2020.3.1 was used.

Each dataset was processed in pairs, the reference (1) and one step (2, 3, 4, 5). The failed 6^{th} load stage was not usable for correlation. An initial local approach correlation was used to determine rigid body movements and large deformations between the two volumes. An autocorrelation on the reference indicated that the microstructure converged within 100 voxels, and therefore a subset size of 350 voxels was used for the local correlation. On screen measurements provided information on the largest feature-to-feature distance, and a maximum displacement search of 40 pixels was selected. A tetrahedral grid was extracted from the surface rendering of the graphite label after interactive thresholding segmentation and pore closing, the fit the entire volume available. The final mesh has 5766 nodes, 58015 triangles, 28031 tetrahedrons, and a mean edge length of 167.7 voxels for approximately 31661 cells. This is too many cells and voxels for a single global correlation approach and the grid was divided in three domains in each of the X, Y and Z directions, resulting in 27 different domains as presented in Figure 49. Multi-domain correlation computes the displacements for each domain separately and merges them together by interpolating the results at the nodes. It was performed with a final maximum displacement increment of 0.01 and a maximum of 200 iterations, however almost all correlations have converged with 70-150 iterations.

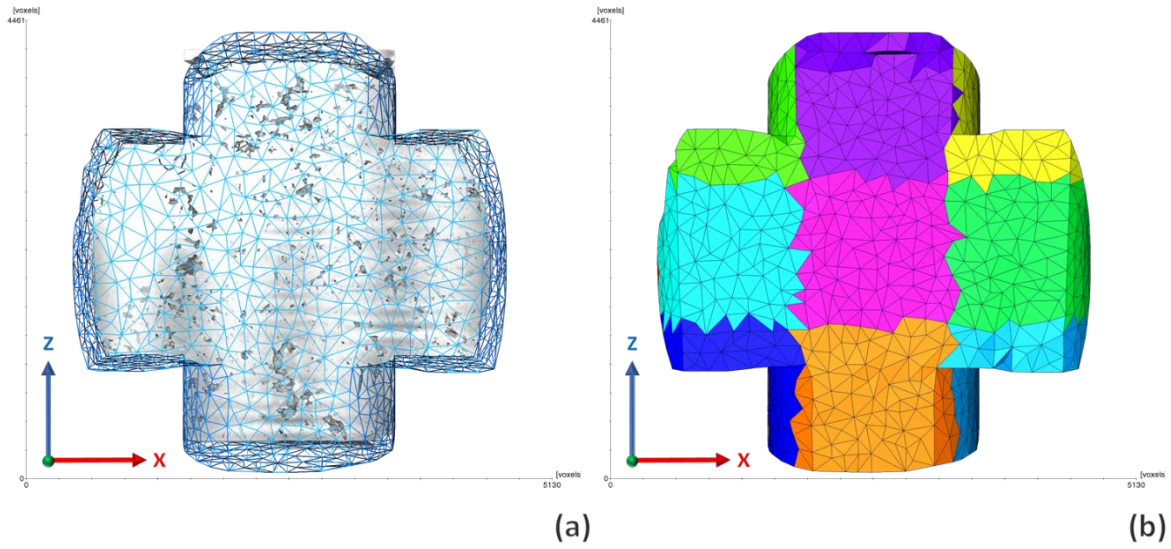


Figure 49: Tetrahedral meshes used in the digital volume correlation with the global multi-domain approach, with the full grid overlaid on top of a volume rendering of the microstructure (a) and the 3 × 3 × 3 mesh split used in the correlation (b)

3.3.3 High-Resolution X-ray Diffraction Mapping

With a slit size of 100 × 100 µm and the brightness of the pink beam, non-spotty diffraction spectrums with well-defined and continuous Debye-Scherrer cones have been obtained as shown in Figure 50. The larger wavelength spectrum however meant that a significant degree of blur and spread affected the quality of each diffraction measurement. In particular, the diffraction ring of the (0002) basal plane had a sufficient intensity above the background to be fitted, but the glass of the container led to a wide ‘doughnut’, within the 002 ring, rendering fitting in this region difficult. Issues related to data backup and unexpected experimental conditions led to the loss of the calibration dataset, and the dark and flat field images.

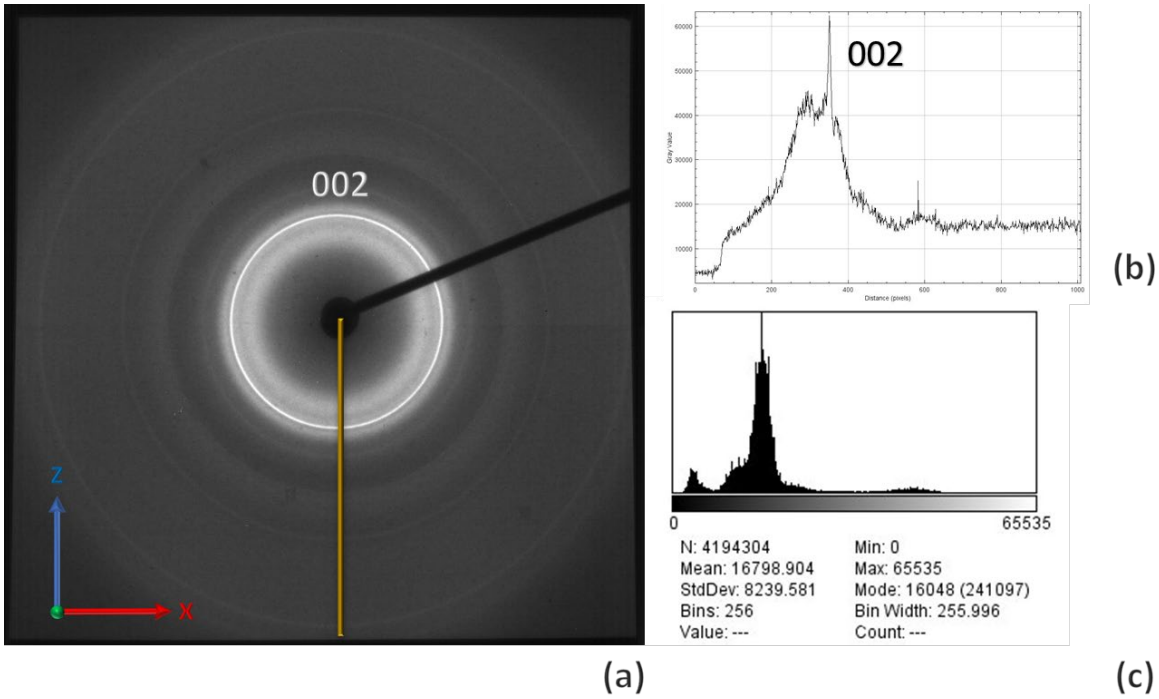


Figure 50: Raw diffraction point acquisition 440 load step 6 (a), and its rescaled histogram (b), and a radial line profile (c) represented by a yellow bar on (a)

Each acquisition was pre-processed using the pyFAI code [168, 169] to obtain corrected diffractograms. Calibration was performed on a single point in the middle of the specimen at preload. Using known crystallography for graphite (3.345 Å for 002, 1.676 Å for 004 and 1.230 Å for 110) as well as the beam energy, the rings were fitted to obtain the essential calibration information such as sample to detector distances. Dark fields from another set of scans from the same experimental beamtime were adapted and matched to provide correction for the camera defects and white noise. A mask was created to exclude the beam stop from the integration. Since only the 002 peak was of interest, the radial integration was performed from 1 to 5° in 6,000 pixel bins. There was no need to integrate from 0° which is mostly composed of the beam stop as the subsequent analysis code now works well with any integration method. Azimuthal integration was computed from 0° to 360° and divided into 360 bins. The

pseudo split method for azimuthal integration provided sufficient accuracy and the diffractograms were saved as ".azim" (EDF format) azimuthal files. Figure 51 presents the radial and azimuthal integration showing the very important background noise in the diffractogram (a).

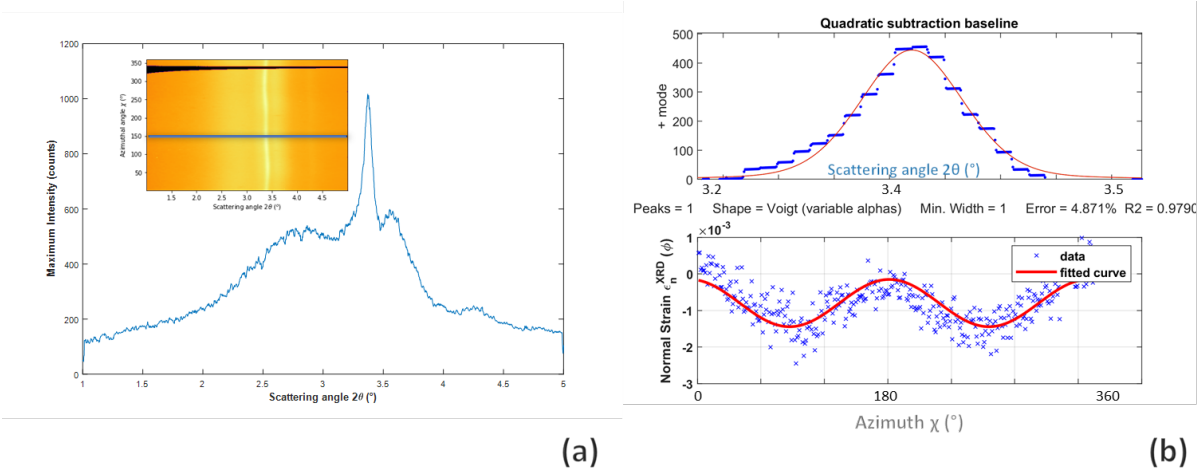


Figure 51: Radial integration and plot of an azimuthal bin after integration (a), and example of peak fitting and sinusoidal strain fitting (b) calculated as in 3.2.3

The diffractograms were then processed in the DIFFRACTX program. The azimuthal ".azim" files are referenced, sorted and moved to the processing folder once the working folder has been defined. The code uses in this case (with the pyFAI option), the 'edfread2' (written by ESRF) reader to load each file when needed by one of the workers in parallel processing. The background noise is compensated by fitting with a quadratic subtraction baseline as presented in Figure 51(b). The fit was performed using a Voigt (variable alpha) shape after giving the approximate peak position and window using a peak finding function, and three trials (passes) per fit. Both the deformed and reference diffractograms were fitted, shifted peaks were also obtained using the XCORR signal shift method (see section 3.2.3). This new fitting approach obtained peak height, Full Width at Half Maximum (FWHM), area, shape factor and an

estimation of the RMS fitting error for each of the points of the reference and deformed volumes. The matrices for the XCORR peak positions were populated with the additional information from the deformed map fitting and the fitted peak positions were compared to the XCORR positions.

3.4 Results: Comparison of Total and Elastic Strains in the Bulk

3.4.1 Quantification of Global Deformation

Figure 52 presents XZ and YZ views of the Digital Volume Correlation (DVC) for the disc compression sample of the I12-JEEP experiment, and particularly the strain results of step 1 (1.5 kN) exported to Avizo and superposed to an orthoslice of the microstructure with a thermal colouring with RGB-alpha transparency presenting the zones of highest strains. As expected, the ε_{zz} stains are highest at the contact points with the loading platens and are two to three times larger than the ε_{xx} strains, which are mostly located in the centre of the specimen due to the Poisson effect. It can be appreciated in (a.ii) and (b.ii) that both radial strain components do not vary significantly along the Y-axis. In order to compare total and elastic strains, a sub-volume of the same size as the diffraction map area was extracted and imported in the Matlab program aforementioned.

The DVC matrix was interpolated onto the XRD map with a nearest neighbour approximation so that both XRD and DVC grids have the same dimensions for further analysis. The interpolated DVC maps are presented in the plots of Figure 53 with an average of 20 contours each. They demonstrate a relatively good symmetry of ε_{zz} and ε_{xx} strains and show that the ε_{xz} strains are not negligible at the location of the XRD map. This was done with the DIFFRACTX code developed for this project.

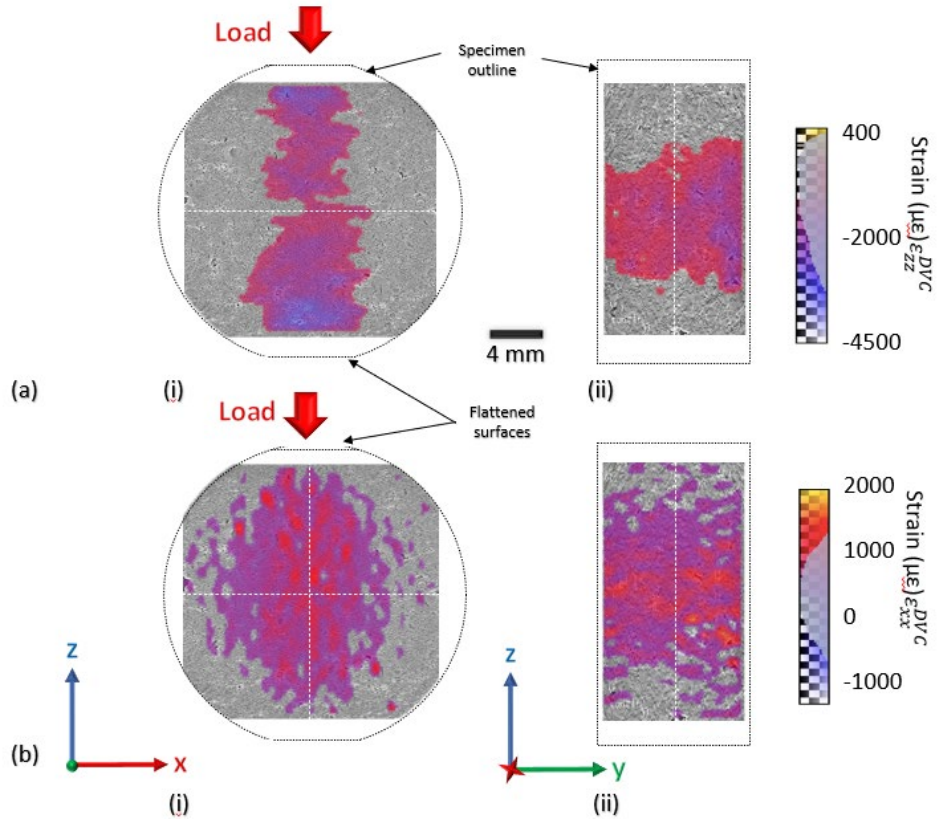


Figure 52: Front (i) and side (ii) views of the JEEP-i12 sample with ε_{zz} (a) and ε_{xx}, (b) strains overlaid on top of the microstructure

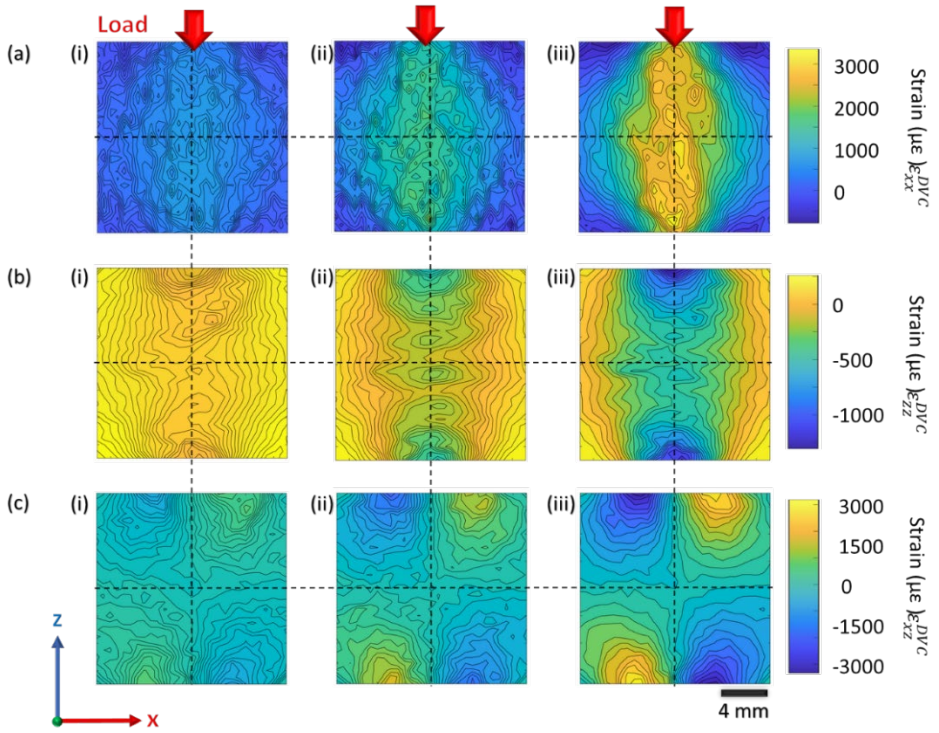


Figure 53: DVC maps of (a) ε_{xx}, (b) ε_{zz} and (c) ε_{xz} strains for load steps 1.5 kN (i), 3 kN (ii) and 4.5 kN (iii) after interpolation on the XRD grid

3.4.2 Distribution of Large Elastic Strains

Figure 54 presents the three elastic strain components from the XRD map computation as contour plots with about 20 lines for each, for the i12-JEEP disc compression experiment. Compressive $\boldsymbol{\varepsilon_{zz}}$ strains are equivalent to those obtained by DVC however tensile strains are more than an order of magnitude lower. The strain distribution is mostly homogeneous, particularly for the Z-axis $\boldsymbol{\varepsilon_{zz}}$ strains. The $\boldsymbol{\varepsilon_{xx}}$ strain maps, however, present heterogeneous zones, with spots of high tensile strains. Although the 1 mm beam size is larger than the average feature size in the microstructure, this indicates significant microcracking from the third load step at 3 kN, which is just 60% of maximum load. Microcracking of any sort is however not visible in the microstructure, and it is shown in chapter 5 that away from notches, observable cracking (micron to sub-micron voxel size) is likely to occur only above 90% of the failure load.

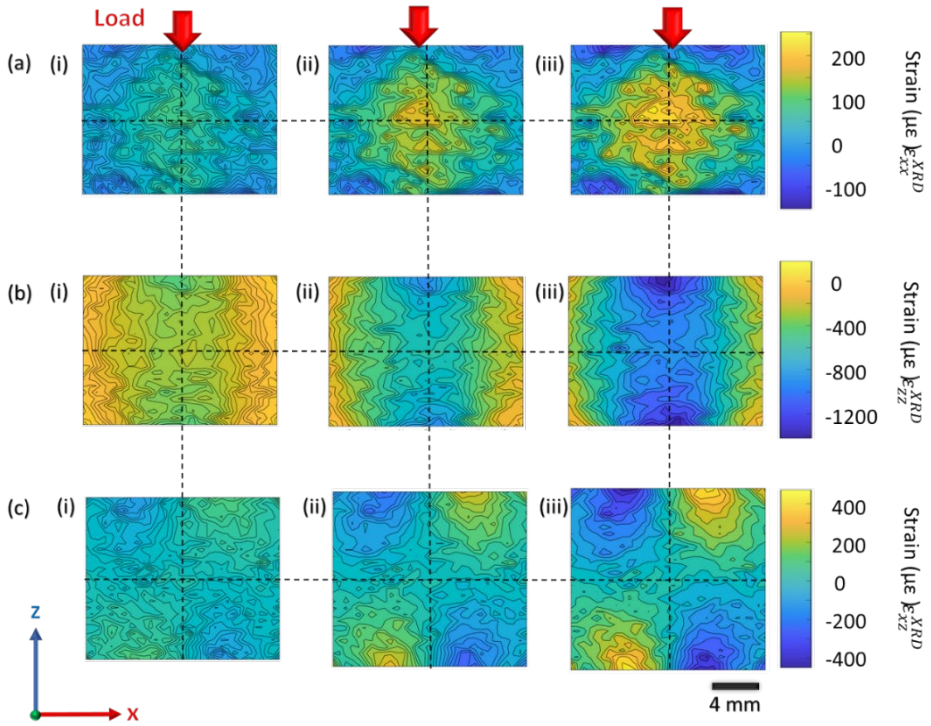


Figure 54: XRD maps of (a) ε_{xx}, (b) ε_{zz} and (c) ε_{xz} strains for load steps 1.5 kN (i), 3 kN (ii) and 4.5 kN (iii)

3.5 Results: Strain Evaluation at High Resolution

3.5.1 Total Strains from Multi-domain DVC of Stitched Tomographies

The results of the small disc compression experiment at ESRF-i12 are presented. Figure 55 shows the output of the multi-domain correlation of the second stage (50 N) with the preload, computed from the stitched Region of Interest (RoI) High-Resolution Tomographies. The compressive strains along the Z-axis are displayed as coloured volume rendering with the microstructure. A Region of Interest (RoI) box crops the volume so that a central region is presented here. As expected, the compressive strains are mostly located at the contact point.

Figure 56 shows the location of the crack that initiated from step 6. A filler particle located in the middle of the front face of the specimen, that on the side of the beam entry, contained a large filler particle partially truncated by the EDM manufacturing process, and presenting a large lenticular crack open to the surface. The failure crack slowly initiates at this location at step 6 before propagating towards the top of the specimen. This slow crack propagation before brittle fracture is likely due to the small size of the specimen. Indeed, I estimate that microcracking occurs earlier before brittle fracture and this supports the hypothesis formulated in Chapter 5 that failure initiates from defects, and most probably filler particles, at the surface.

The total strains obtained here are further used in the CROSSX code which interpolate them onto the XRD grid to enable comparison of tensile and total strains and calculate principal strains. In this case, a small sub-volume has been extracted which matches the dimensions of the XRD map, instead of using the entire volume, which would have slowed the process significantly without any benefit. It is worth noting that this sub-volume still contains the cross-shape and hence ‘zero’ values at grid points, but these have been omitted from further processing.

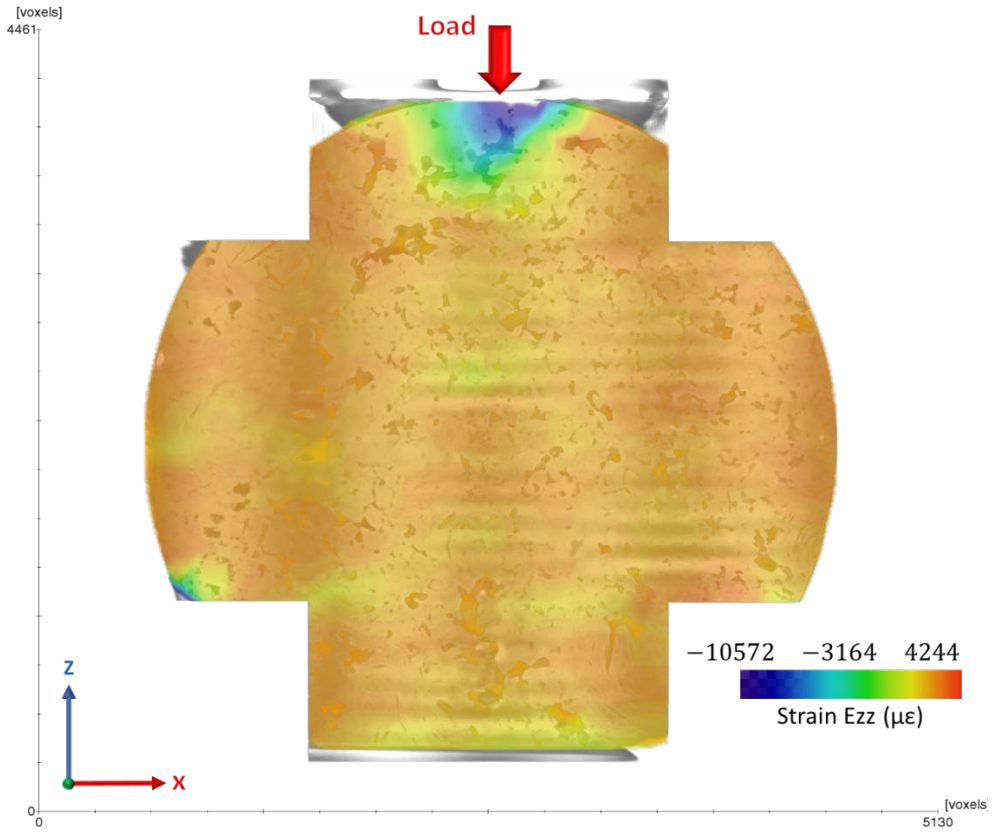


Figure 55: Z- axis compressive strains from the correlation of step 2 (50N) with the reference overlaid on top of a volume rendering of the microstructure

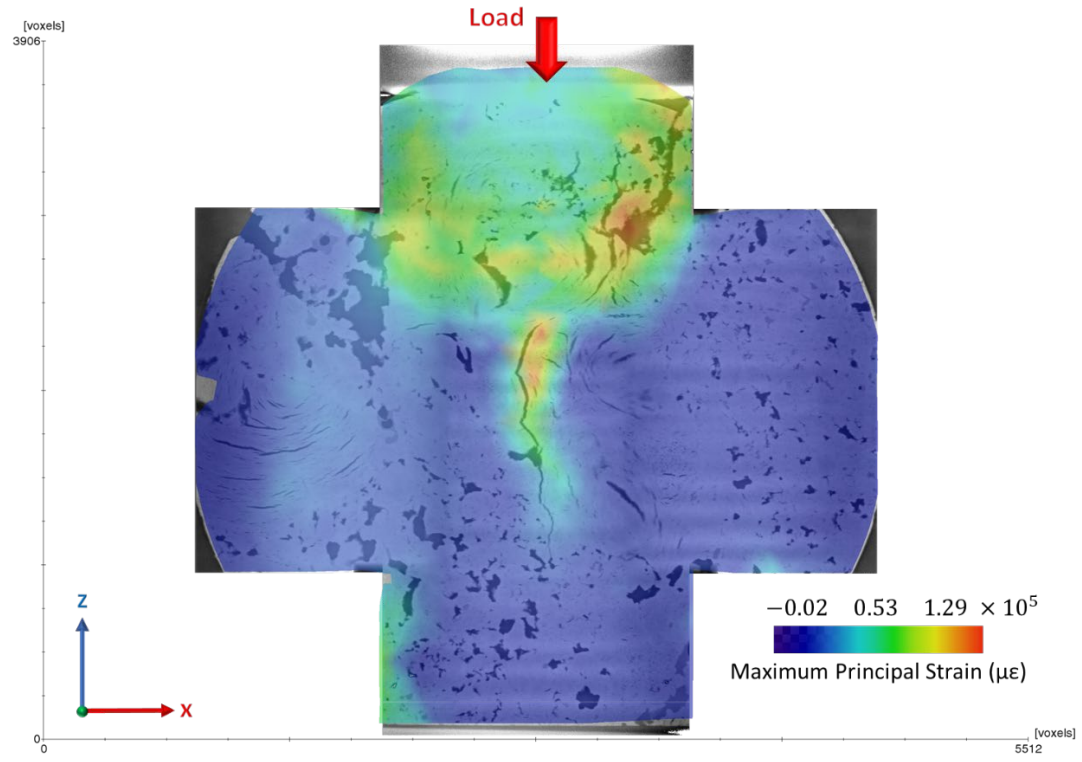


Figure 56: Volume rendering showing initiation of a surface crack from step 6

3.5.2 Elastic Deformation at High Resolution

Figure 57, Figure 58 and Figure 59 present the X-ray Diffraction Maps for the high resolution 100 µm acquisition for the tensile, shear and compressive strains respectively. There are about 20 contour lines for each map which makes good use of the point density (21 × 21) within the area which captures the lattice strain in a 2.1 × 2.1 mm area. As presented in chapter 2, around 70% of these maps is contained within the top and bottom tomography regions of interest whilst the rest lays with the right and left tomography regions. Strains $\boldsymbol{\varepsilon_{zz}}$ evolve mostly uniformly throughout the loading sequence with the highest deformation towards the top of the specimen and the loading contact point. The $\boldsymbol{\varepsilon_{xx}}$ strains however have unusually high local strains from the fourth stage (150 N). This is the step from which a crack starts developing from a filler particle at the surface and with a direction towards the upper contact point from which the load is applied.

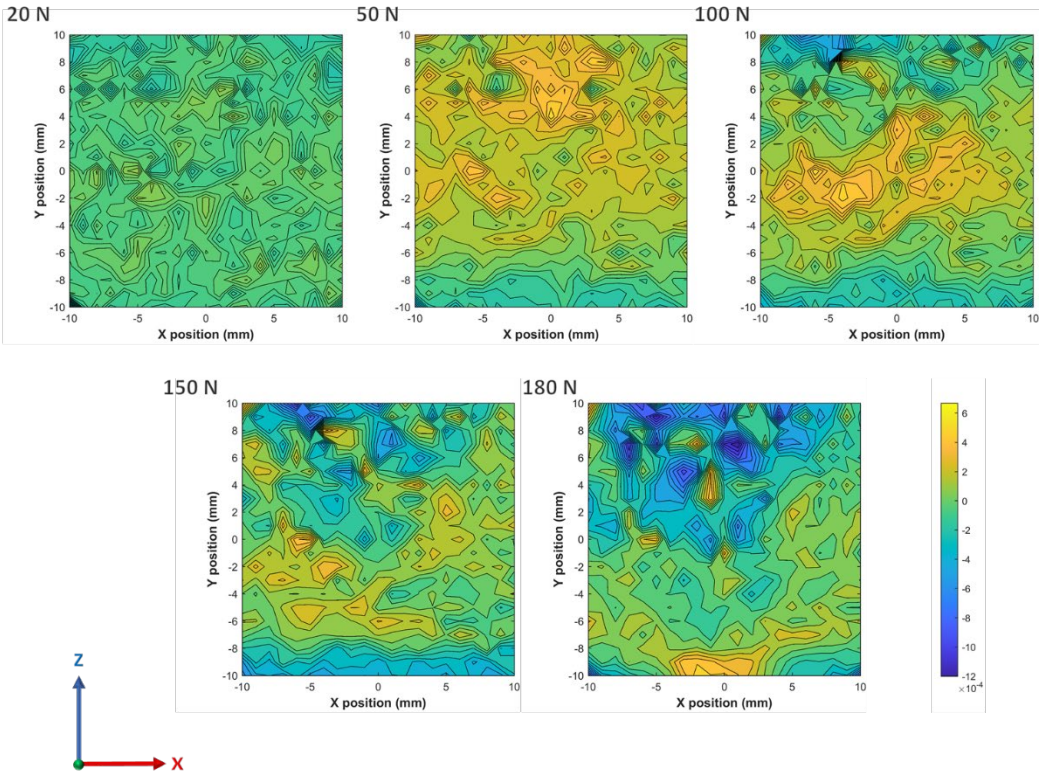


Figure 57: High resolution XRD maps of $\boldsymbol{\varepsilon_{xx}}$ strains of all steps (100 µm slit aperture)

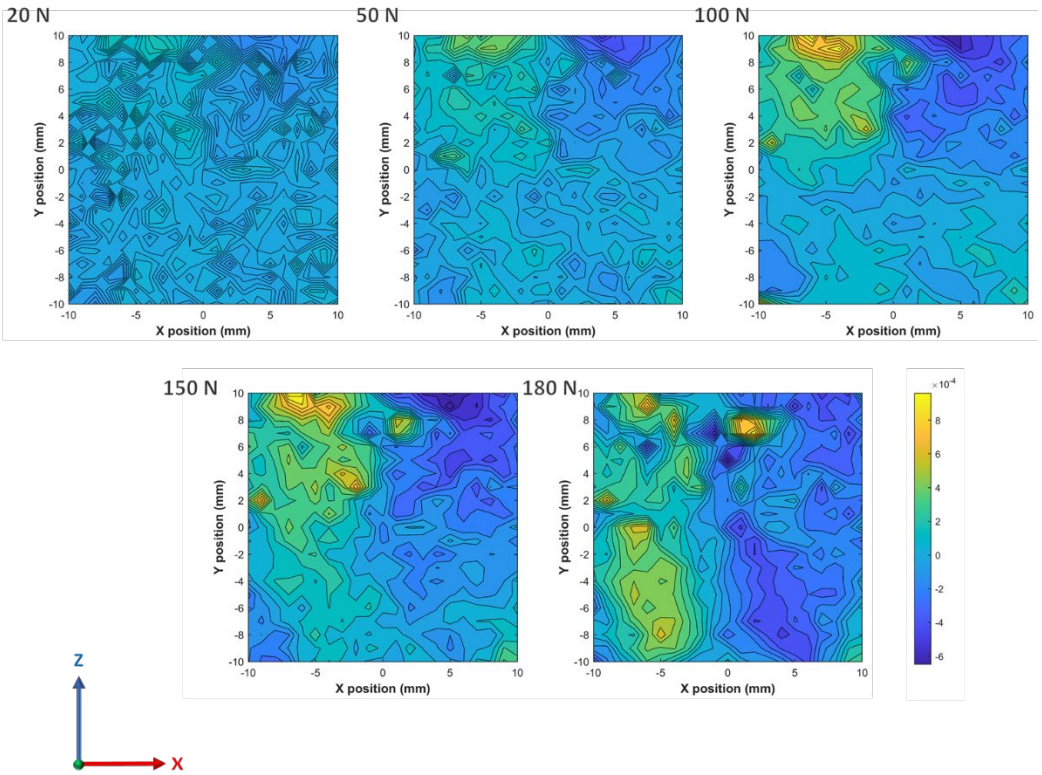


Figure 58: High resolution XRD maps of ε_{xz} of all steps (100 µm slit aperture)

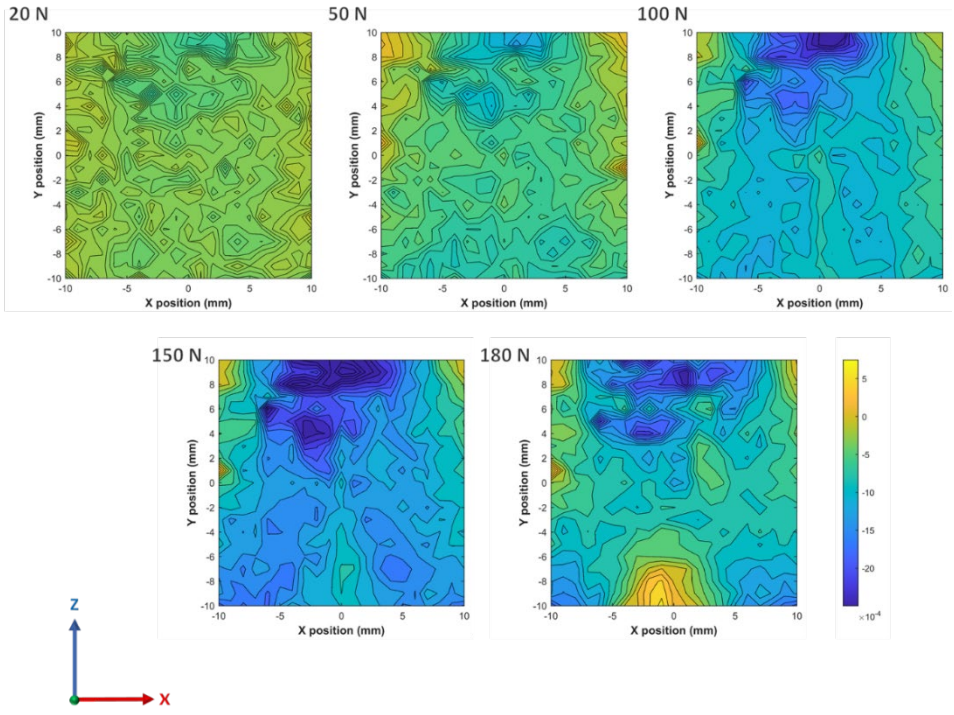


Figure 59: High resolution XRD maps of ε_{zz} strains of all steps (100 µm slit aperture)

3.6 Discussion: Multi-Scale Damage Evaluation and the Role of Microstructure

DVC and XRDM measurements have been performed in the bulk of Gilsocarbon graphite flattened discs of a large specimen and similar measurements have been obtained for a sample almost 10 times smaller, at a much higher resolution. In both cases, the XRD measurements represented the averaged Bragg diffraction through the thickness of the specimen and within each slit 'window size', 1 mm for the Jeep-i12 experiment and 100 µm for the ESRF ID-11 acquisitions. Whereas this gauge for the larger sample included many different features, it was possible to identify from the tomography regions in the smaller specimen with only matrix or filler. In both cases, the CROSSX code (part of DIFFRACTX) has enabled the interpolation of the DVC results on top of the XRD grid, providing a clear comparison of the elastic and total strains (Figure 60 & Figure 61).

The geometry of the specimen is particularly essential to this experiment. Figure 60 plots the XRD elastic strains as a function of the DVC total strains after matching the measurement points within the same regular grid for the JEEP-i12 experiment (large sample, large slit size). It shows a much larger spread when extending the interrogation area at the centre of the specimen from 4 × 4 mm (7% of total area) to 6 × 6 mm (16% of total area). This is likely because the points away from the centre of the specimen are in more heterogeneous zones: compression along the Z-axis and tension along the X-axis. It is particularly interesting to compare this with the same graphs from the ESRF ID-11 high-resolution experiment as seen in Figure 61. The graphs plot the tensile and compressive strains in two reduced areas 0.3132^2 mm^2 (9% of total mapped area) and 0.4176^2 mm^2 (16% of total mapped area).

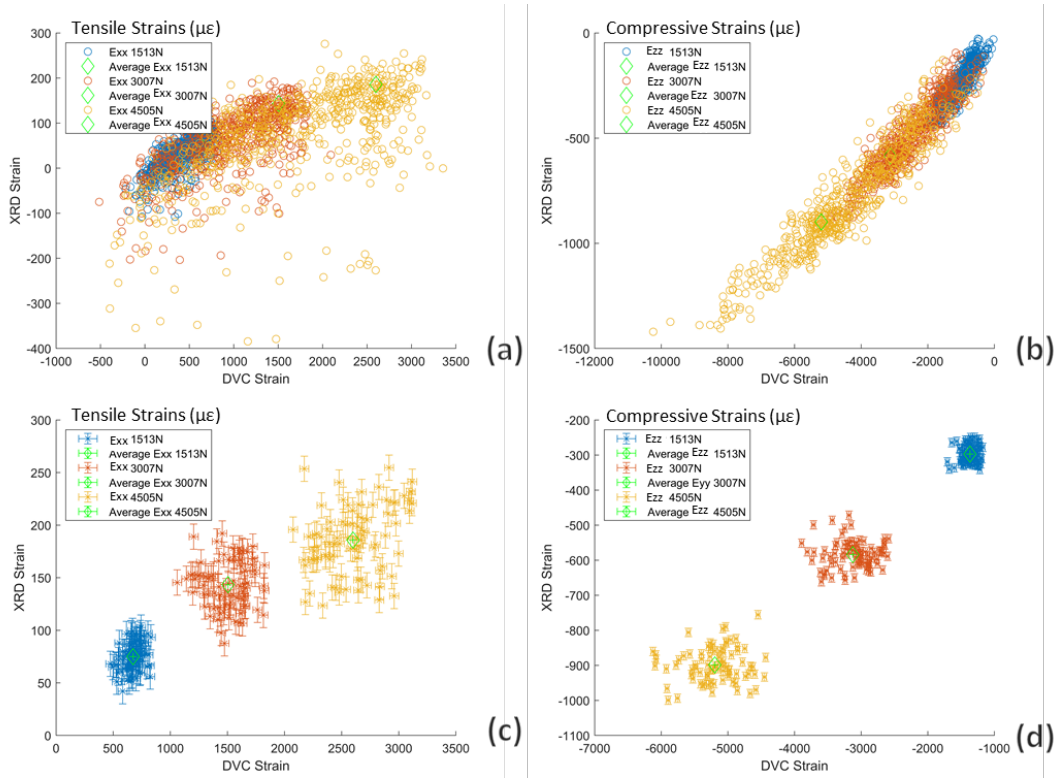


Figure 60: Scatter plot of XRD and DVC tensile (a/c) and compressive (b/d) strains for a 4 × 4 mm area (c/d) and a 6 × 6 mm area (a/b) for the JEEP-I12

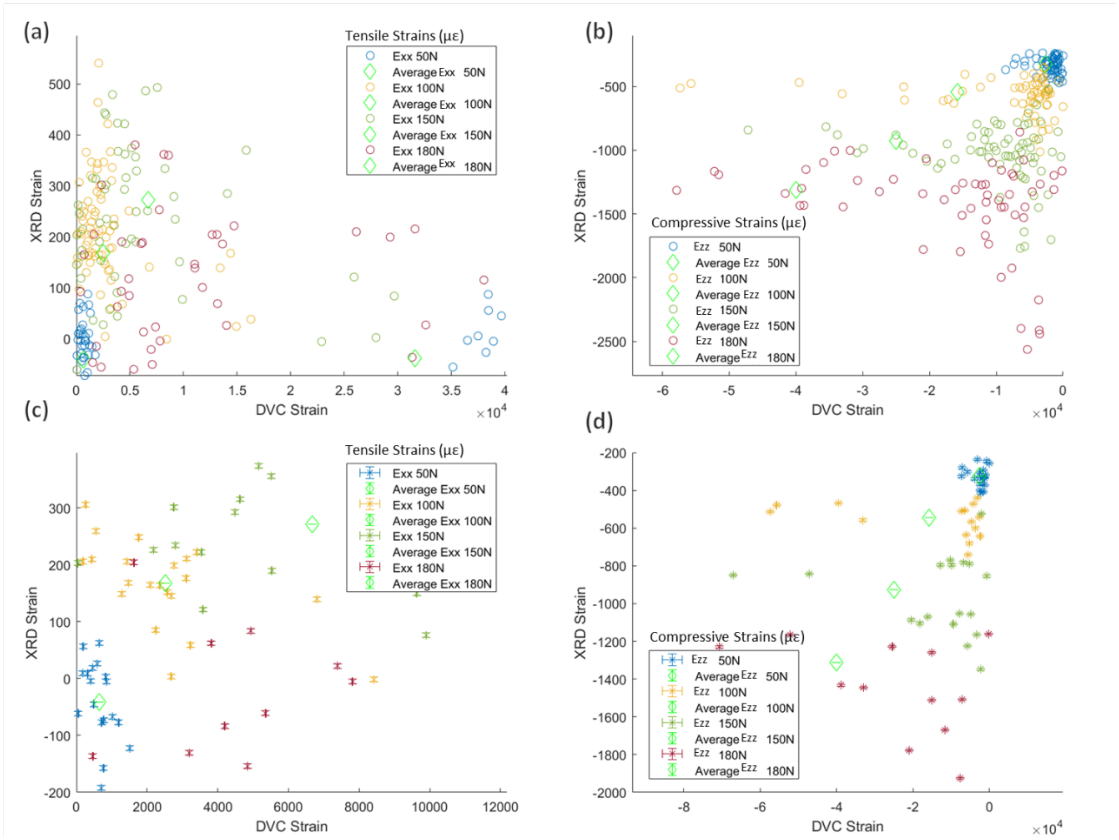


Figure 61:Scatter plot of XRD and DVC tensile (a/c) and compressive (b/d) strains for a 0.3132^2 mm2 area (c/d) and a 0.4176^2 mm area (a/b) for ESRF-id11

We can observe a much more heterogeneous response, with clusters of points for a given step overlapping with other load steps. There is also an important fall in elastic strains for the last load step at 180 N which is likely to be due to the crack initiating from a filler particle at the surface of the specimen (also see in Figure 56). These areas compare in ratio (percent of total mapped area) to that of the larger specimen, but the smaller sampling (100 µm) tends to suggest that within the same area, with an equivalent and homogeneous stress distribution (the centre of the specimen), different parts of the microstructure have a more elastic or plastic response.

Combining all the measurements points after computing the maximum and minimum principal strains provide the graphs of Figure 62 (JEEP-i12) and Figure 63 (ESRF-ID11). The strong density in the tensile region indicates a saturation of tensile strains with increasing load, and this is visible for both experiments. This is likely due to tensile microcracking, as observed elsewhere [46, 170]. As shown elsewhere in this thesis however (see Chapter 5), and based on observations of tomographies in the JEEP-i12 experiment and the higher resolution phase contrast tomographies of ESRF-ID11, this microcracking, if it is the cause, must be of sub-micron size, and it still has not been resolved by any in-situ 3D technique. The high-resolution XRDM has shown a heterogeneous evolution of elastic strains in the microstructure. This demonstrates that different parts of the microstructure, and different features affect strain accommodation differently. This is noticeable in Figure 63 where some points are aligned along the XRD axis (more elasticity) whereas other are along the DVC axis (more plasticity).

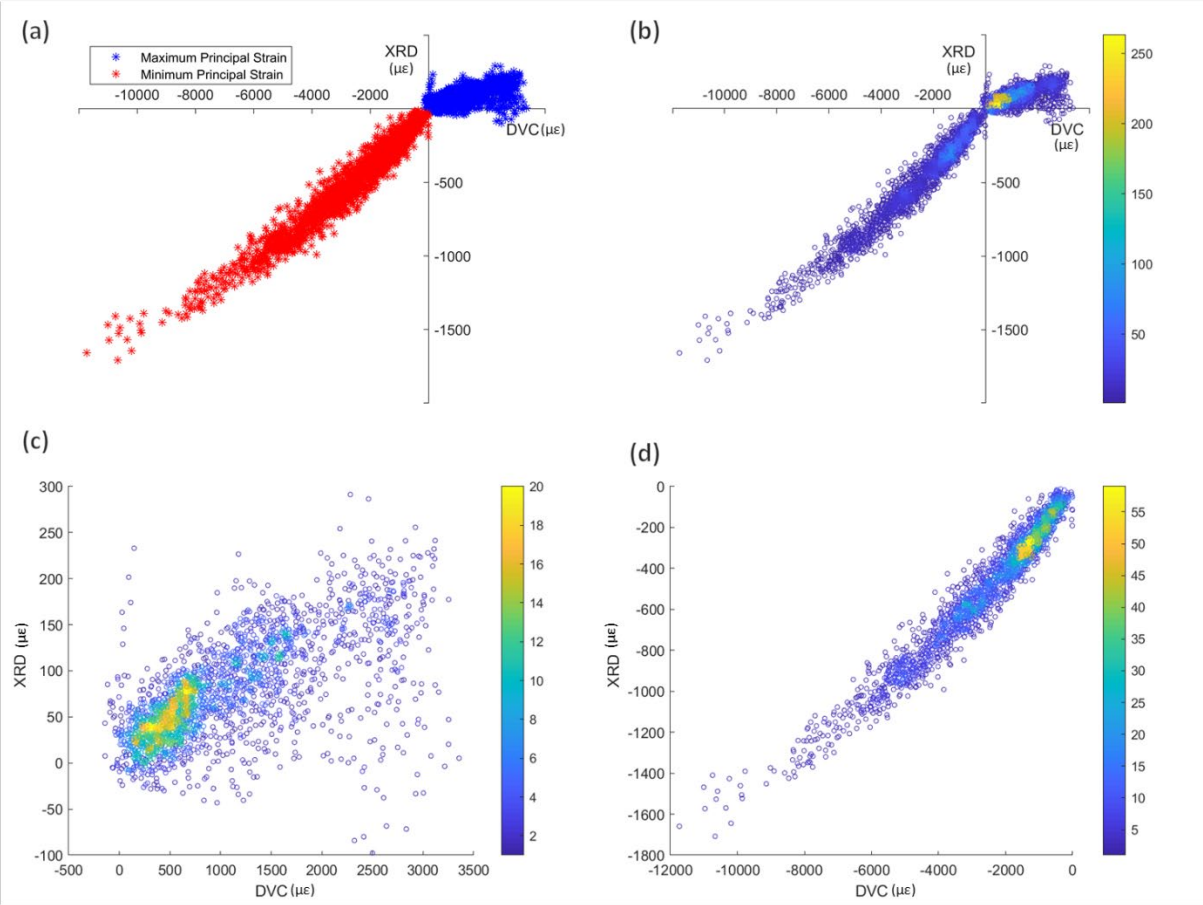


Figure 62: Maximum and minimum principal strains (a), and density plots (b) zoom (c/d) for the JEEP-i12 bulk XRD experiment

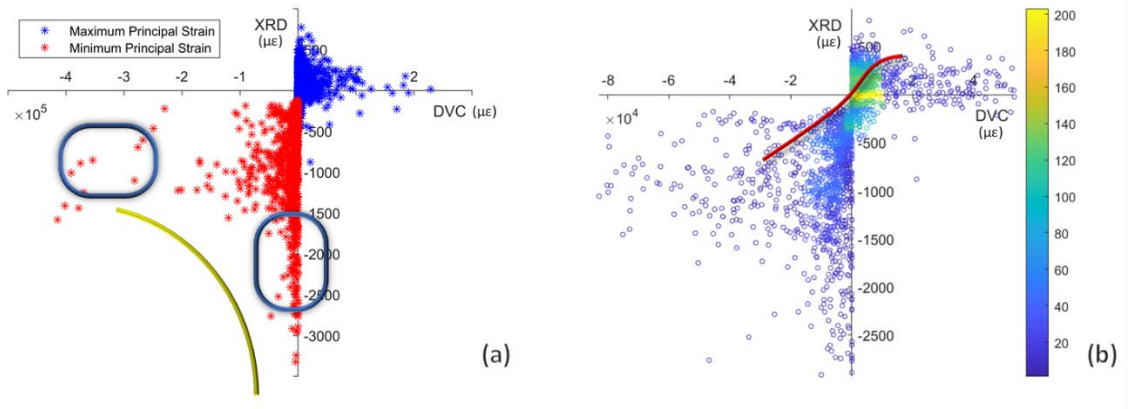


Figure 63: Maximum and minimum principal strains for the HRXD experiment on ESRF-id11 with trends (a) and density plot (b) with trendline from the JEEP-i12 experiment for comparison

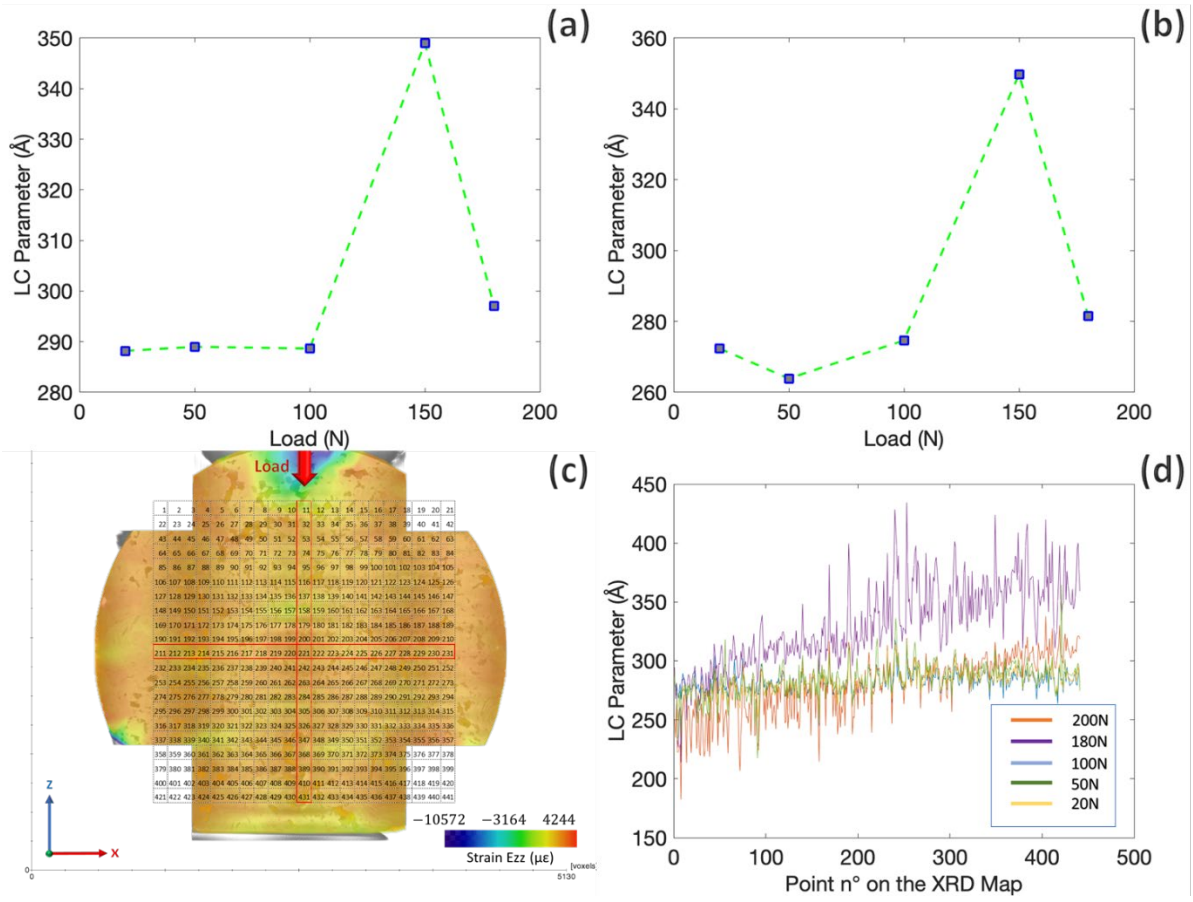


Figure 64: Change in Lc parameter as function of load along the radial X-axis (a) and longitudinal Z-axis (b), and plotted as a function of point number on the map (d), with each point location overlaid on the longitudinal (compressive) strain map at 50 N

The crystal coherent length of graphite (L_c) has been computed for the ESRF-id11 HR-XRD datasets. The diffraction mapping data from the JEEP-i12 experiment, as shown in Figure 60, is sensibly less noisy that the ESRF HR-XRD (Figure 61). However, further to the fact that the new diffraction code including L_c calculation (at the time of analysis) was developed for ESRF dataset formats and not fully retro-compatible (with older DLS datasets), the ESRF data was chosen as it samples smaller gauges (100^2 µm^2) and allows to initiate the work of discriminating within different parts of the microstructure. Figure 64 presents graphs of the evolution of the L_c (crystal coherent length) for the calculated with the Scherrer equation (5):

$$L_c = \frac{\mathrm{K} \times \lambda}{\beta \times \cos\theta} \quad (5)$$

where K is the Scherrer constant taken as 0.9, λ is the wavelength calculated for the beam energy, θ is the scattering angle of the basal plane at each point in the map, and β is the corresponding FWHM of the fitted peak. Plot (a) is within the 170-190° azimuths and (b) is the L_c parameter from 260°-280°. The median of 275 Å is comparable to previous studies for Gilsocarbon [171] for a comparable K, and the crystallite thickness has proven to be invariant with temperature for SNG graphites [172] for a similar L_c (240-260 Å). It is important to note however that this value may be underestimated, and not representative on its own as neither micro-strain nor instrumental broadening are accounted in this method. This approximation is acceptable as we are comparing load steps. It shows that mechanical stress does not affect the L_c up until close to failure, where step 150 N in (a) and (b) (and the purple line in Figure 64(b)) is just before the failure crack starts opening. Recent studies have shown that L_c is invariant with temperature on other types of graphite [172]. Figure 64(c) pictures the locations of the diffraction points on a compressive strains (Z-axis) slice computed from DVC, showing that the range of points 100-300 is located in the middle of the specimen which may indicate the fluctuation observed in Figure 64(d). Although there is a slight increase in L_c at 100 N along the Z-axis (Figure 64(b)), the sharp increase at 180 N represents a 25% jump. It is possible to note that it affects all the points in the map (taken at different times) for this step, and that there is an equally noticeable return to approximately 280 Å at the same step critical cracking is observed to occur in the microstructure. Further work with the I12 data and using the Williamson-Hall approach [173] will help confirm whether the crystallite size is affected by loading.

Chapter 4

4 INVESTIGATION OF CRYSTAL REORIENTATION AS A MECHANISM OF DAMAGE ACCOMMODATION

4.1 Preamble 4:2

4.2 In-Situ Bragg Imaging 4:3

4.2.1 Preamble 4:3

4.2.2 Data Output and Quality, Pre-processing 4:4

4.2.3 Methodology for the Extinction Spot Tracking and Evaluation of Change in Local Coherent Scattering 4:7

4.2.4 Advanced Filtering and Segmentation 4:12

4.2.5 Image Registration 4:14

4.3 Three-Dimensional Synchrotron X-ray Diffraction (3DXRD) of a graphite cylinder 4:15

4.3.1 Preamble 4:15

4.3.2 X-ray Diffraction Finding and Fitting 4:15

4.3.3 3DXRD Tracking 4:19

4.4 Results: In-Situ Bragg Imaging 4:25

4.4.1 Preliminary Observations 4:25

4.4.2 Variation of the Correlation in the Extension Datasets 4:29

4.5 Results: In-Situ Three-Dimensional Synchrotron X-ray Diffraction 4:34

4.5.1 Total (DVC) and elastic (XRD) strains 4:34

4.5.2 Orientation tracking 4:38

4.6 Discussion on Grain Orientation and Elasticity 4:40

4.6.1 Summary of Observations 4:40

4.6.2 Potential Interpretations 4:40

4.6.3 Experimental Aspects 4:44

4.7 Opportunities and Future Work 4:45

4.1 Preamble

As this project is concerned with the response of the microstructure to damage, it was essential to adopt a multiscale approach, particularly as graphite is a quasi-brittle material. It is known from past experiments that pore rotation and pore collapse, as well as interplanar cracking, may be non-recoverable mechanisms that lead to plastic deformation [65, 70], and that the fracture process zone is attributed to the development of a permanent set ahead of cracks with applied tensile strain [45]. It has been shown elsewhere in this thesis (see Chapter 5) that there is strong indication that filler particles are the most likely origins for the development and coalescence of failure cracks. The mechanism behind the elastic response of graphite with applied stress however, and particularly in the first 80-90% of the loading process, has not been properly identified.

In this chapter multiple complementary techniques have been used to investigate the effects of mechanical stress on the change of grain and crystal properties in Gilsocarbon graphite samples. In particular, the results of neutron Bragg imaging experiments RB1910517-1 [130] and RB1910517-2 [131] at the STFC-ISIS neutron and muon spallation source are reported, which have enabled the development of an original technique, as well as the 3DXRD part of experiment ME1504 [126] at the European Synchrotron Radiation Facility (ESRF). Whilst the first two experiments are interested in evaluating grains and particles from approximately 180 μm and larger, the HR-3DXRD experiment averages the combined Bragg reflexions from different crystals inside a 300 μm^3 gauge volume.

It is reported that two new research avenues may be used to investigate grain and crystal reorientation and deformation in quasi-brittle materials. Energy-resolved neutron imaging has demonstrated that a change in the coherent scattering of large

domains of grains may help explain how graphite elastically accommodates strain, and that further study may be able to quantify the spatial distribution of grain reorientations. Three-dimensional X-ray Diffraction has further shown that additional mechanisms may be at play but that they may only be partially recoverable. This could potentially indicate, combined with previous tomography observations, that the contribution of microcracking to deformation before 80%-90% of failure load is not significant.

4.2 In-Situ Bragg Imaging

4.2.1 Preamble

Experiments RB1910517 -1 & -2 were performed at the STFC-ISIS neutron source as presented in section 2.7, and involve a new investigation method using energy-resolved neutron imagining. The proof-of-concept experiment RB1910517-1 demonstrated the potential of the novel technique, and its results are presented here to emphasize the reasoning that helped devise the extension experiment; this has been published in Experimental Mechanics [174]. Although the data collected in the preliminary experiment offered significant insights into the present method, it only allowed for limited conclusions for the case of Gilsocarbon due to poor statistics (i.e. low signal to noise ratio). The extension experiment involved two further samples, two loading methods and provided data with a higher signal to noise ratio.

The purpose of this original method is to enable the quantification of the change in local coherent scattering. Such changes may arise from grain reorientation and plasticity in the microstructure with applied stress. Due to the inherent characteristics of pulsed neutron beams at spallation sources, this technique is best applied to large bulk samples whose ‘grains’ (or domains of similarly oriented smaller grains) can be of a size above 180 μm. Graphite has a high neutron elastic scattering cross-section

[175], a strong Bragg edge associated with its basal plane [176], making it an ideal candidate for this study.

4.2.2 Data Output and Quality, Pre-processing

The time constraints which affected the sample-to-detector distance and the pinhole aperture (minimum flux) for the preliminary experiment meant that the signal to noise ratio of the radiography was quite low, especially away from the instrument's maximum energy peak. In any configuration it is necessary to work over a range of energies for image processing to be feasible, however low signal meant that the range had to be quite wide in the associated data analysis. As seen in Figure 65(b), the raw radiograph has a weak signal. It represents all the neutrons that arrived on the detector with a wavelength of 2.9 Å over an acquisition time of three hours. It is worth noting that the ASIC was configured in Time-of-Arrival (ToA), and not Time-over-Threshold (ToT), synchronised with each emission pulse, which means that the energy resolution is maximum. The energy step between radiographs is approximately 0.0014 Å until 4.96 Å and 0.0028 Å to the maximum at 8.06 Å. This raw image also reveals the four plates forming the detector as well as the dead or invalid pixels that had to be removed. As radiographs were obtained in the highest flux region of the instrument's spectrum and away from the Bragg edge of interest, it was only necessary to work over a small range of energy to perform the image correlation for measurement of sample deformation, from 2.9 Å to 3.23 Å. The initial results were an incentive to acquire datasets with a higher signal-to-noise ratio.

The extension experiment allowed the collection of two more datasets with overall better statistics. Most of the original configuration, such as the energy range, number of bins and energy steps, remained the same, at the exception of the pinhole aperture and the neutron count.

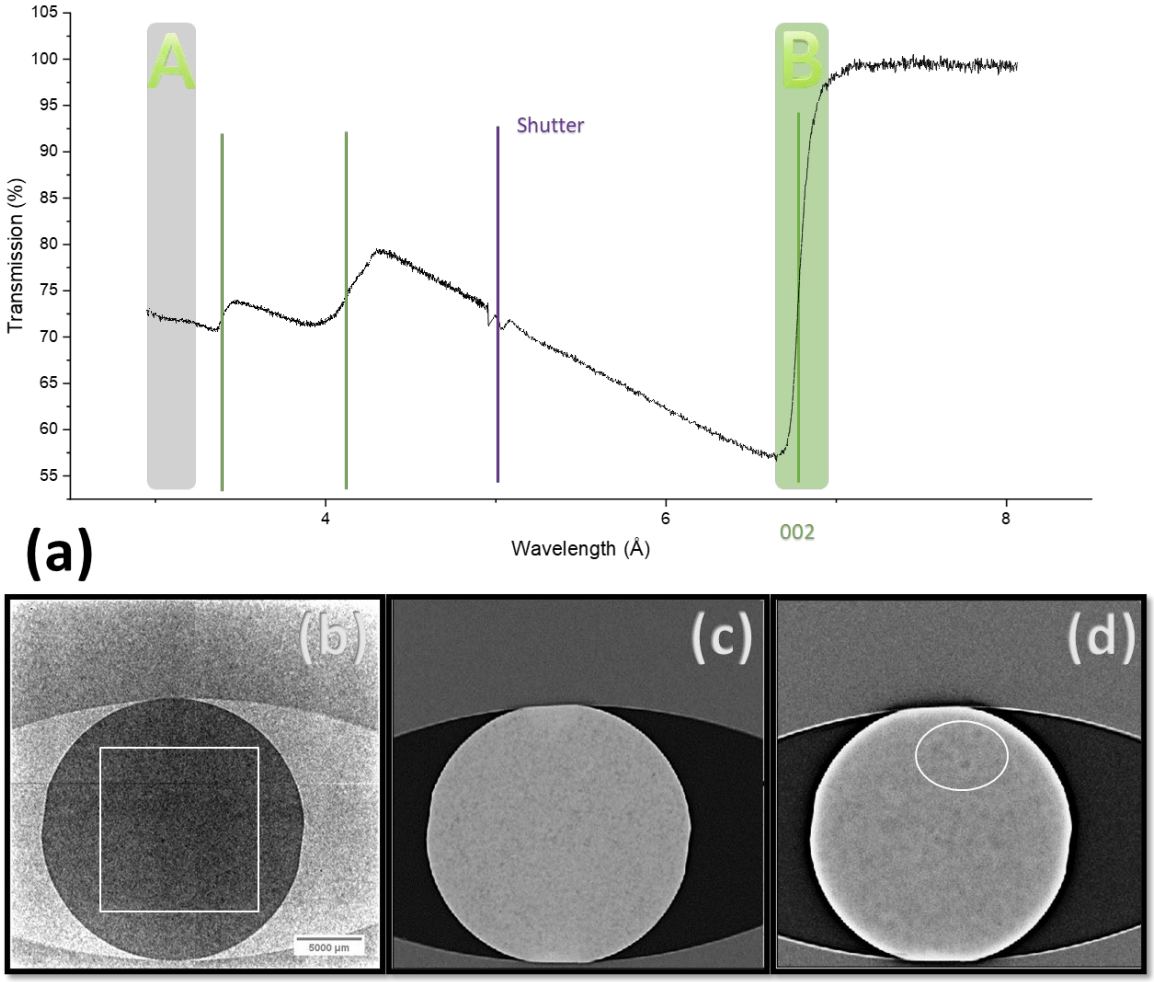


Figure 65: (a) Regions A and B are indicated on a neutron transmission spectrum averaged over the square area that is marked in (b) the raw uncorrected radiography at 2.9 A; (c) pre-processed and averaged image from Region A; and (d) from region B at the (002) Bragg-edge. [A blade with neutron absorption properties is inserted into the beam to avoid sample and detector activation when no data are collected. Even with correction for its insertion, there are residual "dips" on the transmission graph due to this 'shutter', as indicated in (a)].

With the first sample, only the count current has been doubled from 120 µA to 240 µA, which corresponds to an acquisition time increase of approximately 3 hours under optimal conditions (i.e. without beam loss). The sample was of the same size as the initial experiment and similarly loaded with the curved anvils. The second sample of the extension was a larger flattened Brazilian disc with dimensions 25 mm diameter

and 12.5 mm thickness. As it covered most of the active area of the detector, it allowed many more extinction spots to be detected. The current was 120 µA but the pinhole was increased from 40 mm to 60 mm. Figure 66 compares single radiographies at the same wavelength for the two datasets of the extension experiment.

During the acquisition of data, the load was allowed to settle after each step before collecting data. Further stress relaxation led to a small difference of about 50 N over the acquisition time of approximately 3 to 6 hours. Since radiographs do not represent a successive exposure acquisition but rather a collection of neutrons at different energies, it can be considered that all radiographs are acquired at the same time, and at an approximate load.

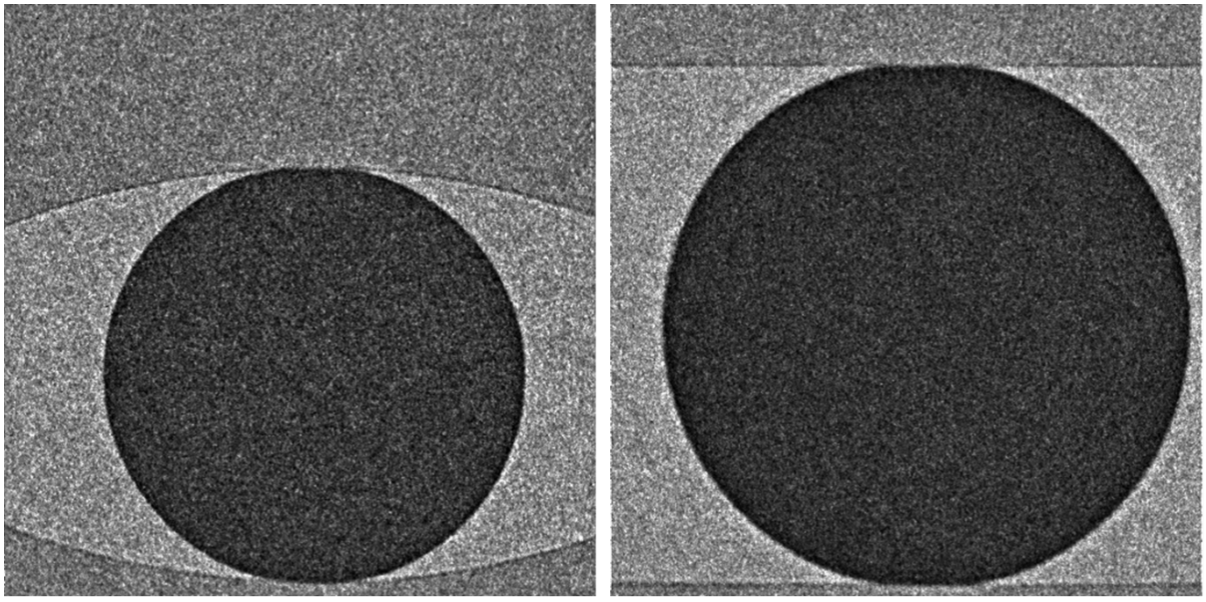


Figure 66: Radiographies n°1900 (3.4 angstroms) for samples IOX20P2B7A (a) and IOX20P2D8B (b), with preliminary corrections applied (window size 28 × 28 mm^2) (see Table 5)

4.2.3 Methodology for the Extinction Spot Tracking and Evaluation of Change in Local Coherent Scattering

A program has been developed in MATLAB in this project for processing the radiographs and identifying local changes in transmitted intensity. The code is compiled as a stand-alone executable file offering a Graphical User Interface (GUI), and the compiled version can be accessed in [177]. It was developed as specific operations needed to be performed on the radiographs at a pixel level, so it was not possible to rely on existing codes. The code works directly with the raw datasets and is optimised for multi-thread processing; GPU acceleration is under development. It has been written to minimise the use of random-access memory at the expense of more frequent access to the external storage. This makes the code compatible with computers with limited specifications while having the flexibility of using the computing power of high-end workstations.

Scaling and overlap correction are applied to the raw datasets produced by the MCP detector in the FITS format. Overlap occurs due to neutrons arriving after the end of a shutter insertion and this is corrected using Poisson's statistics. Scaling of the open beam datasets is preferable for a more accurate flat-field correction as all datasets may not have the same number of triggers. The methods used for overlap and scaling correction are the same as those already used on IMAT, for which a detailed description is available in [178]. This initial pre-processing stage is applied to all radiographs, which are thereafter saved as unsigned 16-bit TIFF images.

The paths to the working folder and stages of the data acquisition in the experiment are defined, then the datasets are listed and checked for consistency. Any subsequent image pre-processing is carried out in an iterative scheme, for each image and repeated as many times as required, and only the final outputs are saved in random-

access memory. Radiographs are first converted to double floating-point precision with no range limits to avoid truncation or saturation. The code initially works at a pixel level to reduce noise and to remove and replace dead or abnormal pixels. This is achieved by linear interpolation of pixels falling outside the 1-100 percentile threshold to remove dead pixels. A shape-preserving piecewise cubic spline interpolation, of pixels with values more than three local scaled median absolute deviations from the local median within a 3x3 pixel window, replaces abnormal pixels. Pixels that suffer from detector edge effects at the border of the radiograph are removed by an initial crop of 6 pixels at each border that is maintained throughout the experiment. Flat-field correction is applied to radiographs individually and iteratively to remove detector aberrations, especially the missing lines between the 4 ASIC chips of the Quad-Timepix sensor and other dust particles, and to obtain the transmitted image sequence using equation (6):

$$T_n = \frac{R_n}{OB_n} \times f_{OB_n} \tag{6}$$

where f_{OBn} is the mean value of the Open Beam radiography OBn representing neutrons with time of flight n, which divides the stage radiography image R_n to obtain the transmitted image T_n with neutrons with time-of-flight n. The sub-program that is tasked with obtaining the transmission spectrum and automatically selecting the wavelength ranges uses a scaling factor f_{OB_n} of 100 to obtain the percentage neutron transmission in the sample.

A subtraction method is used to detect changes in the transmitted image between loading stages. This requires each image to be registered with a reference in terms of deformation and movement. To address the effects of deformation of the specimen (i.e., compression), it is first necessary to measure the relative displacements. This

could not be done using image correlation of optical images (as in Figure 6) due to the configuration of the IMAT instrument, and so was carried out using the attenuation contrast the radiographs. The displacement fields are obtained by Digital Image Correlation (DIC) of averaged images in a wavelength range where it is expected there would be limited Bragg scattering. Figure 65 presents the specific case for transmission in Gilsocarbon graphite. The graphite Bragg-edge, which corresponds to the basal plane (002) reflection, is located in region B. In region A, neutrons have a low scattering probability, but the Gilsocarbon graphite has a very heterogeneous distribution of porosity [29], and all features should be from attenuation differences in the neutron path due to absorption (e.g. density variation). At the resolution of neutron imaging this heterogeneity can be assumed to not change with load, and so it provides the ‘speckle’ for DIC of the specimen’s deformation. Region A is centred around a user defined wavelength in a region away from any Bragg peak. Radiographs are pre-processed and then averaged over an increasing range until the signal quality is sufficient for image registration. A Perception-based Image Quality Evaluator (non-referenced and unsupervised algorithm) is used at each iteration to compute a quality score. When the value of the score falls below 5% of its preceding iteration, the averaging and range extension ends.

After the averaged images are obtained, further pre-processing and image masking was done. This includes outlier removal with a shape-preserving piecewise cubic spline interpolation where there is a three-time local scaled median absolute deviation from the local median over a window length of 3 × 3 pixels, gaussian smoothing with a standard deviation of 0.5, and a threshold-based segmentation to remove the loading anvils and air. To obtain images only of the sample, the grayscale intensity is adjusted by scaling throughout the steps to maintain a constant mean in a 50 × 50 pixels zone

with neutron transmission through air and an algorithmic threshold segmentation is then used to mask the non-sample areas. This uses as input a mean intensity that assumes that the sample is centred (an alternative centre can be defined) and is used to inform a geometric mask for the subsequent analysis of the radiographs. This set of images, each representing an absorption contrast image of the sample at each step of the loading, is then fed to the DIC algorithm. The method uses the demons algorithm developed by Thirion [179] adapted to provide non-diffeomorphic transformations [180]. It employs a 1.5 diffusion-like gaussian regularization at six resolution levels with up to 100 iterations, to obtain the relative displacement of each pixel. The output is a regular array of displacements with an array size determined by resolution of the correlated images.

Region B, or Near Bragg-Edge (NBE), is defined around the Bragg-edge of interest. Each radiograph over this range and for stages under mechanical stress is loaded together with its corresponding open beam and reference radiographs. After image pre-processing and correction, the radiographs for each stage are registered with the displacement fields calculated using the A-region by inverse mapping. Pixel values in the result image are obtained after mapping locations to the corresponding locations in the original image by applying the inverse transformation. Nearest interpolation is applied in the input space to compute the pixel value in the registered image. The reference radiograph undergoes the same pre-processing and intensity adjustment before being compared to the registered stage radiograph by readjusted differentiation. Sequential linear combination of radiographs over the B-range subsequently reduces noise and increases the contrast of the features that are in the Bragg condition. In this analysis, the B-range represents an interval of 30 to 80 radiographs depending on the signal quality of the dataset. The code allows one to

split B into multiple subsets of radiographs. A detailed process workflow of the code is presented in the diagram of Figure 67. Figure 65 also presents a single raw and uncorrected radiograph in the A-range for the 0th pre-load stage (0.2 kN) together with a corrected and averaged image over the A-range and over the B-range. The latter clearly presents contrast from features that are only visible at the Bragg-edge characteristic, with those crystals in the Bragg condition forming an extinction spot. The contrast of these features is relatively low within a single radiograph. The width of the Bragg edge [181] and the range of energy selected for summation will affect the visibility of these features in the processed images.

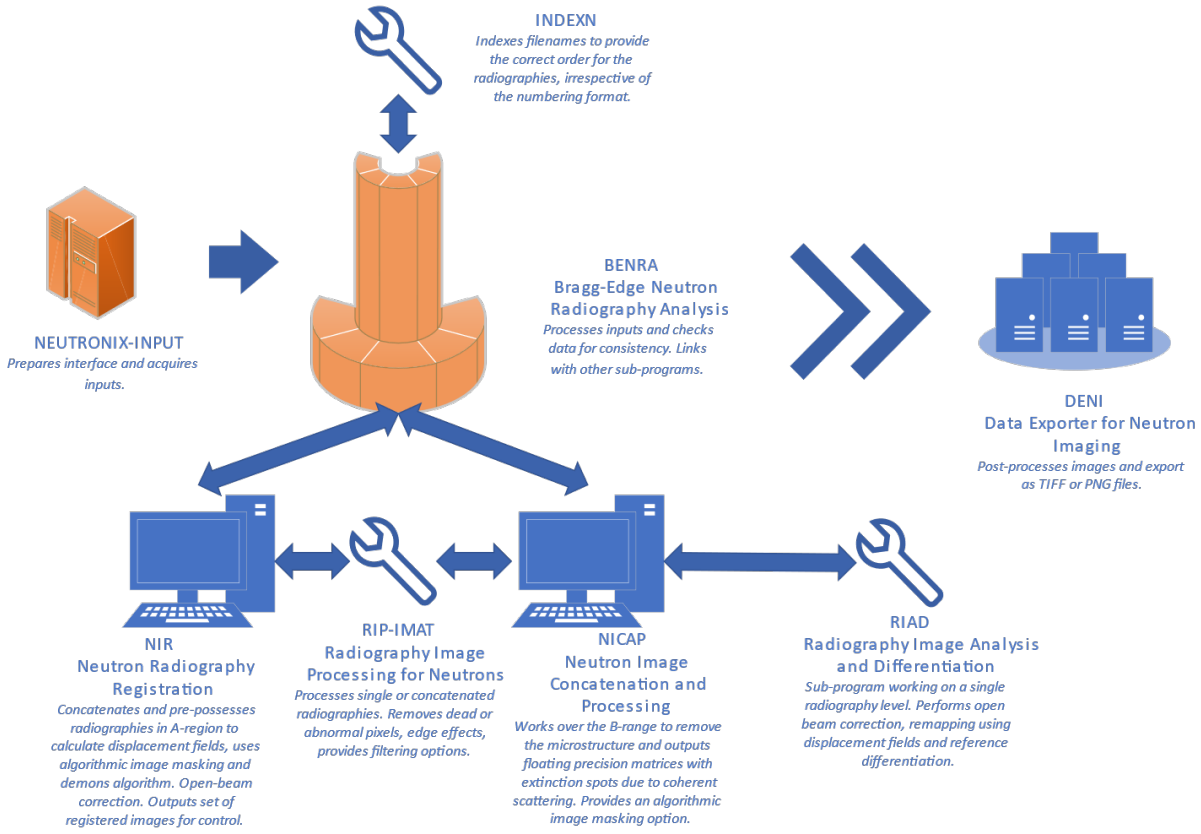


Figure 67: Workflow diagram presenting the NEUTRONIX program and its sub-programs

4.2.4 Advanced Filtering and Segmentation

Although the extension experiment has brought datasets of better overall quality and less noise, there is an inherent difficulty to segment the extinction spots using this 2D technique and for graphite, due to the size of the specimens and the large degree of disorder in the graphite microstructure. Other neutron (non in-situ) Bragg-imaging studies have made use of 3D measurements by rotating the sample stage for materials with only a few large crystallites in the Field of View [158, 182]. In a second iteration of the code, which is currently under development (and outside of the scopes of this thesis), advanced filtering and denoising techniques are investigated and have been able to better highlight extinction spots in the radiography images. In particular, Figure 68 presents the result after the application of a rolling median and multiplicative rotational Savitzky-Golay filter. This particular filter is based on the Finite Impulse Response (FIR) principle, by fitting low-degree polynomials to adjacent data points using the linear least squares method [183]. It is here applied to each line of the rotated image using equation:

$$I_{n+1} = I_n \times R_\theta^{-1}(S(R_\theta I_0)) \quad (7)$$

where R is the rotation with angle θ, S is the line-by-line smoothing function and n is incremented from 1 to 180/ θ.

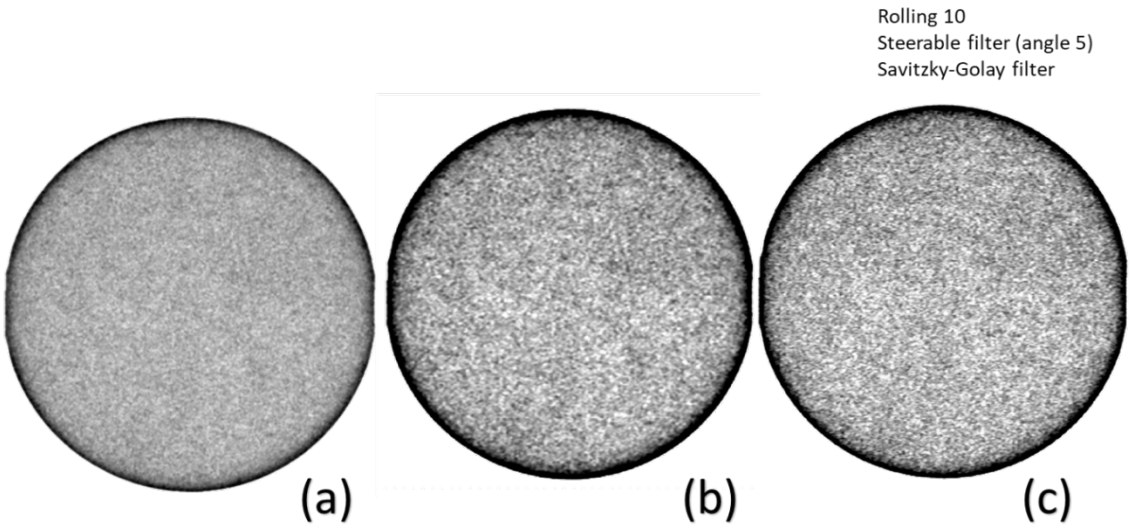


Figure 68: Original radiography N°1867, rolling median and multiplicative rotational Savitzky-Golay filter for preload (b) and maximum load (c)

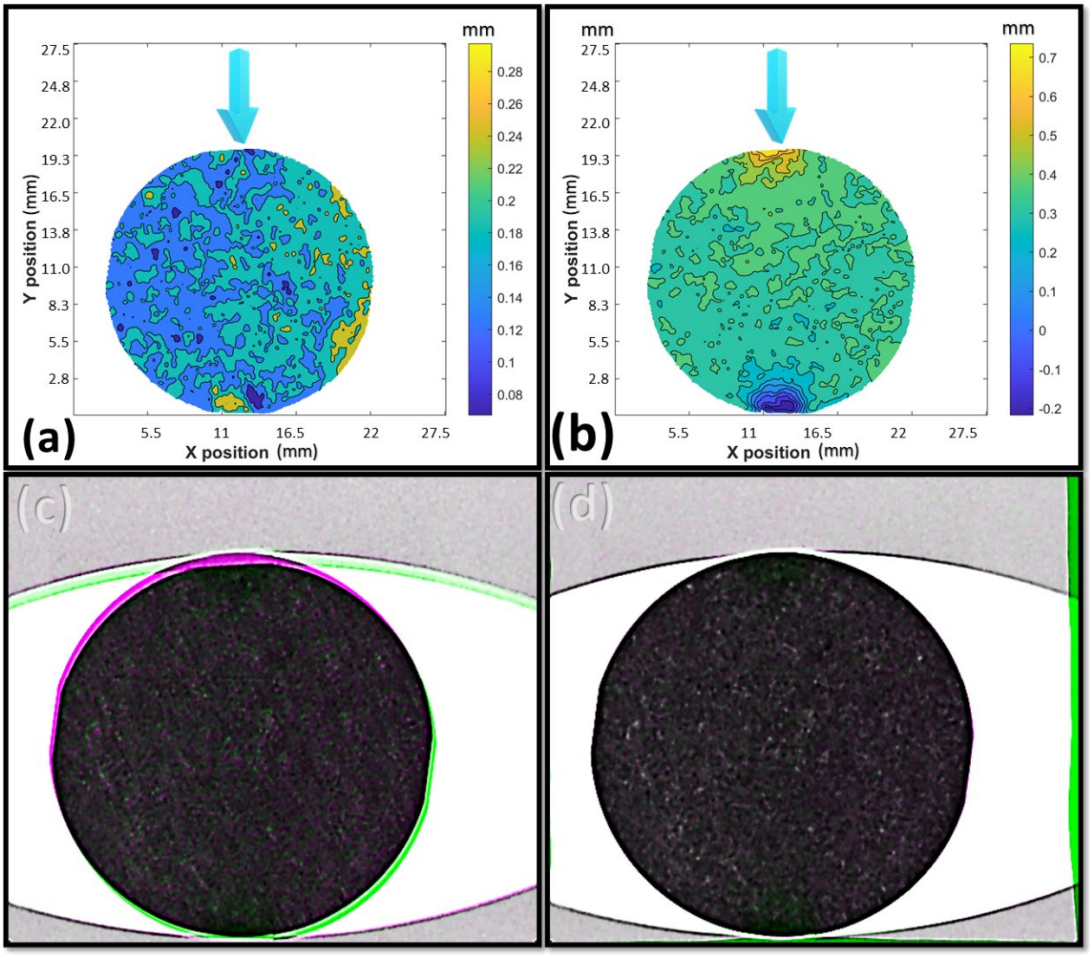


Figure 69: Comparison of 5th stage (4 kN) to reference (0th pre-load stage at 0.2 kN): (a) horizontal displacements; (b) vertical displacements; (c) unregistered image; and (d) registered image

4.2.5 Image Registration

Realignment of energy-resolved images has not been attempted before. The following presents the image registration result for the first dataset, in the preliminary experiments, and details on the other two datasets can be found in the appendices. Displacement fields were obtained from pre-processed, corrected, averaged and masked images over the A-range. The relative vertical and horizontal fields for the 5^{th} stage (4 kN) compared to the reference (0^{th} pre-load stage at 0.2 kN) are presented in Figure 69. This shows the expected bi-axial deformation and compares well to previous correlation studies performed on similar specimens [73]. These particular sets of images have also been correlated using commercial DIC software (LaVision DaVis 8.40) and a comparison that verifies the performance of the demon code is presented in the supplementary materials. Figure 69(a) and (b) show the displacement fields that registered the images. The coloured regions in Figure 69(c) and (d) represent areas of image intensity mismatch, where the disc (and features in its microstructure) and the anvil do not overlap. The realigned and deformed image is shown to correctly fit (i.e. register with) the reference in Figure 69(d). Since radiographs inside A-range (away from the Bragg edge) have the same level of deformation as those in the B-range, the measured displacement fields can be used to register the microstructure images in the B-range, in which extinction spots are observed that will be discussed in detail in the following section (4.4).

4.3 Three-Dimensional Synchrotron X-ray Diffraction (3DXRD) of a graphite cylinder

4.3.1 Preamble

Three-Dimensional Synchrotron X-ray Diffraction (3DXRD) has been developed for low-resolution grain mapping of samples with large grains of the order of a few hundred microns [184, 185]. In most experiments to date, the materials investigated had well-ordered crystal domains and this resulted in spotty diffraction patterns. Programs have been developed to create 3D grain maps based on segmentation of the diffracted spots and pair-matching to provide crystal size, shape and dimension. In the case of graphite and because of the high degree of misorientation of the basal planes along the [0001] direction, this kind of reconstruction is not possible. This stacking of the basal planes also implies that many planes will contribute to the same diffraction peak, and this prevents the use of conventional diffraction techniques (other than strain mapping).

In this collimated 3DXRD experiment (see 2.6.4 for experimental details), the effect of many crystals is averaged in a volume of 300 μm^3. The intent is to evaluate the overall effect of compressive loading and unloading on the preferred crystal orientation within the sampled volume. Although this is an average effect, with crystals coming in and out the Bragg condition independently, and a small proportion of crystals entering and leaving the gauge volume, it is expected that the overall change may provide insights of the behaviour of the microstructure responding to compressive stress in the elastic region.

4.3.2 X-ray Diffraction Finding and Fitting

An example of XRD acquisition is presented in Figure 70, with its histogram and a radial line profile. The image and corresponding histogram were adjusted by saturating

the 5% minimum and 95% maximum range to the full 16-bit range; this is for visualisation only and data processing used the non-adjusted 16-bit range. The rings are centred with the beam stop in the middle of the detector, and the sample to detector distance is 0.15 m at the selected 0.31 Å wavelength. The most intense Debye-Scherrer rings are within the Field of View (FoV). There is significant smearing at angles within the 002 ring mostly due to the glass tube of the loading device.

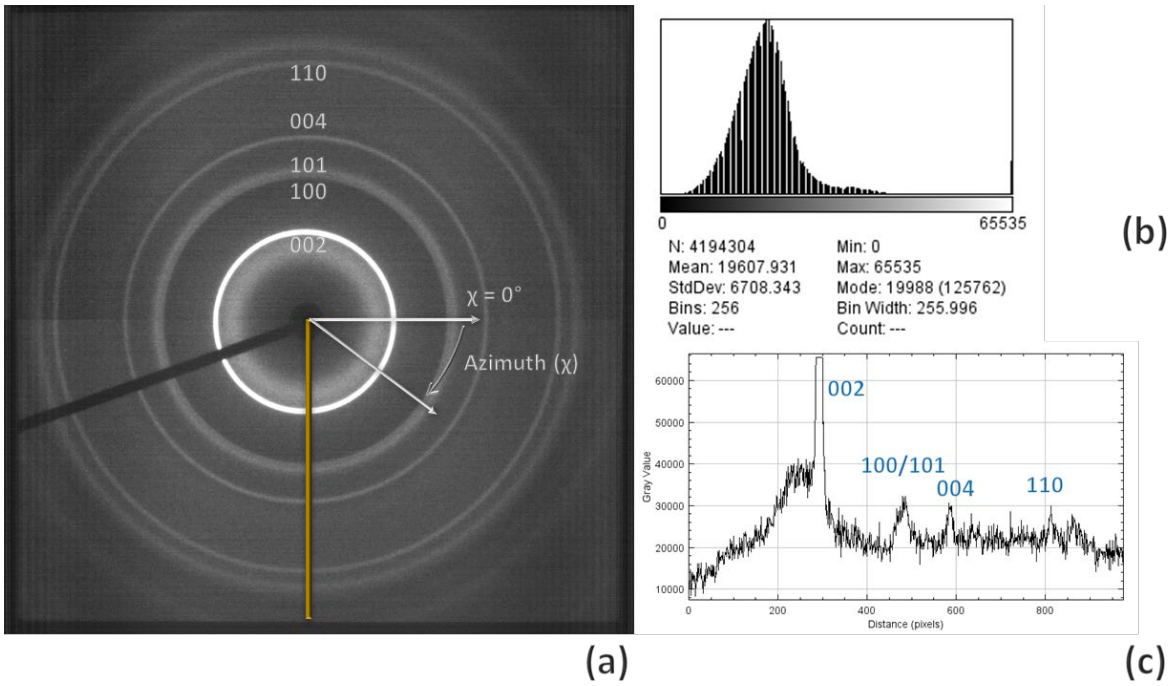


Figure 70: Diffraction image of point 110 at preload and saturated at 5%-95% for visualisation purposes (a) with rescaled histogram after saturation (b) and line profile on saturated image (c) represented by the yellow bar[13]

[13] All three figures are based on the saturated image for visualisation purposes only as otherwise the image would be dark and the graphs would have a low scaling. The data processing however is based on the raw images without saturation.

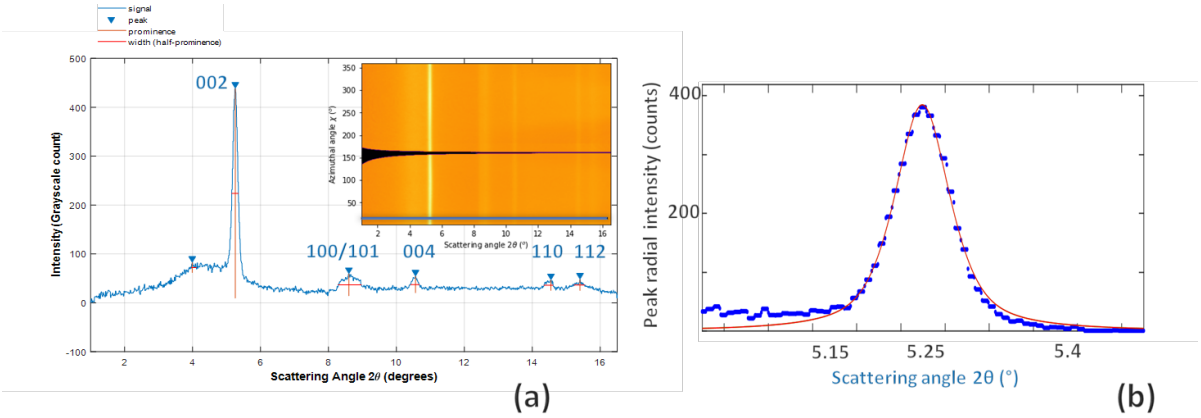


Figure 71: Radial integration and plot of an azimuthal bin after integration (a), and example of peak fitting (b)

Each XRD image was transformed into a set of diffractograms using the ESRF pyFAI code [168, 169]. Calibration was performed on a dummy scan of graphite without load and using the detector positions and pre-calibration files obtained during the experiment. Each acquisition was corrected using a darkfield image. As this image was an average of 20 acquisitions to provide better statistics, it was adapted using a simple 21x scalar point by point division. A radial integration from 1° to 16.5° in 6,000[14] bins was followed by an azimuthal integration from 0° to 360° in 1° bins, using the pseudo pixel splitting algorithm which scales down the bounding box to the pixel area before splitting, a histogram-based direct integration method with a Cython/C implementation. Figure 71(a) presents an example of straightened Debbye-Scherrer rings and the diffractogram corresponding to the azimuthal integration at angle 1°, with the peak height (grayscale value) as a function of the scattering angle 2θ. The most prominent peak is that of the basal plane 0002 at about 5.2° and with a d-spacing of 3.4 Å. A number of other peaks are identifiable and in particular 100/101, 004, 110 and

[14] This is about 3x the pixel array size of the detector, which is the maximum reasonable binning with the pseudo-split method.

112. Although finer integration might permit a more complete crystallography analysis, here the main interest is in the averaged effect of the crystal or crystallite orientation which is best represented by the 002 peak. Furthermore, the 100,101 peaks strongly overlap due to the chosen setup and the limited number of pixels in the active area of the detector, which mean they may not be differentiated. Table 8 presents the approximative results from the peak detection (not fitting) which is based on finding local maxima with user input defining the required minimum width and prominence for a maximum intensity to be identified as a peak.

The position and width values are thereafter used in the peak fitting code to find more accurate positions, width (FWHM), height and area, however for the sake of clarity only the 002 peak results will be presented in this study. The fitting uses as inputs the peak positions as seeding points and twice the width as window size, and it employs a variable alpha-Voigt algorithm. In addition to the main peak properties, outputs include the shape factor as well as the RMS fitting error and the R-squared coefficient of determination which are indications of Goodness of Fit (GoF).

Table 8: Peak finding (not fitting) for the preload, angle 90°, azimuth 1°

Peak	Intensity (count)	Position (°)	Width (°)	Prominence (count)
Error	82.06	3.99	0.14	20.17
002	438.09	5.26	0.20	428.39
100/101	58.95	8.60	0.68	44.50
004	53.98	10.56	0.26	33.35
110	46.32	14.55	0.27	21.02
112	47.73	15.40	0.31	22.49

4.3.3 3DXRD Tracking

In this method for analysis the 3DXRD cylinder axial compression data, whose experimental details are presented in 2.6.4, the intention is to track the preferred orientation in the sampled volume with load. As seen in a heightened contrast and brightness XRD-image in Figure 72(a), the 002 ring presents higher intensities at specific azimuthal angles. This translates as a higher peak height in each associated diffractogram around “Direction A”. Peak intensity is an indication of ordered arrangement. In a polycrystalline specimen, when taking diffraction views at different angles, one can assume the volume fraction of crystallites with their lattice planes aligned in the reflection geometry is proportional to the intensity at a specific sample orientation [186]. In this case, and considering the hexagonal lattice of most of Gilsocarbon graphite, it is postulated that higher peaks is equivalent to a lower mosaic spread in that particular direction, i.e. crystals presenting a common alignment. As mentioned earlier, 3DXRD has mostly been used for anisotropic samples allowing grain segmentation and Friedel Pair matching (“spotty patterns”), which is not possible on graphite samples of the dimension studied here. Other studies however have used partial anisotropy of crystal arrangement in a limited area to perform texture investigation. For instance, Synchrotron X-Ray Diffraction Mapping (SXRDM) has been used to understand the crystallographic texture of enamel by exploiting maps of the Full Width Half Maximum (FWHM) of the distribution of peak intensities as a function of azimuthal angle [187–189]. A similar approach is used here, where instead the position of the highest intensity is recorded. This enables “tracking” of the preferred orientation of the planes within the gauge volume. In other words, it provides a tool to examine for reorientation of the crystals.

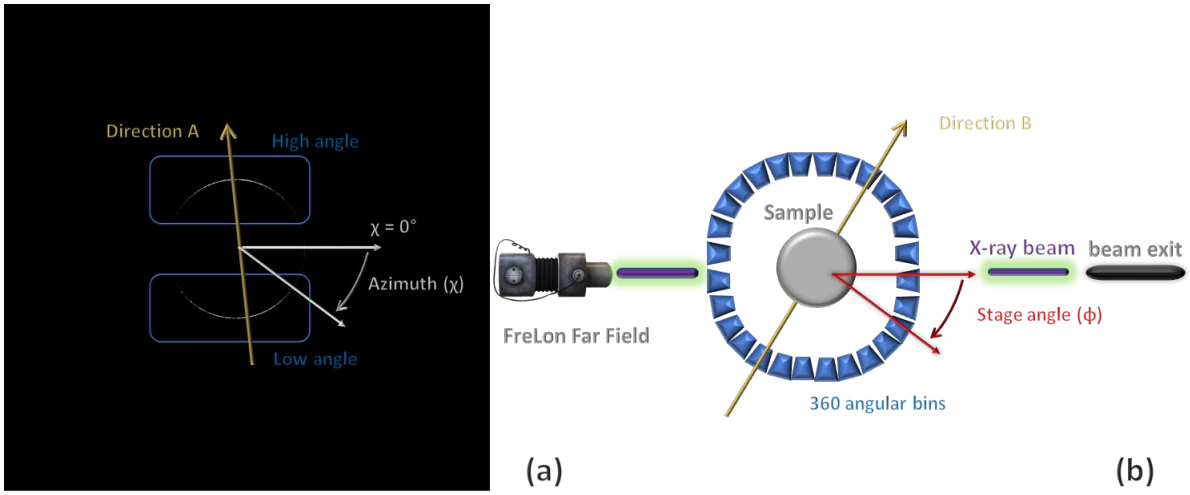


Figure 72: Diffraction acquisition with contrast adjusted to highlight higher intensities (a) and presentation of the method (b)

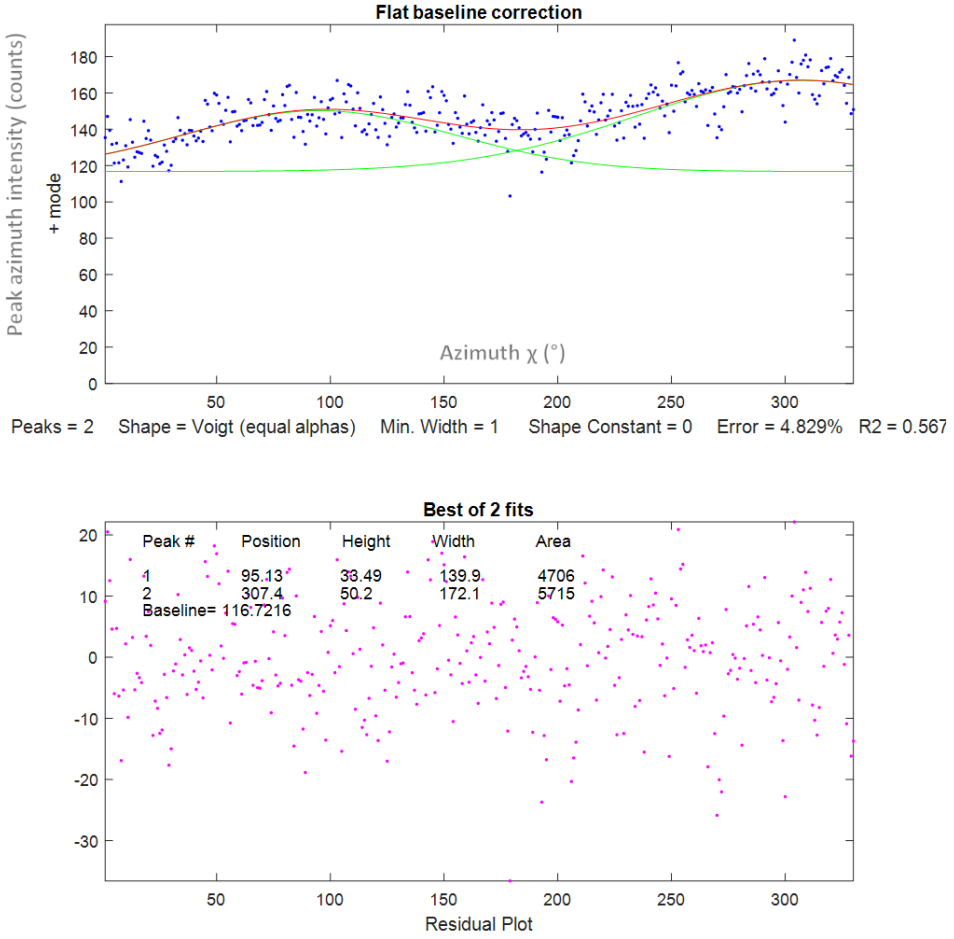


Figure 73: Fit of the distribution of peak intensity with regards to the azimuth angle with low (1) and high (2) angles as pictured in Figure 72

It is worth noting that peak height is only an approximation of intensity, and it is usually preferable to refer to peak area (integral intensity) which has also been computed during the fitting process. Nonetheless, as the interest here lays with the sharp 002 peak, with appropriate background correction it is estimated that the peak height will be the major contributor in the integral intensity. Peak height also does carries over less fitting error than the area. The tracking is allowed by fitting the peak intensity of each azimuthal diffractogram. A Voigt function was used after a flat baseline background correction to identify the positions and shape of the two opposed peaks. An example is presented in Figure 73 where each dot represents the 002 peak height of a diffractogram after fitting, at each azimuth angle.

As pictured by the diagram of Figure 72(b), the next step in this approach is to find whether there is a trend in the orientation of the basal plane around the stage axis Φ. Figure 74(a) plots the results of the azimuth intensity fitting with regards to the stage angle, or in other terms each one of the 362 acquisitions for a single load step. It demonstrates that as the sample is rotated around the perpendicular to the beam, the average azimuthal intensity direction in the gauge volume changes non-monotonically and non-randomly with the angle in the horizontal plane Φ. A 180° symmetry can also be observed, which is in line with the associated pair reflection and suggests that the averaged effect obtained can correspond to tracking a preferred orientation of the grains. The collimated beam size of 300 μm is smaller than the average size of mosaic ‘grains’ in this grade of graphite, and therefore the number of grains in the gauge volume should be small. The approach employed here is similar to monitoring change in integral intensity and finding the projection line by orientation indexing to access basic information on grain position and rotations of the axis of reflection [190].

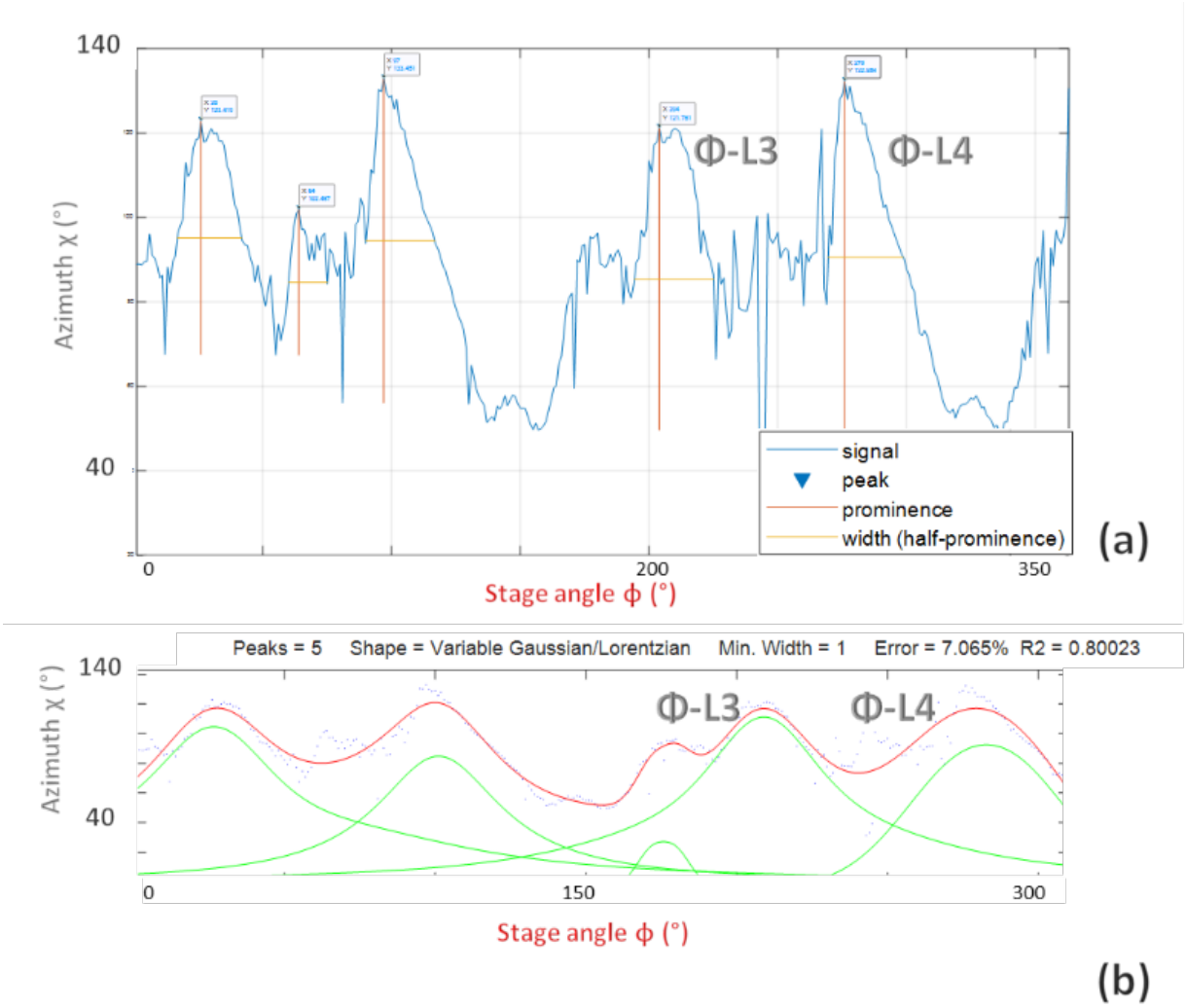


Figure 74: Peak finding (a) and fitting (b) of the low angle for ROI-A datasets of the azimuth positions with regards to the stage angle with the red curve represented the accumulation of the individual green peak fits [15]

Other studies have extracted grain positions and orientation from powder rings with local integral intensity change, from phases “hidden” in randomly oriented crystals [191]. Further fitting the peaks in the change of azimuthal integral intensity provides a fixed orientation in 3D-space that can be tracked with in-situ loading. The multi-peak fitting as presented in Figure 74(b) for the low azimuth angle (40°-140°) of the odd

[15] See Figure 72 for a reminder on the difference between the low angle and its 180° symmetry high angle

datasets (i.e. ROI-A, steps from preload, 3, 5, etc.) used a variable Gaussian/Lorentzian function with up to 10 trials to find peak positions, heights and width. Similarities can be drawn from the high azimuth angle (220°-360°) of the same dataset showing complementary information (Figure 75).

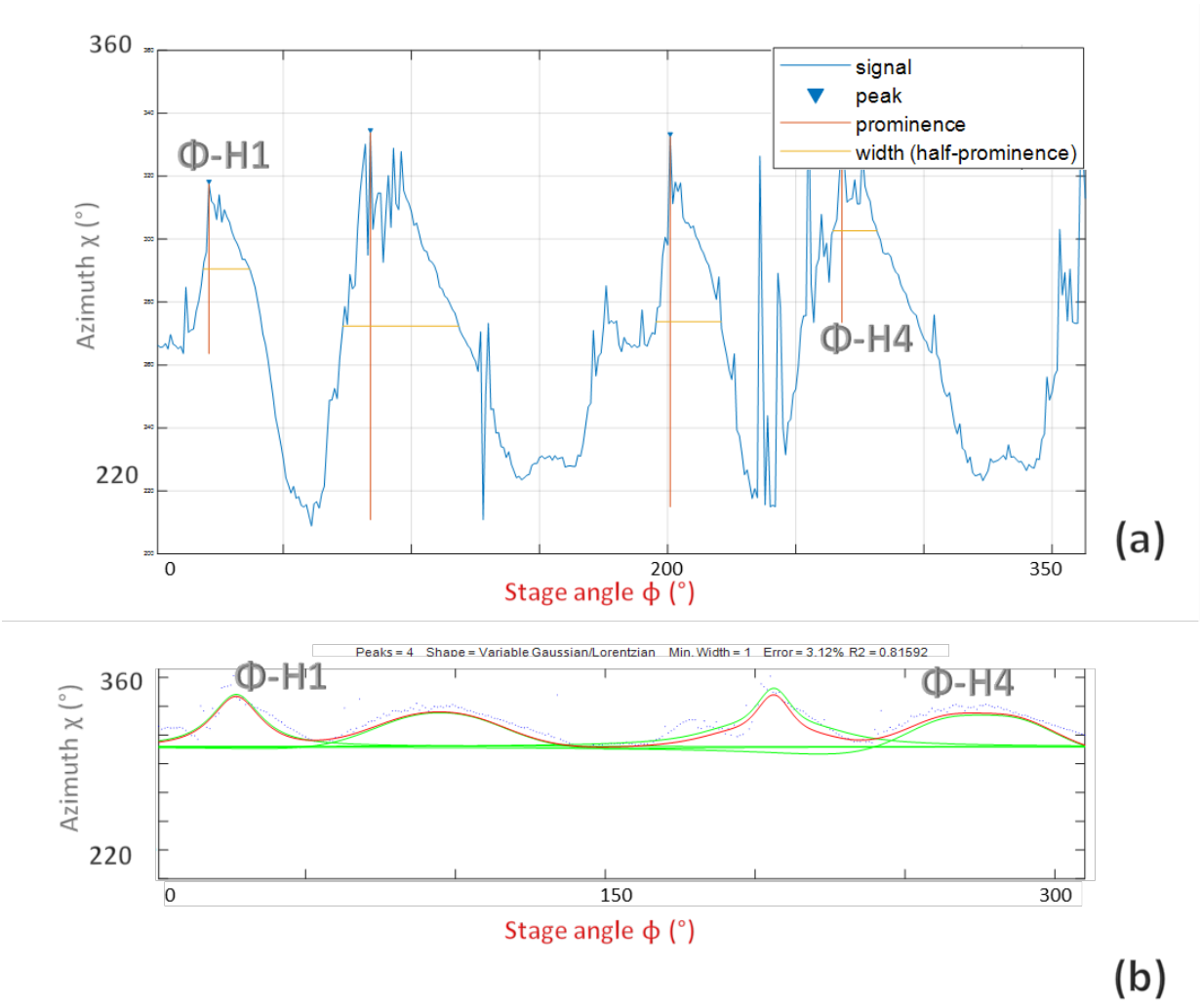


Figure 75: Peak finding (a) and fitting (b) of the high angle for ROI-A datasets of the azimuth positions with regards to the stage angle with the red curve represented the accumulation of the individual green peak fits

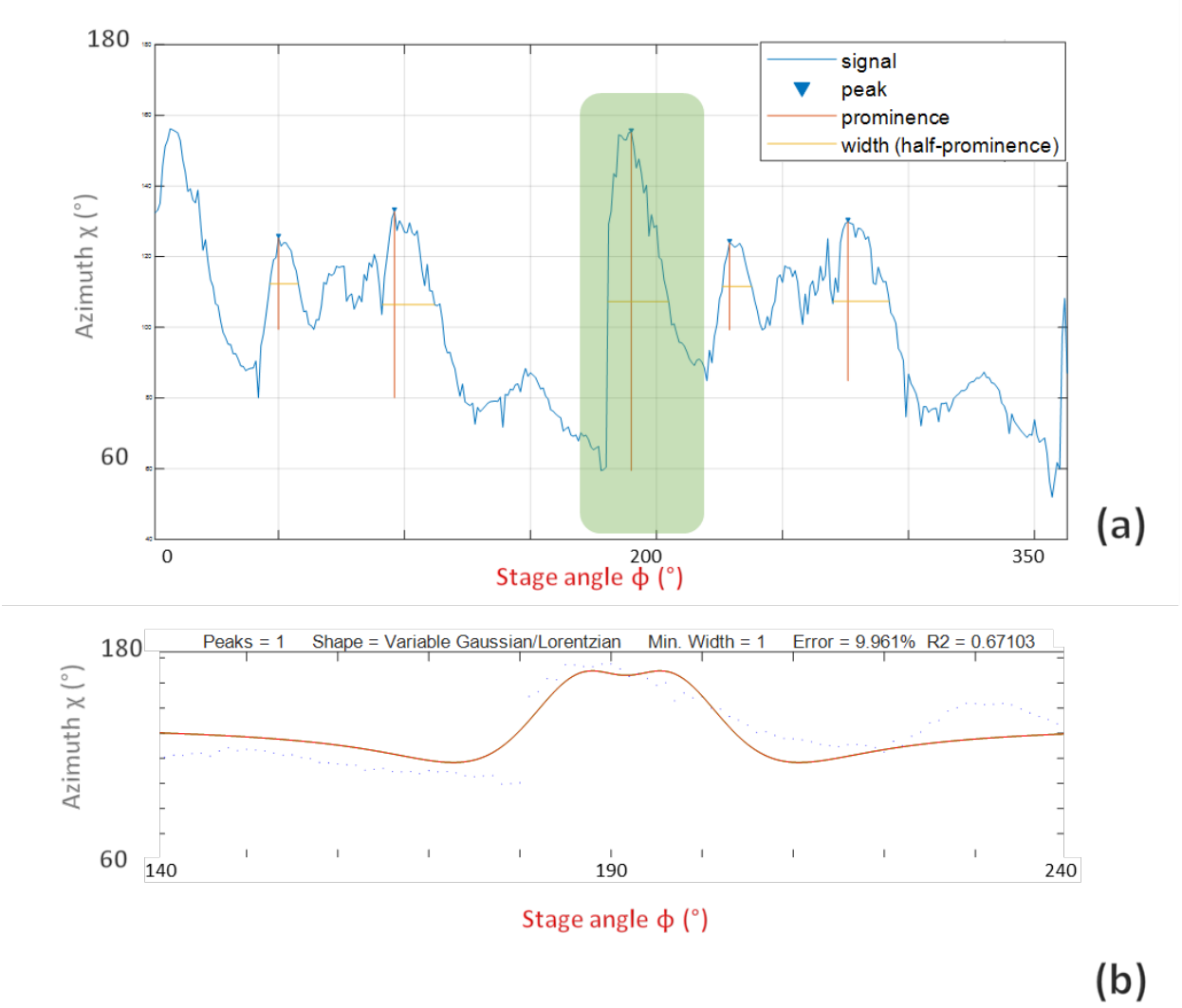


Figure 76: Peak finding (a) and fitting (b) of the low angle for ROI-B datasets of the azimuth positions with regards to the stage angle with the red curve represented the accumulation of the individual green peak fits

Figure 76 applies the same methodology to the ROI-B dataset. For reminder, this is the same sample but with a different region of interest (which is displaced by about 200 µm along the x-axis) and for load step 2 (second preload), 4, 6, etc. Equivalent symmetries and tracking capabilities are found, however in this case only one azimuthal intensity peak (one orientation vector) is tracked with higher accuracy.

4.4 Results: In-Situ Bragg Imaging

4.4.1 Preliminary Observations

This section presents the results of the neutron Bragg imaging experiment as presented in 2.7.3 and 4.2. The final averaged images after differentiation processing of Bragg edge neutron radiographs of the disc compression specimen in region B are presented in Figure 77. A region near the specimen centre (identified by the dashed square) is presented as a close-up view in Figure 78. Within this, several features are highlighted in circles. The images show that there are some features at 1 kN that persist in all subsequent steps (albeit with some change in shape and contrast) of the loading sequence. It can be deduced that the dark persistent features are extinction spots that are not present in the reference stage and that are distinct also from the microstructure attenuation. Similarly, bright spots would arise from grains that were in extinction in the reference image and are no longer in this condition. This points to local changes in scattering, which may be due to either grain reorientation or plastic deformation [82, 184, 192, 193].

The exact number or spatial distribution of these features are yet to be quantified. This would allow the correlations between the applied strain and grain deformation in Gilsocarbon graphite to be confirmed. Nonetheless, comparison of Figure 78(c), (d) and (e) suggests that the local change in Bragg contrast is recovered upon unloading. The feature highlighted by the dashed circle in Figure 78 is mostly visible at the highest load step of 4 kN and returns to a similar appearance as that of the 2 kN step when unloaded. The other feature (solid circle in Figure 78) persists without any significant change throughout the sequence.

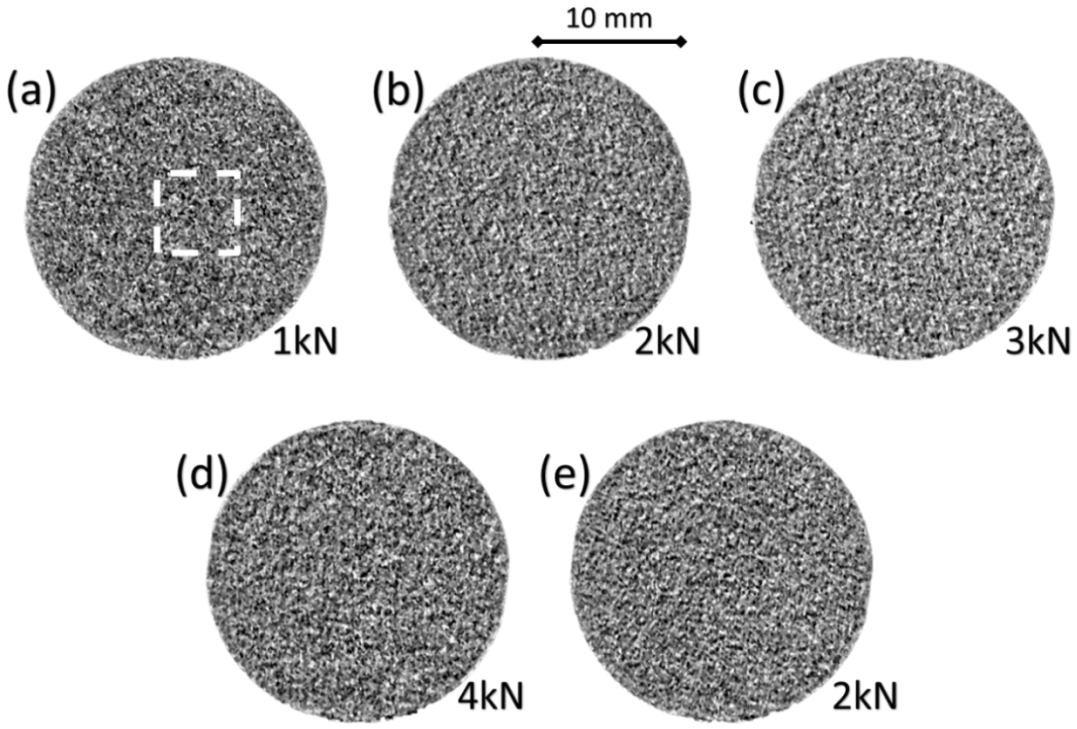


Figure 77: Processed radiographs from energy region B, with increasing load in observation steps from (a) to (d) (1 kN, 2 kN, 3 kN, 4 kN, with respect to stage 0) and then (e) unloading to 2 kN. The dashed square in (a) identifies the feature of interest presented in Figure 78

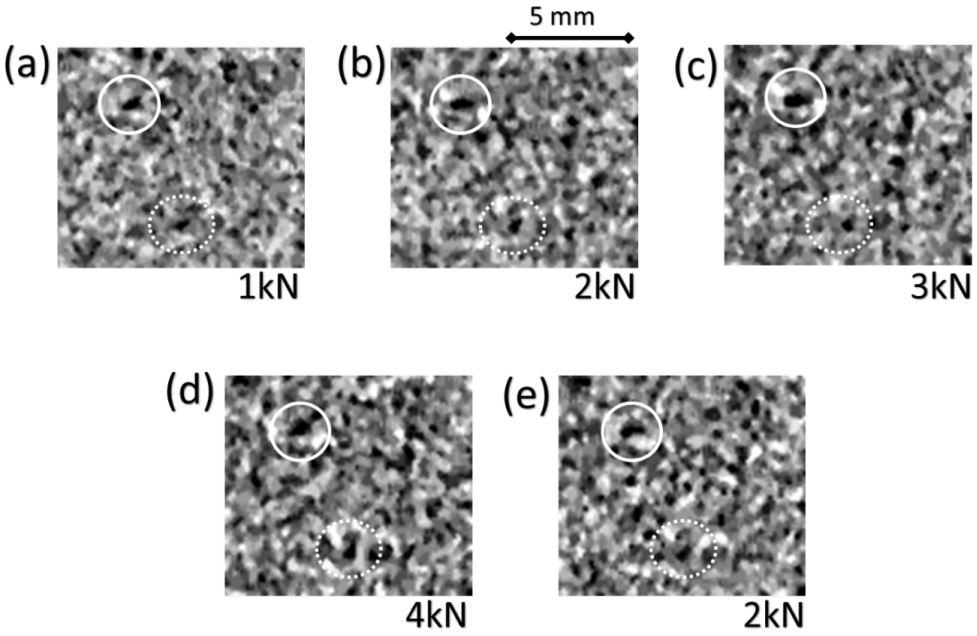


Figure 78: Close-up view at the centre of the specimen (90 × 80 pixels) (region indicated in Figure 77a)

To quantify the general persistence of the contrast features, Figure 79 presents the results of an image correlation analysis applied to the resultant images of stages 2 to 5, with respect to stage 1 (1 kN) (i.e. the images in Figure 77). The analysis was done using the least means squares algorithm with a moving window of 21 pixels and a step size of 4 pixels in the LaVision DaVis StrainMaster 8.4 software, with the objective of mapping the degree of correlation. Image noise and changes in Bragg contrast from grain orientation would lead to low correlation, whereas persistent patterns of features will have higher correlation. The colour scale in Figure 79 represents the correlation value, such that the zones with correlation value exceeding 0.5 have a high match probability with respect to stage 1. The generally high values distributed across the image affirm that the contrast features in the processed difference radiographs are dominated by signal from Bragg diffraction in the microstructure, rather than noise. It can be observed that some regions maintain higher correlation throughout, whereas others change in intensity or shape or appear and disappear. It is interesting to note that correlation with respect to stage 1 appears generally higher for both images at 2 kN (i.e., stage 2, loading and stage 5, unloading). A more detailed analysis of the persistence of high correlation regions, and local decreases in correlation that would indicate changes in Bragg contrast, is feasible but this requires raw data with higher signal to noise for higher confidence.

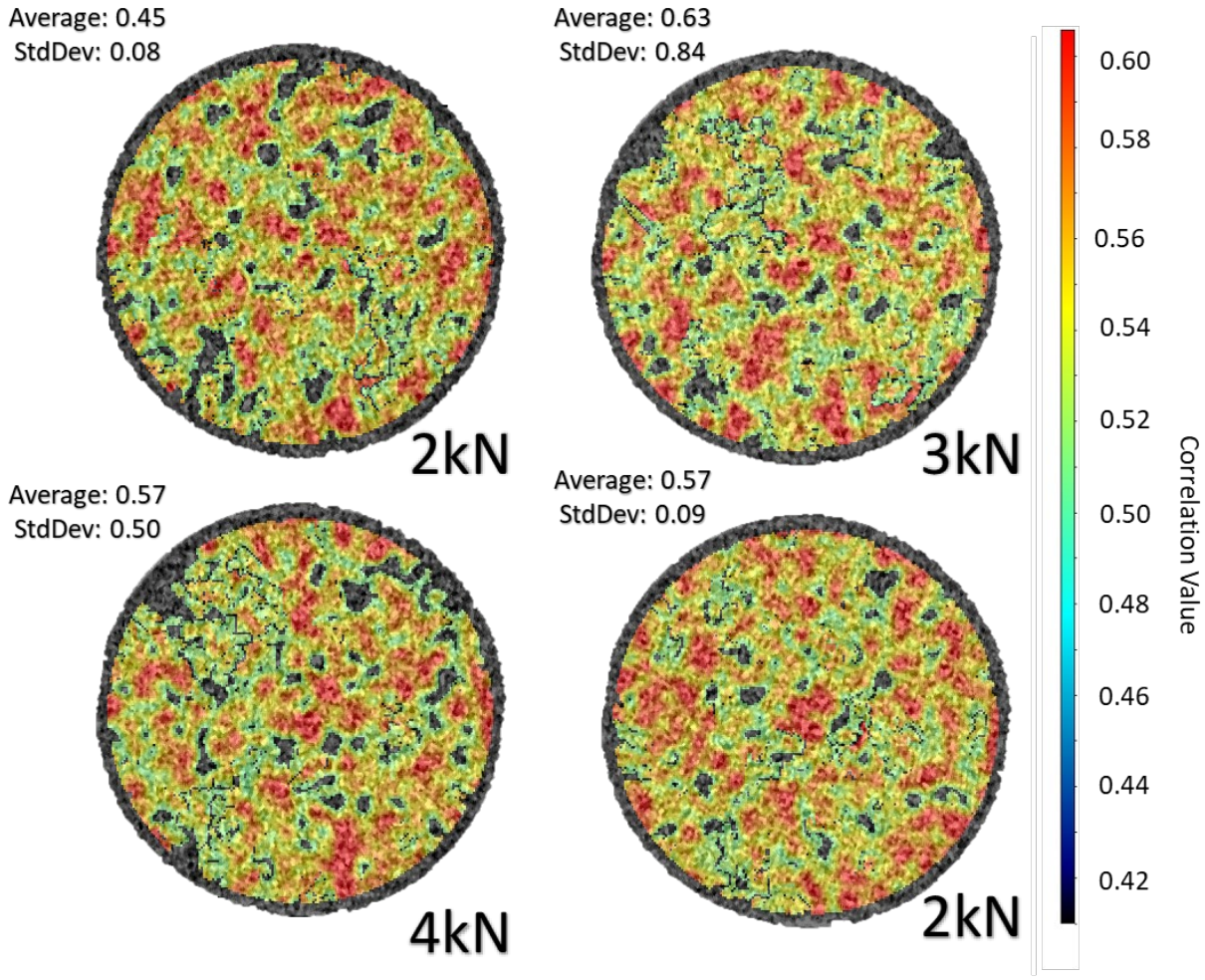


Figure 79: Correlation values for the comparison to stage 1 difference image at 1 kN, zero values are not counted in the standard deviation or the mean

4.4.2 Variation of the Correlation in the Extension Datasets

The datasets obtained in the extension experiments were processed with the same methodology. The second disc compression sample, with a larger diameter of 25 mm, fitted most of the 28 × 28 mm Field of View of the active detector area, which in turns increases the quality of the final image correlation as more extinction spots are available in the averaged radiography images. With more pixels to match the microstructural features, the registration was also substantially better, in that it has required a lower number of energy bins (50 instead of 150) to obtain the averaged images for the determination of the displacement fields, and for the registration to be successful.

Figure 80 and Figure 81 present the final results from the original code, with the microstructure removed and the extinction spots highlighted across all load steps after the reference scan. Many more features are observable, and while some remain the same all along the experiment, other features disappear and reappear as they enter and leave the Bragg condition. More importantly, Figure 82 which presents the correlation of the final results of all stages with step 1 (second step, after preload), show high levels of correlation, indicating that a number of extinction spots are tracked. Particularly, it shows a loss of correlation as the load is further applied, and a higher correlation when returning at the same load as the reference (1 kN). Figure 83 confirms this trend by presenting the histogram of the correlation values for each step (excluding 0 or NaN). It can be seen that the centre of the distribution is around 0.5 and shifts to smaller values when further stress is applied, implying that fewer features are matched within each subset.

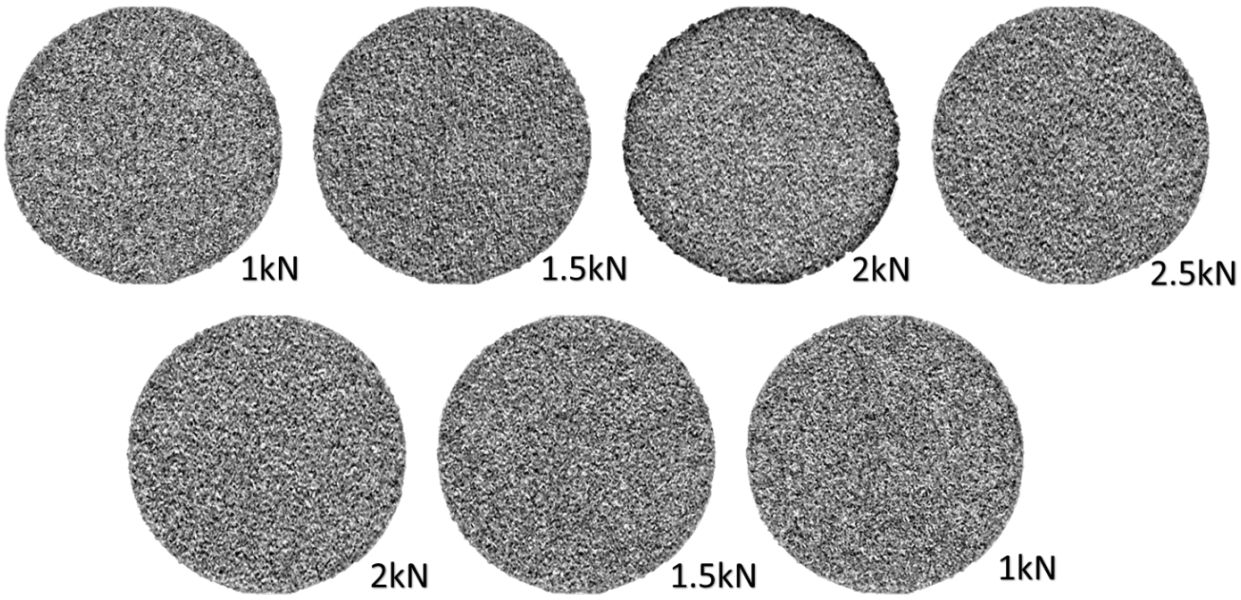


Figure 80: Result of the radiography processing for sample 3, increasing step from (a) to (e): 1kN, 2kN, 3kN, 4kN and 2kN, the circle points to the feature of interest

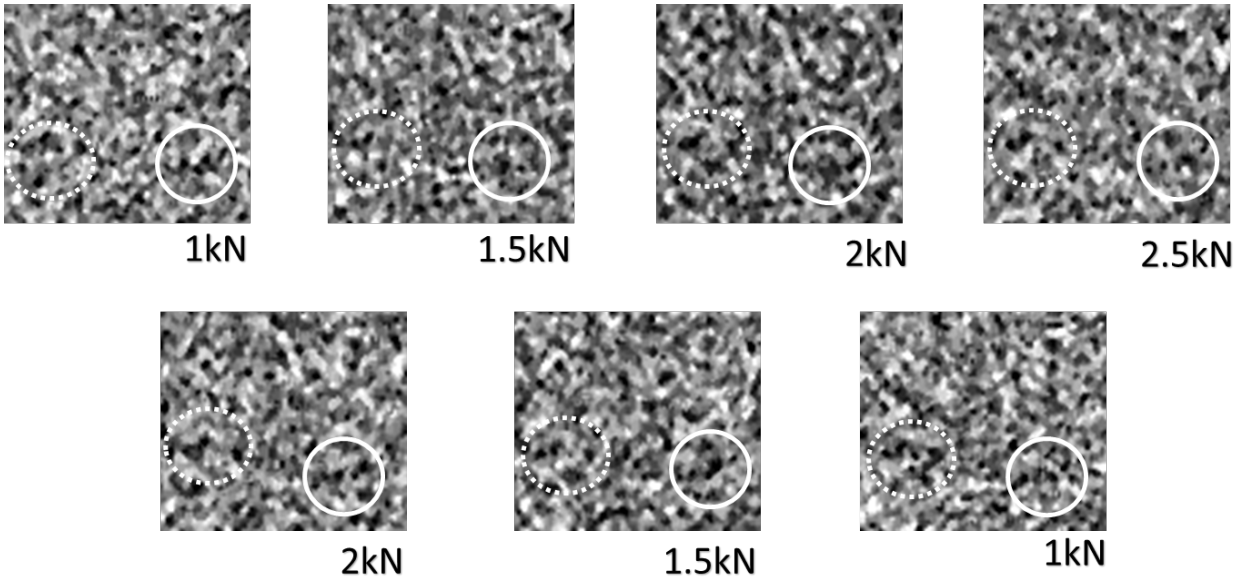


Figure 81: Enlarged view of the area of interest, with increasing load from (a) to (e)

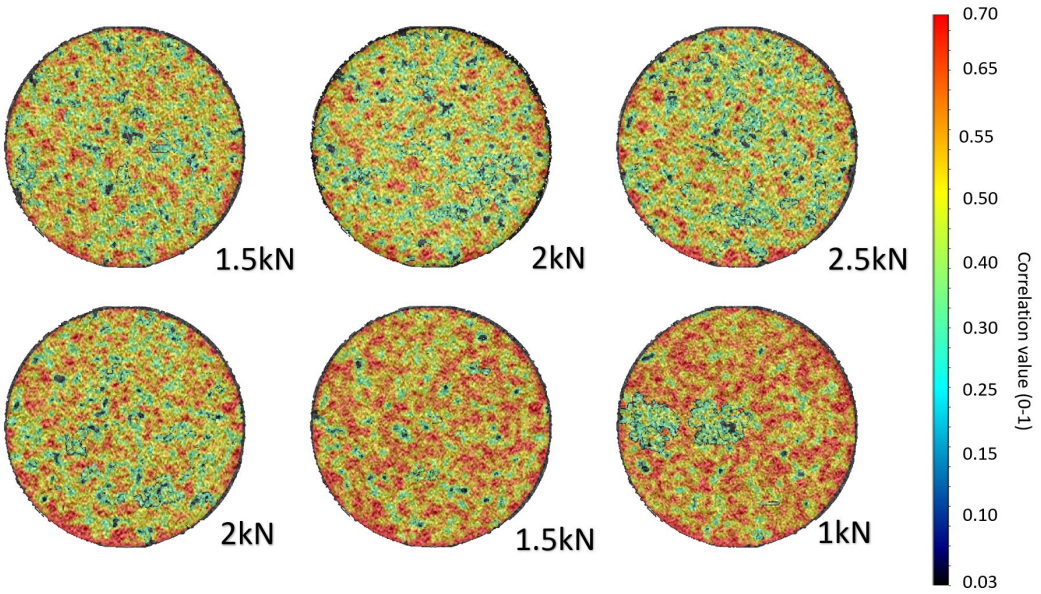


Figure 82: Digital image correlation of all processed stages with stage 1 (1kN), correlation value (preload stage 0 and stage 1 not represented here)

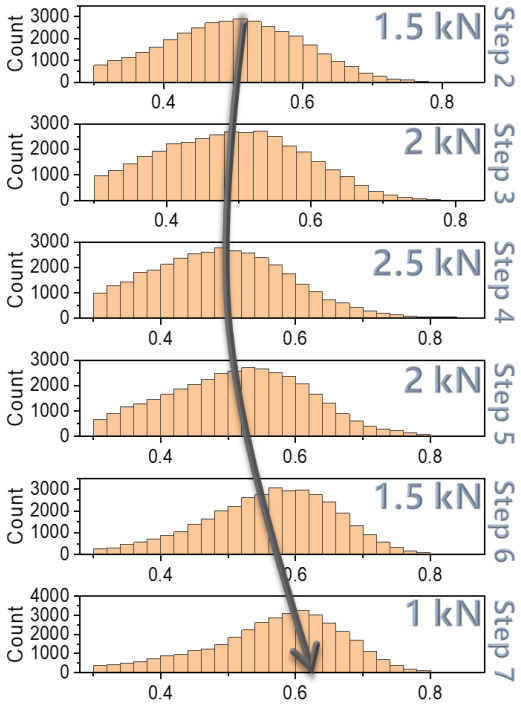


Figure 83: Histograms of the correlation values for the digital image correlation of Figure 82 with curve representing the distribution

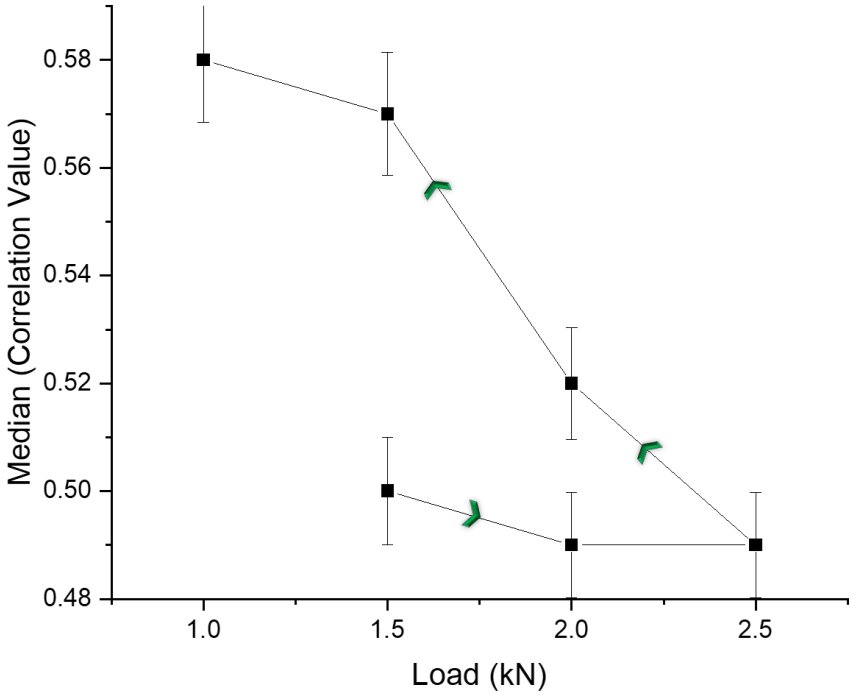


Figure 84: Median of the correlation values for the correlation of Figure 83 with the green arrow representing the succession of loading

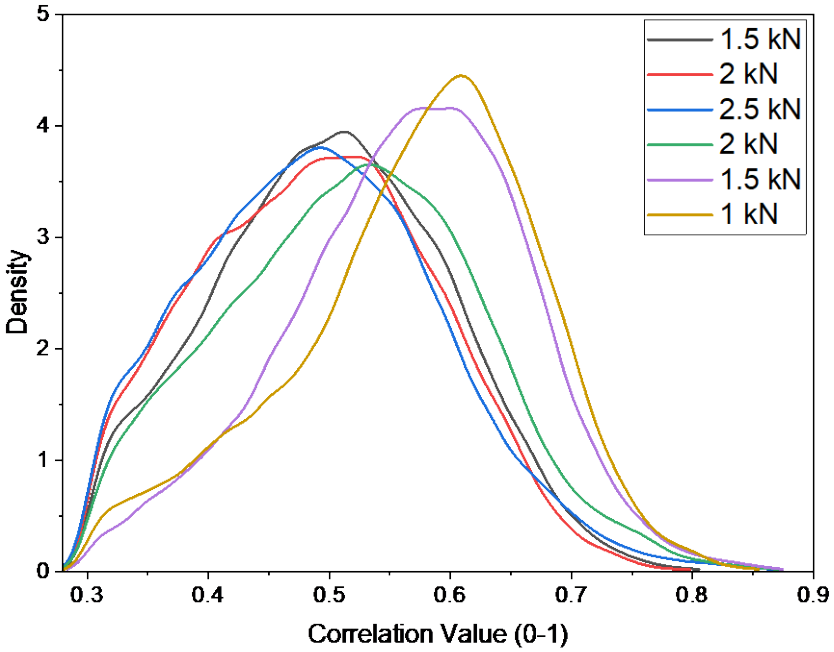


Figure 85: Density plots of the correlation values of Figure 82 presented as curves

Correlation increases as the load is removed, and this process does not happen in a single step but gradually. There are two zones in the last set where there is a complete loss of correlation, and this is likely explained by the selected small subset size rather than any phenomenon in the microstructure.

The correlation value is a measure of how well the algorithm is able to match the pattern in the different images, and in this case a highest correlation value is akin to more extinction spots being matched between the reference (1 kN) and deformed image. Figure 84 summarises this effect by taking the medians of the correlation values in the histograms for each computation. The loss in correlation as the load is increase is small, however the regain in correlation as the load is removed is clearly significant and shows a recovery of the extinction spots present in the 1 kN stage. It is important to note that here the reference is not the preload, but the 1 kN stage, as this is the first stage from which the microstructure can be removed. It is worth noting that for a similar stage (e.g. 2 kN), the correlation is higher on the unload. This may be due to tensile microcracking, in the biaxially stressed Brazilian disc, leading to a reduction of the bulk elastic modulus and the relaxation of residual elastic strains, but some of it may also be an irregularity from the resolution of the technique or the current algorithm. The recovery observed in the correlation value of the DIC is further presented in Figure 85. The view as density plots emphasises the loss and recovery of the correlation. To summarize, there is a change of correlation with load, and hence of local coherent scattering, and this is partially recovered (returns to a similar but not equivalent stage) as the load is removed. This is discussed in more detail in Chapter 6.

4.5 Results: In-Situ Three-Dimensional Synchrotron X-ray Diffraction

4.5.1 Total (DVC) and elastic (XRD) strains

These are the results from the cylinder 3D-XRD and Phase Contrast Tomography (PCT) as presented in 2.6.4. The Digital Volume Correlation (DVC) in DaVis for both datasets allowed to track the movement of the sample under load, with above 0.7 correlation values and low standard deviations. A combined FFT with a 256^3 voxels subset and a search radius of 16 voxels with a 4-step DC completing with a 64^3 voxels subset at 75% overlap. Whilst the 5.4 N preload was used for the ROI-A dataset, the ROI-B dataset whose FoV was shifted by 200 µm used the 50 N step as reference, with in both cases a correlation always relative to the preload. Figure 86 presents the change in displacements averaged over the entire Regions of Interest (RoIs). As expected, displacements along the loading axis (VZ) increase with load and decrease as the applied stress is removed. If the last step at 500 N (estimated) is omitted, the largest displacements are along this axis and below, in any case, 0.05 mm or 50 µm. This is equivalent to a $1/6^{th}$ of the slit size for each diffraction acquisition in this experiment and allows one to safely assume that most of sampled volume for the 3DXRD remains the same throughout the experiment. Indeed, the combined reflections from all the crystals in the $(300\ \mu m)^3$ gauge are already averaged, and it is not expected that, considering the size of grains in graphite, the contribution from crystals entering or leaving the volume will be significant.

The compressive strains, again averaged over the RoIs computed by DVC in DaVis 8.4 are presented in Figure 87. Note that the scale difference between the graphs is due to the ROI-A dataset having a final load step at 500 N.

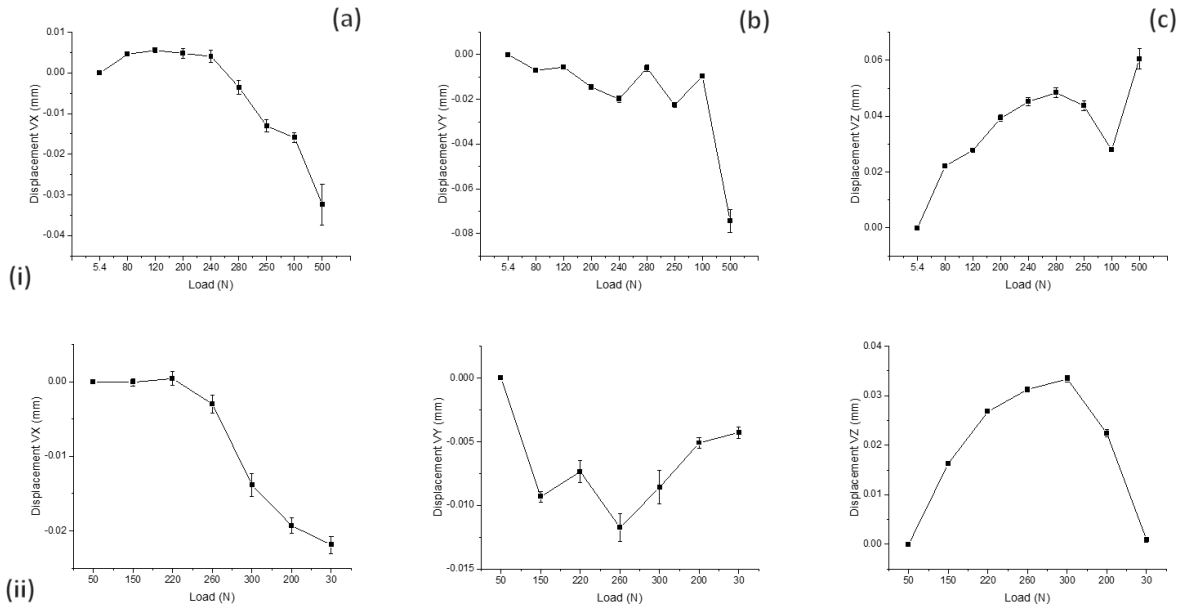


Figure 86: Displacements calculated by DVC and uncorrected for rigid body motion along the X-axis (a), Y-axis (b) and Z-axis (c) for ROI-A (i) and ROI-B even (ii), non-linear step scale

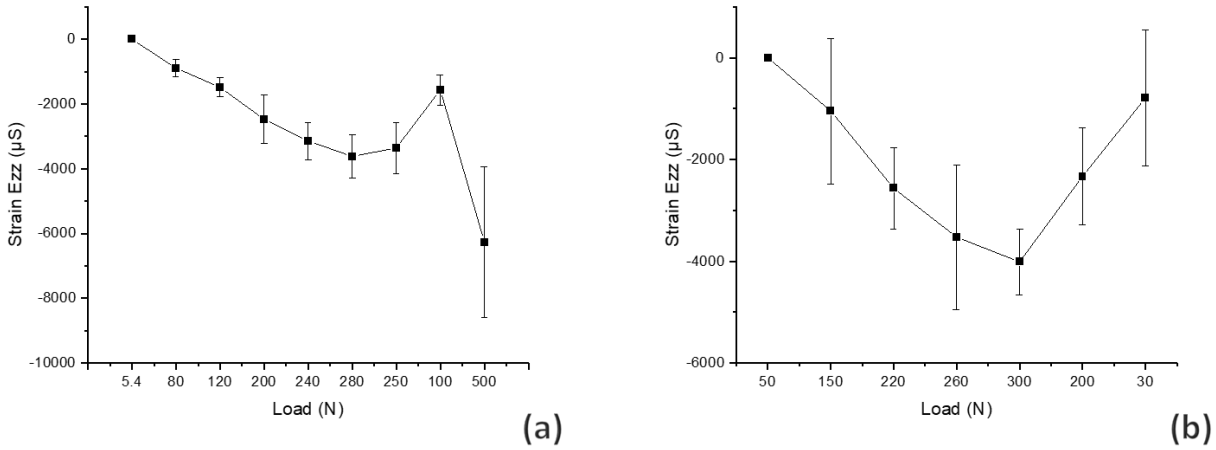


Figure 87: Compressive strains (along the Z-axis) computed by DVC for ROI-A (a) and ROI-B (b) sets, non-linear step scale

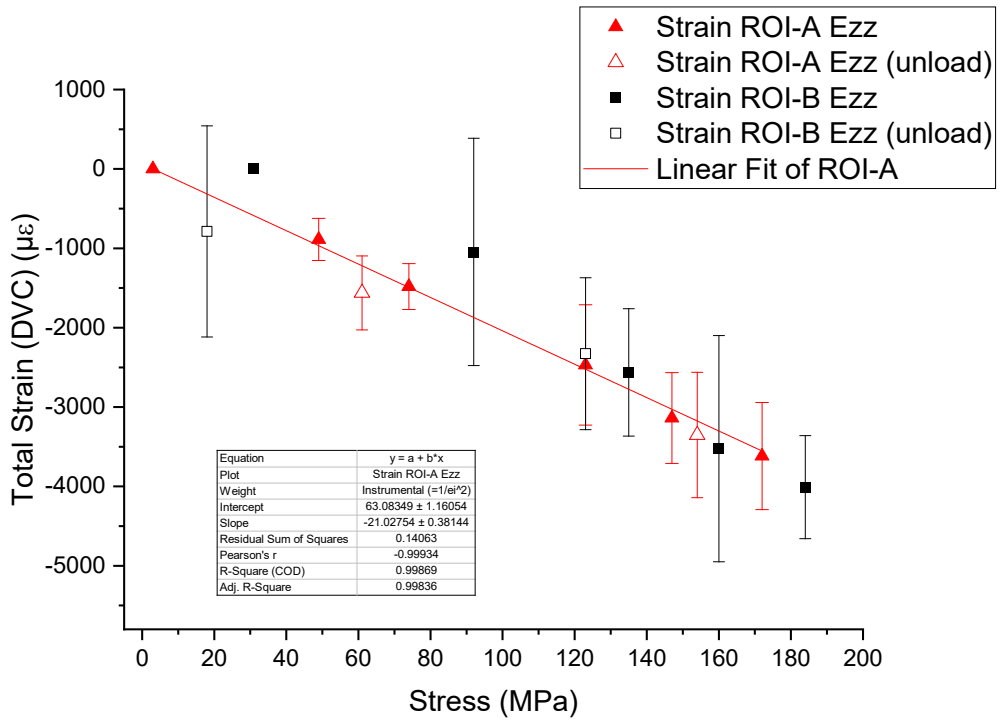


Figure 88: Z-axis total strains for both Regions of Interest (RoI) and associated error bars from the independent DaVis DVC of LR-PCT

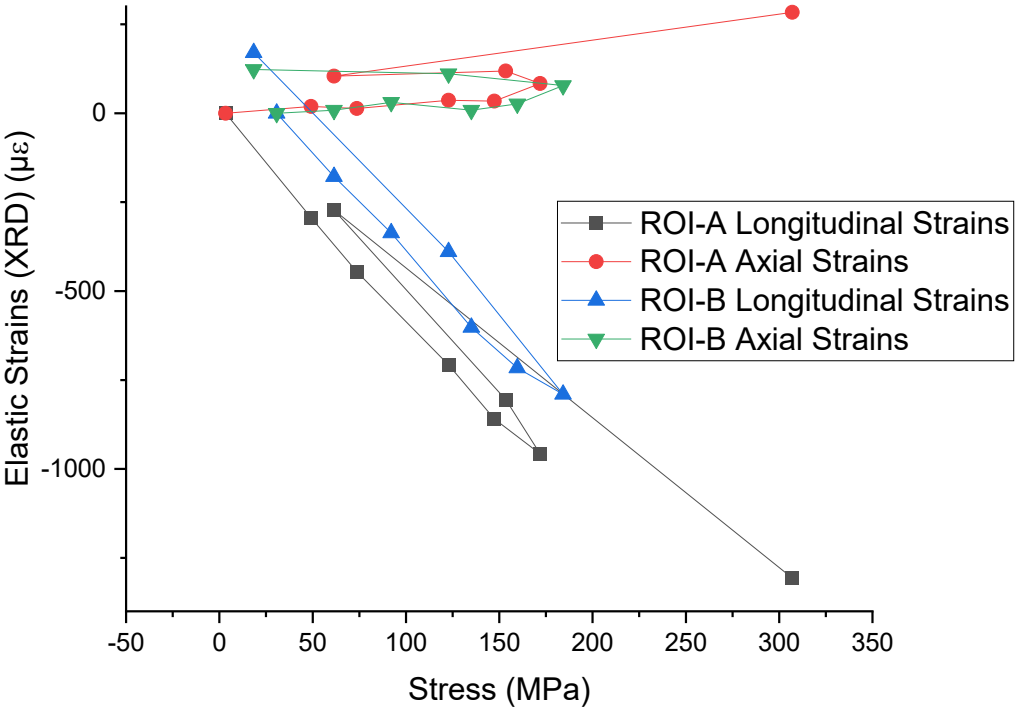


Figure 89: Elastic strains (XRD) for ROI-A and ROI-B of the cylinder compression

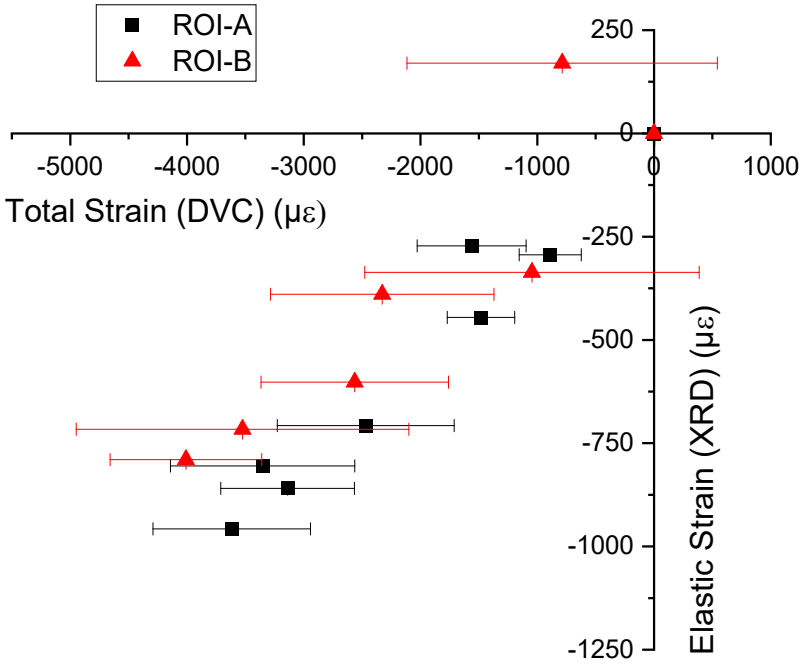


Figure 90: Plot of XRD strains as a function of DVC strains for the cylinder compression

These values are otherwise within the expected range and there seems to be little difference between the centred (ROI-A) and shifted (ROI-B) volumes. It can be noted that although the last step of 500 N may provide indications of orientation at higher stresses (closer to failure), it is much less accurate and should be considered on its own. It presents important shifts, especially along the Y-axis, and a much larger standard deviation. Figure 88 presents a stress-strain plot of the total compressive strains computed by DVC (DaVis) showing that the experiment is within the elastic region. The elastic strains (XRD) were calculated as presented by equation (4), and are presented in Figure 89 for both axial and longitudinal (compression) strains. They show the quasi-elastic response of the sample with load at these stress levels. Figure 90 further plots the longitudinal total (DVC) and elastic (XRD), which compares to results obtained elsewhere (3.4.1).

4.5.2 Orientation tracking

Three-dimensional orientation tracking has been computed for the centred and shifted datasets. High and low azimuthal angles are not matched but presented independently in order to compare and validate the methodology. Figure 91 presents the results of the tracking for two stage directions with load for the ROI-A datasets and for a low and high azimuthal angle each, corresponding to the fitting for each load as presented in Figure 74 and Figure 75 respectively. The Y-axis Φ represents the stage angle at which a particular peak of azimuth angle is observed and tracked with load (as presented in Figure 70). The angles fitted and selected here are those for which the tracking was most successful (best fit). There is a mostly monotonic change in stage angle for ROI-A with increasing load of up to ten degrees, and this change is opposite when comparing both azimuth angles: increase for the low angle and decrease for the high angle. This confirms that the method is detecting a change in physical orientation of the preferred averaged crystal direction, or orientation vector, with increasing load (i.e. a change in grain orientation), which is also confirmed by the crystal symmetry in the low and high azimuth angles. Furthermore, this seems to be partially recovered as the load is removed, potentially indicating a recoverable mechanism. Indeed, for instance looking at Φ-L3 and Φ-L4, the 100 N steps at load and unload are close at approximately 204° and 276° respectively. Figure 92 additionally presents the tracking, as explained in 4.3.2, for the ROI-B dataset. It presents a change in stage position as the load is applied, a decrease from about 191.5° to 191.0°, and a sharp increase 192.0° at around 220 N, before a more stable increase to 192.3° as the load is removed. Although the sharp peak may be due to sudden microcracking in this location, what is important to note here is the negative slope with increasing load and the positive slope with unloading.

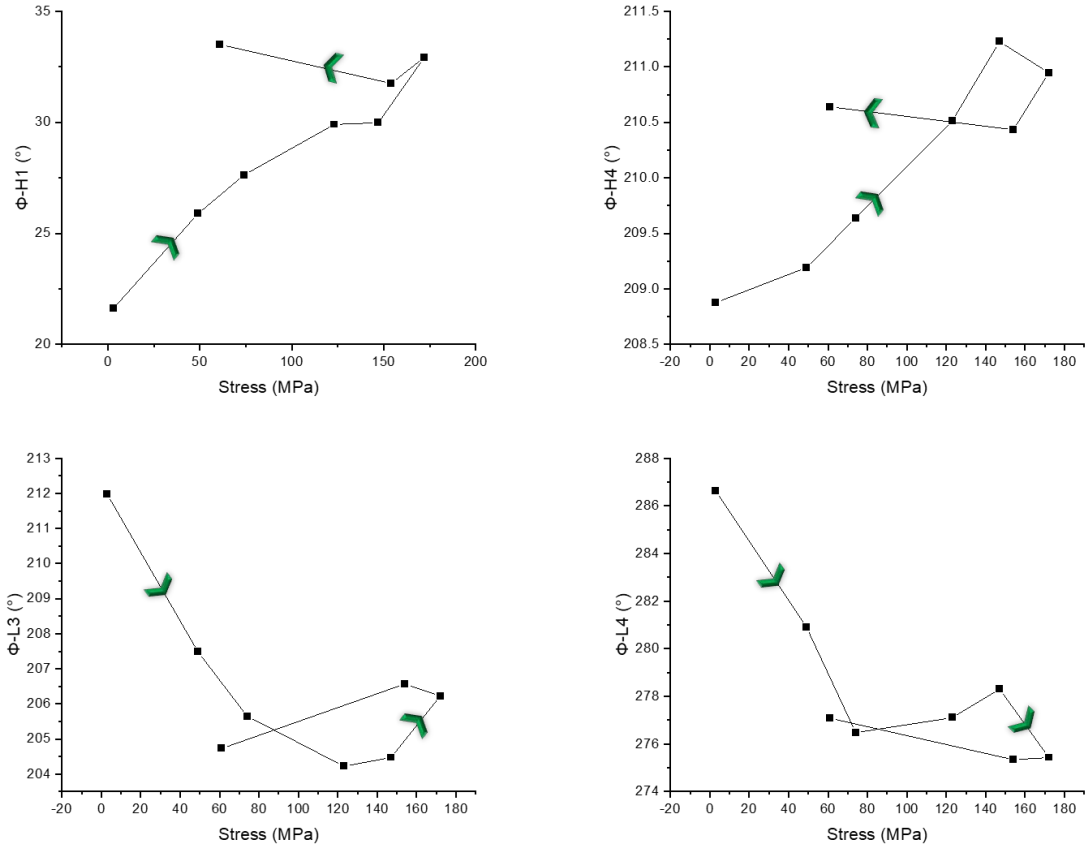


Figure 91: Linear plots of high and low angle tracking, representing the angular stage position (phi) as a function of load (in ROI-A)

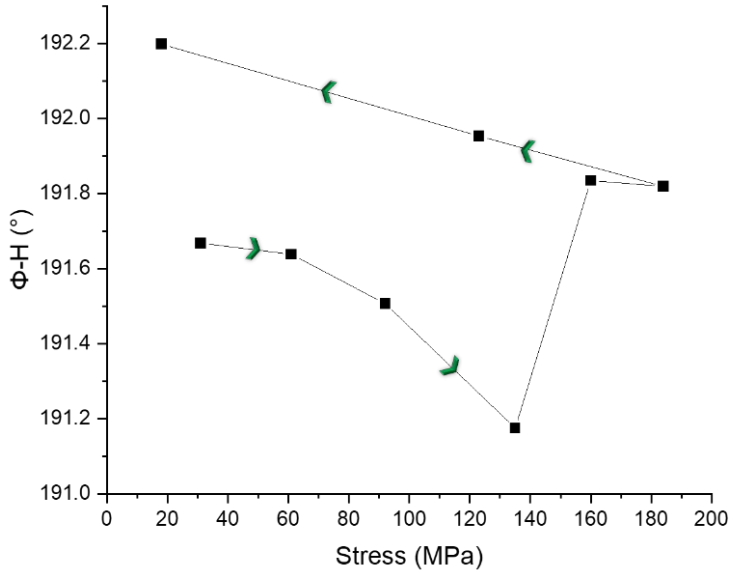


Figure 92: Stage angle of the orientation with regards to load for ROI-B and high azimuthal angle (peak highlighted in green in Figure 76)

4.6 Discussion on Grain Orientation and Elasticity

4.6.1 Summary of Observations

In the previous sections, a few observations have been made with two complementary techniques. The energy-resolved neutron imaging has shown that with increasing load, there is a loss of correlation between registered images not containing microstructure but instead keeping grain domains. As the load is removed, the correlation value increases, which means that more features are in common with the lower load step used as reference. The 3DXRD study shows a change in texture with load, as presented in Figure 91 and Figure 92. Tracking indicated a change of the computed orientation vector with load, which upon unloading, seemed to indicate a partial reversibility. Indeed, there was an apparent change in the direction of angular rotation. It has also been confirmed that the experiment remained in the linear-elastic range of the deformation, by computing the DVC strains. Measurements of the elastic strains have also confirmed this. Together, these points demonstrate recoverable changes in grain orientation with increasing load.

4.6.2 Potential Interpretations

The qualitative results presented by the Bragg-imaging experiment have shown the presence of persistent and non-persistent local features from coherent Bragg scattering during loading that are different from observable microscopic features. As demonstrated in Chapter 3, there is a significant variation in stress state with position in the disc compression specimen. However, there is no particular spatial distribution in the correlation of these extinction spots that might be related to the stress or strain state at that position. Whereas it could have been expected that greater changes would occur at the contact points for instance, where the compressive strains are highest, there seems to be no particular tendency to the distribution of the position of

the highlighted grains. There is nonetheless a more prominent loss of correlation along the vertical perpendicular to the direction of the beam (Figure 82), particularly as the effects of sample rotation have been neglected and the sample is assumed immobile. In brittle materials, plasticity is mostly caused by the formation of microcracks and sliding or slip at corresponding interfaces. In the case of graphite, there are indications elsewhere in this project (see 5) that major plastic deformation occurs only close to failure, but that is far from the cases studied here. Plasticity at the stresses applied in the Bragg-imaging experiment may be negligible compared to the resolution scale of a few hundred microns. The extinction spots observed here and tracked with DIC are more than 200 μm in size. At this stage however, it is not yet possible to identify the shape of the grains or to acquire the position and track specific grains. The novel technique allows one to quantify the extent to which two stages are similar when mostly considering extinction spots caused by Bragg diffraction. If these grains are possibly reorienting, the mechanism that cause this reorientation is less clear. There is knowledge of twinning and kinking in graphite [77], both potentially recoverable, but past observations have been carried out at different scales. It may therefore be concluded here that extinction spots potentially from local coherent scattering can be extracted from the microstructure and correlated between different load steps, and in the centre of the specimen, which is most visible with the discontinuity lines which carry no colour. To lose correlation, the patterns in the subsets of the DIC must change. This may be due to extinction spots appearing or disappearing as the load changes. It is possible that grains come in and out of the Bragg condition, and a potential explanation for this is that they change orientation. The loss of correlation is recovered as the load is removed, which indicates that the orientation change is also recovered.

The elastic recovery of this change can also be appreciated in the 3DXRD data. Compared to the Bragg-imagining data where the Field-of-View allows for many large grains to be detected, this method uses a FoV smaller than the size of the extinction spots observed in the neutron experiment and therefore highlights the combined effect of many small crystals within the 300 μm slit opening. It has been possible to track the effects of applied compressive stress on the change in orientation and especially it has offered another indication that the mechanism involved may be recoverable. The sample, a cylinder, is significantly different than the Brazilian discs used in the neutron experiment, but as presented in Figure 88 the compressive strains are similar to those experienced by the disc specimens in 3.2.3. Another point of comparison is that the applied stress is below the 80-90% to failure load threshold at which microcracking starts to be visible in tomographies. The second view shifted from the centre of the specimen (ROI-B, Figure 91) indicates a slightly stronger reorientation with higher strains, and this is possibly due to a difference in microstructure. There is evidence that this technique captures the averaged effect of reorientating grain domains, and recoverability as the load is removed.

In both cases the recovery seems only partial. This could be a combination of various inelastic mechanisms such as Incipient Kink Bands (IKBs) as previously observed in single crystals [75], grains reorienting, twinning, production of rhombohedral graphite [194] or dislocation glide. Potentially greater effects may occur in the binder, which has shown a higher degree of orientation [154]. The IKB's two walls of dislocation with opposite polarity probably have the lesser impact on the diffraction data, in these experiments where an averaged effect is recorded, except perhaps when stress is sufficient to form mobile dislocation walls, as the basal planes will mostly keep the

same direction. Twins on the other hand are likely to be an important contributor to what is being observed here, but on a much smaller scale, with proven recoverability.

There has not been to date attempts the acquire X-ray diffraction data on filler and binder separately and in-situ, however as observed elsewhere in this thesis with high resolution tomography (3.3 and 5.3.2), and considering the stresses applied in these two experiments, it is not expected that the strain on particular features such as Gilsonite will adversely affect the result and contribute to the change in angle for the 3DXRD or correlation value for the Bragg imaging. It may nonetheless be essential to realise that two branches of work separate here: bulk studies, as presented here, and crystal studies under the SEM or TEM. What is shown here is an averaged effect of reorientation, in the bulk, and that to some extent and at these low stresses, there may be some form of recoverability. This would not have been possible with other types of studies, and not in 3D or semi-3D, and higher-resolution in-situ techniques (which have already highlighted these specific mechanisms), would not explain the effects we are seeing here. It is most likely that more than one mechanism is involved (explored in more details in 6), but that those techniques currently available are unable to help properly discriminate them. Indeed, the main interest here resides with investigating mechanisms at the crystal domain size in bulk specimens (with a diverse microstructure) in-situ and in three dimensions. There are still clear limitations in bridging studies at different length scales. A potential avenue would be to design a novel loading apparatus and extract a single Gilsonite particle for studies with ptychography and Coherent Bragg Imaging in-situ. This would enable to study twinning, kinking and basal slip in the filler. Better quantifying what is presented here would perhaps be more useful to current microstructural deformation models.

4.6.3 Experimental Aspects

The loading rig used in the Bragg-imaging experiment has been designed for brittle and quasi-brittle materials, and the Brazilian disc mechanical testing method, whose use for graphite is supported by a relevant standard [159], is routinely applied to other such materials including cements and geological materials. The developed method offers a means to investigate crystal reorientation or deformation for materials whose grain size, mosaicity and/or surface roughness would not make it practical for any other more straightforward studies. On IMAT, in the best-case scenario, where the 20 mm aperture is sufficient to provide data within a reasonable experimental timeframe, the best achievable resolution would be 70 μm, which is just above the ASIC sensor pixel size of 55 μm. This method is most suited to investigate grain reorientation and deformation in large grain samples, with potential applications in materials such as uranium [195], or those with long range domain structures such as titanium alloys [196, 197]. Although this technique is geared towards large samples, there is an upper limit which is simply defined by the active area of the available detector. The $28 \times 28\,mm^2$ active detector used in this preliminary experiment constrains the possible sample cross-section to below $26 \times 26\,mm^2$. A possible workaround for large samples, apart from stacking up Timepix chips in a new detector, would be to perform acquisitions at multiple regions of interest by movement of the loading rig. The resulting stacks of overlapping radiographs can then be stitched using image correlation methods; however, this would increase the experimental time significantly.

Whilst 3DXRD has mostly been used for grain mapping, another use has been investigated here. Gilsocarbon graphite has been tested for large and small to very small specimens both with far-field and/or near-field detectors for 3DXRD/DCT

configurations during experiment ME1504 [126]. None of the attempts have allowed a sufficient order and “spotty” pattern to properly envisage the option of grain mapping in graphite. As demonstrated here however, 3DXRD measurements can still be exploited and provide valuable information for highly disordered polycrystalline materials.

4.7 Opportunities and Future Work

The in-situ Bragg imaging technique offers insights on elasticity and potential grain reorientation, but however lacks certainty and the ability to separate the different mechanisms that might be involved in the loss of coherent scattering. This could be achieved by denoising further the images and segmenting the extinction spots for each energy bin around the Bragg edge. A new version of the program is currently under development with other partners for this purpose. It includes direct segmentation of the extinction spots, subset tracking with angular dependence and quantification of the changes in image contrast. The manual loading of the rig has limitations on the maximum load that can be attained and requires user interventions at each load step. The current apparatus could be upgraded with automatic loading, and the next design iteration will apply loading direction from the bottom with a motor. This would allow for fully automatic and remotely supervised acquisitions as well as more precise load increments, and the direct tracking of displacement. Further experiments using this methodology, may then be conducted on irradiated samples and/or at high temperatures, to better understand how these affect the structural integrity of graphites.

Chapter 5

5 SUB-CRITICAL MICROCRACK INITIATION, COALESCENCE AND PROPAGATION

5.1 Preamble 5:2

5.2 Data, Challenges and Methodology 5:3

5.2.1 Varied and Large Datasets 5:3

5.2.2 Pre-processing and Shortlisting 5:5

5.2.3 Selection and Methodology Justification 5:8

5.2.4 Advanced Crack Identification, Detection and Tracking 5:9

5.3 Results of Microcrack Identification and Detection 5:10

5.3.1 First Observations of Microcrack Development 5:10

5.3.2 Residuals from a Multi-Correlation Approach 5:15

5.3.3 Crack Detection with Data Remapping 5:34

5.4 Discussion on Crack Initiation and Brittle Fracture 5:40

5.4.1 Relevance of the Technique 5:40

5.4.2 Prevalence of Microcrack Formation 5:41

5.4.3 Preferred Microcrack Path 5:41

5.4.4 Onsets of Brittle Fracture 5:42

5.4.5 Outlook and Future Work 5:43

5.1 Preamble

The observation of initiation of microcracking under compressive load in the microstructure is unfeasible in normal laboratory conditions (chapter 2). The relative unpredictability of the fracture of graphite discs is incompatible with the scan time in laboratories. The study of the last stages before failure requires tomography scan times of a few seconds. In this chapter, part of the results of the high-speed tomography experiment carried out at the Soleil synchrotron on (flattened) Brazilian disc specimens are presented and discussed [129]. Graphite fails by brittle fracture, and although the presence of stress concentrators such as notches or sharp corners offers a guide for crack growth, failure of unnotched samples requires the initiation of cracking from features within the microstructure or from zones of higher stresses such as contact points. Understanding the prevalence of cracking within the microstructure is essential to guide the design and selection of the next generation of nuclear graphites and will also help improving current fracture prediction models. TEM of Gilsocarbon has highlighted the presence of lenticular-shaped cracks parallel to basal planes in Gilsonite particles and bending of the basal plane [70], that these Mrozowski cracks might potentially be empty [71] or filled with amorphous carbon [69], and are accompanied by nanoscale voids [71]. It has also been shown with polarized light and Raman spectroscopy that filler particles have much finer domains than the binder matrix [154] and that Gilsonite particles account for only around 20% of total volume and the presence of a binder barrier around this filler [32]. SANS has also indicated that up to 70% of the pore structure may be accessible from the surface [66]. Understanding preferred initiation, coalescence, and propagation of microcracks inside the microstructure, away from design stress concentrators such as notches or keyways is of major interest.

5.2 Data, Challenges and Methodology

5.2.1 Varied and Large Datasets

The experimental setup and methodology, presented in Chapter 2, hints at the possibility of producing a significant size of data using the methods described, either by the number of tomographies or their individual pixel size. With many samples and the ability to collect full-resolution datasets in less than two seconds, data management is essential and requires appropriate methodology and planning. In fact, this experiment alone has led to an estimated 40 TB of projection images, of which, after a first pre-selection and reconstruction, about 20 TB became usable volumes. The list drawn up for prioritising for reconstruction of the datasets was based on the records from the experiment, and excluded samples that failed too early for instance, or those that failed far from a trigger. The output volumes were of two types, depending on the acquisition modes. Most of the synchronised acquisition and some of the triggered acquisition tomographs provided $1{,}000^3$ voxels volumes at 2.2 µm/pixel whilst the stepwise and some of the triggered acquisition led to higher quality datasets of $2{,}000^3$ voxels at 1.1 µm/pixel. In this chapter, “fast” acquisition mode refers to the tomographies acquired in stepwise or synchronised modes with python scripts, and “buffer” those that used the trigger-based acquisition and the direct dimax camera software. Since the lens assembly was not exchanged, all tomographies have the same resolution and a field of view of $2{,}200^3$ µm. As projections were acquired over the full 180° range, the reconstruction of most tomographies made use of a simple Filtered Back-Projection (FBP) algorithm from the Astra toolbox and ring artefacts removal; apart from the “buffer” series which due to fast movement of the sample required advanced reconstruction. The final volumes had close to no artefact and were

saved as RAW files of stacks of images along the loading direction, which will be the Z-axis in this chapter.

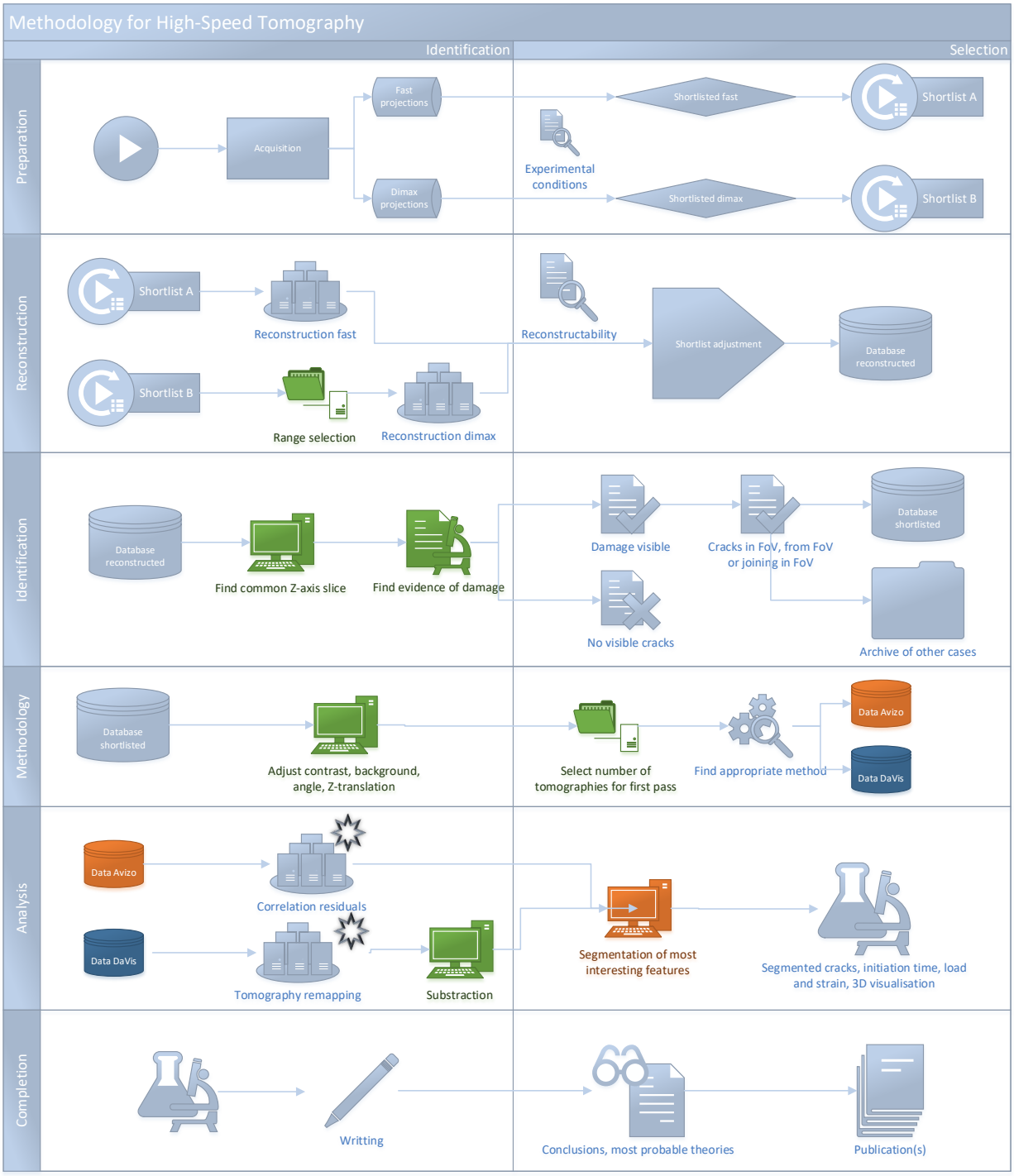


Figure 93: Flowchart describing the methodology of this analysis, with black stars indicating further methodologies for each advanced crack detection

5.2.2 Pre-processing and Shortlisting

Major cracks, from notches for instance, are readily visible by eye on tomography slices and they can be highlighted in image processing programs such as ImageJ. Considering the low deformation of the graphite microstructure, it can be sufficient to extract sub-stacks to remove the most important rigid body displacement along the loading direction (Z). Rotations of the samples were negligible around the X and Y axis (those for which there would be a loss of microstructure), however a handful of volumes had also shifted in the X-Y plane, and they were not shortlisted as they left a combined FoV too small to work with. This shortlist was made prior to any form of realignment as to avoid unnecessary time-consuming operations. Indeed, at the time of writing there is no program available to automatically detect cracks without an extensive amount of user input, putting aside the computer processing power that would be required.

As presented in the diagram of Figure 93, each reconstructed volume was pre-analysed in ImageJ by finding the slice difference along the loading direction between the reference and the last time available, and visually identifying whether a crack from a step was not present in the preload. If there were indications that a crack had potentially formed, the analysis was continued to the next step, where the two same volumes would be realigned manually. This consisted in matching the contrast and readjusting through the unsigned 16-bit (0 to 65,536) or 8-bit range, making sub-stacks to remove the Z-axis rigid body motion, and recovering the Z-axis rotation. Because these tomographies were acquired with a continuous rotation stage, acquisition triggers from the camera did not always match the stage angular position for a specific set of projections. This was corrected by working out the angle between the Y or X

axes and a particular feature with a sharp edge or, if available, one of the sample faces, as pictured in Figure 94.

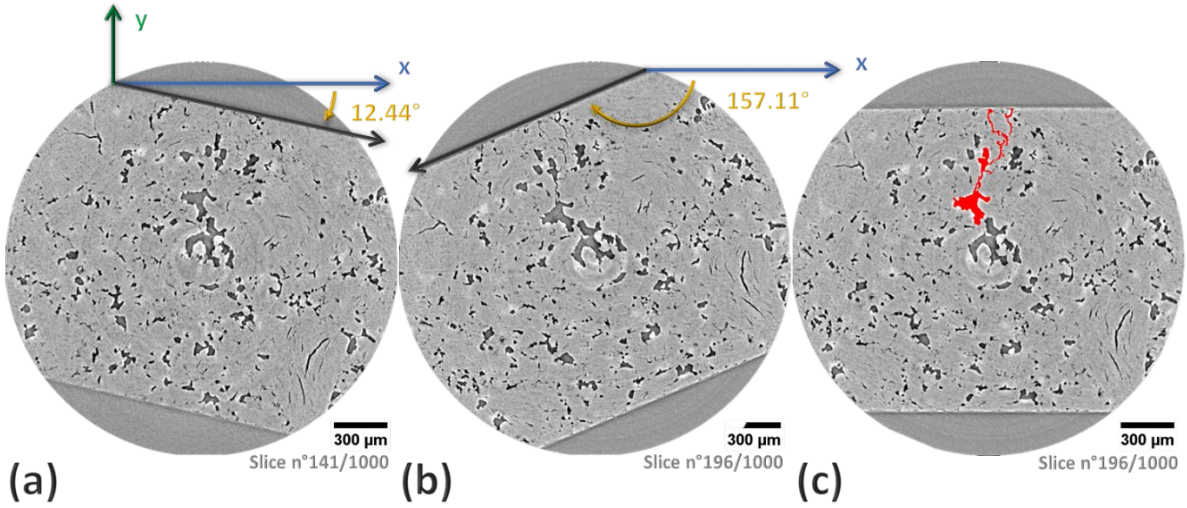


Figure 94: Tomography slices of sample SPKX2 at the reference (a) and final 44th step (b) after finding the common slice along the Z-axis, contrast adjustment and background removal (air still displayed), as well as the same 44th stage realigned for rotation and with the damage segmented using propagation thresholding

Although this pre-analysis was reliant on the human eye and might have arguably left out time-series with microcracks, it was sufficiently thorough to identify those which offered the most interesting prospects. The presence of damage was significantly noticeable, and those time-series that had no damage were easy to rule out as there would also be very little microstructural deformation. The visual identification of cracks was also compared to the notebook and the information recorded during the experiment. This sample list as well as their respective dimensions, are presented in Table 9. It is also worth noting that the reconstruction of the trigger “buffer” series has not been fully completed at the time of writing due to the complexities in choosing the correct projection range and reconstruction method, and there might be more observable damage amongst these samples (see columns ‘crack’ and ‘recon’ in Table 10).

Table 9: Sample specifications for the PSICHE experiment, values with a star denote an engineering target, not an exact measurement, where that was not practical

Sample	Geometry	Diameter (mm)	Thickness (mm)
SPBX3	Disc	3	2.25
SPD701	Disc	10	5
SPD702	Disc	10	5
SPD703	Disc	10	5
SPD705	Disc	10	5
SPD707	Disc	10	5
SPD708	Disc	10	5
SPFX1	Disc	4	1.82
SPHX2	Disc	4	1.86
SPHX3	Disc	4	3.24
SPJX1	Disc	4	2.06
SPJX3	Disc	4	3.93
SPKX1	Disc	4	1.7
SPKX2	Disc	4	1.87
SPKX3	Disc	4	4.06
SPLX2	Disc	4	1.91
SPLX3	Disc	4	3.38
SPMX1	Disc	4	1.95
SPMX2	Disc	4	2.17
SPOX1	Disc	3	3.09
SPOX2	Disc	3	3*

Table 10: Identification of microcracking in the tomography volumes, initiating in the field of view (IFOV), in the field of view (FOV), secondary crack (2^{ND}), in the fast acquisition mode (Fast), in the continuous acquisition mode (Dimax)

Sample	Crack	IFOV	FOV	2ND	Interest	Fast	Dimax	Recon
SPBX3	✓	✓	✓	✓	▮	!	✓	✓
SPD701	✗	✗	✗	✗	▮	✗	.	✗
SPD702	!	!	!	!	▮	✓	.	✓
SPD703	✓	!	✗	✗	▮	✗	✓	✓
SPD705	✗	✗	✗	✗	▮	✗	!	✓
SPD707	✓	!	✗	✗	▮	✗	✓	✓
SPD708	!	!	!	!	▮	!	!	✗
SPFX1	✗	✗	✗	✗	▮	✗	!	✗
SPHX2	✗	✗	✗	✗	▮	✗	!	✗
SPHX3	✓	✓	✓	!	▮	✗	✓	✓
SPJX1	✓	!	!	!	▮	✗	✓	✓
SPJX3	✗	✗	✗	✗	▮	✗	!	✗
SPKX1	✗	✗	✗	✗	▮	✗	!	✗
SPKX2	✓	✓	✓	✓	▮	✓	.	✓
SPKX3	✗	✗	✗	✗	▮	✗	!	✗
SPLX2	✗	!	✗	✗	▮	✗	!	✗
SPLX3	✓	!	!	✗	▮	✓	.	✓
SPMX1	✓	✓	✓	✗	▮	✓	.	✓
SPMX2	✓	✗	✗	✗	▮	✓	.	✓
SPOX1	✗	✗	✗	✗	▮	✗	.	✓
SPOX2	✓	✗	✗	✗	▮	✓	.	✓

5.2.3 Selection and Methodology Justification

A priority list was drawn from the qualitative observations, and this identified samples SPMX1 and SPBX3 as particularly interesting for further processing, either for the size of the cracks or their locations. The next stage of the analysis included their entire time-series with the objectives of identifying the precise location and shape of the cracks, as well as the levels of strains that led to cracking and the time at which cracks initiated. Even though it is possible to have a rough idea of when cracking initiated from the time series through qualitative observations, this is not sufficiently precise due to the presence of many other features and their presence in the 3D (not 2D) domain; and therefore this required additional tools. Both specimens were small Brazilian discs of similar sizes, however the times-series were very different, and this led to two analysis methodologies. Indeed, although Avizo and DaVis can both address the objectives aforementioned, they have their own specificities making them more or less adequate. DaVis is relatively good with a small number of large volumes, preferably 16-bit unsigned (little endian) or 32-bit floating point, as it converts all volumes to 32-bit (which is most efficient when the original volumes are in 16 or 32-bit), but also keeps the entire time-series and duplicate volumes in the live memory (RAM); it does not work well in swap memory mode (RAM to disk). Avizo on the other hand is performant with many small volumes, as it is much more responsive at memory swapping, and it also offers more visualisation, segmentation and correlation tools. Due to its high demand in GPU clock speed and memory however, and because its global correlation algorithm cannot handle too many pixels, it is not adapted for large volumes. Mesh splitting is possible for very large volumes (understood to be above $2k^3$ voxels) and has been used elsewhere in this thesis, but mesh discontinuities prevent its use for crack identification. In summary, the first method (with Avizo) is

used to “rewind” a time series where the crack position is already known and for small volumes, whereas the second method (with DaVis) provides a precise crack detection for high-resolution volumes. These additional methods were necessary, as opposed to simpler manual crack segmentation, due to their number, orientation, position in a very diverse microstructure, and the inability of current segmentation techniques to accurately resolve small feature opening, such as from pre-existing defects.

5.2.4 Advanced Crack Identification, Detection and Tracking

Although many specimens have been tested, in this section the interest is in observing microcracking within one RoI and quantifying the number of cracks that can be seen within it, as well as their positions, their orientations and their preferred growth direction, and more importantly the time, strain and stress at which this damage initiated. Crack detection techniques mainly revolve around two principles. (Iterative) Phase Congruency is an interesting concept which allows to identify and record the position in the 3D space of crack with little use input, providing with higher degree of confidence in the methodology, however its use is currently limited to cracks which have a single direction and a known starting or crack tip position or orientation, due to the conversion into polar coordinates as well as the use of a morphological filter [198, 199]. This technique is therefore not adapted for the current situation as there is no prior information on the crack location, or one needs the direction of propagation, or it may meet with other propagating cracks. Although it is preferable to use the same method and parameters for a given sample, to remove potential user error, different sets of parameters were used across the samples at this stage to make use of the diversity of the datasets. Therefore, a combination of volume remapping with 3D local displacement fields and residuals from a global correlation approach with segmentation by machine-learning based texture classification has been used.

5.3 Results of Microcrack Identification and Detection

5.3.1 First Observations of Microcrack Development

A few examples of cracks developing in the microstructure and away from any bulk stress concentration are presented here, including for samples SPBX3 and SPMX1, at the second stage of the procedure. Compared to large macrocracks initiated from a notch and from a controlled fracture, which can often be analysed and comprehended in two dimensions and slice by slice as they evolve in a known and fixed direction, such as a single crack opening from a notched specimen with wedge insertion [57], microcracks in the microstructure are true three-dimensional features which can take any orientation and propagation direction, and this is even more challenging when looking at a time series. However, it is possible to make initial observations on 2D slices prior to further analysis. The objective of this shortlist is to identify cracks that satisfy a number of conditions. In order to provide information on initiation and coalescence, and compared to stable crack studies previously completed, they must initiate in the field in the field of view or join with another crack within the field of view. This is more easily assessed for cracks that are self-contained in the Field-of-View when comparing reference and final stages, and otherwise requires to look at the entire time series. This is because cracks initiating within the Field of View (FoV) may propagate outside, and would resemble those less interesting that have initiated outside the FoV. In particular, sample SPKX2 presented in Figure 94 both has damage contained in the FoV and damage reaching outside the FoV. It is an interesting specimen as it seems its surface crack originated from the side of a filler particle (below the slice presented), and because it was one of the very few samples that both employed synchronised “fast” acquisition and trigger “buffer” modes and had damage visible before initiating the trigger modality. Nonetheless, as the

reconstruction of the buffer/dimax images was not complete at the time of this analysis, it has been left for further work.

Sample number SPMX1 is a Brazilian disc of dimensions 3 × 1.5 mm, part of the synchronised acquisition batch; there is no trigger mode available. Because tomographies have been collected until failure (as opposed to just before failure), this resulted in a very large number of datasets, 88 for this sample. The steps are presented in Table 11, with the number of scans per step and the load for each step initiation. See 2.9 for experimental details.

Table 11: Synchronised loading of sample SPMX1 with the start load at each phase and the number of scans per phase (*percent from estimated failure, 100% is the calculated estimation of maximum load)

Phase	Percent*	Load (N)	Number of scans
1	PL	30	1
2	RBM	30	1
3	25%	62	6
4	50%	124	6
5	75%	186	6
6	90%	223.2	6
7	95%	235.6	6
8	100%	248	6
9	105%	260.4	6
10	110%	272.8	6
11	115%	285.2	6
12	120%	297.6	6
13	125%	310	6
14	130%	322.4	6
15	135%	334.8	6
16	140%	347.2	6
17	150%	372	2
Total			88

All of these volumes are in $1k^3$ voxels (1 Gigavoxel) with a factor 2 binning, bringing the voxel size to 2.2 µm. Sample movement outside the field of view is negligible, with the largest loss being about 10 pixels along the Y-axis (along the sample diameter). At most, 3% of the sample area falls outside in the field of view, which also contains the entire thickness from face to face, enabling surface observations. Figure 95 offers a top and a side view of the reference volume. The 3D volume rendering has been thresholded by removing grey values associated with the air to better highlight the microstructure, including the pores and lenticular cracks.

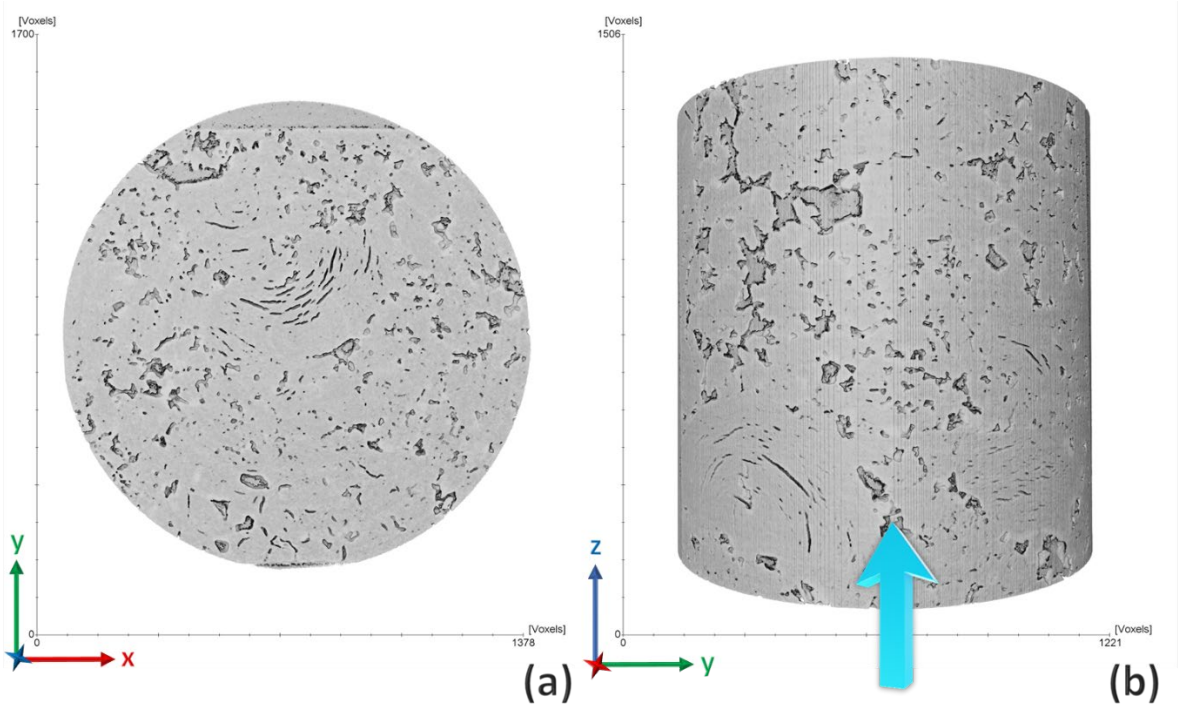


Figure 95: Volume rendering of the initial step (30 N preload) of disc sample SPMX1 with thresholding from the upper XY-plane (a) and side XZ-plane (b) views with the loading direction indicated by an arrow

Figure 96 presents two slices at the reference and final (88) step, after the volumes have been realigned along the loading (Z) axis for Rigid Body Displacement and for the rotation around the Z-axis due to the acquisition method (not sample movement).

The rotation correction was based on the angle between the surface and the X-axis offering a uniform precision, however due to significant deformation and a small Rigid Body Rotation around the Y-axis, the Z realignment was based on observing the microstructure around the most prominent (and interesting) crack, and on this 2D slice, features away from the filler particles slightly change. The damage that will be of interest is a crack that links the filler particle to one of the disc faces, and which is completely contained in the field of view, at its centre.

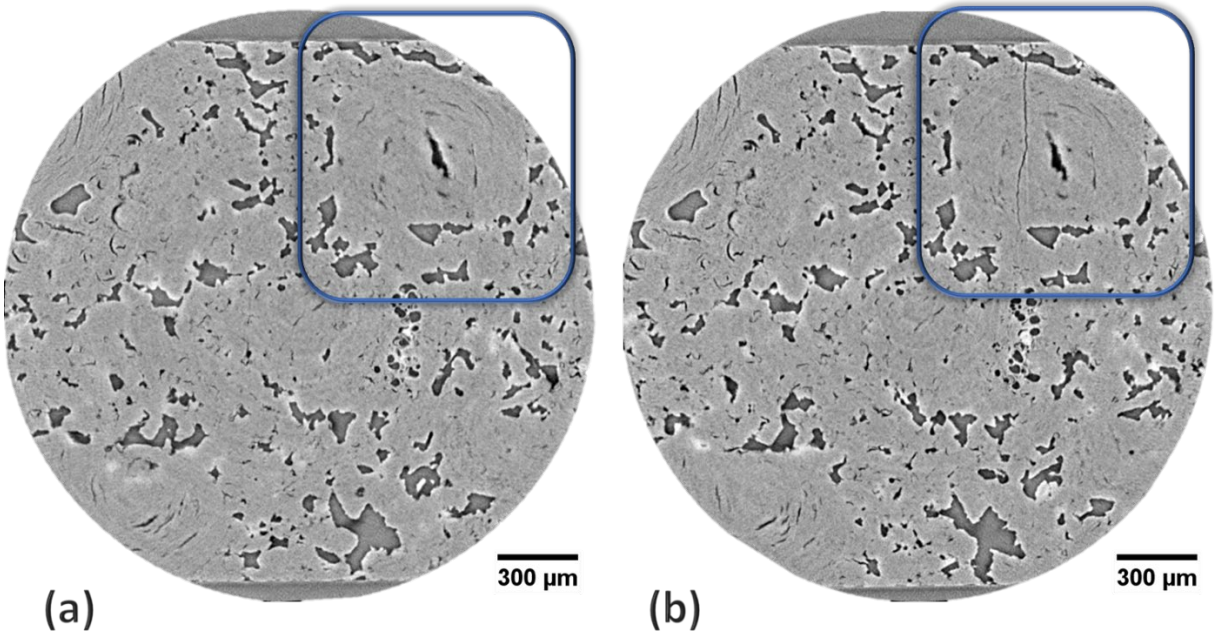


Figure 96: Manually realigned tomography cross-sectional slices (XY-plane) in the centre of specimen SPMX1 at 30 N preload (a) and 355 N final load (b) with a blue frame indicating the location of a microcrack and with the loading direction being perpendicular to the plane of these slices

The second sample selected for this advanced analysis is one whose damage only started to appear in the very last stages of loading. The failure of sample SPBX3, a Brazilian disc, has been recorded in high resolution, starting with 7 stepwise acquisitions (L01-L07) from 10% to 80% of the estimated failure load. It then entered the “buffer” mode and was loaded progressively to failure at a constant speed of

10 N/m. The trigger was successful in stopping the acquisition and saving the buffer at the right time leading to 8 usable tomographies (D01-D08) and three not usable (past the failure or with too much sample movement). The sample movement outside the field of view in the X-Y plane was below 10 voxels. Figure 97 presents tomography slices of the volumes corrected for sample-stage rotation and for rigid body displacement along the loading direction. At first sight, it seems that the damage observed extends outside the Field of View, and this crack actually does not initiate in the FoV, however it will be seen that it is another characteristic that is particularly of interest.

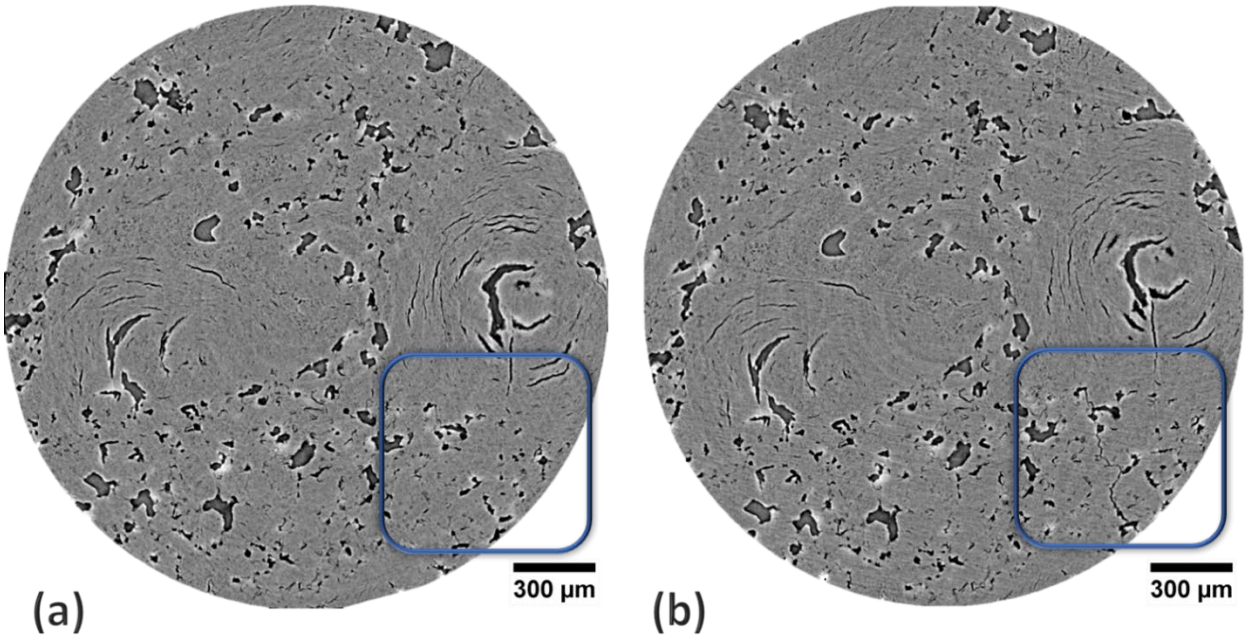


Figure 97: Manually realigned tomography cross-sectional slices (XY-plane) in the centre of specimen SPBX3 at preload (a) and prior to brittle fracture (b) with a blue frame indicating the location of a microcrack and with the loading direction being perpendicular to the plane of these slices

5.3.2 Residuals from a Multi-Correlation Approach

In this part, use is made of the ThermoFisher AvizoFire suite (version 2020.3.1) and the extensions XDigitalVolumeCorrelation and XWind, to process the many “small” volumes acquired by synchronised acquisition for sample SPMX1. Note that “small” here is relative, as these volumes have a billion voxels each of which about 78% is usable; the rest being outside the reconstruction cylinder. It is also worth noting that in this section, no scale has been set and all units are in voxels unless otherwise specified. By design Avizo is more precise and reliable when avoiding the use of real-world dimensions such as micrometres. The general idea of this approach is to run a coarse incremental correlation over all of the 88 available scans, from the reference, and use these displacement fields as inputs for a “time rewinding approach” to find the stage at which the crack initiated.

For this initial pass, stages 1, 2 (RBM), 10, 20, 30, 50, 60, 70, 80, 85 and 88 have been selected. Pre-processing in ImageJ consisted in adjusting and matching the contrast between stages and correcting for the sample stage position by realigning the front face of the disc (where the RoI is) with the radial X-axis perpendicular to the loading direction (where tensile strains are), and saving as RAW files. Contrarily to the manual segmentation as presented before, no filtering has been applied ahead of calculating displacement fields. Note that in this case, the RBDs in compression (Z-axis) have not been removed in the pre-processing stage. It is a considerably time-consuming process as no automation can be planned (the factor will change at each step) and its difficulty rises exponentially as the number of scans increases. However, Avizo has a vast array of registration tools which can subsequently do a more accurate job at realigning the microstructure of deformed volumes efficiently and repetitively, particularly for samples with relatively small strains.

Figure 98 presents an example of such realignment between the preload and the final available volume for the times series of SPMX1. This registration is performed using the entire volumes using a normalised mutual information and an extensive direction optimiser with a tolerance of 0.0001 to find and correct Rigid Body Translations and Rotations only (no scaling), after realigning the principal axes as a first step. The figure shows a colourwash of the reference on top of the same realigned slice of the 88th stage, and it means that everything that is light green is in common but any pixel that is grey or dark green only belongs to one of the volumes. The success of the realignment can be best seen at the edges of pores, for which at most locations no shift (duplicate of the same pore in different colours) can be seen.

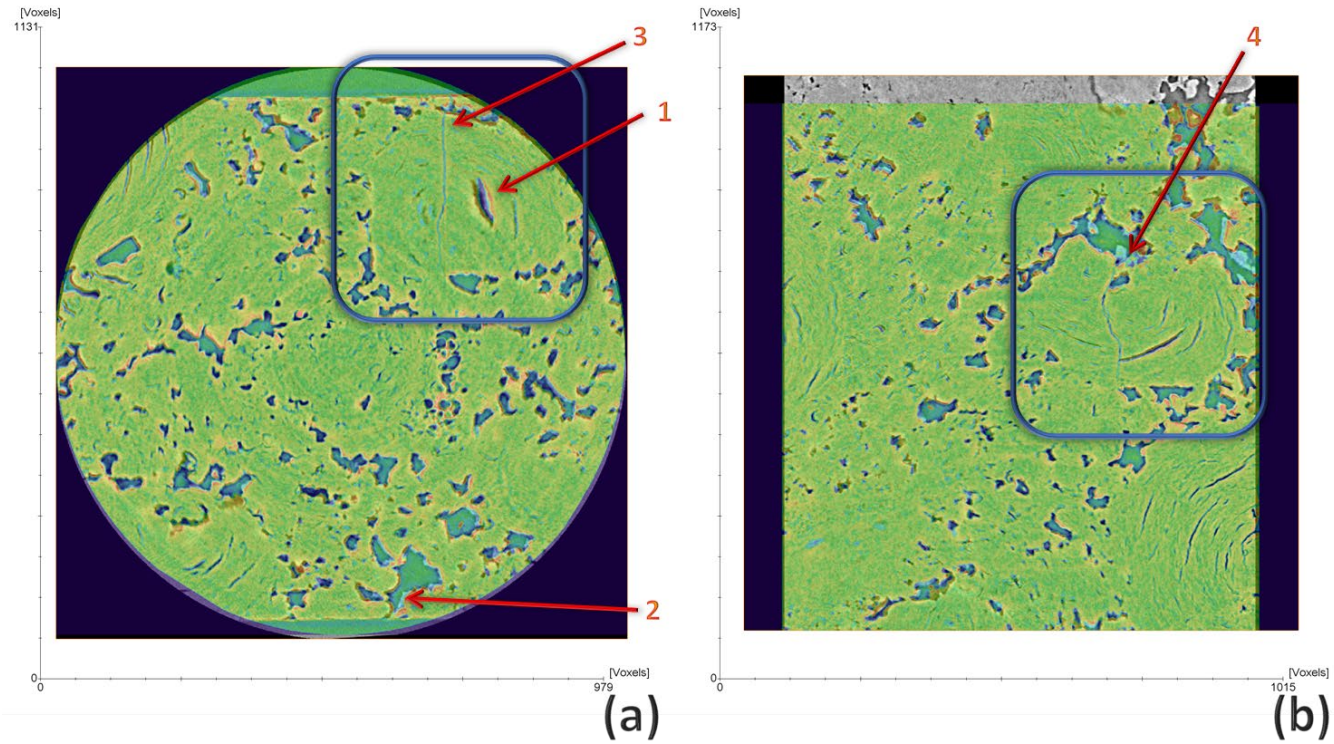


Figure 98: Top XY-plane (a) and side XZ-plane (b) views of the colourwash (overlay) of stages 1 (preload) and 88 (last load) of specimen SPMX1 after realignment using the normalised mutualised information metric (rigid translation and rotation only) with a blue frame indicating the location of the microcrack of interest which clearly appears as a difference between the two stages (everything that is not green or common porosity expresses difference – note the high levels of deformation around the filler particle)

There are a few occurrences where a strong rigid shift is visible (e.g. 1), or a scaling shift (e.g. 2). While the former is likely due to high levels of strain shifting the feature, such as the pore shift caused by the crack opening (3), the latter is likely the result of pore collapse or opening. There are also a number of mismatches (see 4) where new material is visible in the pores, which can be due to damage or features coming in the active slice due to deformation. The crack that is of interest to this particular case is highlighted by a blue frame. The new coordinates in the global reference system of the 88th stage after realignment with the preload provides the maximum Rigid Body Displacements (RBD) experienced by the sample. Table 12 shows that Rigid Body Rotations (RBRs) are below 1° and that Rigid Body Translations (RBTs) have a maximum of 17 µm in the X-Y plane, and 111 µm along the Z-axis. This indicates that more than 94% of the sample's Region of Interest is still in the field of view after the maximum load step.

Table 12: Rigid Body Displacements between preload (30 N) and the final stage 88 (approx. 350 N)

Transformation	**X**	**Y**	**Z**
Translations (voxels)	-0.66	7.51	50.62
Rotations (degrees)	0.71	0.00	-0.70
Translations (µm)	-1.46	16.52	111.36

With the objective of extracting the position of the crack, and by rewinding time to find its origin and associated strains, the global correlation approach requires preparation. The idea is to first find the average length of the microstructure which allows one to set the most appropriate subset size. This is done by running an autocorrelation on a subvolume of the reference stage as pictured in Figure 99, extracted from a central region of the sample, here at location X=371, Y=360 and Z=271 and dimensions 251^3. The algorithm rigidly translates a copy of the same subvolume by minute amounts and tries to match by correlation. The results of the autocorrelation presented in Figure 100 indicate that the length of the microstructure is on average about 22 voxels in any direction.

The autocorrelation results help define the minimum grid size for the correlations of different stages. For a good match, the grid size should be at least three to four times the size of the microstructure. Although realigning the datasets to remove RBDs and applying the transformation can reduce computational work, it requires more memory as duplicates or sub-volumes need to be made from the common volume of the registered datasets in order to define the correlation grid, and the interpolation required to apply the RBD transform may also lead to higher displacement errors. In the present case it was decided that memory efficiency and displacement precision was more important, and realignment has only been used for preliminary qualitative observations, in particular to determine the maximum displacement (or search window), and for the uncertainty measurements.

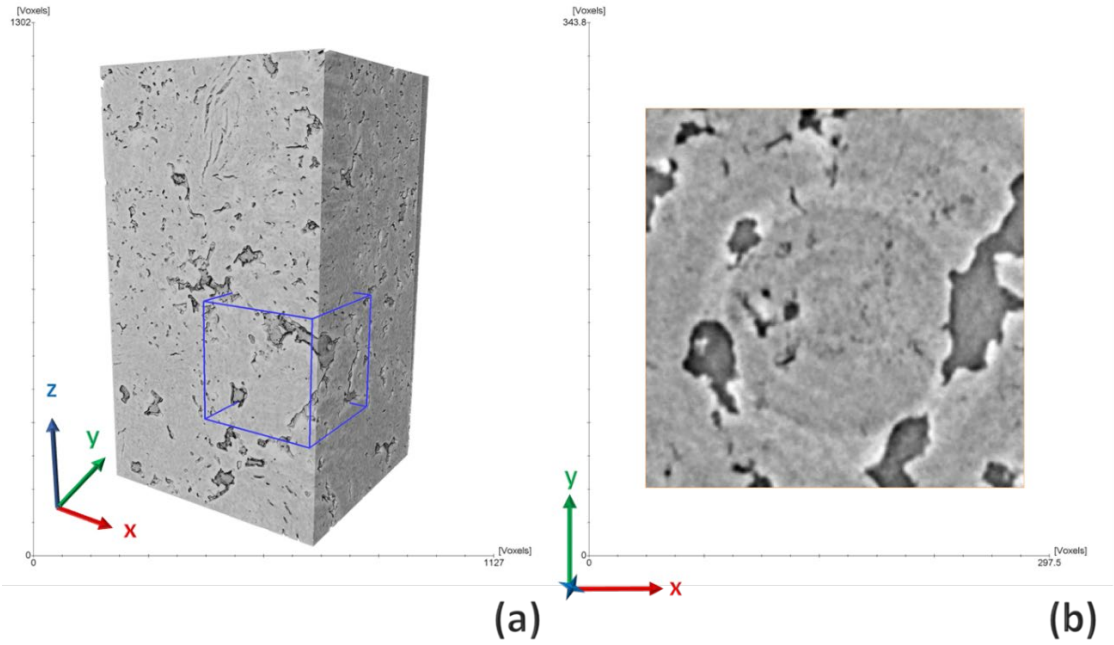


Figure 99: The sub-volume for the microstructure autocorrelation was extracted from the bounding box in (a) shown here with a RoI of the volume rendering (full height of the sample along the vertical Z-axis) from which a XY-slice is presented in (b)

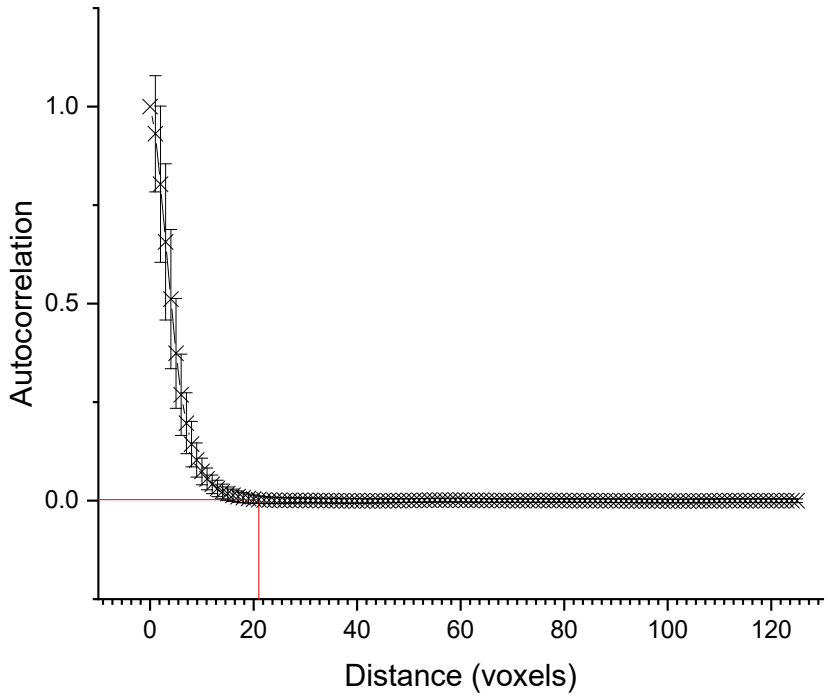


Figure 100: Autocorrelation of the sub-volume indicating that the average size of the microstructure is approximately 22 voxels

The rest of the data was analysed in a differential manner starting with an initial two-stage local correlation approach between steps 1 and 10. A first correlation for translation only, therefore including Rigid Body Translations (RBTs) and local displacements, with a subset size of 130 voxels indicated Z-axis displacements of up to 35 voxels in the upwards direction as shown by the displacement vectors in Figure 101(a), which is in line with the fact that the load is applied from the bottom of the specimen, and corresponds to a vertical displacement of 77 µm for a load applied of about 100 N. Sample movements in the X-Y planes are limited to a maximum of 15 voxels or 33 µm.

The local displacements found in the coarse local approach was then fed to a finer grid with a subset size of 60 voxels. This corresponds to a little bit less than three times the characteristic size of the microstructure, and it was set to find all displacements, including RBDs and deformation, by translation and rotation of the subsets. As indicated by Figure 102(a), there is a good match as the correlation value at the centre of the specimen is close to 1. Figure 102(b) presents the displacement vectors coloured by the correlation value and indicate that most of the displacement is along the Z-axis, with little rotation, as the Z-axis rigid rotation has already been removed. Because of the higher resolution of the second local correlation, one can identify the regions of higher strains and displacement such as on the slice presented in Figure 103. Particularly, one can observe a higher degree of heterogenous deformation at the contact point with the lower platen from which the stress is applied with the electric drive.

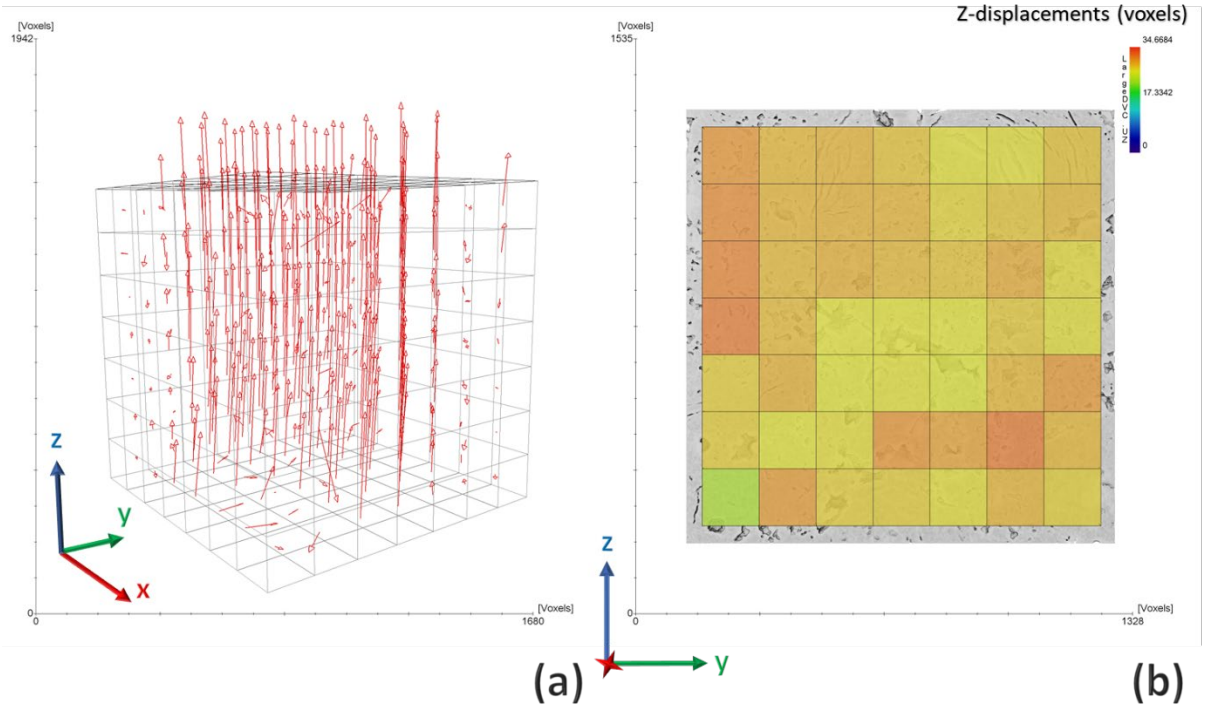


Figure 101: Displacement vectors on top of correlation grid (a) and displacements along the loading direction (b) between the preload (30 N) and the 10th step (appr. 90 N) after the coarse grid local correlation (130 voxel subset size)

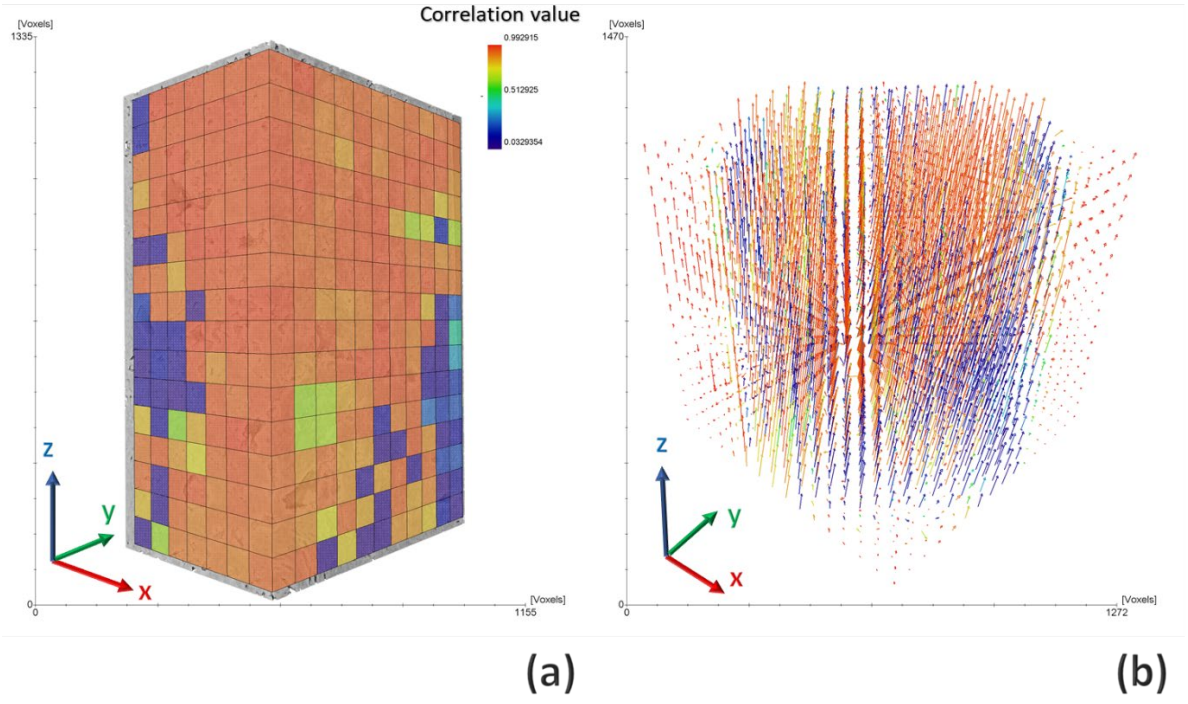


Figure 102: Correlation value (a) and displacements vectors (b) coloured with the correlation value (1 is best) between the preload (30 N) and the 10th step (appr. 90 N) after the fine grid local correlation (60 voxel subset size)

The initial two-stage local correlation approach allowed one to quantify the RBDs, obtain initial results for the deformation, as well as provided displacement fields for the subsequent global approach. In order to estimate the random errors from the acquisition and help define the most appropriate grid size for the global approach, a DVC uncertainty measurement was performed. Whilst all other stages are in a synchronised tomography mode, the first two are single acquisition tomographies to capture the volume at preload (step 1), and at preload with a stage shift of 100 µm (step 2). The shift was made along the X-axis of the stage aligned with the X-axis of the sample, horizontally and perpendicular to the beam. A subvolume was extracted within the centre of the specimen and with dimensions of 500^3 voxels, as presented by Figure 104.

The DVC uncertainty measurement computes the displacement and strain between the two steps after realignment with the method aforementioned, and with a series of increasing grid sizes. From the specified minimum cell size of 30 voxels and the increment of 50 voxels, the algorithm creates four global DVC subset-based tetrahedral grids (based on a mask of the sample region) and perform a volume correlation with each of them. The plots in Figure 105 present the standard deviation of the displacements (a) and that of the strains (b) with increasing grid size. The decrease is a representation of the accuracy of the correlation as a function of the cell size. With grids from about 80 voxels per subset, the standard deviation in strain nears zero, whilst the standard deviation of displacements requires slightly larger grids of up to 120 voxels per subset to converge and plateau. The benefits in displacements accuracy however are minimal from 70 voxels, and this tends to indicate that appropriate precision can be achieved with a subset size from 80 voxels.

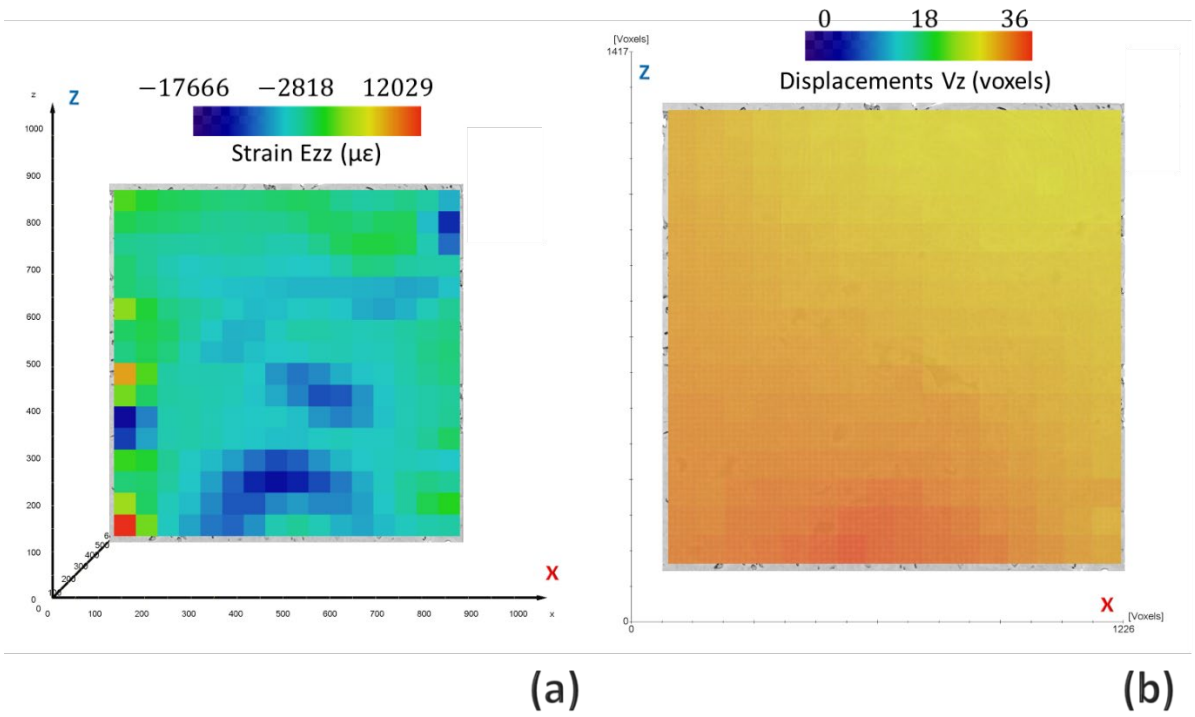


Figure 103: Z-axis strains (a) and displacement (b) between the preload (30 N) and the 10th step (appr. 90 N) after the fine grid local correlation (60 voxel subset size), with (a) displayed scaled down with the axes showing the position of the slice (n°500) in the volume (same volume cut-out / ROI view for both Ezz and Uz)

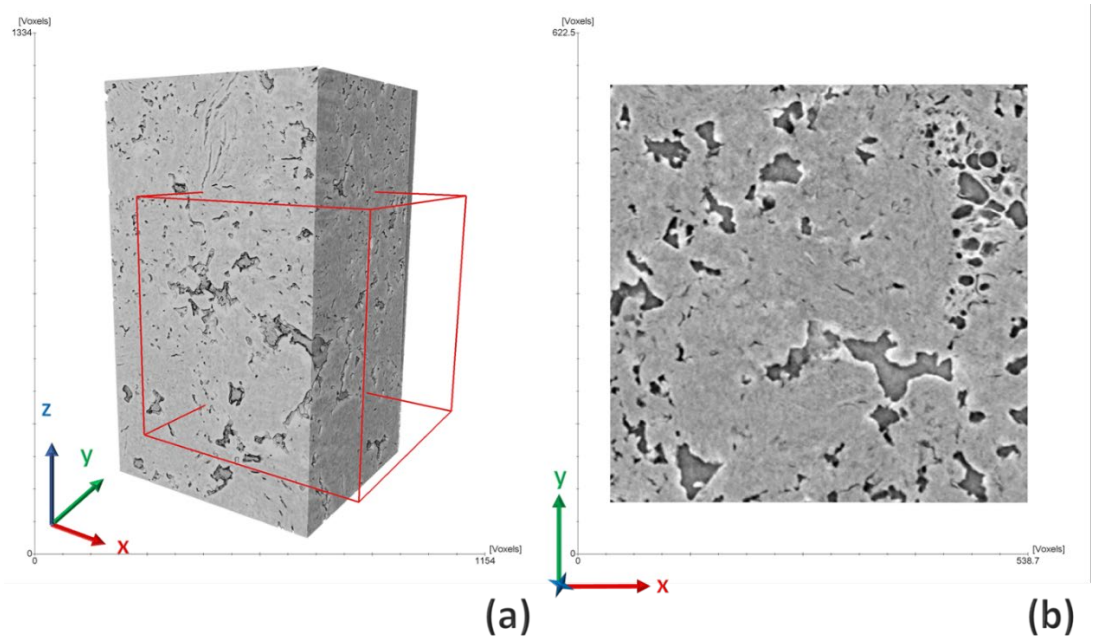


Figure 104: The sub-volume for the microstructure DVC uncertainty measurement was extracted from the bounding box in (a) of stage 1 (and similar for stage 2 once realigned) shown here with a RoI of the volume rendering (full height of the sample along the vertical Z-axis) from which a slice is presented in (b)

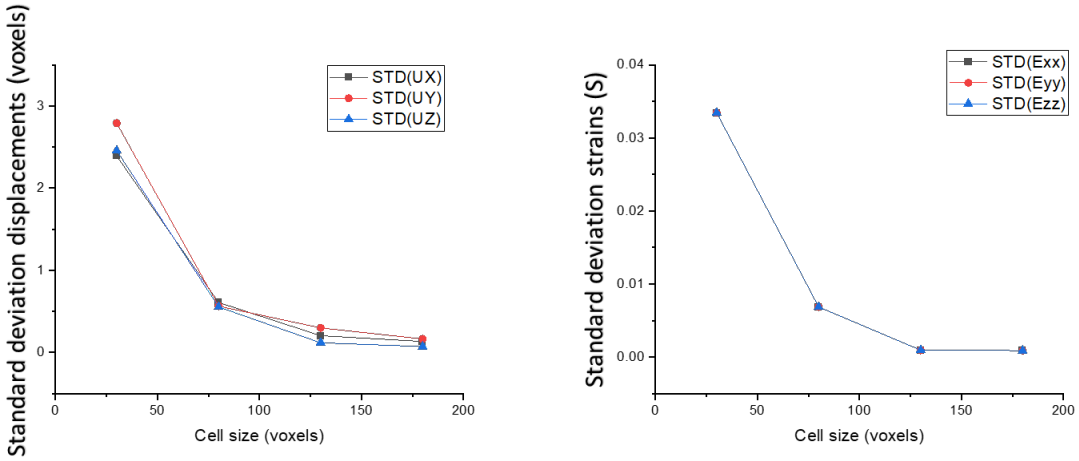


Figure 105: Standard deviation of the displacements (a) and strains (b) along the X, Y and Z axis between the preload (stage 1) and the RBM scan translated by 100 µm along Y (and realigned)

Automatically generated global DVC meshes are based on the subdivision of cuboidal subsets and lead to the edges of the tomography not being included in the correlation because that region and corresponding mask is a cylinder. A surface based tetrahedral mesh was composed. Interactive thresholding was used to remove the volume that is not part of the sample (outside the cylindrical reconstruction), and it provided a binary volumetric mask (0s outside the sample, and 1s inside). This mask was closed using a 3D 6 neighbouring voxels ball closing function with a half kernel size of 3 voxels to include the porosity inside the sample which then was used to produce a homogeneous surface with a constrained smoothing extent of 2. This is necessary because porosity is essential to the correlation process, and interactive thresholding does not provide segmentation uniformly over all features, and because heterogenous grids do not work well with global correlation. Two different grids were produced from this surface, by contracting the edges while preserving the structure, by 90 voxels for

the Coarse Grid (CG1) and by 48 voxels for the Fine Grid (FG1). After fixing intersections and triangles, tetrahedral grids were extracted from these two surfaces whose dimensions and main parameters are presented in Table 13.

Table 13: Properties of the global correlation grids

Grid	Mean Edge length (voxels)	Estimated number of cells	Triangles	Tetrahedrons	Nodes
CG1	121	3659	6872	3235	770
FG1	81	12457	22307	10696	2295

Views of both grids are available in Figure 106 and Figure 107 overlaid on a volume rendering of the microstructure. Each cell of the finest grid contains at least a few features and its mean edge in voxels is almost four times the microstructural length as found by the autocorrelation. The larger grid CG1 will be used for the global correlation of all volumes from 10 to 88 with 1 in a small strains incremental approach, where each stage will take as input the displacement field of the previous correlation, whilst the first correlation in the series (10 to 1) takes the fine local subset-based correlation displacement field as input. Note that this is different from the sum of differential in DaVis, because in this case the correlation is relative to the reference at any stage. The finer tetrahedral mesh is used to “rewind”, by computing a global approach correlation between stage 88-X and the reference and taking the results of the incremental approach as input (X from 0). To summarize, the coarse global incremental correlation was computed as a whole and automatically in the increasing step order (1 with 10, 1 with 20, 1 with 30, etc.), and the fine global correlation was computed in reverse order and manually one-by-one (1 with 88, 1 with 85, 1 with 80, etc.).

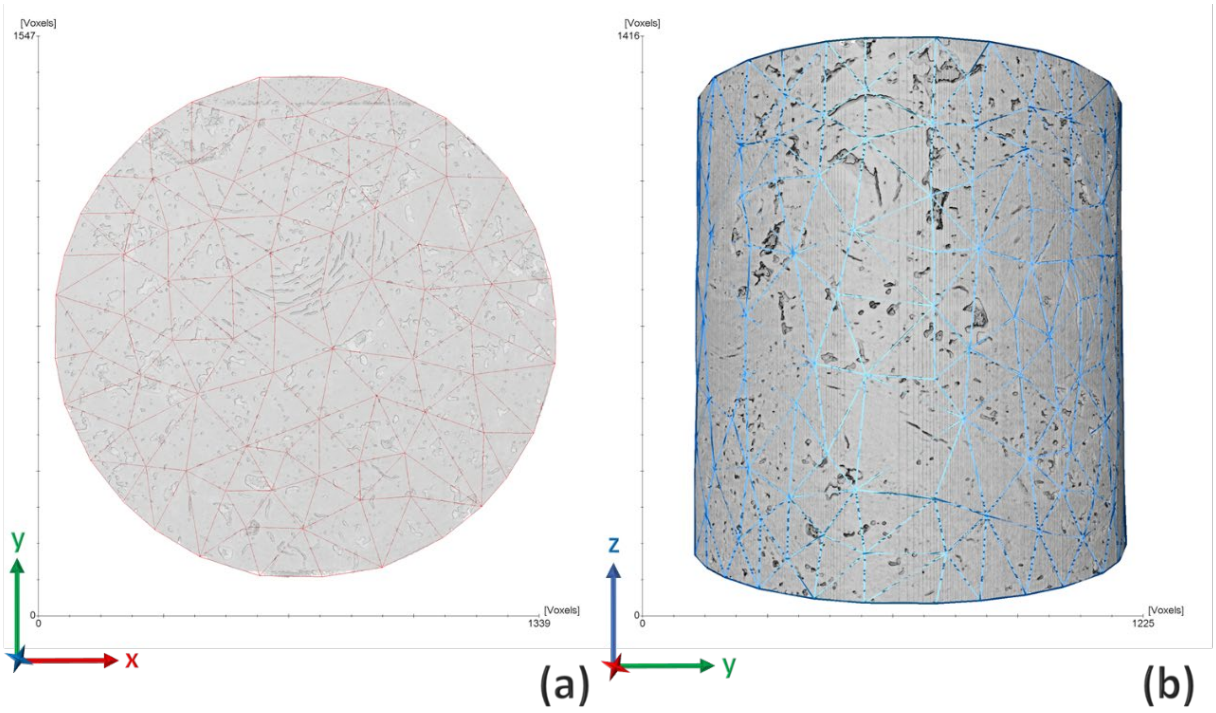


Figure 106: First tetrahedral mesh for the coarse incremental global DVC calculation with an estimated 2,025 cells viewed on top of a volume rendering of the microstructure from the XY-plane (a) and the XZ-plane (b)

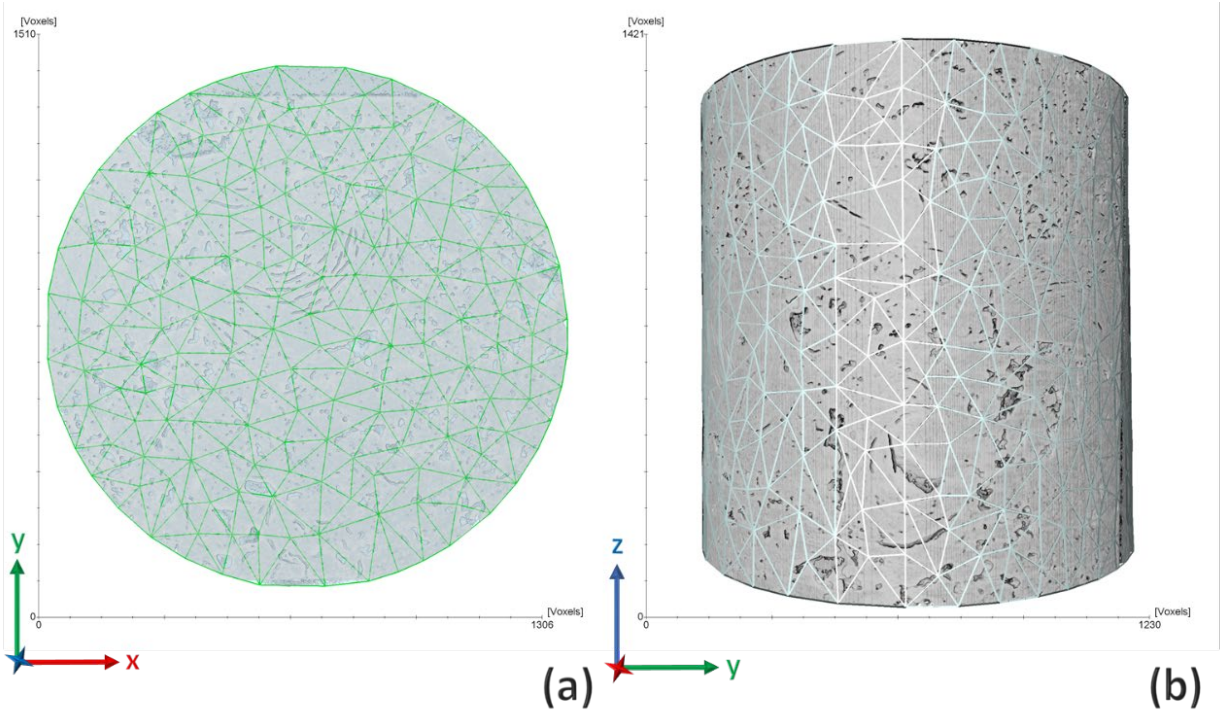


Figure 107: Second tetrahedral mesh for the fine global DVC calculation with an estimated 12,457 cells viewed on top of a volume rendering of the microstructure from the XY-plane (a) and the XZ-plane (b)

The first coarse tetra grid correlation extracted the Rigid Body Displacements as well the major deformations in the sample. On the X stages, Y converged before the limit of maximum iteration, whilst the rest failed to converge for the 0.001 convergence criterion as presented in Table 14. Convergence at this precision is not a requirement for the first pass of correlations. The displacement and strain results from this stage are not relevant, as they are only used as input for the next stage.

Table 14: Summary of results from the coarse global incremental volume correlation of sample SPMX1

Reference	Deformed	residual	Std (residual)	std(residual) /range	Iterations	Convergence Value
01	10	-5914.43	3365.31	0.05	200.00	0.03
01	20	2334.51	5243.32	0.08	200.00	4.93
01	30	374.46	3918.97	0.06	200.00	2.53
01	40	-1833.06	4067.44	0.06	200.00	4.53
01	50	-4030.79	4301.08	0.07	200.00	0.44
01	60	-1679.64	4261.58	0.07	75.00	0.00
01	70	-6789.00	4212.28	0.06	98.00	0.00
01	80	-1052.48	4696.79	0.07	106.00	0.00
01	85	-3730.36	4865.73	0.07	132.00	0.00
01	88	-621.73	5086.03	0.08	200.00	0.00

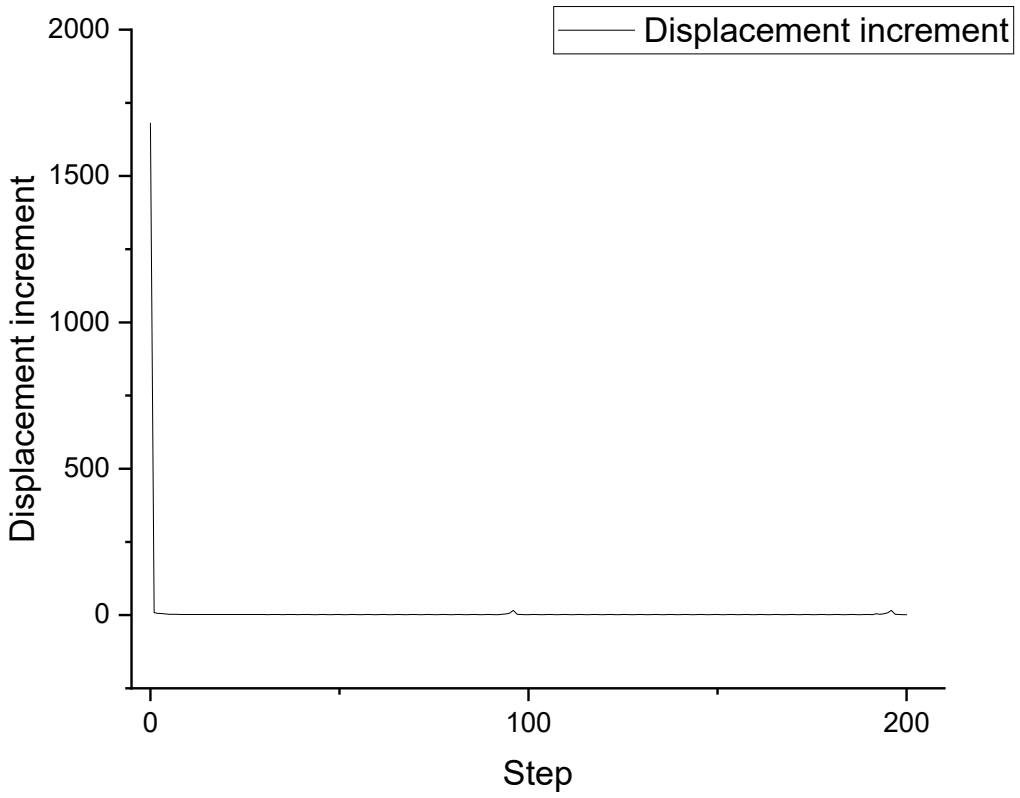


Figure 108: Displacement increment of the fine global DVC correlation between steps 1 (30 N) and 30 (approx. 230 N, 95% to failure) of sample SPMX1 with the results of the coarse incremental DVC as an input showing a fast convergence towards 0

Figure 108 presents the evolution of the displacement increment with the iteration number of the fine correlation of the reference and step 30, which made use of the preliminary displacement calculated by the coarse incremental correlation. It shows that the convergence (or certainty in the measurements) is reached within a few iterations when fed with the larger displacements allowing to reduce the single correlation iteration number from 200 to about 20 for the same convergence criterion of 0.001, saving computation time. The convergence criterion is the maximum change of the displacement increment between two iterations of the same correlation.

Figure 109 presents the strain fields along (a) and perpendicular (b) to the loading direction overlaid on top of a halfway view of a volume rendering of the microstructure for the fine global correlation of steps 1 (reference) and 10 using the results of the incremental coarse iteration as input. It shows, as expected, large compressive strains close to the contact point with the loading platen and tensile strains along the X-axis in the middle of the disc compression specimen. The range of local strains, down to -12,000 μS in compression and up to 4,000 μS in tension is the same range as previous studies when averaged [73]. For visualisation purposes, Figure 110 displays a slice in the same plane without the strain colours.

The second “fine” correlation was carried out until step 30 (from step 88 backward), for which the crack had disappeared completely from the correlation residual image. The Avizo XDVC Global DVC algorithm outputs a dataset of the difference of the reference by the deformed volume after application of the total displacement field, hereafter called “residual volume”. This residual field is able to highlight damage features such as cracks as the displacement field loses continuity, and here these features will have low (dark) grayscale pixel values.

As the subset site remains quite large due to current G-DVC limitations, it is the case that white features also appear, however these are pre-existing (from the reference) and are only artifacts in the residuals. The residuals of stages 30, 40, 50 and 85 of the fine global correlation with the reference step 1 are presented in Figure 111 for the same slice number, it can be seen as highlighted by the blue box that the crack starts appearing from step 40 onwards, which correspond to a load of 255 N (105% of expected failure load). More interestingly, and by comparing Figure 111 with Figure 96 the crack originates from the opening and propagation into the matrix of a lenticular crack within the filler particle, as opposed to initiating from a surface defect.

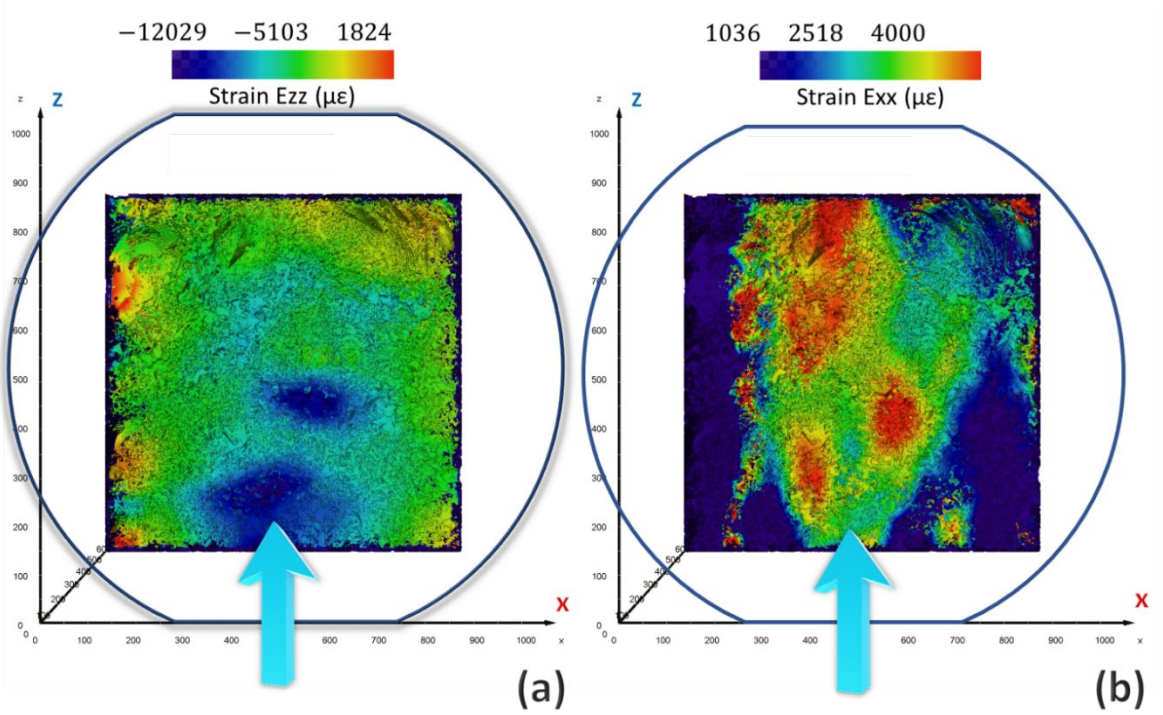


Figure 109: ROI cut-out of the volume rendering (at slice n°500) with thresholding segmentation of the preload (30 N) of sample SPMX1 with Z-axis (a) and X-axis (b) strained colour overlays from the fine global DVC correlation between steps 1 (30 N) and 10 (approx. 90 N), sample outline and loading direction

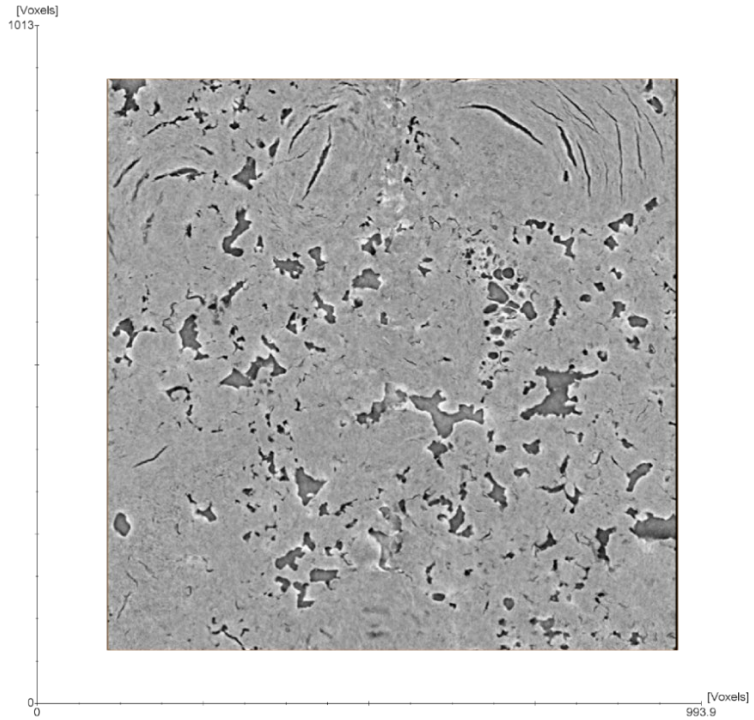


Figure 110: Tomography slice of the same plane as presented in Figure 109

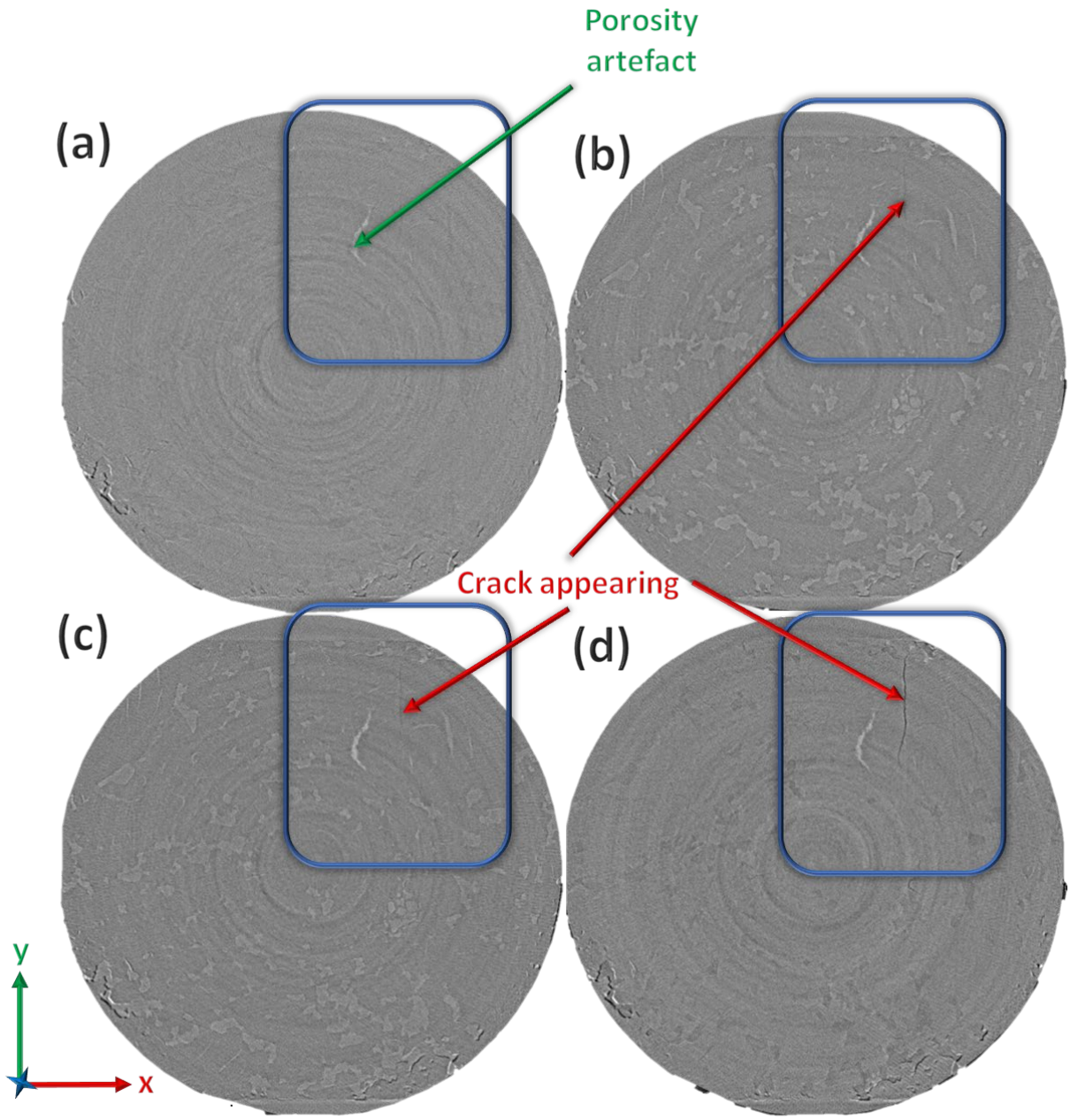


Figure 111: Correlation residuals of sample SPMX1 from the reference to stages 30 (a), 40 (b), 50 (c) and 85 (d), at loads approximatively 230 N, 250 N, 272 N and 347 N respectively with a blue frame showing the appearance of the crack after fine global correlation, the red arrows pointing at the forming crack and the green arrow showing an example of artifact due to the G-DVC limited spatial resolution

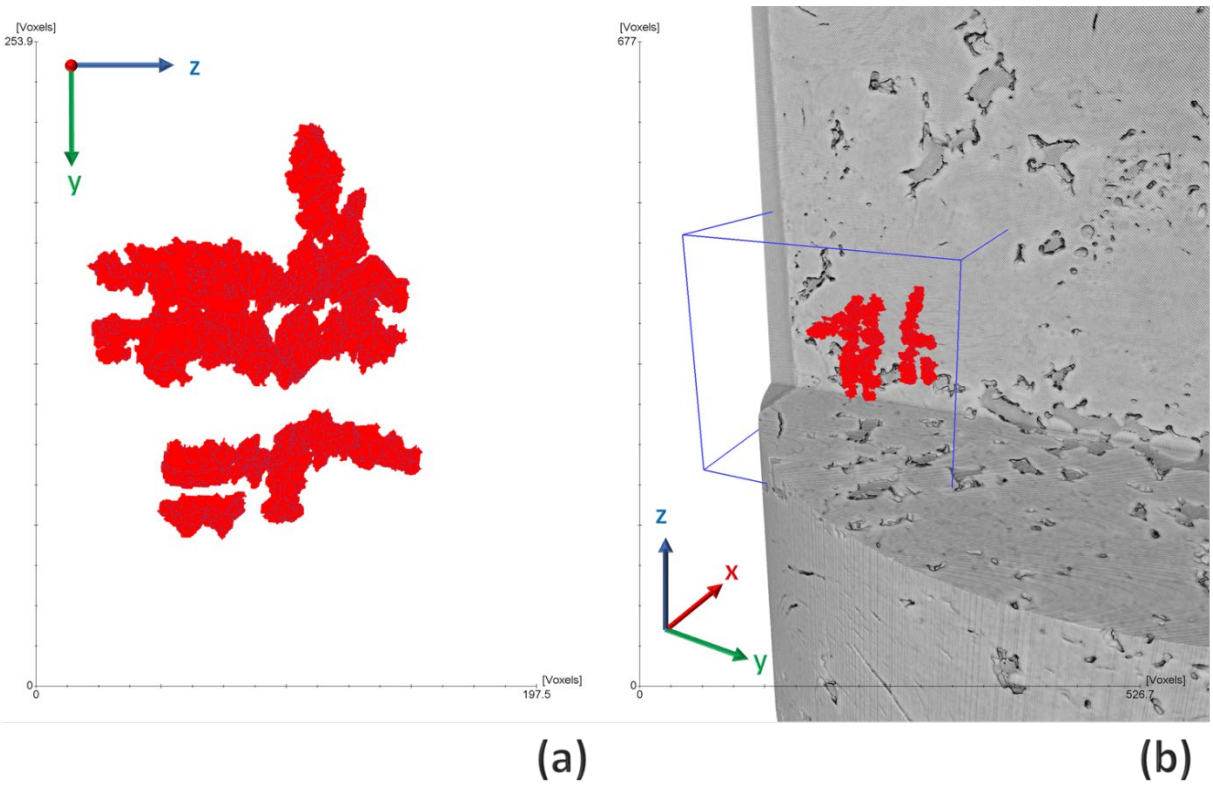


Figure 112: Crack segmented from the correlation residuals between steps 1 (30 N) and 85 (347 N) in a close-up view (a) and overlaid in the volume rendering of stage 85 after thresholding segmentation and in a blue bounding box to highlight the position in the filler particle

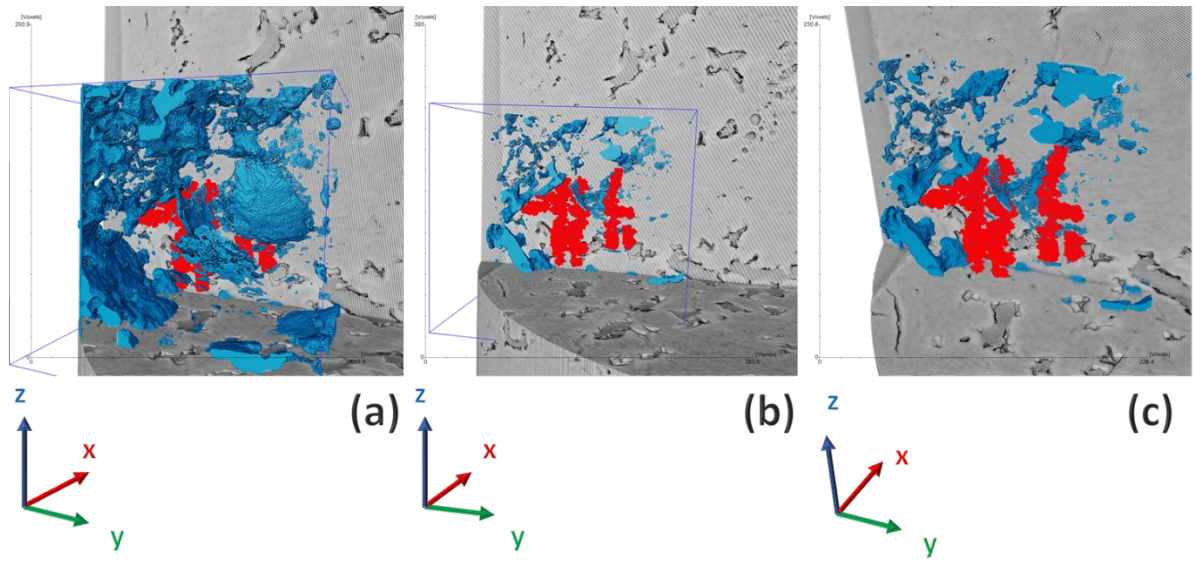


Figure 113: Same as Figure 112 with original porosity surrounding the crack (a), ROI in the plane of the crack (b) and close-up view (c)

A 3D rendering close-up view of the crack as well as a rendering at its position in the microstructure is presented in Figure 112. The segmentation was initiated with a top-hat algorithm on an extracted sub-volume (about 3 times the size of the filler) of the correlation residuals of step 85 (fine correlation) with the reference. A black top-hat segmentation was performed with a 26 neighbourhood, 3 voxel size cubical kernel. A texture classification method was then used to expand the segmentation using the initial results of both the crack and non-crack regions as seeding points. This method of supervised classification works by training a classifier to discriminate between the materials or phases in the volume. First order statistics were used to discriminate bright and dark textures and histogram statistics for homogeneous and irregular textures. A radius of 10 was chosen as best match considering the average width of the crack. The texton, pixel offset for computing co-occurrence features, was set to a cube shape and a size of 2 voxels. A feature rejection of 5% and an uncertainty threshold of 3 helped filter outliers. Note that as the segmentation is based on the residuals only, it does not include the porosity to which the crack is connected. This is instead shown in Figure 113 by further segmenting the pre-existing porosity in the reference stage; and this has been done using the same segmentation methodology.

5.3.3 Crack Detection with Data Remapping

Sample SPBX3 has both stepwise and trigger modes high-resolution volumes, and Lavision DaVis 8.4 version 66797 was used for the analysis. Because of the size of these datasets, and as there was no damage observed in the fast stepwise mode (L01-L07), four volumes were processed: L01 (reference), L07 (last fast tomography), D01, and D08 (last buffer tomography). They were prepared in ImageJ by realigning the rotation around the Z-axis so that the faces of the discs are parallel to the X-axis, matching and adjusting the contrast, and extracting sub-stacks to crop the same common volume in the Z-direction and compensate for RBDs along the loading axis. The pre-processed volumes were imported in DaVis without any filtering. An initial fast Fourier Transform pre-shift with a windows size of 352 voxels was used to extract RBDs and major deformations. A four (4) stage Direct Correlation with decreasing subset size from 192 voxels to 64 voxels, increasing passes from 1 to 4, decreasing peak search from 16 to 4 voxels and binning size from $8 \times 8 \times 8$ to none and with a Gaussian shape interrogation volume was then used to determine the deformation to a high precision. A smaller final subset size could have increased the strain resolution, but this would have been at the expense of precision and is not preferable. Indeed the data remapping works best with more precise displacements and a high correlation resolution may lead to damage being “closed”. As the Region of Interest (RoI) studied here is at the centre of the specimen, the strain components have been averaged to produce the graph of Figure 114. The compressive (Z-axis) and tensile (X-axis) strains increase sharply to step 3 (D01) and reach an asymptote as the microcracking is evolving from step 3 onwards. Both compressive and tensile strains are in the same range as past experiments [73]. Figure 115 presents a central slice of the reference step 1/L01 (a) and the final step 4/D08 (b) after data remapping. A microcrack that has

developed between two pores can be observed. It is interesting to note that the crack has propagated from pre-existing defects or sharp edges of the pores and through a path of least resistance offered by additional small pores.

The reference and remapped volumes were then exported in 32-bit Tiff files and uploaded to ImageJ. Each remapped n+1 step was subtracted to the reference in 32-bit floating point to remove the microstructure not related to the propagating crack as presented on the tomography slices of Figure 116. On these images, which correspond to the same position along the Z-axis, it can be noted that the main crack has been highlighted effectively, and that it is propagating inwards from the lower Y-axis side of the volume, for by about 100 µm on this slice. More interestingly, one can observe a secondary crack coming from the top of the Y-axis and towards the primary crack. The resulting volumes were grayscale-matched and exported in 16-bit RAW datasets for segmentation in Avizo. A top-hat segmentation was used to provide seeding points for a texture classification, and based on a subvolume extracted from the centre to avoid edge effects. The segmentation of the resulting remapped and subtracted volumes of both “buffer” steps (D08-L01 and D01-L01) was identical. The black top-hat image was produced using a cubical kernel with a size of 4 voxels and a neighbourhood of 26 voxels. The histogram crack range was 0 to 6,025 for the “void” phase and 42,849 for the “crack” phase in both cases. The texture classification used both first order and histogram statistics, a cube size of 2 voxels, a search radius of 10 pixels and a 5% feature rejection. Since the same segmentation parameters were used on the two volumes, whose contrast ranges had also been matched, the results are repeatable.

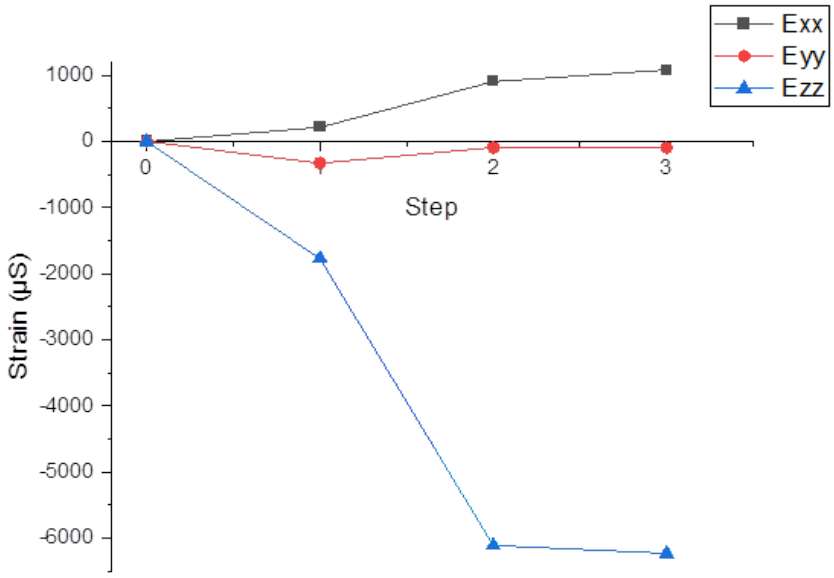


Figure 114: X-axis (perpendicular to loading direction), Y-axis (along specimen thickness) and Z-axis (loading direction) strains from the correlation between the preload (L01) and the last available stage (D08) averaged over the entire SPBX3 sample tomographed Region of Interest

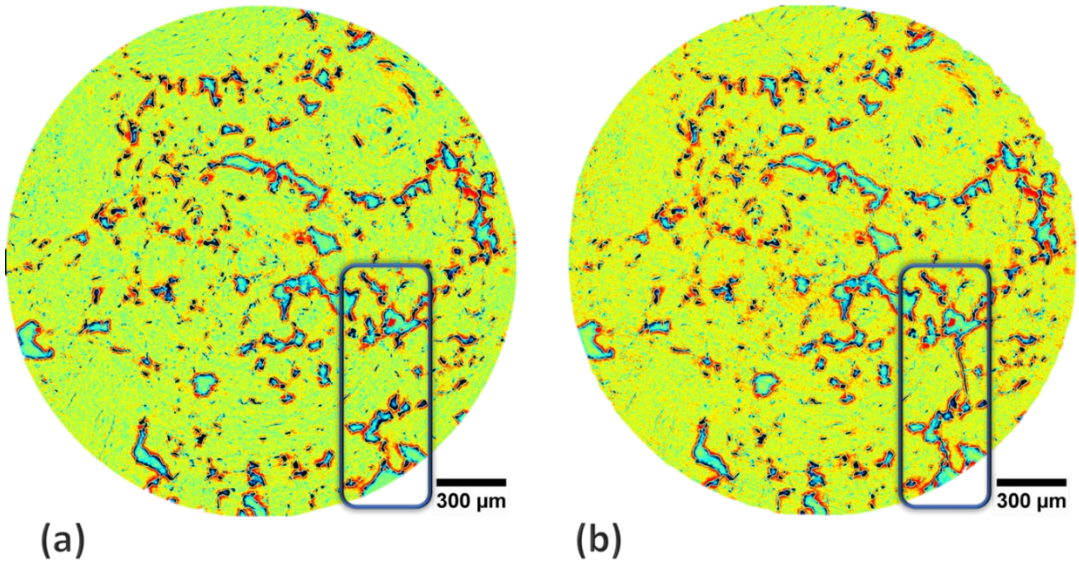


Figure 115: Tomography false colour cross-sectional slices (XY-plane) in the centre of specimen SPBX3 after correlation and remapping at preload (a) and prior to brittle fracture (b) with a blue frame indicating the location of a microcrack and with the loading direction being perpendicular to the plane of these slices

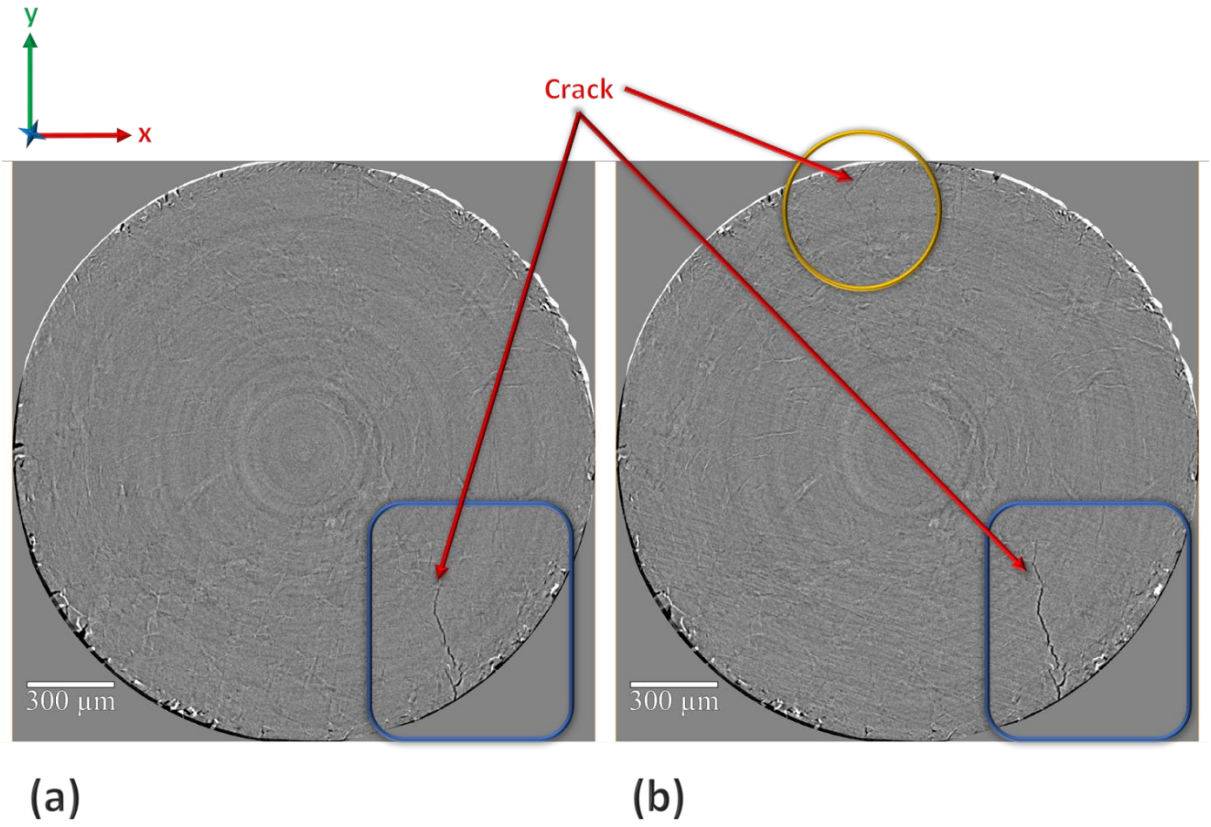


Figure 116: Same slice n°526 from the remapped volumes and after subtraction in 32-bit floating point of D01 first dimax by L01 preload (a), and D08 last dimax by L01 preload (b), with blue frames showing the extension of the cracks and a yellow circle showing the apparition of new damage on the other side

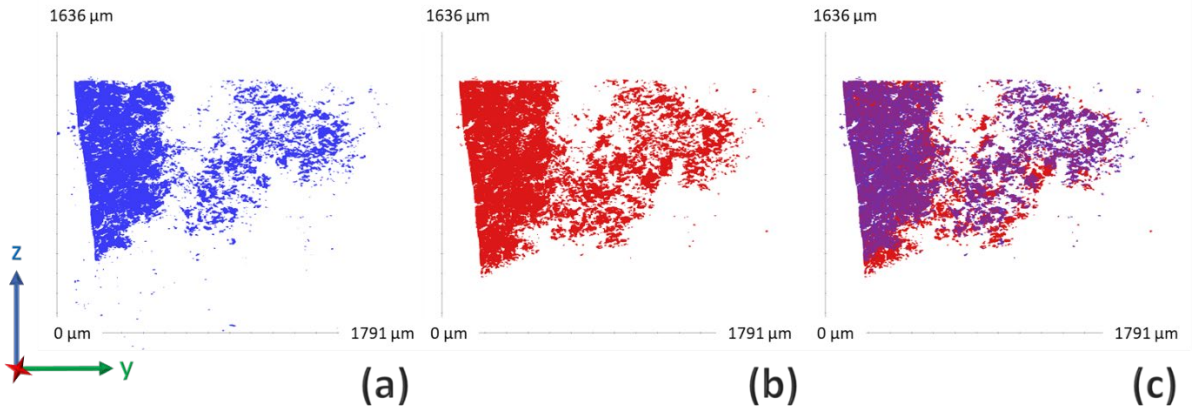


Figure 117: Volume rendering of the crack segmented by top-hat and texture classification from the subtracted remapped volumes of the first dimax D01 (a) and the last dimax available D08 (b) by the preload, and overlaid (c)

Figure 117 presents volume renderings of the labels from the segmentations. The blue volume rendering, which represents the crack at stage 3 (D01), shows that the two cracks have not yet connected. However, at the final step 4 (D08) before failure, as presented by the red volume rendering, the secondary crack extends significantly and connects with the primary crack. Overlaying both segmentations shows in purple the areas in common and in red the additional crack length at the final step.

Figure 118 displays the overlaid segmentations over a RoI volume rendering of the microstructure and over a tomography slice. The figure shows the start position of the final crack detection with a blue frame. Although there is more crack length that could have been segmented, this is of lesser interest to this study as both cracks originated outside the RoI, and to avoid edge-effects only the central region of the specimen was considered for the final steps of the crack detection. It can also be observed that the cracks seem to join in a non-uniform way, circling around a zone deprived of large microstructural features. Figure 119 presents views of the crack detections with the volume rendering of the microstructure aligned with the reference coordinate system. It shows that the cracks are relatively at the centre of the specimen, between the two faces and aligned with the Y-axis, as expected by the failure of Brazilian discs [200, 201]. However, it also indicates that the cracks are propagating along the horizontal Y-axis (through the thickness) instead of the vertical Z-axis (loading axis).

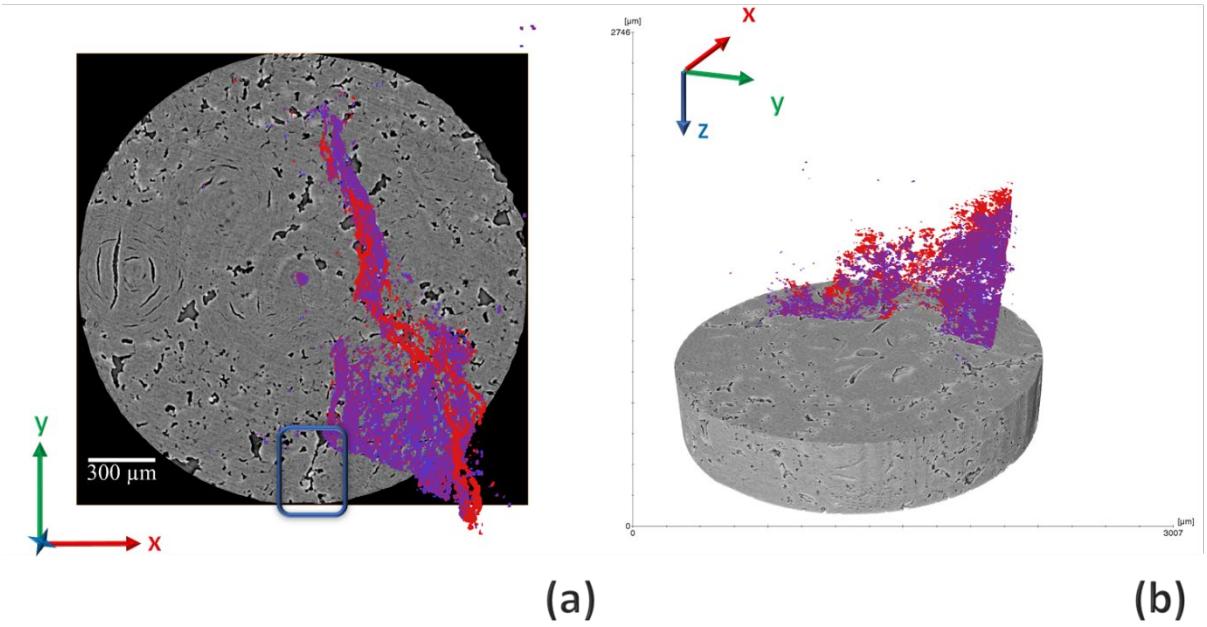


Figure 118: Both segmented cracks (blue for D01-L01, red for D08-L01) overlaid and presented on top of a tomography slice (a) and a thresholded volume rendering (b), note that the segmentation did not include the entire crack as highlighted by the blue frame

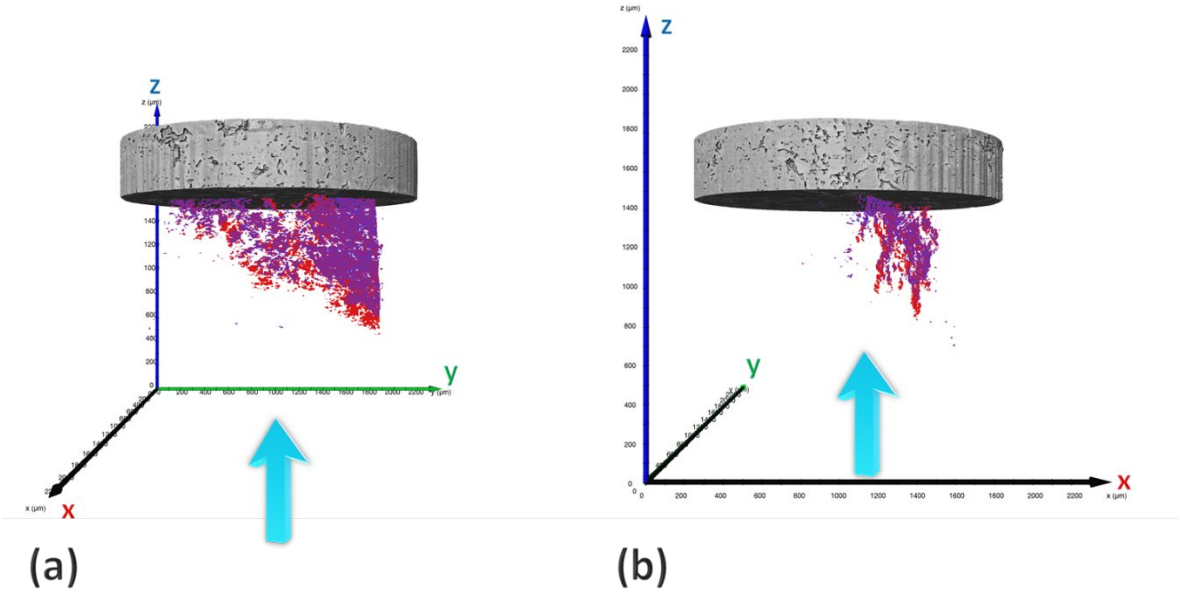


Figure 119: Further views of the overlaid cracks showing the orientation of propagation along the specimen diameter and Y-axis (loading direction represented by a blue arrow)

5.4 Discussion on Crack Initiation and Brittle Fracture

5.4.1 Relevance of the Technique

Through all the samples presented in this chapter, damage occurred extremely close to failure. The high-speed high-resolution tomography technique in its trigger “buffer” mode was particularly relevant to observing the initiation and/or propagation of damage occurring within the last few seconds and few newtons before failure, which would have been otherwise impossible to observe in three dimensions with any other modality, in the lab, or at a beamline unable to reach 1-2s tomography speed or with stage rewinding (i.e. not continuous). It is estimated that of all steps that present visible damage, 80% are in this final stage and in the samples that had a “dimax” mode. Notwithstanding, the other two acquisition modes proved their superiority compared to any other experimental setting. After shortlisting and pre-analysing all the samples, it can be affirmed that 100% of the observable damage occurred after 90% of the estimated failure load. Even though a number of these samples have failed at up to 120% the expected maximum load based on Brazilian disc strength calculations [159], it is not usually common to plan a scan above 80% of failure due to the scan time and the unpredictability of brittle fracture. Particularly, a disc kept under compression at the same load for a long time has higher chances to fail prematurely.

The incremental global and “rewinding” method was particularly adequate to find the location and associated strains of the initiation associated to a small crack fully contained in the field of view and whose position was known. It was efficient at processing a large number of steps in a way that only performs the highest resolution correlation level on the interesting stages, where the crack is visible and propagating. It would not have been possible to indicate the crack origin with another method. The

local sum of differential and data remapping approach using the DaVis engine offered high accuracy in the detection of crack propagation in a few high-resolution volumes.

5.4.2 Prevalence of Microcrack Formation

The crack observed in sample SPMX1 is one example that allowed us to confirm a crack initiation in a filler particle and from a pre-existing lenticular crack or pore. However qualitative observations of all other samples have indicated that cracks tend to initiate in or around a filler particle. This supports a potential theory that the Gilsonite filler particles may act as stress concentrators, and that lenticular cracks and pores are more susceptible to opening and leading to microcrack formation under diametral compressive load. In the matrix, there are far fewer pre-existing cracks than there are pores, and pores may in fact be better at accommodating deformation than fillers.

This interrogates on the case of other graphite materials, such as PGA which has needle shaped filler particles, or the newer Generation IV graphites such as MG-2 and FG-2 which use petroleum coke as filler instead of Gilsonite, but which share many mechanical properties with Gilsocarbon. Studies of baked carbon and other nuclear graphites have postulated that pores have a high degree of strain accommodation [202], which in this case may confirm the theory that filler particles, and potentially the ‘binder coating filler’ as described in [32], are much more likely contributors to microcrack initiation in Gilsocarbon graphite.

5.4.3 Preferred Microcrack Path

The two cases presented may seem to lead to different conclusions. The most noticeable crack in SPMX1 originates from the filler particle, and it extends horizontally towards the surface as well as vertically beyond the filler particle. It does not split the filler particle in half, but instead propagates through large pre-existing pores. This

seems to indicate that filler particles have a higher strength compared to the matrix. This may be due to the orientation of the crystallite domains inside the filler particle, in an onion shape arrangement [32]. However, this seems to contradict the case of SPBX3 where the crack propagates from the faces of the specimen inwards. It could be postulated that cracks are more likely to initiate from filler particles at the surface and expanding towards the nearest face, before propagating inside the sample. The cracks presented in SPBX3 are at a much later stage in the fracture process, towards the very final seconds before failure, whereas the crack in SPMX1 initiate from 90% of failure, with 48 more tomography steps before fracture. It is worth noting that the specimens studied here were of small dimensions which may lead to heterogeneous results which could be confirmed by looking at portions of larger samples.

5.4.4 Onsets of Brittle Fracture

The trigger “buffer” acquisition mode has proven to be useful in detecting the formation and propagation of cracking before failure. For the higher resolution volumes of $2{,}000^3$ voxels, the acquisition time of just above 1 second provides three-dimensional microstructural information of the sample just before failure. In the case of sample SPBX3 presented in this chapter, of particular interest is the orientation of propagation of the crack. Brittle failure of a Brazilian disk in compression should occur in the centre of the specimen, in the Y-Z plane, which is the case for the disc studied here. However, there has not been evidence in the past of cracks merging at the centre from the two faces.

The second interesting observation from this sequence is the secondary crack developing on the other side of the specimen. It propagates on the opposite direction, towards the centre of the specimen, to finally merge with the primary crack. Previous studies have indicated using indentation of meso-scale cantilevers that millimetre size

pores contribute to the brittleness of Gilsocarbon [64], however the present study tends to indicate that omitting filler particles in the analysis of meso- to macro-scale samples may lead to omitting the important role of filler particles in the fracture process.

5.4.5 Outlook and Future Work

Although the same method can be applied multiple times and to other specimens in a way that ensures repeatability, it was unfortunately not possible to batch process all the samples scanned for this experiment. The time constraints of this project have limited the work to two samples, but there is opportunity to gain valuable information by looking at the remaining samples in a more quantitative way. In addition to the many observations of damage, those samples that do not readily present damage could still have microcrack formation hidden in the microstructure that have been missed. The methodology designed specifically for this analysis and presented in this chapter has proven to be efficient and accurate for two different configurations, and it is readily applicable to the other samples. This could provide a quantitative evaluation of the statistical distribution of microcrack origin and direction. Furthermore, a refinement of the study of SPMX1, including more intermediary steps where the crack initiates, is necessary to increase the confidence in the stress that was applied to the sample at the origin of the crack, i.e. a better time resolution.

As mentioned earlier, because there is evidence that microcrack formation initiates inside or around Gilsonite particles, which are very particular to Gilsocarbon, there is an interest to repeat this experiment with candidates for the next generation of graphite moderated reactors such as the VHTRs and MSRs. A number of them use petroleum coke fillers with a smaller size than Gilsonite particles, by a factor of 10 to 20. For instance, it has been found for 4th gen fine grained graphite that NBG-18 is more

anisotropic (which is not a desirable situation) than IG-110 but however that the width of the graphite sheet in IG-110, part of the filler, is larger [203]. If the theories expressed here are confirmed, this could assist the selection of graphite materials based on raw materials for the next generation of nuclear reactor [203], neutron targets [33] or lithium battery anodes [204].

Chapter 6

6 ADVANCES ON THE UNDERSTANDING OF THE ROLE OF THE MICROSTRUCTURE ON ACCOMMODATING STRESS IN GILSOCARBON GRAPHITE

In this project, a number of advanced synchrotron radiation and neutron techniques have been used and developed to investigate how the Gilsocarbon graphite microstructure changes with damage and deformation. The main objectives addressed in this thesis cover a wide range of length scales, from crystal structure parameters to microcracking. The project focused on trying to better understand how the microstructure of virgin Gilsocarbon graphite is able to accommodate stress at ambient temperatures.

In Chapter 2, the techniques used throughout were presented in detail. It was shown that conventional lab-based tomography has numerous limitations, and particularly for the research questions that remained to be answered for graphite. As the interest is to better understand how the microstructure changes in the bulk with direct engineering applications, and sampling multiple microstructural features, it became evident at the start of this project that electron microscopy would not necessary be helpful in addressing the questions either. Laboratory work however has been particularly useful to write the proposals to the synchrotron radiation and neutron facilities. Laboratory Digital Image Correlation has also been used to validate experimental methods used in other experiments, aided the development of the IMAT loading apparatus and prepared the use of other in-line DIC systems during the experiments. Of the synchrotron experiments presented, four involved the design and development of new methods and codes which have been published and/or may be used by other researchers and for other brittle materials.

Chapter 3 has combined the results from two experiments to try and elucidate the evolution elastic and total strains at two resolutions. Low resolution total and elastic strain mapping have demonstrated a saturation of tensile stress with increasing tensile strain in a Brazilian disk, whilst a higher resolution study has indicated that the evolution of elastic strains in the microstructure is not homogeneous but may be dependent on the concentration of different features. This has been shown by interpolating the total (DVC) strains onto the elastic (XRD) strains grid. The larger slit size (JEEP-i12) showed a “clustering” of the points in load steps (i.e. average strain) and with a clear linear-elastic evolution of the compressive strains. The ESRF-ID11 sample however, with a finer resolution (smaller parallel beam) able to sample a gauge area of the size of microstructural features and grains, showed a much more heterogenous response.

A number of new techniques have been developed for this project, and this is particularly the case for Chapter 4, which combined the results from 3DXRD and Bragg imagining to investigate changes in crystal orientation with stress. The new energy resolved neutron imaging method involved the development of a new rig and associated data post-processing code which has already been peer-reviewed [174]. The correlation of the Bragg extinction spots indicated a change in local coherent scattering as the load is applied, and a clear increase as the load is removed. This is an evidence of a change in the orientation of crystal domains as the load is applied and which may highlight both recoverable and non-recoverable parts. Additional coding work with external partners on segmenting, tracking and differentiating bright and dark spots may be able to distinguish between these two parts. A 3DXRD experiment at ESRF, which tracked the evolution of preferred orientation in a small cylinder under axial compression, further indicated that the change (increase or

decrease) of the angle between the orientation vector and the beam reversed when the stress was removed. This indicated that strain may be accommodated by reversible mechanisms in the bulk. Previous synchrotron diffraction work had attempted to study reorientation in pre-stressed samples but had concluded in very little change [81]. Its is clear from the work presented here that both in-situ loading, and a combination of techniques, were beneficial in highlighting this recoverable phenomenon.

Finally, Chapter 5 presented perhaps the most directly usable and outstanding results of this project. For the first time, observation of microcrack initiation and propagation have been made using high-speed and high-resolution continuous pink-beam X-ray synchrotron tomography. Microcracks had already been shown to precede macrocracks in compression and indentation experiments [205], but never in 3D and at a scale allowing one to determine the conditions favouring crack formation. The different methods used, including stepwise and synchronised acquisition, as well as buffer-mode acquisition, have enabled a large amount of usable data to be obtained, with only about 5% of this presented in this thesis. Contrarily to the other streams of this project, this has not required the development of new techniques or computational codes, but rather methods to store, prepare and analyse large amounts of high-resolution tomography data. It was demonstrated that the two major commercial solutions available for Digital Volume Correlation, and by extension crack detection, were more appropriate to specific objectives, and thereby further explored the engineering application of the global and local DVC methods. It was found that the microcracking visible at tomography resolution, meaning with a crack opening width of at least 1 µm, were visible only from over 90% of the failure load in Brazilian disks. It was observed in most of the specimen, which are not notched, that cracks have a

tendency to preferentially initiate from lenticular cracks in filler particles. A clear example has been presented, with the crack tracked and segmented using residuals from G-DVC. It showed the crack initiating from a pre-existing defect in a filler particle close to the surface. A second sample investigated showed crack coalescence in the buffer mode, within the last six seconds preceding fracture at very slow loading rates. This coalescence seemed to develop through the thickness of the specimen, propagating inward from the surface. These observations have not only been made on the two specimens presented in this thesis, but on the many (21) samples tested during the experiment.

Filler particles have already been shown to play an important role in fracture, and particularly high temperature experiments have shown that above 1000°C the filler particles have a tendency to deflect the failure crack [51]. The case of filler particles is particularly interesting in that Gilsonite spherules are unique to GCMB IM-24 graphite, but many new graphites present smaller spherical fillers such as petroleum coke [33]. It seems from all the experimental work presented here that past studies have underestimated the role of filler particles and their ability to accommodate damage. Indeed, previously the work mostly focused on comparing the type of filler, considering the effects of temperature on the properties of graphite, as opposed to mechanical stress, and the semi-isotropic characteristic provided by spherical fillers [29].

Chapter 4 offers clear indications that a partially recoverable effect is at play in the elastic region of the loading curve. The mosaic spread of the binder matrix implies that there is low ordering of the crystal domains, and its effect may not be visible in the diffraction data. However, we have knowledge of large domains (1-2 μm) oriented in an ‘onion shape’ in Gilsonite filler particles [32, 154]. In the binder, and specifically the

binder surrounding Gilsonite particles, flour or aggregate, there may be larger domains (up to 20 µm), but they are less likely to share a common orientation and to contribute to the diffraction peak of the basal plane. Their proportion is also much less (6%) than that of filler particles (19%), and this suggests that the change[16] observed may be mostly explained by Gilsonite particle. As presented in Figure 120, it is possible to suggest that due to the 'onion' layering, the change in contribution from the domains in the filler particles is the most noticeable effect. Whereas the orientation in the matrix is perhaps more random (less texture), domains in the filler particles present an order.

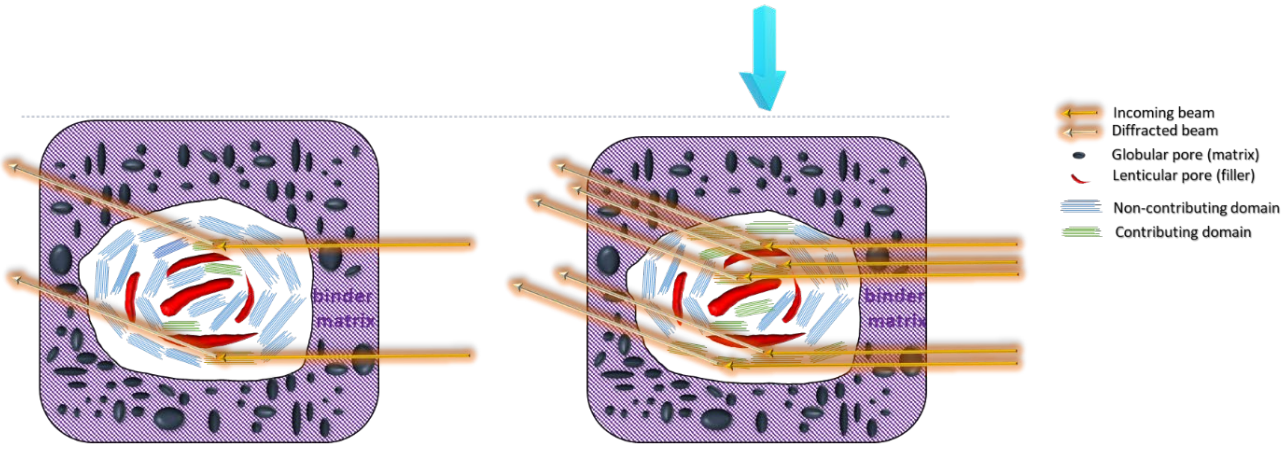


Figure 120: Diagram of potential mechanism explaining the change in coherent scattering

The phenomenon observed with 3DXRD and neutron Bragg imaging has both a recoverable and non-recoverable part; it is partially recoverable. As filler particles are 'squished' or 'unsquished' (compression/tension/loading/unloading), more or less domains contribute to the diffraction observation. Because of the random initial orientation and shape of that ellipsoid, and its location in the sample (disc or cylinder here), we can infer that the actual shape at any time is decoupled from the loading or unloading stage, but that the shape change is intertwined with the strain.

[16] Note that here I refer to change in diffraction intensity (3DXRD) and local coherent scattering (Bragg imaging), i.e. an in-situ loading comparison.

$$\frac{x^2}{a^2} + \frac{y^2}{b^2} = 1 \tag{8}$$

$$\Longrightarrow \frac{dy}{dx} = -\frac{b^2}{a^2} \times \frac{x}{y} \tag{9}$$

$$\therefore s = -\frac{b^2 \cdot \cos\chi}{a^2 \cdot \sin\chi} \tag{10}$$

$$\because \psi = \tan^{-1} s = \tan^{-1}\left(-\frac{b^2 \cdot \cos\chi}{a^2 \cdot \sin\chi}\right) \tag{11}$$

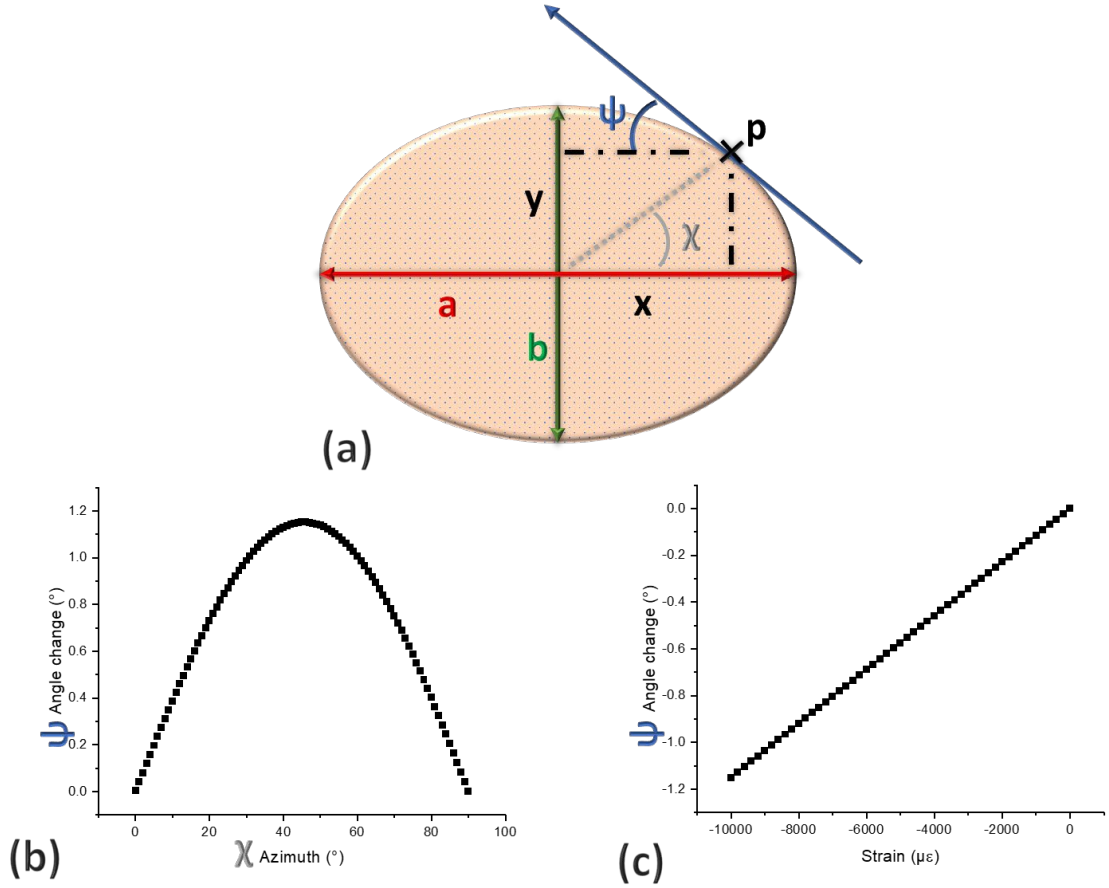


Figure 121: Shape change of an ellipse (a) under load (area kept constant), tangential angle change as a function of azimuth (b) and angle change as a function of strain at azimuth 45° (b)

At this scale, it is impossible to highlight the individual mechanisms involved in the change in contribution. Nonetheless, it is safe to assume that most of the recoverable component is due to the elasticity to the grains, and more particularly due to the deformation of the filler particles, with likely contribution from twinning and kinking of many domains. Basal slip, and sub-micron cracking likely explain the non-recoverable component of what is observed. This ability of the microstructure to accommodate deformation elastically has also been shown by the ESRD-ID11 XRD mapping experiment. It has allowed to show the heterogeneity of the response of the microstructure when submitted to the same type of stress; in this case by only looking at the centre of the specimen. However, this experiment rules out the elasticity of the sphere as sole mechanism for the angular change. A simplistic 2D approach allows one to estimate the shape change of an ellipse as it is compressed. This is represented by a compression along *a* (y-axis) in the ellipse of Figure 121(a). By differentiating the equation of an ellipse, the angle of the tangent with the horizontal axis can be calculated from the slope of the tangent for a given azimuth, as seen in equations (8)-(11). At fixed area, *b* can be calculated as *a* is reduced, in this case from 0.5 mm to 0.495 mm and compressive strains estimated. The angular change is highest at 45° between these two '*a*' values, as presented in Figure 121(b). At this azimuth, the angular change can be plotted against strain (Figure 121(c)). At the strains sustained in the cylinder compression experiment, the angular change is below 1.2°, as opposed to up to 10° found in 4.5.2. This simple approach will not translate in higher angular changes in 3D, and we can therefore postulate that the elasticity of filler particles only partially explains the change in orientation.

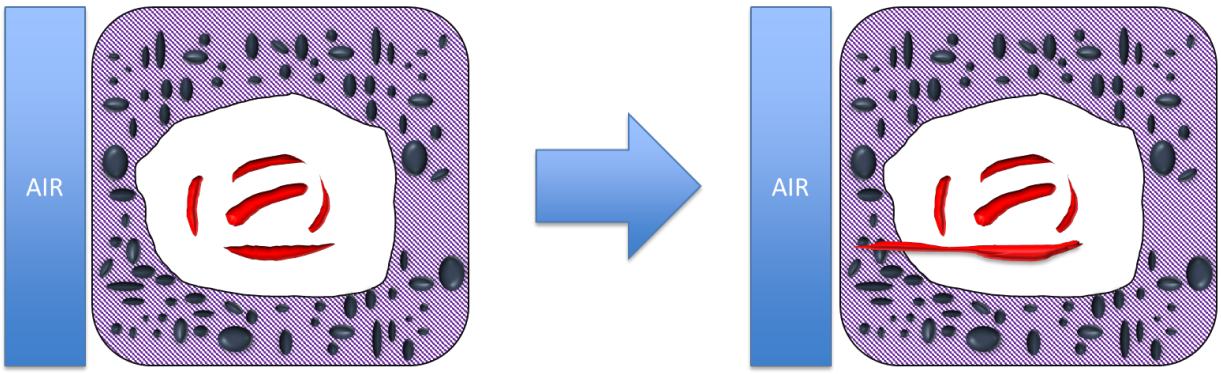


Figure 122: Gilsonite particles acting as stress concentrators

The role of the filler particles is further highlighted by the high-speed tomography experiment. Microcracking visible at the highest resolutions currently available in-situ (0.8-1.6 µm) have suggested that pre-existing lenticular cracks in filler particles are likely to initiate microcracking, above 90% of the failure load, but with a stable crack propagation. These microcracks have a tendency to extend to the nearby surface before becoming sufficiently important to initiate fracture. Figure 122 shows how the filler particles can act as stress concentrations when near the surface, independent of whether there is a keyway. In the case presented in 5.3.2, the lenticular pore from which the crack originates is almost perpendicular to the surface of the sample. This has only been observed on small specimens, but on fillers of varying sizes and at locations close to the centreline of the disc. This also correlates well with the crack coalescing from the faces inwards and may be a suitable representation of brittle fracture in bulk samples. The fine resolution (0.7-1.4 µm/vx) achieved here was perhaps not quite sufficient to compare the total strains within the filler particle and surrounding matrix, but allowed to track for the first time the initiation of microcracking, from its onset.

Chapter 7

7 THE PROSPECTS OF NUCLEAR GRAPHITE RESEARCH

Early on in this project, it has been clear that nuclear graphite research is taking the direction of improved modelling, as well as, perhaps to a lesser extent, experimental research that more closely reflect reactor-core conditions, such as high-temperature, and irradiated or trepanned samples. Recent advances in experimental designs, with new apparatus becoming available, has enabled to initiate this process soon after this project started [111, 112]. Of all the techniques presented in this work, the IMAT Bragg imaging is perhaps the easiest to apply to neutron irradiated or trepanned samples. Radioactive graphite has been tested on ENGINX and generally neutron sources are more flexible with regards to radioactive samples. Due to the required proximity to the detector (IMAT/ESRF-ID11) or the specificities of the rig employed (PSICHE/SALSA), it does not seem possible, at the time of writing, to perform similar investigation at high temperature, without extensive methodology and apparatus development. The PSICHE technique might be applicable to larger specimens in the future, perhaps using the EBS upgrade of the ESRF, but of greater importance would be to repeat high-speed tomography acquisitions on graphites with different types of filler particles, including fine-grain petroleum coke graphites.

The current understanding is that the c-axis shrinkage and a-axis expansion in single crystal graphite is due to the accumulation of interstitial loops forming new basal planes, whilst in the bulk this is combined to the formation of cracks in between the basal planes leading to a complex effect [36, 206]. This may potentially adversely affect the reorientation of grains observed with Bragg imaging and 3DXRD. This could potentially affect graphite crystal's ability to twin under load, however non-recoverable basal slip and interplanar cracking in the filler may be more likely. Radiolytic oxidation leads to important volume loses and an increase in porosity in Gilsocarbon graphite,

as presented in 1.6.3. The preference in crack initiation in the filler particles may change in graphite with a higher porosity volume and more connected or open porosity, with potentially more microcracks initiating from the surface. With cracking initiation and inelastic deformation potentially facilitated by the effects of irradiation, the saturation of the principal strains investigated in the graphite discs experiments at Diamond Light Source and ESRF may happen earlier and more significantly. The recovery of crystal orientation observed with Bragg Imaging and 3DXRD may be less significant and there would potentially be more microcracking initiation observable with high-speed tomography. This may be compensated by the strengthening effects of temperature observed [51, 73], and perhaps it would be preferable to repeat these experiments at elevated temperature on trepanned samples (as opposed to just one component) to better describe in-operando deformation and damage.

An experiment that would be interesting would be ptychography or Coherent Diffraction Imaging (CDI) on a single Gilsonite particle, or similar techniques able to resolve Mrozowski cracks in three-dimensions [33, 207]. The Phase Contrast Imaging presented here also highlighted the presence of impurities in graphite, which could be investigated with fluorescence or high-resolution energy discriminative techniques. Finally, there is a significant amount of data generated by this project which may still contain interesting points to investigate. This includes the many other datasets of the high-speed tomography experiment which could provide more certainty on crack initiation and propagation, as well as investigate crack coalescence in the DC specimens, advanced segmentation for better tracking of white and dark extinction spots in the Bragg imaging data (both in progress), further investigation of the microstrain and crystallite size in the i12 and ID11 datasets, and analysis of the GEM, SALSA and HOPG datasets (dependant on external factors).

CONCLUSIONS

The research presented here not only offers new techniques and methods for investigations on the role of the microstructure in quasi-brittle materials deformation, but it has also taken forward the understanding of the microstructure of Gilsocarbon graphite. Through the use of advanced synchrotron and neutron techniques, this work has highlighted the role of the microstructure in the bulk deformation of virgin Gilsocarbon graphite at room temperature. Particularly, varied and novel experiments led to conclusions related to the role of a major component in this graphite, filler particles.

A new novel experimental technique has been developed to study grain reorientation using time-of-flight neutron imaging *in-situ*, including a loading apparatus and post-processing code. Using this method for two experiments at a neutron spallation source, extinction spots have been tracked and related to grains entering and leaving Bragg condition as the load is applied. This represents evidence that grain reorientation is a mechanism for accommodating mechanical strain and that most of it is likely to be concentrated in the filler particles. This has been further demonstrated by a 3DXRD experiment for which a novel crystallography code has been able to track preferred crystal orientation when load is applied, similarly indicating recoverability.

Further indications of the ability of filler particles to elastically accommodate damage have come from two other experiments combining tomography and diffraction mapping in the bulk and at high resolution, using new tomography

reconstruction routines for limited angle and phase contrast retrieval. A novel post-processing code developed for this project enabled to combine and correlate the total strains from digital volume correlation and the elastic strain calculated from fitting and processing the X-ray diffraction mapping data. The bulk ‘lower resolution’ experiment has indicated that there must be a mechanism involved in the non-linear tensile behaviour in the central region of Gilsocarbon discs, also noted in the high-resolution experiment, but in neither experiments microcracks can be observed simultaneously and at these stresses, as previously indicated by sub-micron laboratory tomography. Indeed, at higher resolution, there is a clear heterogeneity of strain distribution in the microstructure indicating the ability of certain grains to elastically accommodate damage by reorientation. Large compressive deformations in the elastic loading can be accommodated in this way, as there is no microcracking that can be observed at the high resolutions achieved here up until 90% to failure. It is also possible that the current techniques are unable to resolve very small crack initiation and propagation, but the theory presented here offer a unique new perspective.

Microcracking does occur prior to fracture in Gilsocarbon graphite at room temperature, and observations have been possible with the use of high-speed continuous tomography. Novel crack detection methods using digital volume correlation of large datasets have highlighted that cracks initiate within the last 10% to failure. It has been further shown that the location of these initiations can be pre-existing lenticular cracks in filler particles acting as stress concentrators. This relates well to the theory that filler particles tend to

accommodate most of the strain, and after a no-return point they become the location of initial critical damage. Cracks have also been observed to coalesce from the disc surfaces to fracture in the centre of the specimen, supporting the idea that failure cracks may develop near the surface and propagate towards zones of high tensile strains.

Overall, this project has completed two objectives. It has brought valuable contribution to the understanding of the mechanisms involved in the ability of Gilsocarbon graphite to accommodate stress, formulating hypotheses on the comparison with trepanned samples. It has also pioneered and developed methods and techniques which may be used to validate these findings with different environmental conditions, different graphites, or other ceramic-like materials, and which can also be used in other research streams. Laboratory work has been essential in preparing the beamtime experiments, without which the work completed in this project would not have been possible. The amount and diversity of data collected have proven challenging, but have been concisely presented in this document. Work will continue beyond this thesis with the aim of further publishing the results presented.

Thomas Zillhardt

“I agree that faith is essential to success in life, but I do not accept your definition of faith, i.e., belief in life after death. In my view, all that is necessary for faith is the belief that by doing our best we shall come nearer to success and that success in our aims (the improvement of the lot of mankind, present and future) is worth attaining.”

– Rosalind Franklin, pioneer of X-ray diffraction on carbons and graphite [1], letter to Ellis Franklin, 1940

PUBLICATIONS

Published

Zillhardt TAC, Burca G, Liu D, Marrow TJ (2021) In Situ Mechanical Loading and Neutron Bragg-edge Imaging, Applied to Polygranular Graphite On IMAT@ISIS. Exp Mech. https://doi.org/10.1007/s11340-021-00754-1

Conceptualisation, Investigation, Methodology, Software, Writing – original draft preparation

Liu D, Zillhardt T, Earp P, et al (2020) In situ measurement of elastic and total strains during ambient and high temperature deformation of a polygranular graphite. Carbon N Y 163:308–323. https://doi.org/10.1016/j.carbon.2020.03.020

Data analysis, Methodology, Software, Writing – review and editing

Under preparation

Zillhardt TAC, Burca G, Ametova E, Ludwig W, Liu D, Marrow TJ (Expected mid-2022) Investigation of Crystal Reorientation as a Mechanism of Damage Accommodation in Gilsocarbon Nuclear Graphite using In-Situ Three-Dimensional Far-Field Synchrotron X-Ray Diffraction and In-Situ Energy-Resolved Neutron Imaging.

Conceptualisation, Investigation, Methodology, Software, Writing – original draft preparation

Zillhardt TAC, King A, Liu D, Marrow TJ (Expected early 2022) Time series high-speed pink beam continuous tomography of nuclear graphite for the observation of sub-critical crack initiation, coalescence and propagation and the onsets of brittle fracture.

Conceptualisation, Investigation, Methodology, Software, Writing – original draft preparation

Additional articles under preparation with data already acquired during this degree (Expected late 2022 – early 2023; content or titles may change):

- Evaluation of the Heterogeneity of Damage Distribution in Gilsocarbon Graphite with High-Resolution Synchrotron Pink Beam Phase Contrast Tomography and Diffraction Mapping (main author)
- On the Notch Sensitivity of Gilsocarbon Nuclear Graphite: Evaluation of Stress Relaxation with High-Resolution Neutron Diffraction and Detailed Crack Propagation using High-Speed Continuous Synchrotron Tomography (main author)
- Twinning and Kinking Mechanisms in Highly-Oriented Pyrolytic Graphite Investigated by In-Situ 6D Synchrotron Topo-Tomography (main author)
- DIFFRACTX: a Program to Correlate Total and Elastic Strains using Digital Volume Correlation of Synchrotron X-Ray Tomography and Synchrotron X-Ray Diffraction Maps (main author)
- In situ X-ray diffraction and tomography of short fatigue crack behaviour: the roles of microstructure and residual stresses (data acquisition and analysis, secondary author)
- Situ Study of Damage Development in a 3D needle-stitched Carbon/Carbon-Silicon Carbide (C/C-SiC) Ceramic Matrix Composite (data acquisition and analysis, secondary author)
- Intergranular Cracking in a Nickel Superalloy Revealed by High Temperature Imaging and In-Situ Diffraction Contrast Tomography (data acquisition and analysis, secondary author)

REFERENCES

1. Harris PJF, Suarez-Martinez I (2021) Rosalind Franklin, carbon scientist. Carbon N Y 171:289–293. https://doi.org/https://doi.org/10.1016/j.carbon.2020.09.022
2. Boardman J (1982) The Cambridge ancient history. Volume 3. Part 1, The prehistory of the Balkans, 2nd ed. Cambridge University Press, Cambridge
3. Novoselov KS, Geim AK, Morozov S V, et al (2004) Electric Field Effect in Atomically Thin Carbon Films. Science (80-) 306:666 LP – 669. https://doi.org/10.1126/science.1102896
4. von Steiger AL (1922) The graphite approach to aromatic carbon. BERICHTE DER Dtsch Chem GESELLSCHAFT 55:1968–1979
5. Pirani M, Fehse W (1923) Origin and characteristics of pure graphite. ZEITSCHRIFT FUR ELEKTROCHEMIE UND Angew Phys CHEMIE 29:168–174
6. Huggins ML (1923) The structure and dimensions of graphite. J Am Chem Soc 45:264–278. https://doi.org/10.1021/ja01655a002
7. Burchell TD, Fuller EL, Romanoski GR, Strizak JP (1991) Graphite for the nuclear industry. United States
8. Breeze P (2017) Chapter 5 - Gas-Cooled Reactors. In: Breeze PBT-NP (ed). Academic Press, pp 45–51
9. McLachlan N, Reed J, Metcalfe MP (1996) AGR core safety assessment methodologies. International Atomic Energy Agency (IAEA)
10. Broomby R (2014) New cracks in Hunterston reactor - BBC News. In: BBC News Online. http://www.bbc.co.uk/news/science-environment-29481481. Accessed 4 Dec 2017
11. Kretchman HF (1957) The story of gilsonite. American Gilsonite Co., Salt Lake City, Utah
12. Page DJ (1991) The industrial graphite engineering handbook. UCAR Carbon Co., Danbury, CT (39 Old Ridgebury Rd., Danbury 06817-0001)
13. Eatherly WP, Piper EL (2013) Chapter Two – Manufacture. In: Nuclear Graphite. pp 21–51
14. Marsden BJ, Hall GN (2012) Graphite in Gas-Cooled Reactors. In:

Comprehensive Nuclear Materials. Elsevier, pp 325–390

15. Ouzilleau P, Gheribi AE, Chartrand P, et al (2019) Why some carbons may or may not graphitize? The point of view of thermodynamics. Carbon N Y 149:419–435. https://doi.org/https://doi.org/10.1016/j.carbon.2019.04.018

16. Franklin RE, Randall JT (1951) Crystallite growth in graphitizing and non-graphitizing carbons. Proc R Soc London Ser A Math Phys Sci 209:196–218. https://doi.org/10.1098/rspa.1951.0197

17. Franklin RE (1951) The structure of graphitic carbons. Acta Crystallogr 4:253–261. https://doi.org/https://doi.org/10.1107/S0365110X51000842

18. Oberlin A (1984) Carbonization and graphitization. Carbon N Y 22:521–541. https://doi.org/https://doi.org/10.1016/0008-6223(84)90086-1

19. Sauerteig D, Ivanov S, Reinshagen H, Bund A (2017) Reversible and irreversible dilation of lithium-ion battery electrodes investigated by in-situ dilatometry. J Power Sources 342:939–946. https://doi.org/https://doi.org/10.1016/j.jpowsour.2016.12.121

20. Michael H, Iacoviello F, Heenan TMM, et al (2021) A Dilatometric Study of Graphite Electrodes during Cycling with X-ray Computed Tomography. J Electrochem Soc 168:10507. https://doi.org/10.1149/1945-7111/abd648

21. Bystrov M V, Yachikov IM, Portnova I V (2020) Modelling of the thermal state and the melting loss of a graphite electrode in the conditions of the evaporative cooling in the arc furnace. IOP Conf Ser Mater Sci Eng 966:12019. https://doi.org/10.1088/1757-899x/966/1/012019

22. Kuptsov KA, Sheveyko AN, Sidorenko DA, Shtansky D V (2021) Electro-spark deposition in vacuum using graphite electrode at different electrode polarities: Peculiarities of microstructure, electrochemical and tribological properties. Appl Surf Sci 566:150722. https://doi.org/https://doi.org/10.1016/j.apsusc.2021.150722

23. Miyahara A, Tanabe T (1988) Graphite as plasma facing material. J Nucl Mater 155–157:49–57. https://doi.org/https://doi.org/10.1016/0022-3115(88)90226-7

24. Vergari L, Scarlat RO (2021) Thermodynamics of hydrogen in graphite at high temperature and the effects of oxidation, irradiation and isotopics. J Nucl Mater 552:152797. https://doi.org/https://doi.org/10.1016/j.jnucmat.2021.152797

25. Marsden BJ, Jones AN, Hall GN, et al (2017) 14 - Graphite as a core material for Generation IV nuclear reactors. In: Yvon PBT-SM for GIVNR (ed). Woodhead Publishing, pp 495–532

26. Zhou X, Tang Y, Lu Z, et al (2017) Nuclear graphite for high temperature gas-cooled reactors. New Carbon Mater 32:193–204. https://doi.org/10.1016/S1872-5805(17)60116-1

27. Zhou X, Yang Y, Song J, et al (2018) Carbon materials in a high temperature gas-cooled reactor pebble-bed module. New Carbon Mater 33:97–108. https://doi.org/https://doi.org/10.1016/S1872-5805(18)60328-2

28. Mignacca B, Locatelli G (2020) Economics and finance of Molten Salt Reactors. Prog Nucl Energy 129:103503. https://doi.org/https://doi.org/10.1016/j.pnucene.2020.103503

29. Marsden BJ, Haverty M, Bodel W, et al (2016) Dimensional change, irradiation creep and thermal/mechanical property changes in nuclear graphite. Int Mater Rev 61:155–182. https://doi.org/10.1080/09506608.2015.1136460

30. Lee JJ, Arregui-Mena JD, Contescu CI, et al (2020) Protection of graphite from salt and gas permeation in molten salt reactors. J Nucl Mater 534:152119. https://doi.org/https://doi.org/10.1016/j.jnucmat.2020.152119

31. Arregui-Mena JD, Edmondson PD, Margetts L, et al (2018) Characterisation of the spatial variability of material properties of Gilsocarbon and NBG-18 using random fields. J Nucl Mater 511:91–108. https://doi.org/https://doi.org/10.1016/j.jnucmat.2018.09.008

32. Shen K, Xu K, Yu S, Kang F (2021) The optical texture of PGA, Gilsocarbon, NBG-18, and IG-110 nuclear graphite. J Nucl Mater 552:153013. https://doi.org/https://doi.org/10.1016/j.jnucmat.2021.153013

33. Jiang M, El-Turke A, Lolov G, et al (2021) Multiple length-scale microstructural characterisation of four grades of fine-grained graphite. J Nucl Mater 550:152876. https://doi.org/https://doi.org/10.1016/j.jnucmat.2021.152876

34. Burchell TD (2012) Radiation Effects in Graphite. In: Comprehensive Nuclear Materials. Elsevier, pp 299–324

35. Kelly BT (1981) Physics of graphite. Applied Science, London

36. Nightingale RE (2013) CHAPTER FIVE – Structure. In: Nuclear Graphite. pp 87–115

37. Hodgkins A, Marrow TJ, Wootton MR, et al (2010) Fracture behaviour of radiolytically oxidised reactor core graphites: a view. Mater Sci Technol 26:899–907. https://doi.org/10.1179/026708309X12526555493477

38. Griffith AA (1921) The Phenomena of Rupture and Flow in Solids.

Philos Trans R Soc London Ser A, Contain Pap a Math or Phys Character 221:163–198

39. Barinov SM, Sakai M (1994) The work-of-fracture of brittle materials: Principle, determination, and applications. J Mater Res 9:1412–1425. https://doi.org/10.1557/JMR.1994.1412

40. Mostafavi M, Marrow TJ (2012) Quantitative in situ study of short crack propagation in polygranular graphite by digital image correlation. Fatigue Fract Eng Mater Struct 35:695–707. https://doi.org/10.1111/j.1460-2695.2012.01648.x

41. Joyce MR, Marrow TJ, Mummery P, Marsden BJ (2008) Observation of microstructure deformation and damage in nuclear graphite. Eng Fract Mech 75:3633–3645. https://doi.org/10.1016/J.ENGFRACMECH.2007.11.003

42. Mostafavi M, McDonald SA, Mummery PM, Marrow TJ (2013) Observation and quantification of three-dimensional crack propagation in poly-granular graphite. Eng Fract Mech 110:410–420. https://doi.org/10.1016/J.ENGFRACMECH.2012.11.023

43. Göldner H (1978) Broek, D., Elementary Engineering Fracture Mechanics, Leyden. Noordhoff International Publishing. 1974. 408 S., Dfl. 120.00. $ 52.25. ZAMM - J Appl Math Mech / Zeitschrift für Angew Math und Mech 58:423. https://doi.org/10.1002/zamm.19780580919

44. Becker TH, Marrow TJ, Tait RB (2011) Damage, crack growth and fracture characteristics of nuclear grade graphite using the Double Torsion technique. J Nucl Mater 414:32–43. https://doi.org/https://doi.org/10.1016/j.jnucmat.2011.04.058

45. Marrow TJ, Liu D, Barhli SM, et al (2016) In situ measurement of the strains within a mechanically loaded polygranular graphite. Carbon N Y 96:285–302. https://doi.org/10.1016/j.carbon.2015.09.058

46. Mostafavi M, McDonald SA, Çetinel H, et al (2013) Flexural strength and defect behaviour of polygranular graphite under different states of stress. Carbon N Y 59:325–336. https://doi.org/10.1016/J.CARBON.2013.03.025

47. Tang P-Y (1983) Interpretation of bend strength increase of graphite by the couple-stress theory. Comput Struct 16:45–49. https://doi.org/10.1016/0045-7949(83)90146-3

48. Brocklehurst J., Darby M. (1974) Concerning the fracture of graphite under different test conditions. Mater Sci Eng 16:91–106. https://doi.org/10.1016/0025-5416(74)90143-8

49. Shahani R, Nejadi M (2015) Investigation on the mechanical properties and fracture toughness of graphite. Fatigue Fract Eng Mater Struct 38:1209–1218. https://doi.org/10.1111/ffe.12300

50. ASTM E1820 - 20b Standard Test Method for Measurement of Fracture Toughness. https://www.astm.org/Standards/E1820.htm. Accessed 4 Nov 2021

51. Liu D, Gludovatz B, Barnard HS, et al (2017) Damage tolerance of nuclear graphite at elevated temperatures. Nat Commun 8:15942

52. Kelly BT (1978) Radiation damage in graphite and its relevance to reactor design. Prog Nucl Energy 2:219–269. https://doi.org/10.1016/0149-1970(78)90005-7

53. Mostafavi M, Marrow TJ (2011) In situ observation of crack nuclei in poly-granular graphite under ring-on-ring equi-biaxial and flexural loading. Eng Fract Mech 78:1756–1770. https://doi.org/https://doi.org/10.1016/j.engfracmech.2010.11.004

54. Knibbs RH (1967) Fracture in polycrystalline graphite. J Nucl Mater 24:174–187. https://doi.org/10.1016/0022-3115(67)90006-2

55. Bazaj DK, Cox EE (1969) Stress-concentration factors and notch-sensitivity of graphite. Carbon N Y 7:689–697. https://doi.org/10.1016/0008-6223(69)90524-7

56. Berto F, Campagnolo A, Ayatollahi M, Barnoush A (2016) Fracture assessment of graphite components weakened by rounded V-notches and subjected to static multiaxial loading. Procedia Struct Integr 2:1805–1812. https://doi.org/10.1016/J.PROSTR.2016.06.227

57. Barhli SM, Saucedo-Mora L, Jordan MSL, et al (2017) Synchrotron X-ray characterization of crack strain fields in polygranular graphite. Carbon N Y 124:357–371. https://doi.org/10.1016/J.CARBON.2017.08.075

58. Vertyagina Y, Marrow TJ (2017) A multi-scale three-dimensional Cellular Automata fracture model of radiolytically oxidised nuclear graphite. Carbon N Y 121:574–590. https://doi.org/https://doi.org/10.1016/j.carbon.2017.06.031

59. Ziegeldorf S, Müller HS, Hilsdorf HK (1980) A model law for the notch sensitivity of brittle materials. Cem Concr Res 10:589–599. https://doi.org/10.1016/0008-8846(80)90022-8

60. Leguillon D, Yosibash Z (2017) Failure initiation at V-notch tips in quasi-brittle materials. Int J Solids Struct 122–123:1–13. https://doi.org/10.1016/J.IJSOLSTR.2017.05.036

61. Torabi AR, Fakoor M, Pirhadi E (2013) Tensile fracture in coarse-grained polycrystalline graphite weakened by a U-shaped notch. Eng Fract Mech 111:77–85. https://doi.org/10.1016/J.ENGFRACMECH.2013.08.015

62. Taylor R, Brown RG, Gilchrist K, et al (1967) The mechanical

properties of reactor graphite. Carbon N Y 5:519–531. https://doi.org/10.1016/0008-6223(67)90029-2

63. Krishna R, Jones AN, Edge R, Marsden BJ (2015) Residual stress measurements in polycrystalline graphite with micro-Raman spectroscopy. Radiat Phys Chem 111:14–23. https://doi.org/10.1016/J.RADPHYSCHEM.2015.02.007

64. Liu D, Mingard K, Lord OT, Flewitt P (2017) On the damage and fracture of nuclear graphite at multiple length-scales. J Nucl Mater 493:246–254

65. Taylor JEL, Hall GN, Mummery PM (2016) Investigating the effects of stress on the pore structures of nuclear grade graphites. J Nucl Mater 470:216–228. https://doi.org/10.1016/J.JNUCMAT.2015.12.031

66. Mileeva Z, Ross DK, King SM (2013) A study of the porosity of nuclear graphite using small-angle neutron scattering. Carbon N Y 64:20–26. https://doi.org/10.1016/J.CARBON.2013.06.030

67. Mrozowski S (1953) Mechanical strength, thermal expansion and structure of cokes and carbons. In: Society AC (ed) First biennial conference on carbon. Buffalo

68. Sutton AL, Howard VC (1962) The role of porosity in the accommodation of thermal expansion in graphite. J Nucl Mater 7:58–71. https://doi.org/10.1016/0022-3115(62)90194-0

69. Freeman HM, Jones AN, Ward MB, et al (2016) On the nature of cracks and voids in nuclear graphite. Carbon N Y 103:45–55. https://doi.org/https://doi.org/10.1016/j.carbon.2016.03.011

70. Wen K, Marrow J, Marsden B (2008) Microcracks in nuclear graphite and highly oriented pyrolytic graphite (HOPG). J Nucl Mater 381:199–203

71. Liu D, Cherns D (2018) Nano-cracks in a synthetic graphite composite for nuclear applications. Philos Mag 98:1272–1283. https://doi.org/10.1080/14786435.2018.1433886

72. Best JV, Stephen WJ, Wickham AJ (1985) Radiolytic graphite oxidation. Prog Nucl Energy 16:127–178. https://doi.org/10.1016/0149-1970(85)90002-2

73. Liu D, Zillhardt T, Earp P, et al (2020) In situ measurement of elastic and total strains during ambient and high temperature deformation of a polygranular graphite. Carbon N Y 163:308–323. https://doi.org/10.1016/j.carbon.2020.03.020

74. Soule DE, Nezbeda CW (1968) Direct Basal-Plane Shear in Single-Crystal Graphite. J Appl Phys 39:5122–5139. https://doi.org/10.1063/1.1655933

75. Barsoum MW, Murugaiah A, Kalidindi SR, et al (2004) Kink bands, nonlinear elasticity and nanoindentations in graphite. Carbon N Y 42:1435–1445. https://doi.org/https://doi.org/10.1016/j.carbon.2003.12.090

76. Palache C (1941) Contributions to the mineralogy of sterling hill, new jersey: morphology of graphite, arsenopyrite, pyrite, and arsenic. Am Mineral 26:709–717

77. Freise EJ, Kelly A (1961) Twinning in Graphite. Proc R Soc Lond A Math Phys Sci 264:269–276

78. Kennedy AJ (1960) Dislocations and Twinning in Graphite. Proc Phys Soc 75:607–611. https://doi.org/10.1088/0370-1328/75/4/314

79. Skinner J, Gane N (1973) The deformation and twinning of graphite crystals under a point load. Philos Mag A J Theor Exp Appl Phys 28:827–837. https://doi.org/10.1080/14786437308220986

80. Heard PJ, Wootton MR, Moskovic R, Flewitt PEJ (2011) Deformation and fracture of irradiated polygranular pile grade A reactor core graphite. J Nucl Mater 418:223–232. https://doi.org/https://doi.org/10.1016/j.jnucmat.2011.07.003

81. Haverty M (2015) The microstructure, texture and thermal expansion of nuclear graphite. [Thesis] Manchester, UK Univ Manchester; 2015

82. Gonzalez D, King A, Mostafavi M, et al (2013) Three-dimensional observation and image-based modelling of thermal strains in polycrystalline alumina. Acta Mater 61:7521–7533. https://doi.org/10.1016/J.ACTAMAT.2013.06.005

83. King A, Johnson G, Engelberg D, et al (2008) Observations of Intergranular Stress Corrosion Cracking in a Grain-Mapped Polycrystal. Science (80-) 321:382 LP – 385

84. Viganò N, Ludwig W (2020) X-ray orientation microscopy using topo-tomography and multi-mode diffraction contrast tomography. Curr Opin Solid State Mater Sci 24:100832. https://doi.org/https://doi.org/10.1016/j.cossms.2020.100832

85. Poulsen HF (2012) An introduction to three-dimensional X-ray diffraction microscopy. J Appl Crystallogr 45:1084–1097. https://doi.org/10.1107/S0021889812039143

86. Preston SD, Marsden BJ (2006) Changes in the coefficient of thermal expansion in stressed Gilsocarbon graphite. Carbon N Y 44:1250–1257. https://doi.org/10.1016/j.carbon.2005.10.045

87. Oku T, Kurumada A, Imamura Y, et al (1998) Effects of prestresses on mechanical properties of isotropic graphite materials. J Nucl Mater 258–263:814–820. https://doi.org/10.1016/S0022-3115(98)00071-3

88. Eason ED, Hall GN, Marsden BJ, Heys GB (2013) Models of coefficient of thermal expansion (CTE) for Gilsocarbon graphites irradiated in inert and oxidising environments. J Nucl Mater 436:191–200. https://doi.org/10.1016/J.JNUCMAT.2012.08.022

89. Bradford MR, Steer AG (2008) A structurally-based model of irradiated graphite properties. J Nucl Mater 381:137–144. https://doi.org/https://doi.org/10.1016/j.jnucmat.2008.07.040

90. Gray BS, Brocklehurst JE, McFarlane AA (1967) The irradiation induced plasticity in graphite under constant stress. Carbon N Y 5:173–180. https://doi.org/10.1016/0008-6223(67)90071-1

91. J. C. Bell, H. Bridge, A. H. Cottrell, G. B. Greenough, W. N. Reynolds JHWS (1962) Stored energy in the graphite of power-producing reactors. Philos Trans R Soc London Ser A, Math Phys Sci 254:361 LP – 395

92. Simmons JHW (John HW (1965) Radiation damage in graphite. Pergamon Press

93. Kelly BT (1977) The theory of irradiation damage in graphite. Carbon N Y 15:117–127. https://doi.org/10.1016/0008-6223(77)90027-6

94. Brocklehurst JE, Kelly BT (1993) Analysis of the dimensional changes and structural changes in polycrystalline graphite under fast neutron irradiation. Carbon N Y 31:155–178. https://doi.org/10.1016/0008-6223(93)90169-B

95. Kennedy CR, Cundy M, Kleist G (1988) The irradiation creep characteristics of graphite to high fluences

96. Kelly BT, Foreman AJE (1974) The theory of irradiation creep in reactor graphite—The dislocation pinning-unpinning model. Carbon N Y 12:151–158. https://doi.org/10.1016/0008-6223(74)90021-9

97. Kelly BT, Brocklehurst JE (1977) UKAEA Reactor Group studies of irradiation-induced creep in graphite. J Nucl Mater 65:79–85. https://doi.org/10.1016/0022-3115(77)90044-7

98. Bodel W, Martinuzzi P, Davies B, et al (2021) Mimicking irradiation-induced cracking of nuclear graphite using bromine intercalation. Scr Mater 199:113889. https://doi.org/https://doi.org/10.1016/j.scriptamat.2021.113889

99. Burchell TD, Strizak JP (2014) The effect of neutron irradiation on the fracture toughness of graphite. Nucl Eng Des 271:262–269. https://doi.org/https://doi.org/10.1016/j.nucengdes.2013.11.046

100. Sato S, Imamura Y, Kawamata K, et al (1980) Irradiation effects on thermal shock resistance and fracture toughness of HTGR-graphite. Nucl Eng Des 61:383–397. https://doi.org/https://doi.org/10.1016/0029-

5493(80)90008-4

101. Sato S, Kurumada A, Kawamata K, et al (1989) Neutron irradiation effects on thermal shock resistance and fracture toughness of graphites as plasma-facing first wall components for fusion reactor devices. Carbon N Y 27:507–516. https://doi.org/https://doi.org/10.1016/0008-6223(89)90001-8

102. Theodosiou A, Jones AN, Marsden BJ (2017) Thermal oxidation of nuclear graphite: A large scale waste treatment option. PLoS One 12:e0182860

103. Best J V, Stephen WJ, Wickham AJ (1985) RADIOLYTIC GRAPHITE OXIDATION

104. Lim Y-S, Chi S-H, Cho K-Y (2008) Change of properties after oxidation of IG-11 graphite by air and CO2 gas. J Nucl Mater 374:123–128. https://doi.org/10.1016/J.JNUCMAT.2007.07.015

105. Gallego NC, Arregui-Mena JD, Contescu CI (2021) Probing basal planes and edge sites in polygranular nuclear graphite by gas adsorption: Estimation of active surface area. Carbon N Y 179:633–645. https://doi.org/https://doi.org/10.1016/j.carbon.2021.04.044

106. Jones KL, Matthews GP, Laudone GM (2020) The effect of irradiation and radiolytic oxidation on the porous space of Gilsocarbon nuclear graphite measured with mercury porosimetry and helium pycnometry. Carbon N Y 158:256–266. https://doi.org/https://doi.org/10.1016/j.carbon.2019.11.084

107. Kelly BT, Faircloth RL, Best JV (1982) Reduction in the strength of graphite by radiolytic oxidation in carbon dioxide

108. Kelly BT, Johnson PA V, Schofield P, et al (1983) UKAEA Northern Division Studies Of The Radiolytic Oxidation Of Graphite In Carbon-Dioxide. Carbon N Y 21:441–449. https://doi.org/10.1016/0008-6223(83)90135-5

109. Tzelepi A, Ramsay P, Steer AG, Dinsdale-Potter J (2018) Measuring the fracture properties of irradiated reactor core graphite. J Nucl Mater 509:667–678. https://doi.org/https://doi.org/10.1016/j.jnucmat.2018.07.024

110. J Bodey A, Mileeva Z, Lowe T, et al (2017) Simultaneous heating and compression of irradiated graphite during synchrotron microtomographic imaging. J Phys Conf Ser 849:

111. Wade-Zhu J, Krishna R, Bodey AJ, et al (2020) 4D synchrotron X-ray microtomography of fracture in nuclear graphite after neutron irradiation and radiolytic oxidation. Carbon N Y 168:230–244. https://doi.org/https://doi.org/10.1016/j.carbon.2020.06.051

112. Jin X, Wade-Zhu J, Chen Y, et al (2021) Assessment of the fracture toughness of neutron-irradiated nuclear graphite by 3D analysis of the crack displacement field. Carbon N Y 171:882–893. https://doi.org/https://doi.org/10.1016/j.carbon.2020.09.072

113. Bonse U, Busch F (1996) X-ray computed microtomography (μCT) using synchrotron radiation (SR). Prog Biophys Mol Biol 65:133–169. https://doi.org/https://doi.org/10.1016/S0079-6107(96)00011-9

114. Suzuki Y, Yagi N, Uesugi K (2002) X-ray refraction-enhanced imaging and a method for phase retrieval for a simple object. J Synchrotron Radiat 9:160–165. https://doi.org/10.1107/S090904950200554X

115. Cloetens P, Ludwig W, Baruchel J, et al (1999) Holotomography: Quantitative phase tomography with micrometer resolution using hard synchrotron radiation x rays. Appl Phys Lett 75:2912–2914. https://doi.org/10.1063/1.125225

116. Dall'Ara E, Peña-Fernández M, Palanca M, et al (2017) Precision of Digital Volume Correlation Approaches for Strain Analysis in Bone Imaged with Micro-Computed Tomography at Different Dimensional Levels. Front Mater 4:31. https://doi.org/10.3389/fmats.2017.00031

117. Tudisco E, Andò E, Cailletaud R, Hall SA (2017) TomoWarp2: A local digital volume correlation code. SoftwareX 6:267–270. https://doi.org/10.1016/J.SOFTX.2017.10.002

118. Berre C, Fok SL, Marsden BJ, et al (2008) Microstructural modelling of nuclear graphite using multi-phase models. J Nucl Mater 380:46–58. https://doi.org/10.1016/J.JNUCMAT.2008.07.006

119. Morrison CNN, Jivkov APP, Vertyagina Y, Marrow TJJ (2016) Multi-scale modelling of nuclear graphite tensile strength using the site-bond lattice model. Carbon N Y 100:273–282

120. Vertyagina Y, Marrow TJ (2017) 3D Cellular Automata fracture model for porous graphite microstructures. Nucl Eng Des 323:202–208. https://doi.org/10.1016/j.nucengdes.2016.10.015

121. Fahad M, McNally K, Yates T, et al (2017) Finite element modelling of multilayer Advanced Gas-cooled Reactor bricks and creep interaction. Nucl Eng Des 324:390–401. https://doi.org/10.1016/J.NUCENGDES.2017.09.014

122. Mummery PM, Treifi M, Marsden BJ, Hall GN (2015) Keyway Root Crack Arrest In An AGR Graphite Brick. 23rd Conf Struct Mech React Technol 10 Aug 2015-14 Aug 2015; Manchester, United Kingdom 2015

123. Saucedo-Mora L, Marrow TJ (2015) FEMME: A multi-scale Finite Element Microstructure MEshfree fracture model for quasi-brittle materials with complex microstructures. Eng Fract Mech 147:355–372. https://doi.org/10.1016/J.ENGFRACMECH.2015.05.059

124. Saucedo-Mora L, James Marrow T (2015) Method for the explicit insertion of microstructure in Cellular Automata Finite Element (CAFE) models based on an irregular tetrahedral Finite Element mesh: Application in a multi-scale Finite Element Microstructure MEshfree framework (FEMME). Finite Elem Anal Des 105:56–62. https://doi.org/https://doi.org/10.1016/j.finel.2015.07.001

125. Zou Z, Fok SL, Marsden BJ, Oyadiji SO (2006) Numerical simulation of strength test on graphite moderator bricks using a continuum damage mechanics model. Eng Fract Mech 73:318–330. https://doi.org/https://doi.org/10.1016/j.engfracmech.2005.08.002

126. Zillhardt T, Koko A, Chen Y, et al (2018) ME1504: In-situ Mapping of Twinning in Graphite by Diffraction Contrast Tomography @ID11. Eur Synchrotron Radiat Facil. https://doi.org/10.15151/ESRF-ES-158876748

127. Zillhardt T, Cabeza S, Earp P, et al (2021) 1-02-241: High-resolution neutron diffraction residual stress analysis of nuclear graphite @SALSA. Inst Laue-Langevin. https://doi.org/10.5291/ILL-DATA.1-02-241

128. Zillhardt T, Cabeza S, Marrow TJ (2021) 1-02-299: High-resolution neutron diffraction residual stress analysis of nuclear graphite @SALSA. Inst Laue-Langevin. https://doi.org/10.5291/ILL-DATA.1-02-299

129. Zillhardt T, Marrow TJ, Kelleher JF, et al (2020) 20190926: Time series high-resolution pink beam tomography of nuclear graphite: strain accommodation, crack coalescence and propagation @PSICHE. Soleil Synchrotron. https://doi.org/DOI UNAVAILABLE

130. Marrow TJ, Zillhardt T, Williamson M, et al (2020) RB1910517-1: High Resolution Neutron Bragg Imaging of Gilsocarbon Graphite for the Investigation of Crystal Reorientation @IMAT. STFC ISIS Neutron Muon Source. https://doi.org/10.5286/ISIS.E.RB1910517-1

131. Marrow TJ, Zillhardt T, Burca G (2020) RB1910517-2: High Resolution Neutron Bragg Imaging of Gilsocarbon Graphite for the Investigation of Crystal Reorientation @IMAT. STFC ISIS Neutron Muon Source. https://doi.org/10.5286/ISIS.E.RB1910517-2

132. Marrow TJ, Buffière J-Y, Mostafavi M, et al (2016) EE12585-2: Full 3-Dimensional Deformation Mapping of a Short Fatigue Crack @i12. Diam Light Source. https://doi.org/DOI UNAVAILABLE

133. Anuta PE (1970) Spatial Registration of Multispectral and Multitemporal Digital Imagery Using Fast Fourier Transform Techniques. IEEE Trans Geosci Electron 8:353–368. https://doi.org/10.1109/TGE.1970.271435

134. Peters WH, Ranson WF (1982) DIGITAL IMAGING TECHNIQUES IN EXPERIMENTAL STRESS ANALYSIS. Opt Eng 21:427–431.

https://doi.org/10.1117/12.7972925

135. Sutton MA, Wolters WJ, Peters WH, et al (1983) Determination of displacements using an improved digital correlation method. Image Vis Comput 1:133–139. https://doi.org/https://doi.org/10.1016/0262-8856(83)90064-1

136. McNeill SR, Peters WH, Sutton MA (1987) Estimation of stress intensity factor by digital image correlation. Eng Fract Mech 28:101–112. https://doi.org/https://doi.org/10.1016/0013-7944(87)90124-X

137. Hassan GM (2021) Deformation measurement in the presence of discontinuities with digital image correlation: A review. Opt Lasers Eng 137:106394. https://doi.org/https://doi.org/10.1016/j.optlaseng.2020.106394

138. Chen F, Chen X, Xie X, et al (2013) Full-field 3D measurement using multi-camera digital image correlation system. Opt Lasers Eng 51:1044–1052. https://doi.org/https://doi.org/10.1016/j.optlaseng.2013.03.001

139. Pan B, Yu L, Zhang Q (2018) Review of single-camera stereo-digital image correlation techniques for full-field 3D shape and deformation measurement. Sci China Technol Sci 61:2–20. https://doi.org/10.1007/s11431-017-9090-x

140. Becker TH, Marrow TJ (2021) A Robust Finite Element-based Filter for Digital Image and Volume Correlation Displacement Data. Exp Mech. https://doi.org/10.1007/s11340-021-00718-5

141. (2015) GOM Correlate Professional V8 SR1 Manual Basic Inspection-3D Testing

142. Shoemake K (1994) Euler Angle Conversion. In: Heckbert PSBT-GG (ed) Graphics Gems. Elsevier, pp 222–229

143. Rodenburg J, Maiden A (2019) Ptychography BT - Springer Handbook of Microscopy. In: Hawkes PW, Spence JCH (eds). Springer International Publishing, Cham, pp 819–904

144. Santisteban JR, Daymond MR, James JA, Edwards L (2006) ENGIN-X: a third-generation neutron strain scanner. J Appl Crystallogr 39:812–825. https://doi.org/10.1107/S0021889806042245

145. Nervo L, King A, Wright JP, et al (2014) Comparison between a near-field and a far-field indexing approach for characterization of a polycrystalline sample volume containing more than 1500 grains. J Appl Crystallogr 47:1402–1416. https://doi.org/10.1107/S160057671401406X

146. Burca G, Kockelmann W, James JA, Fitzpatrick ME (2013) Modelling of an imaging beamline at the ISIS pulsed neutron source. J Instrum

8:P10001–P10001. https://doi.org/10.1088/1748-0221/8/10/p10001

147. Kockelmann W, Minniti T, Pooley D, et al (2018) Time-of-Flight Neutron Imaging on IMAT@ISIS: A New User Facility for Materials Science. J Imaging 4:47. https://doi.org/10.3390/jimaging4030047

148. Strobl M, Woracek R, Kardjilov N, et al (2012) Time-of-flight neutron imaging for spatially resolved strain investigations based on Bragg edge transmission at a reactor source. Nucl Instruments Methods Phys Res Sect A Accel Spectrometers, Detect Assoc Equip 680:27–34. https://doi.org/10.1016/j.nima.2012.04.026

149. Strobl M, Hilger A, Boin M, et al (2011) Time-of-flight neutron imaging at a continuous source: Proof of principle using a scintillator CCD imaging detector. In: Nuclear Instruments and Methods in Physics Research, Section A: Accelerators, Spectrometers, Detectors and Associated Equipment. North-Holland, pp 149–155

150. Woracek R, Penumadu D, Kardjilov N, et al (2011) Neutron Bragg-edge-imaging for strain mapping under in situ tensile loading. J Appl Phys 109:93506. https://doi.org/10.1063/1.3582138

151. Strickland J, Tassenberg K, Sheppard G, et al (2020) 2D single crystal Bragg-dip mapping by time-of-flight energy-resolved neutron imaging on IMAT@ISIS. Sci Rep 10:20751. https://doi.org/10.1038/s41598-020-77572-3

152. Song G, Lin J, Bilheux J, et al (2017) Characterization of Crystallographic Structures Using Bragg-Edge Neutron Imaging at the Spallation Neutron Source. J Imaging 3:65. https://doi.org/10.3390/jimaging3040065

153. Tremsin AS, Vallerga J V., McPhate JB, et al (2013) High Resolution Photon Counting With MCP-Timepix Quad Parallel Readout Operating at >1 KHz Frame Rates. IEEE Trans Nucl Sci 60:578–585. https://doi.org/10.1109/TNS.2012.2223714

154. Shen K, Yu S, Kang F (2019) The microstructure and texture of Gilsocarbon graphite. Carbon N Y 153:428–437. https://doi.org/https://doi.org/10.1016/j.carbon.2019.06.108

155. Reischig P, King A, Nervo L, et al (2013) Advances in X-ray diffraction contrast tomography: flexibility in the setup geometry and application to multiphase materials. J Appl Crystallogr 46:297–311. https://doi.org/10.1107/S0021889813002604

156. King A, Ludwig W, Herbig M, et al (2011) Three-dimensional in situ observations of short fatigue crack growth in magnesium. Acta Mater 59:6761–6771. https://doi.org/10.1016/J.ACTAMAT.2011.07.034

157. Gustafson S, Ludwig W, Shade P, et al (2020) Quantifying microscale drivers for fatigue failure via coupled synchrotron X-ray characterization

and simulations. Nat Commun 11:3189. https://doi.org/10.1038/s41467-020-16894-2

158. Cereser A, Strobl M, Hall SA, et al (2017) Time-of-Flight Three Dimensional Neutron Diffraction in Transmission Mode for Mapping Crystal Grain Structures. Sci Rep 7:9561. https://doi.org/10.1038/s41598-017-09717-w

159. ASTM D8289 - 19 Standard Test Method for Tensile Strength Estimate by Disc Compression of Manufactured Graphite. https://www.astm.org/DATABASE.CART/HISTORICAL/D8289-19.htm. Accessed 20 Nov 2020

160. Earp P, Kabra S, Zillhardt T, Marrow TJ (2018) RB1810071: The effect of the onset of plastic deformation on texture in cast alpha-uranium @GEM. STFC ISIS Neutron Muon Source. https://doi.org/10.5286/ISIS.E.RB1810071

161. Marone F, Stampanoni M (2012) Regridding reconstruction algorithm for real-time tomographic imaging. J Synchrotron Radiat 19:1029–1037. https://doi.org/10.1107/S0909049512032864

162. Schofield R, King L, Tayal U, et al (2020) Image reconstruction: Part 1 – understanding filtered back projection, noise and image acquisition. J Cardiovasc Comput Tomogr 14:219–225. https://doi.org/https://doi.org/10.1016/j.jcct.2019.04.008

163. Mirone A, Brun E, Gouillart E, et al (2014) The PyHST2 hybrid distributed code for high speed tomographic reconstruction with iterative reconstruction and a priori knowledge capabilities. Nucl Instruments Methods Phys Res Sect B Beam Interact with Mater Atoms 324:41–48. https://doi.org/https://doi.org/10.1016/j.nimb.2013.09.030

164. van Aarle W, Palenstijn WJ, Cant J, et al (2016) Fast and flexible X-ray tomography using the ASTRA toolbox. Opt Express 24:25129–25147. https://doi.org/10.1364/OE.24.025129

165. Vo NT, Atwood RC, Drakopoulos M (2018) Superior techniques for eliminating ring artifacts in X-ray micro-tomography. Opt Express 26:28396–28412. https://doi.org/10.1364/OE.26.028396

166. Buck JR, Daniel MM, Singer A (1997) Computer Explorations in Signals and Systems Using MATLAB. Prentice Hall

167. Stoica P, Moses RL (2005) Spectral Analysis of Signals. Pearson Prentice Hall

168. Kieffer J, Wright JP (2013) PyFAI: a Python library for high performance azimuthal integration on GPU. Powder Diffr 28:S339–S350. https://doi.org/DOI: 10.1017/S0885715613000924

169. Kieffer J, Karkoulis D (2013) PyFAI, a versatile library for azimuthal regrouping. J Phys Conf Ser 425:202012. https://doi.org/10.1088/1742-6596/425/20/202012

170. Hodgkins A, Marrow TJ, Mummery P, et al (2006) X-ray tomography observation of crack propagation in nuclear graphite. Mater Sci Technol 22:1045–1051. https://doi.org/10.1179/174328406X114126

171. Lasithiotakis M, Marrow JT, Marsden BJ (2020) Evaluation of damage induced in graphite due to sample preparation by standard non-destructive techniques. Mater Phys Mech 77:271–287. https://doi.org/10.18720/MPM.4432020_1

172. Hallam KR, Darnbrough JE, Paraskevoulakos C, et al (2021) Measurements by x-ray diffraction of the temperature dependence of lattice parameter and crystallite size for isostatically-pressed graphite. Carbon Trends 100071. https://doi.org/https://doi.org/10.1016/j.cartre.2021.100071

173. Williamson GK, Hall WH (1953) X-ray line broadening from filed aluminium and wolfram. Acta Metall 1:22–31. https://doi.org/https://doi.org/10.1016/0001-6160(53)90006-6

174. Zillhardt TAC, Burca G, Liu D, Marrow TJ (2021) In Situ Mechanical Loading and Neutron Bragg-edge Imaging, Applied to Polygranular Graphite On IMAT@ISIS. Exp Mech. https://doi.org/10.1007/s11340-021-00754-1

175. Mattes M, Keinert J (2005) Status of thermal neutron scattering data for graphite

176. Chung DDL (2002) Review Graphite. J Mater Sci 37:1475–1489. https://doi.org/10.1023/A:1014915307738

177. Zillhardt T (2021) NEUTRONIX: Program for the detection of grain reorientation with in-situ Bragg imaging. https://github.com/olayne/NEUTRONIX

178. Liptak A, Burca G, Kelleher J, et al (2019) Developments towards Bragg edge imaging on the IMAT beamline at the ISIS Pulsed Neutron and Muon Source: BEAn software. J Phys Commun. https://doi.org/10.1088/2399-6528/ab5575

179. Thirion J-P (1998) Image matching as a diffusion process: an analogy with Maxwell's demons. Med Image Anal 2:243–260. https://doi.org/https://doi.org/10.1016/S1361-8415(98)80022-4

180. Vercauteren T, Pennec X, Perchant A, Ayache N (2009) Diffeomorphic demons: Efficient non-parametric image registration. Neuroimage 45:S61–S72. https://doi.org/https://doi.org/10.1016/j.neuroimage.2008.10.040

181. Fermi E, Sturm WJ, Sachs RG (1947) The Transmission of Slow Neutrons through Microcrystalline Materials. Phys Rev 71:589–594. https://doi.org/10.1103/PhysRev.71.589

182. Venkatakrishnan S, Zhang Y, Dessieux L, et al (2021) Improved Acquisition and Reconstruction for Wavelength-Resolved Neutron Tomography. J. Imaging 7

183. Savitzky A, Golay MJE (1964) Smoothing and Differentiation of Data by Simplified Least Squares Procedures. Anal Chem 36:1627–1639. https://doi.org/10.1021/ac60214a047

184. Renversade L, Quey R (2019) Analysis of in-grain orientation distributions in deformed aluminium using X-ray diffraction and finite elements. In: IOP Conference Series: Materials Science and Engineering. IOP Publishing Ltd, p 012022

185. Hayashi Y, Hirose Y, Seno Y (2015) Polycrystal orientation mapping using scanning three-dimensional X-ray diffraction microscopy. J Appl Crystallogr 48:1094–1101. https://doi.org/10.1107/S1600576715009899

186. Kocks UF, Tomé CN, Wenk HR, et al (1998) Texture and Anisotropy: Preferred Orientations in Polycrystals and Their Effect on Materials Properties. Cambridge University Press

187. Al-Jawad M, Addison O, Khan MA, et al (2012) Disruption of enamel crystal formation quantified by synchrotron microdiffraction. J Dent 40:1074–1080. https://doi.org/https://doi.org/10.1016/j.jdent.2012.08.020

188. Free R, DeRocher K, Xu R, et al (2020) A method for mapping submicron-scale crystallographic order/disorder applied to human tooth enamel. Powder Diffr 35:117–123. https://doi.org/DOI: 10.1017/S0885715620000251

189. Al-Mosawi M, Davis GR, Bushby A, et al (2018) Crystallographic texture and mineral concentration quantification of developing and mature human incisal enamel. Sci Rep 8:14449. https://doi.org/10.1038/s41598-018-32425-y

190. Poulsen HF (2012) An introduction to three-dimensional X-ray diffraction microscopy. J Appl Crystallogr 45:1084–1097. https://doi.org/10.1107/S0021889812039143

191. Sørensen HO, Hakim SS, Pedersen S, et al (2012) NON-DESTRUCTIVE IDENTIFICATION OF MICROMETER-SCALE MINERALS AND THEIR POSITION WITHIN A BULK SAMPLE. Can Mineral 50:501–509. https://doi.org/10.3749/canmin.50.2.501

192. Nakai Y, Shiozawa D, Kikuchi S, et al (2019) Observations of twinning and detwinning in magnesium alloy by synchrotron radiation DCT and

EBSD. In: Procedia Structural Integrity. Elsevier B.V., pp 83–88

193. Proudhon H, Guéninchault N, Forest S, Ludwig W (2018) Incipient Bulk Polycrystal Plasticity Observed by Synchrotron In-Situ Topotomography. Materials (Basel) 11:2018. https://doi.org/10.3390/ma11102018

194. Freise EJ, Kelly A (1963) The deformation of graphite crystals and the production of the rhombohedral form. Philos Mag 8:

195. Earp P, Kabra S, Askew J, Marrow TJ (2018) Lattice strain and texture development in coarse-grained uranium-a neutron diffraction study. 12012. https://doi.org/10.1088/1742-6596/1106/1/012012

196. Hoye N, Li HJ, Cuiuri D, Paradowska A (2014) Measurement of residual stresses in titanium aerospace components formed via additive manufacturing. In: Materials Science Forum. Trans Tech Publications Ltd, pp 124–129

197. Nervo L, King A, Fitzner A, et al (2016) A study of deformation twinning in a titanium alloy by X-ray diffraction contrast tomography. Acta Mater 105:417–428. https://doi.org/10.1016/j.actamat.2015.12.032

198. Deng X, Zuo F, Li H (2018) Cracks Detection Using Iterative Phase Congruency. J Math Imaging Vis 60:1065–1080. https://doi.org/10.1007/s10851-018-0796-y

199. Cinar AF, Barhli SM, Hollis D, et al (2017) An autonomous surface discontinuity detection and quantification method by digital image correlation and phase congruency. Opt Lasers Eng 96:94–106. https://doi.org/https://doi.org/10.1016/j.optlaseng.2017.04.010

200. Lin H, Xiong W, Xiong Z, Gong F (2015) Three-dimensional effects in a flattened Brazilian disk test. Int J Rock Mech Min Sci 74:10–14. https://doi.org/10.1016/j.ijrmms.2014.11.006

201. Imani M, Nejati HR, Goshtasbi K (2017) Dynamic response and failure mechanism of Brazilian disk specimens at high strain rate. Soil Dyn Earthq Eng 100:261–269. https://doi.org/10.1016/J.SOILDYN.2017.06.007

202. Jones AN, Hall GN, Joyce M, et al (2008) Microstructural characterisation of nuclear grade graphite. J Nucl Mater 381:152–157. https://doi.org/https://doi.org/10.1016/j.jnucmat.2008.07.038

203. Zheng G, Xu P, Sridharan K, Allen T (2014) Characterization of structural defects in nuclear graphite IG-110 and NBG-18. J Nucl Mater 446:193–199. https://doi.org/https://doi.org/10.1016/j.jnucmat.2013.12.013

204. Shearing PR, Howard LE, Jørgensen PS, et al (2010) Characterization of the 3-dimensional microstructure of a graphite negative electrode

from a Li-ion battery. Electrochem commun 12:374–377. https://doi.org/https://doi.org/10.1016/j.elecom.2009.12.038

205. Heard PJ, Wootton MR, Moskovic R, Flewitt PEJ (2010) Crack initiation and propagation in pile grade A (PGA) reactor core graphite under a range of loading conditions. J Nucl Mater 401:71–77. https://doi.org/https://doi.org/10.1016/j.jnucmat.2010.03.023

206. Hall G, Marsden BJ, Fok SL (2006) The microstructural modelling of nuclear grade graphite. J Nucl Mater 353:12–18. https://doi.org/https://doi.org/10.1016/j.jnucmat.2006.02.082

207. Withers PJ (2007) X-ray nanotomography. Mater Today 10:26–34. https://doi.org/https://doi.org/10.1016/S1369-7021(07)70305-X

Appendix A APPENDICES

A.1 Codes

A number of codes have been developed for this project, either with foundations from past work or from scratch. The codes and algorithms used in this work have between 5 and 40 scripts and functions each, and hundreds of files. This would represent an extra 100-200 pages to this Thesis and without the search options available on a computer, cluttering the document, as many functions have further functions and calls embedded. It was therefore decided to describe the workings of each code in the methodology of the experiment for which it was used, rather than including them here. As some of these codes have not yet been published, they are not all available online. They are available in electronic format to the examiners upon request.

A.2 SALSA Experiments 1-02-241 and 1-02-299 on the notch sensitivity of Gilsocarbon graphite studied with High-Resolution Neutron Scattering

These experiments were presented in 2.8, as both represented an important allocation of time and effort to this project. These have, however suffered added complexities which meant that the results and conclusions are not sufficient given the limited space in this thesis, and compared to the other branches of this research. It is also a work in still progress, which cannot be completed before the end of this project due to many external factors.

The first major difficulty was face when, during the initial experiment (1-02-241), we found (with the beamline scientists) that the experimental setup was incompatible with the beamline arrangements. The Instron hydraulic rig had never been rotated in front of the high-resolution collimators, which take more space and took hours to calibrate at the time (before automation), and a collision with the secondary collimator stopped the experiment. A further delay was imposed by the failure of the Instron pump cooling system due to the high summer temperatures, and this meant that we were unable to adapt the experiment within the beam time to collect the tensile (and most important) component. The extension experiment was granted, but delayed many times because of the COVID-19 pandemic. When it was finally possible in March 2021, it was further delayed by Brexit import difficulties. By that time, I was already in the writing phase of this work, and the datasets are difficult to processing which is inherently due to the 2D detector and the very small peak changes in graphite. Hereafter I present the current stage of the analysis, but I will not intend to make any conclusion at this stage. Fig. A 1 and Fig. A 2 present the result of the tensile experiment to the time of writing.

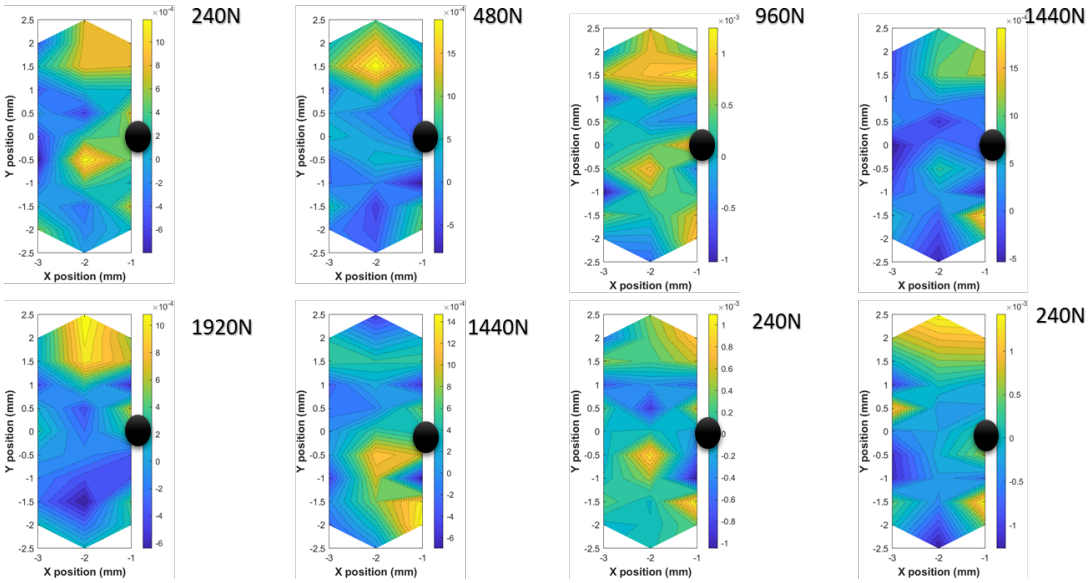


Fig. A 1: Diffraction maps (tensile strains) at the notch (black circle), calculated using signal cross-correlation

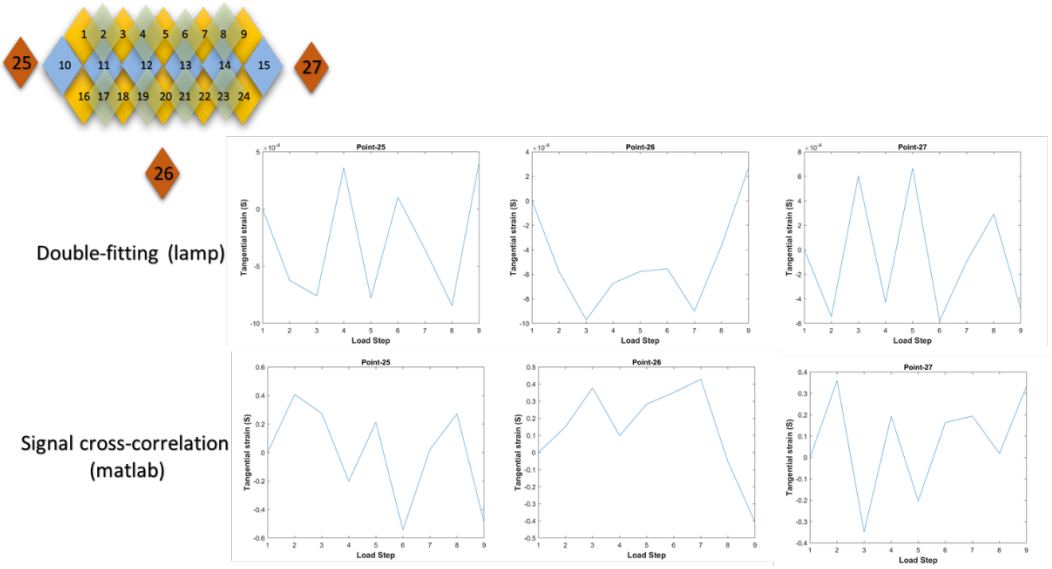


Fig. A 2: Comparison of the control points calculated with two methods, double fitting (reference/deformed), and signel cross-correlation, showing inconsitency in the measured values

A.3 Project Partners

